

2011

# A Theoretical Model of a Lateral-Field Excited Sensor Element Under Liquid Loading

Lester A. French

Follow this and additional works at: <http://digitalcommons.library.umaine.edu/etd>



Part of the [Electrical and Computer Engineering Commons](#)

---

## Recommended Citation

French, Lester A., "A Theoretical Model of a Lateral-Field Excited Sensor Element Under Liquid Loading" (2011). *Electronic Theses and Dissertations*. 1636.

<http://digitalcommons.library.umaine.edu/etd/1636>

This Open-Access Dissertation is brought to you for free and open access by DigitalCommons@UMaine. It has been accepted for inclusion in Electronic Theses and Dissertations by an authorized administrator of DigitalCommons@UMaine.

**A THEORETICAL MODEL OF A LATERAL-FIELD  
EXCITED SENSOR ELEMENT UNDER  
LIQUID LOADING**

by

Lester A. French Jr.

B.S. University of New Hampshire, 1993

M.S. University of Maine, 2002

A THESIS

Submitted in Partial Fulfillment of the  
Requirements for the Degree of  
Doctor of Philosophy Interdisciplinary

(in Sensors)

The Graduate School

The University of Maine

August 2011

Advisory Committee:

John Vetelino, Professor of Electrical Engineering, Advisor

Douglas Bousfield, Professor of Chemical and Biological Engineering

Fabien Josse, Professor of Electrical and Computer Engineering

Robert Lad, Professor of Physics

Mauricio Pereira da Cunha, Professor of Electrical Engineering

## **THESIS ACCEPTANCE STATEMENT**

On behalf of the graduate committee for Lester A. French Jr. I affirm that this manuscript is the final and accepted dissertation. Signatures of all committee members are on file with the Graduate School at the University of Maine, 42 Stodder Hall, Orono, Maine.

---

John Vetelino, Professor of Electrical Engineering

12 August 2011

© 2011 Lester A. French Jr.

All Rights Reserved

## **LIBRARY RIGHTS STATEMENT**

In presenting this dissertation in partial fulfillment for a degree of Doctor of Philosophy at the University of Maine, I agree that the library shall make it freely available for inspection. I further agree that permission for “fair use” copying of this dissertation for scholarly purposes may be granted by the Librarian. It is understood that any copying or publication of this dissertation for financial gain shall not be granted without my written permission.

Signature:

Date:

**A THEORETICAL MODEL OF A LATERAL-FIELD  
EXCITED SENSOR ELEMENT UNDER  
LIQUID LOADING**

by

Lester A. French Jr.

Dissertation Advisor: Dr. John Vetelino

An Abstract of the Dissertation Presented  
in Partial Fulfillment for the  
Requirements for the  
Degree of Doctor of Philosophy Interdisciplinary  
(in Sensors)  
August 2011

The lateral-field excited (LFE) acoustic wave sensor element has been shown to be more sensitive to mass, viscous, and electrical loading than the quartz crystal microbalance. Despite this, no equivalent circuit exists to model the LFE sensor element under simultaneous mechanical and electrical loading by a liquid. In this work an equivalent circuit model of the LFE sensor element loaded with a Newtonian liquid is developed. This equivalent circuit model is the first to model an LFE sensor under liquid loads with lumped elements that relate to the piezoelectric crystal and the material properties of the contacting liquid.

The LFE sensor element is examined by solving the coupled-wave equations for the thickness-shear mode in the multi-layered LFE sensor structure, resulting in an expression for the admittance of the LFE sensor element. The effects of liquid perturbations to the admittance of the LFE sensor element are modeled as discrete circuit elements in an equivalent circuit. The model is verified independently by measuring the sensor response of

LFE sensor elements with a variety of electrode gap separations, (0.5, 1.0, and 2.0 mm), to changes in liquid viscosity, permittivity, and conductivity.

The equivalent circuit model developed is accurate, within  $\pm 5\%$ , admittance near the resonant frequency for LFE sensor elements in deionized water. The model predicts the frequency shift of the LFE sensor element to perturbations in the density, viscosity, permittivity, and conductivity of the contacting liquid

## ACKNOWLEDGEMENTS

I thank my advisor Dr. John Vetelino, for his support and faith in me to see this dissertation through to its conclusion. I also thank my committee Drs. Bousfield, Josse, Lad, and Pereira da Cunha for their assistance and invaluable advice throughout this project. I also want to thank a former member of my committee, Dr. Chao Zhang for many useful conversations regarding the LFE sensor element.

This work, as is typical of scientific research, is not solely the work of one person. I am indebted to the many people who contributed to this project many of who will go unnamed. At the top of the list is my colleague Dr. Don McCann for many useful discussions, both substantive and philosophical. The staff of the Laboratory for Surface Science and Technology, including Drs. David Frankel and George Bernhardt, Mr. Eric Martin, and Ms. Sue Ashley and Ms. Patricia Paul for all of the technical and administrative support that they have provided. Special mention goes out to Matt Jones, who as an NSF-REU participant, started the substantive work on acquiring much of the data that formed the experimental portion of this dissertation.

Finally, I thank my lovely wife, Laura Wilson, and our two children Audrie and Jack, without whose infinite support, patience, and love, I would not have finished.

I was partially supported by a National Science Foundation GK-12: *Sensors* Fellowship #0538457.



## TABLE OF CONTENTS

ACKNOWLEDGEMENTS .....	iv
TABLE OF CONTENTS.....	v
LIST OF TABLES.....	ix
LIST OF FIGURES .....	xii
LIST OF SYMBOLS.....	xvii
LIST OF ABBREVIATIONS .....	xxiii
Chapter 1 INTRODUCTION.....	1
1.1. Background .....	1
1.2. Approach.....	8
1.3. Organization .....	9
Chapter 2 BACKGROUND THEORY .....	10
2.1. Acoustic Waves in Non-Piezoelectric Crystals .....	10
2.1.1. Mechanical Considerations .....	10
2.1.2. Electromagnetic Considerations.....	16
2.2. Acoustic Waves in Piezoelectric Crystals.....	17
2.2.1. The Quasistatic Approximation .....	18
2.3. Bulk Acoustic Wave Resonators .....	19
2.3.1. Thickness-Field Excited BAW Resonators .....	21
2.3.2. Lateral-Field Excitation of BAW Resonators.....	24

2.4. Modeling Bulk Acoustic Waves .....	25
2.4.1. An Analysis of the Thickness Shear Mode in BAW Resonators.....	26
2.4.1.1. Thickness-Field Excited BAW Resonator .....	27
2.4.1.2. Lateral-Field Excited BAW Resonator .....	32
2.4.2. Mason Circuit Model .....	41
2.4.2.1. Thickness-Field Excited BAW Resonator .....	42
2.4.2.2. Lateral-Field Excited BAW Resonator .....	46
2.4.3. Martin Circuit Model.....	48
2.4.4. Transmission Line Model.....	52
2.4.4.1. Thickness-Field Excited BAW Resonator .....	53
2.4.4.2. Lateral-Field Excited BAW Resonator .....	55
 Chapter 3 EQUIVALENT CIRCUIT FOR A LATERAL-FIELD EXCITED SENSOR ELEMENT.....	 57
3.1. Setting up the Analysis .....	57
3.2. Analysis of a Vibrating Lateral-Field Excited AT-Cut Quartz Sensor Element under Liquid Load.....	 58
3.2.1. Equations for a Vibrating Quartz Plate.....	58
3.2.2. Boundary Conditions .....	64
3.2.2.1. Mechanical Boundary Conditions .....	64
3.2.2.2. Electrical Boundary Conditions.....	67
3.2.2.3. Summary of Boundary Conditions.....	74
3.2.3. Admittance of the LFE Sensor Element .....	74

3.3. Equivalent Circuit Model.....	76
3.3.1. Change in Resonant Frequency.....	94
3.3.1.1. Frequency Changes Due to Liquid Kinematic Viscosity.....	95
3.3.1.2. Frequency Changes Due to Liquid Permittivity.....	97
3.3.1.3. Frequency Changes Due to Liquid Conductivity.....	102
3.3.1.4. Frequency Changes Due to an Arbitrary Liquid.....	104
Chapter 4 EXPERIMENTAL METHODS.....	106
4.1. Lateral-Field Excited Sensors.....	106
4.2. Lateral-Field Excited Sensor Element Characterization.....	107
Chapter 5 RESULTS AND DISCUSSION.....	111
5.1. Experimentally Determined Parameters for LFE Sensor Elements.....	111
5.2. Admittance in Deionized Water.....	114
5.3. LFE Sensor Element Response to Kinematic Viscosity.....	119
5.4. LFE Sensor Element Response to Relative Permittivity.....	128
5.5. LFE Sensor Element Response to Conductivity.....	138
5.6. Discussion.....	147
Chapter 6 SUMMARY, CONCLUSIONS, AND FUTURE WORK.....	153
6.1. Summary.....	153
6.2. Conclusions.....	154
6.3. Future Work.....	155
APPENDIX A Piezoelectric Coupling Factor for Lateral-Field Excited Acoustic Modes in AT-Cut Quartz.....	157
APPENDIX B Bulk Acoustic Wave Resonator Models.....	160
APPENDIX C Material Properties of Liquids.....	172

APPENDIX D Measured and Theoretical Data for Liquid-Loaded Lateral-Field	
Excited Sensor Elements .....	174
REFERENCES.....	183
BIOGRAPHY OF THE AUTHOR.....	189

## LIST OF TABLES

Table 1. Index transformation for elastic wave equations .....	12
Table 2. The equivalent circuit models for BAW resonators and the loads under which the admittance is presented.....	26
Table 3. Non zero material constants for AT-cut quartz.....	29
Table 4. The relationship between the acoustic modes and the eigenvalues for an LFE resonator on AT-cut quartz.....	37
Table 5. Experimentally determined parameters for LFE sensor elements .....	112
Table 6. Effective penetration of the electric field in sodium chloride solutions.....	152
Table A.1. The relationship between the acoustic modes and the eigenvalues for an LFE resonator on quartz.....	158
Table C.1. Material properties of glycerol solutions .....	172
Table C.2. Material properties of isopropyl alcohol solutions.....	172
Table C.3. Material properties of sodium chloride solutions .....	173
Table D.1. Measured data for LFE sensor elements with a 0.5-mm electrode gap under glycerol solution loads .....	174
Table D.2. Model data for LFE sensor elements with a 0.5-mm electrode gap under glycerol solution loads .....	174
Table D.3. Measured data for LFE sensor elements with a 0.5-mm electrode gap under isopropyl alcohol solution loads .....	175
Table D.4. Model data for LFE sensor elements with a 0.5-mm electrode gap under isopropyl alcohol solution loads.....	175
Table D.5. Measured data for LFE sensor elements with a 0.5-mm electrode gap under sodium chloride solution loads .....	176

Table D.6. Model data for LFE sensor elements with a 0.5-mm electrode gap under sodium chloride solution loads .....	176
Table D.7. Measured data for LFE sensor elements with a 1.0-mm electrode gap under glycerol solution loads .....	177
Table D.8. Model data for LFE sensor elements with a 1.0-mm electrode gap under glycerol solution loads .....	177
Table D.9. Measured data for LFE sensor elements with a 1.0-mm electrode gap under isopropyl alcohol solution loads .....	178
Table D.10. Model data for LFE sensor elements with a 1.0-mm electrode gap under isopropyl alcohol solution loads.....	178
Table D.11. Measured data for LFE sensor elements with a 1.0-mm electrode gap under sodium chloride solution loads .....	179
Table D.12. Model data for LFE sensor elements with a 1.0-mm electrode gap under sodium chloride solution loads .....	179
Table D.13. Measured data for LFE sensor elements with a 2.0-mm electrode gap under glycerol solution loads .....	180
Table D.14. Model data for LFE sensor elements with a 2.0-mm electrode gap under glycerol solution loads .....	180
Table D.15. Measured data for LFE sensor elements with a 2.0-mm electrode gap under isopropyl alcohol solution loads .....	181
Table D.16. Model data for LFE sensor elements with a 2.0-mm electrode gap under isopropyl alcohol solution loads.....	181

Table D.17. Measured data for LFE sensor elements with a 2.0-mm electrode gap under sodium chloride solution loads .....	182
Table D.18. Model data for LFE sensor elements with a 2.0-mm electrode gap under sodium chloride solution loads .....	182

## LIST OF FIGURES

Figure 1. Crystal and electrode orientation for LFE sensor element on AT-cut quartz .....	3
Figure 2. Geometries of thickness shear mode resonators with a small sensing electrode, ring-shaped sensing electrode, and open ring sensing electrode.....	4
Figure 3. Lateral coupling factors for the $a$ , $b$ , and $c$ modes in AT-cut quartz for an electric field directed along $\psi$ .....	6
Figure 4. Electrode orientation for excitation of thickness shear mode in LFE resonator on AT-cut quartz: the shaded regions are the metalized electrodes .....	6
Figure 5. Stresses on a surface of a cube of arbitrary material .....	13
Figure 6. Geometry of a simple bulk acoustic wave resonator on quartz .....	19
Figure 7. The particle displacement profile of the thickness shear mode having arbitrary amplitude, $A$ , in a quartz disc for the fundamental and the third harmonic. ....	21
Figure 8. The top view of a standard QCM sensor.....	22
Figure 9. Cross-sectional view BAW resonator with infinitesimally thin electrodes at $x_2 = 0$ and $x_2 = h$ .....	27
Figure 10. A lateral-field excited BAW resonator with the origin of the coordinate system centered on the bottom surface of the plate.....	33
Figure 11. A three-port Mason model for a thickness-field excited BAW resonator.....	44
Figure 12. A three-port Mason model for a lateral-field excited BAW resonator.....	47
Figure 13. Equivalent circuit under mass and liquid loading including parasitic capacitance $C_p$ . ....	50
Figure 14. Butterworth-Van Dyke equivalent circuit for resonator .....	52



Figure 15. A transmission line model for a thickness-field excited BAW resonator with an acoustic load on one side .....	54
Figure 16. A transmission line model for an LFE BAW resonator with an acoustic load on one side .....	56
Figure 17. LFE sensor element geometry — the electrodes are shaded and on the reference side only.....	58
Figure 18. Acoustic energy of an LFE sensor element under the electrodes in the $x_1$ and $x_3$ directions.....	60
Figure 19. Propagation of a plane harmonic electromagnetic wave in quartz – the shaded region is the LFE electrode. ....	61
Figure 20. Configuration of LFE resonator for analysis of equivalent circuit with shaded regions representing a virtual electrode through the thickness of the quartz disc .....	68
Figure 21. The total current between the electrodes is the parallel combination of the current in the quartz plate, $I_1$ , and the current in the contacting liquid, $I_2$ .....	76
Figure 22. Equivalent circuit for admittance $Y_a$ .....	80
Figure 23. Equivalent circuit of LFE sensor element under liquid load.....	82
Figure 24. Equivalent circuit with lumped circuit elements for an LFE sensor element under liquid loading .....	86
Figure 25. An LFE sensor element showing the interaction of the driving electric field, $E$ , with contacting liquid .....	89
Figure 26. Equivalent circuit including the elements $C_\ell$ and $R_\ell$ , for an LFE sensor element under liquid loading .....	90
Figure 27. Simplified equivalent circuit model for the LFE sensor element.....	92

Figure 28. Admittance for the equivalent circuits in Figure 26 and Figure 27.....	93
Figure 29. The photolithography process.....	107
Figure 30. Equivalent circuit for LFE sensor element incorporating the electrical influence of the sensor holder.....	113
Figure 31. Theoretical and measured admittance for an LFE sensor element with a 0.5-mm electrode gap under a deionized water load.....	116
Figure 32. Theoretical and measured admittance for an LFE sensor element with a 1.0-mm electrode gap under a deionized water load.....	117
Figure 33. Theoretical and measured admittance for an LFE sensor element with a 2.0-mm electrode gap under a deionized water load.....	118
Figure 34. Normalized frequency shift of an LFE sensor element with a 0.5-mm electrode gap as a function of kinematic viscosity .....	120
Figure 35. Normalized frequency shift of an LFE sensor element with a 1.0-mm electrode gap as a function of kinematic viscosity .....	121
Figure 36. Normalized frequency shift of an LFE sensor element with a 2.0-mm electrode gap as a function of kinematic viscosity .....	122
Figure 37. Normalized peak admittance of an LFE sensor element with a 0.5-mm electrode gap as a function of kinematic viscosity .....	123
Figure 38. Normalized peak admittance of an LFE sensor element with a 1.0-mm electrode gap as a function of kinematic viscosity .....	124
Figure 39. Normalized peak admittance of an LFE sensor element with a 2.0-mm electrode gap as a function of kinematic viscosity .....	125
Figure 40. Phase at resonance of an LFE sensor element with a 0.5-mm electrode gap as a function of kinematic viscosity .....	126

Figure 41. Phase at resonance of an LFE sensor element with a 1.0-mm electrode gap as a function of kinematic viscosity .....	127
Figure 42. Phase at resonance of an LFE sensor element with a 2.0-mm electrode gap as a function of kinematic viscosity .....	128
Figure 43. Normalized frequency shift of an LFE sensor element with a 0.5-mm electrode gap as a function of isopropyl alcohol concentration.....	129
Figure 44. Normalized frequency shift of an LFE sensor element with a 1.0-mm electrode gap as a function of isopropyl alcohol concentration.....	130
Figure 45. Normalized frequency shift of an LFE sensor element with a 2.0-mm electrode gap as a function of isopropyl alcohol concentration.....	131
Figure 46. Normalized peak admittance of an LFE sensor element with a 0.5-mm electrode gap as a function of relative permittivity .....	132
Figure 47. Normalized peak admittance of an LFE sensor element with a 1.0-mm electrode gap as a function of relative permittivity .....	133
Figure 48. Normalized peak admittance of an LFE sensor element with a 2.0-mm electrode gap as a function of relative permittivity .....	134
Figure 49. Phase at resonance of an LFE sensor element with a 0.5-mm electrode gap as a function of relative permittivity.....	135
Figure 50. Phase at resonance of an LFE sensor element with a 1.0-mm electrode gap as a function of relative permittivity.....	136
Figure 51. Phase at resonance of an LFE sensor element with a 2.0-mm electrode gap as a function of relative permittivity.....	137
Figure 52. Normalized frequency shift of an LFE sensor element with a 0.5-mm electrode gap as a function of sodium chloride concentration.....	139

Figure 53. Normalized frequency shift of an LFE sensor element with a 1.0-mm electrode gap as a function of sodium chloride concentration.....	140
Figure 54. Normalized frequency shift of an LFE sensor element with a 2.0-mm electrode gap as a function of sodium chloride concentration.....	141
Figure 55. Normalized peak admittance of an LFE sensor element with a 0.5-mm electrode gap as a function of conductivity.....	142
Figure 56. Normalized peak admittance of an LFE sensor element with a 1.0-mm electrode gap as a function of conductivity.....	143
Figure 57. Normalized peak admittance of an LFE sensor element with a 2.0-mm electrode gap as a function of conductivity.....	144
Figure 58. Phase at resonance of an LFE sensor element with a 0.5-mm electrode gap as a function of conductivity .....	145
Figure 59. Phase at resonance of an LFE sensor element with a 1.0-mm electrode gap as a function of conductivity .....	146
Figure 60. Phase at resonance of an LFE sensor element with a 2.0-mm electrode gap as a function of conductivity .....	147
Figure 61. Normalized frequency shift of an LFE sensor element with a 0.5-mm electrode gap as a function of kinematic viscosity with the frequency shift due to kinematic viscosity and permittivity separated.....	149
Figure 62. Normalized frequency shift of an LFE sensor element with a 0.5-mm electrode gap as a function of relative permittivity with the frequency shift due to kinematic viscosity and permittivity separated.....	150

## LIST OF SYMBOLS

$S$	mechanical strain
$T$	mechanical stress ( $\text{N}/\text{m}^2$ )
$x_1, x_2, x_3$	Cartesian axes
$c$	elastic stiffness constant ( $\text{N}/\text{m}^2$ )
$s$	elastic compliance constant ( $\text{m}^2/\text{N}$ )
$\eta$	viscosity constant of AT-cut quartz ( $\text{N}\cdot\text{s}/\text{m}^2$ )
$\rho$	density of AT-cut quartz ( $\text{kg}/\text{m}^3$ )
$u_1, u_2, u_3$	particle displacement along the given direction, corresponding to the Cartesian coordinates (m)
$H$	magnetic field intensity (A/m)
$D$	electric displacement ( $\text{C}/\text{m}^2$ )
$J$	current density ( $\text{A}/\text{m}^2$ )
$E$	electric field intensity (V/m)
$B$	magnetic flux ( $\text{V}\cdot\text{s}/\text{m}^2$ )
$\rho_e$	electric charge density ( $\text{C}/\text{m}^3$ )
$\varepsilon$	permittivity (F/m)
$\mu$	permeability (H/m)
$\sigma$	conductivity (S/m)
$e_{ijk}$	piezoelectric stress constants ( $\text{C}/\text{m}^2$ )
$d_{ijk}$	piezoelectric strain constants
$\phi$	scalar potential (V)

$h$	thickness of the lateral-field excited sensor element (m)
$v_s$	velocity of the thickness-shear mode (m/s)
$f$	frequency (Hz)
$\lambda$	wavelength (m)
$n$	harmonic index
$j$	imaginary number $j = \sqrt{-1}$
$\omega$	radial frequency (rotations/s)
$t$	time (s)
$\bar{c}_{66}$	piezoelectrically stiffened elastic constant of AT-cut quartz ( $\text{N}/\text{m}^2$ )
$k_t$	wave propagation vector for thickness-field excited thickness-shear mode (rotations/m)
$c_l$	shear modulus of liquid ( $\text{N}/\text{m}^2$ )
$\rho_l$	density of liquid ( $\text{kg}/\text{m}^3$ )
$\eta_l$	viscosity of liquid ( $\text{N}\cdot\text{s}/\text{m}^2$ )
$k_l$	wave propagation vector for liquid (rotations/m)
$C_0$	static capacitance (F)
$Z$	electrical impedance ( $\Omega$ )
$Z_L$	load impedance ( $\Omega$ )
$d$	width of the lateral-field excited electrode (m)
$d_q$	diameter of the quartz plate (m)
$w$	electrode gap of the lateral-field excited sensor element (m)

$c^{(i)}$	eigenvalue for each of the acoustic modes (N/m <sup>2</sup> )
$k_l^{(e)}$	wave propagation vector for lateral-field excited thickness-shear mode (rotations/m)
$k_m^{(e)}$	lateral coupling factor to the thickness-shear mode
$Q$	charge (C)
$A$	area (m <sup>2</sup> )
$I$	electric current (A)
$V$	electric potential (V)
$Y$	electrical admittance (S)
$Z_c$	characteristic impedance of AT-cut quartz ( $\Omega$ )
$v$	particle velocity (m/s)
$F$	force (N)
$\bar{Z}_c$	characteristic impedance of AT-cut quartz acting on a surface area ( $\Omega \cdot \text{m}^2$ )
$N_t$	turns ratio of Mason model transformer for thickness-field excited resonators
$k_m$	thickness coupling factor to the thickness-shear mode
$N_l$	turns ratio of Mason model transformer for lateral-field excited resonators
$K_l$	lateral coupling factor to the thickness-shear mode
$\rho_m$	density of mass load (kg/m <sup>3</sup> )
$\Lambda$	complex perturbation parameter

$\Lambda_r$	real part of the complex perturbation parameter
$\Lambda_i$	imaginary part of the complex perturbation parameter
$C_p$	parasitic capacitance (F)
$C_1, C_2, C_3$	equivalent circuit model capacitance (F)
$L_1, \dots, L_6$	equivalent circuit model inductance (H)
$R_1, \dots, R_6$	equivalent circuit model resistance ( $\Omega$ )
$N_{tx}$	turns ratio of transmission line model transformer for thickness-field excited resonators
$Z_{cl}$	characteristic impedance of liquid ( $\Omega$ )
$N_{lx}$	turns ratio of transmission line model transformer for lateral-field excited resonators
$Y_c^{(c)}$	characteristic admittance of the thickness-shear mode (S)
$\bar{e}_{36}$	modified piezoelectric stress constant, $e_{36}$ , for lateral-field excited thickness-shear mode (C/m <sup>2</sup> )
$\bar{\epsilon}_{33}$	modified permittivity, $\epsilon_{33}$ , for lateral-field excited thickness-shear mode (F/m)
$\bar{k}$	wave propagation vector for lateral-field excited thickness-shear mode (rotations/m)
$\gamma$	complex decay constant for the liquid velocity field (m <sup>-1</sup> )
$h'$	thickness of the liquid layer (m)
$\phi_l$	scalar potential in the liquid (V)



$\varepsilon_l$	permittivity of the liquid (F/m)
$1/\kappa$	ion atmosphere radius (m)
$\varepsilon_l^*$	complex permittivity of the liquid (F/m)
$\sigma_l$	conductivity of the liquid (S/m)
$\rho_s$	surface charge density (C/m <sup>2</sup> )
$\psi$	lateral-field excited propagation term
$Y_1, \dots, Y_6$	lateral-field excited model admittance (S)
$K^2$	lateral-field excited coupling factor of the thickness-shear mode to the applied electric field, $E_3$
$\bar{K}^2$	lateral-field excited coupling factor of the thickness-shear mode to the induced electric field, $E_2$
$\bar{c}_{66}$	piezoelectrically stiffened elastic constant of AT-cut quartz (N/m <sup>2</sup> )
$\xi$	quartz loss term
$\psi'$	modified lateral-field excited propagation term with quartz loss
$K'^2$	modified lateral-field excited coupling factor, with quartz loss, of the thickness-shear mode to the applied electric field, $E_3$
$\bar{K}'^2$	modified lateral-field excited coupling factor, with quartz loss, of the thickness-shear mode to the induced electric field, $E_2$
$f_s$	series resonant frequency (Hz)
$\omega_s$	series resonant radial frequency (rotations/s)
$C_l$	equivalent circuit model capacitance due to liquid load (F)

$R_l$	equivalent circuit model resistance due to liquid load ( $\Omega$ )
$h_{eff}$	effective thickness of the liquid (m)
$Z_m$	resistance of the motional branch of the equivalent circuit model ( $\Omega$ )
$C$	total capacitance of the motional branch of the equivalent circuit model (F)
$L$	total inductance of the motional branch of the equivalent circuit model (H)
$G_l$	equivalent circuit model conductance due to liquid load (S)
$C_l^*$	complex capacitance, $C_l$ (F)
$f_s'$	series resonant frequency, perturbed by a liquid load (Hz)
$L'$	inductance, $L'$ , perturbed by a liquid load (H)
$C_l'$	capacitance, $C_l$ , perturbed by a liquid load (F)
$G_l'$	conductance, $G_l$ , perturbed by a liquid load (S)
$\epsilon_l'$	liquid permittivity, perturbed by a liquid load (F/m)
$\sigma_l'$	liquid conductivity, perturbed by a liquid load (S/m)
$R_p$	parasitic resistance ( $\Omega$ )

## LIST OF ABBREVIATIONS

BAW	bulk acoustic wave
EQCM	electrochemical quartz crystal microbalance
LASST	Laboratory for Surface Science and Technology
LFE	lateral-field excited
QCM	quartz crystal microbalance
QCM-D	quartz crystal microbalance with dissipation monitoring

## Chapter 1

### INTRODUCTION

Sensors are prevalent in many areas of society. They are used in healthcare, automobiles, security systems, and environmental protection to name but a small number of applications [1, 2]. This dissertation focuses on a novel bulk acoustic wave (BAW) sensor element for chemical and biological analytes, the lateral-field excited (LFE) sensor element, developed by Dr. Vetelino [3] and his research group at the Laboratory for Surface Science and Technology (LASST), University of Maine, Orono, ME. Specifically, an equivalent circuit model is developed for the LFE sensor element on AT-cut quartz, under liquid loads that accurately predicts the sensor response due to mechanical and electrical perturbations of measured liquids.

#### **1.1. Background**

BAW devices are a well-established technology and have a long history of use as feedback elements in oscillators, electronic filters, and sensors [4]. A BAW device consists of a piezoelectric crystal with two exciting electrodes. Piezoelectricity is the generation of bound electrical charges in a material due to strain in that material [5]. This effect is bidirectional and an applied electric field causes strain in the material. Two methods of exciting acoustic waves in BAW devices are thickness-field excitation, where the applied electric field is directed along the thickness of a piezoelectric plate, and lateral-field excitation, where the electric field is directed parallel to the major surfaces of a piezoelectric plate [6]. Generally, there are many types of vibrations that can occur in piezoelectric crystals including thickness shear, face shear, extension, flexure, to name a few [7]. The discussion in this work will be limited to thickness shear vibrations. There are three

thickness modes that occur in BAW resonators, the  $a$ ,  $b$ , and  $c$  modes, with each mode having perpendicular particle displacements from the others [7, 8].

One of the more common BAW structures is an AT-cut quartz crystal resonator with metal electrodes deposited directly on both major surfaces [7, 9]. This method of excitation is thickness-field excitation because the electric field is directed through the thickness of the quartz plate. The AT-cut of quartz is a singly-rotated cut, described relative to the crystallographic axes in Figure 1. This orientation is particularly attractive for quartz crystal resonators, since only the thickness shear mode, also referred to as the  $c$  mode, is excited [8]. Further, the velocity of the  $c$  mode does not vary appreciably with temperature over a wide range near room temperature [8]. This mode propagates through the thickness of the plate and has particle displacements parallel to the major surfaces of the plate [7, 9]. Quartz crystal resonators are used as the timekeeping element in watches and clocks [10], as electronic filters [11], and as physical, chemical, or biological sensors [12]. When operated at its resonant frequency, the induced strain in the quartz crystal resonator generates an elastic standing wave that propagates through the thickness of the crystal [6, 7]. Conversely, the propagated elastic wave generates an electric field that can be measured at the electrodes [12]. A more detailed theory of operation for quartz crystal resonators is discussed in chapter 2.

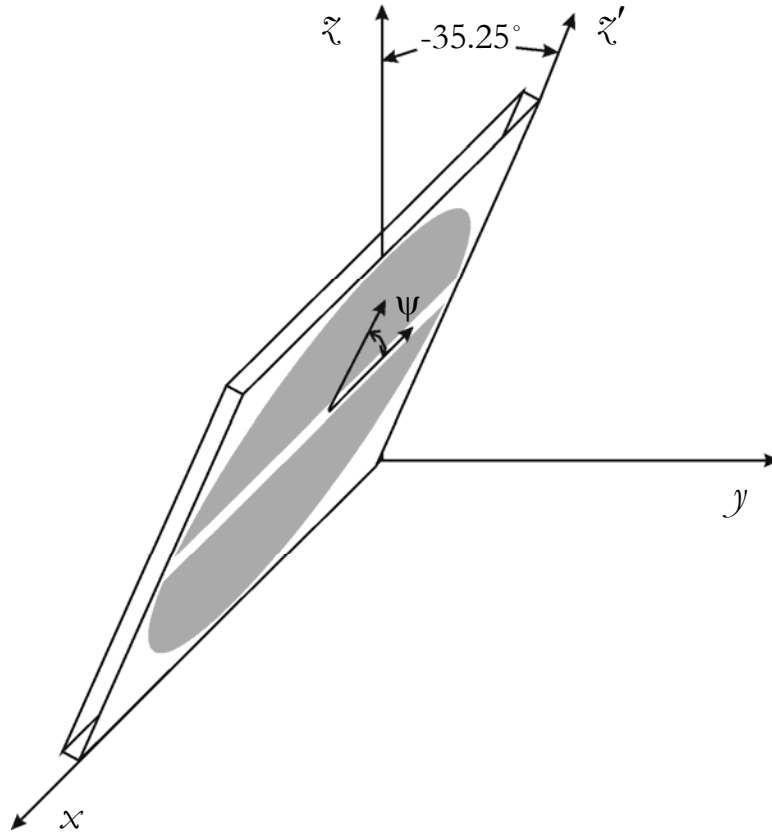


**Figure 1. Crystal and electrode orientation for LFE sensor element on AT-cut quartz**

The quartz crystal resonator is often used as a gravimetric sensor, where it is called a quartz crystal microbalance (QCM) [13, 14]. The electric field associated with the BAW does not penetrate into the sensing medium due to shielding by the sensing electrode on the surface. The QCM is in widespread use as a deposition monitor to measure the amount of material deposited in chemical and vacuum deposition systems. The simplicity of the QCM design and the linearity of the sensor response as mass accumulates on the sensing surface make the QCM a popular choice for vacuum deposition. Numerous published studies exist on the QCM as a sensing element for chemical and biochemical analytes in gas-, liquid-, and solid- phase environments, see for example [4, 12, 15]. The low cost and durability of the QCM sensor makes it a good choice for many physical, chemical, and biological sensors. However, when operating in liquid-phase environments or with a film that is not

mechanically rigid, the QCM exhibits a response that is not linear as mass accumulates on the surface.

Variations of the QCM have been examined and some are still in use such as the electrochemical QCM (EQCM) [16] and the QCM with dissipation monitoring (QCM-D) [17-20]. Several researchers have investigated probing electrical properties of a medium or sensing layer using thickness shear mode resonators by modifying the electrode geometry of the QCM. Josse, *et al.* [21, 22] modified the size and/or shape of the sensing electrode and found the resulting electrodes were effective in detecting conductivity and permittivity changes in liquid environments. In particular they investigated the effect of decreasing the size of the sensing electrode (Figure 2a) and used a ring-shaped sensing electrode (Figure 2b) to detect electrical properties in liquid environments. They recognized that resonators with these modified electrodes were capacitance sensors. Measurement of static capacitance changes due to perturbations in the liquid environment is made through measurement of the anti-resonant frequency. Thus, these devices combine advantages of a mass-sensitive QCM with those of a capacitive sensor.

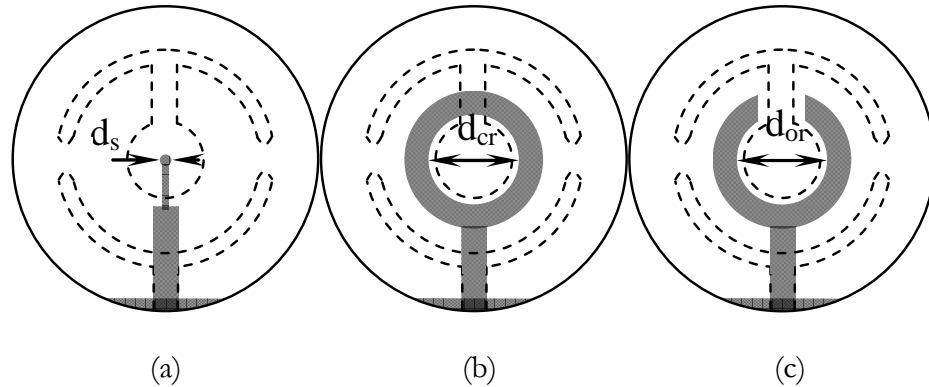


**Figure 2. Geometries of thickness shear mode resonators with a (a) small sensing electrode, (b) ring-shaped sensing electrode, and (c) open ring sensing electrode**

Zhang and Vetelino [23, 24] also examined resonators with small sensing electrodes (Figure 2a) and ring-shaped sensing electrodes (Figure 2b) as well as open ring electrodes

(Figure 2c). They performed extensive experiments characterizing these modified electrode resonators exposed to liquids while independently changing viscosity, conductivity, and permittivity of different solutions. They found that as the overlap between the sensing electrode and the reference electrode was minimized, sensitivity of the thickness shear mode resonator to liquid electrical property changes was almost 25 times greater than for the standard QCM electrode.

The thickness shear mode can also be excited in piezoelectric materials by application of an electric field parallel to the major crystal surfaces. This method of excitation is known as lateral-field excitation, and was previously called parallel-field excitation [6]. With LFE sensor elements the electrodes are commonly positioned on the same crystal face and an applied electric field is directed parallel to the face of the crystal. In order to excite only the thickness shear mode in AT-cut quartz, (Figure 3), the electrodes must be oriented with the electric field directed along the crystallographic  $z'$  axis, , where  $\psi = \pm 90^\circ$ , as shown in Figures 1 and 4. The bare sensing surface allows the LFE sensor element to detect both electrical and mechanical property changes in the analyte or sensing film.



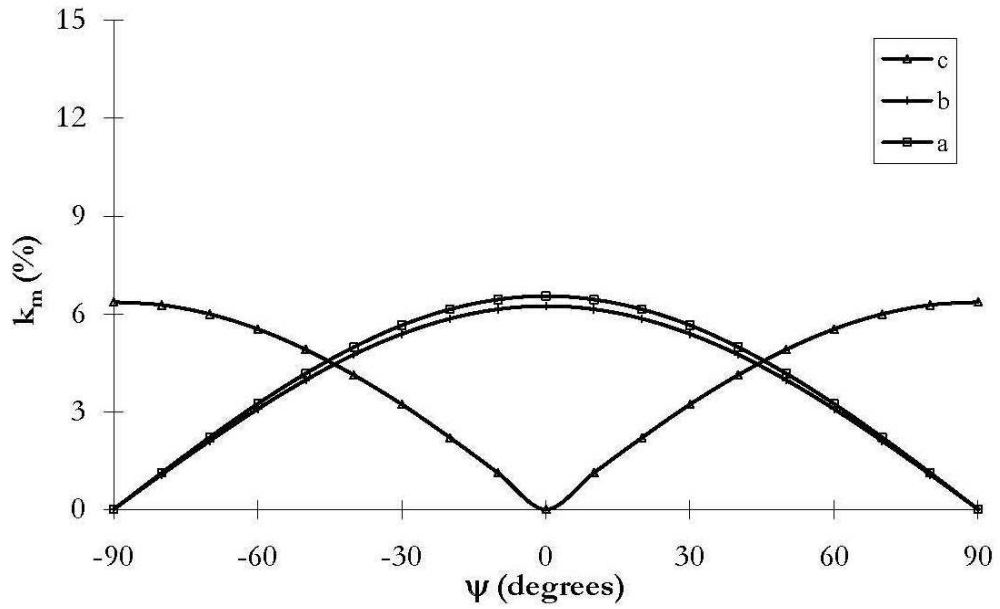


Figure 3. Lateral coupling factors for the  $a$ ,  $b$ , and  $c$  modes in AT-cut quartz for an electric field directed along  $\psi$  [25]

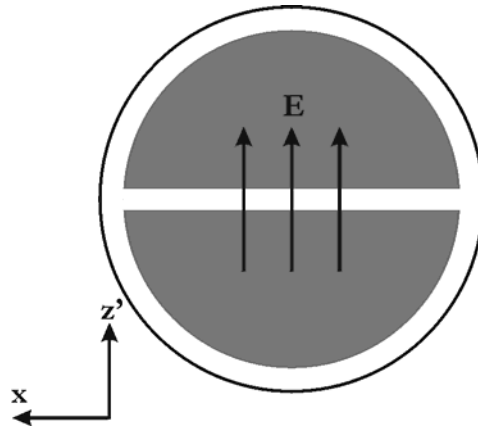


Figure 4. Electrode orientation for excitation of thickness shear mode in LFE resonator on AT-cut quartz: the shaded regions are the metalized electrodes

Lateral-field excitation of piezoelectric crystals has been used since 1941, when Atanasoff and Hart [26] determined the elastic parameters of quartz crystals using this method. Since then research has been performed on the lateral-field excitation of piezoelectric crystals for their use as bulk resonant filters [27-37]. Although Vig and Ballato [38, 39] suggested the possibility of LFE devices as sensors, Vetelino *et al.* [3, 25, 40] were the first to use LFE devices as sensors.

In an LFE sensor element both electrodes are placed on the surface opposite the sensing medium while still exciting the thickness shear mode (Figure 4). In this case, the sensing surface of the device is bare and one can either expose it directly to an analyte or attach a chemi-selective or bio-selective layer directly on the bare crystal surface. Recently Hempel, *et al.* [41] have shown that changes in electrical properties of the analyte can cause a redistribution of the electric field from the lateral direction to the thickness direction. This redistribution results in a piezoelectric stiffening, which produces a change in the velocity of the acoustic wave.

The primary advantage of the LFE sensor element is the detection of both mechanical and electrical property changes at the sensor surface. It should be noted that the ability to detect both mechanical and electrical property changes in an LFE sensor element necessitates measurement techniques in which both effects on the sensor element can be differentiated. There may also be measurement environments where electrical effects on the sensor element are so large as to mask mechanical effects and *vice versa*. Other advantages of LFE resonators include the ability to excite multiple modes and reduced stress at the non-metallized surface [32-35]. The LFE sensing element has a simpler electrode structure than the QCM sensor and can be realized in a small portable package. Like the QCM sensor, the

measurable output from an LFE sensing element is a change in its resonant frequency due to mechanical and electrical property changes in the sensing film caused by the measurand.

Although a significant amount of research has been performed on the lateral-field excitation of the thickness shear mode in BAW resonant filters [27-37], it has been focused on operation in benign and stable environments, such as air. However, the use of LFE resonators as chemical and biological sensors often requires that they be exposed to liquid environments. To date, the theory describing an LFE sensor element operating in a liquid environment has not been explored in detail.

## **1.2. Approach**

The primary goal of this work is to develop the theory and subsequent experimental verification of an LFE sensor element operating in liquid environments. The thickness shear mode in the LFE sensor element will be examined by solving the coupled wave equations, subject to the appropriate boundary conditions, in a multi-layered LFE sensor structure. A theoretical expression for the admittance of the LFE sensor element will be derived. The admittance will be examined and circuit elements relating to the material properties of the substrate and liquid will be derived. The circuit elements will then be configured as an equivalent circuit for the LFE sensor element operating in liquid environments. A simplified relationship for the admittance at or near the resonant frequency of the LFE sensor element will be derived, along with an explicit expression for the change in resonant frequency of the LFE device under liquid loading. The model will be verified by experimental measurements of the admittance of the LFE sensor element to changes in viscosity, permittivity, and conductivity in the contacting liquid.

### **1.3. Organization**

Chapter 1 presents a historical perspective of BAW resonators with a specific focus on LFE resonators and sensor elements to date. Limitations of the current theoretical models and the need for developing a model for the LFE sensor element operating in liquid environments are discussed. The introduction closes, qualitatively describing the approach used in developing the model for the LFE sensor element.

In chapter 2, the theory of acoustic waves in non-piezoelectric and piezoelectric solids is presented and applied to describe the operation of BAW resonators. The chapter concludes with commonly used models for describing BAW resonators.

An equivalent circuit model for LFE sensor elements under liquid loads is developed in chapter 3. The chapter begins with a detailed discussion of LFE resonator theory. The theory is extended to LFE resonators perturbed by different mechanical and electrical loading conditions at the sensor surface. An expression for the admittance of LFE sensor elements is derived and a theoretical equivalent circuit model for the LFE sensor element is presented for the sensor operating under liquid loads. A simplified admittance equation for the LFE sensor element operating at, or near, resonance is given. Finally, an expression for the frequency change of the LFE sensor element due to mechanical and electrical variations in the contacting liquids is developed.

The experimental methods used to measure the LFE sensor elements' responses to different liquid loads are presented in chapter 4. The equipment used, the solutions measured, and the rationale for the choice of liquids is discussed in this chapter.

The experimental results for the LFE sensor element tests are presented in chapter 5. The data are analyzed and the results are discussed. The summary, conclusions of the research, and future research directions are presented in chapter 6.

## Chapter 2

### BACKGROUND THEORY

The introductory chapter presented a qualitative discussion of lateral-field excited (LFE) resonators, which included a brief historical perspective and the rationale for the research. In this chapter the theory of acoustic waves in non-piezoelectric and piezoelectric crystals is discussed. Next, the theory associated with bulk acoustic wave (BAW) resonators is presented, followed by an analysis of the thickness shear mode in AT-cut quartz for thickness-field excitation and lateral-field excitation under air loading. Finally, three equivalent circuit models are examined for BAW resonators, the Mason model [42], the Martin model [43], and the transmission line model [35, 44]. The Mason model is given for thickness-field excited and LFE BAW resonators under air loading. The Martin model is given for thickness-field excited resonators under simultaneous mass and liquid loading and is shown to reduce to the air loaded case. Finally, the transmission line model is examined for thickness-field excited resonators under air and liquid loading and LFE sensor elements under air loading. This leads to chapter 3 in which an equivalent circuit model for a liquid-loaded LFE sensor element is derived and presented.

#### **2.1. Acoustic Waves in Non-Piezoelectric Crystals**

##### ***2.1.1. Mechanical Considerations***

“Acoustics is the study of time-varying deformations, or vibrations, in material media [45].” This simple definition of acoustics is the starting point in developing a mathematical description of acoustic waves in solid media. However, before a mathematical description of acoustic waves can be presented, the physical phenomena of strains,  $S$ , and traction forces,  $T$ , more commonly known as stresses, in solids will be discussed.

When external forces are applied to a solid body, it may undergo a rigid translation or rigid rotation, such as when one moves a box from one position to another or rotates the box. However, the box may become deformed and internal forces may result from the external forces applied to the box in addition to, or instead of, the rigid translation or rigid rotation of the body. It should be noted that an applied force to a rigid body results in material deformation if and only if the particles of the body are displaced with respect to the other particles, not if the body undergoes rigid translation or rigid rotation. The deformations of a material can be described by strain,  $S$ , a measure of deformation representing the relative displacement between particles in the material [46]. Strain is a dimensionless quantity, having no units.

When evaluating acoustic waves in three dimensions, using Cartesian coordinates, the strain is represented by a 3 x 3 matrix.

$$S = \begin{bmatrix} S_{11} & S_{12} & S_{13} \\ S_{21} & S_{22} & S_{23} \\ S_{31} & S_{32} & S_{33} \end{bmatrix}, \quad (2.1)$$

where the subscripts relate the differential particle displacement in the direction of the first subscript with respect to the direction of the second subscript, *i.e.*  $S_{12}$  is the strain component relating the differential particle displacement in the  $x_1$  direction with respect to the  $x_2$  direction. Due to symmetry  $S_{ij} = S_{ji}$  where  $i$  and  $j$  are any Cartesian coordinates  $x_1$ ,  $x_2$ , and  $x_3$ . The result is that  $S$  has a maximum of 6 independent values instead of 9, allowing us to write  $S$  as a 1 x 6 matrix,

$$S = \begin{bmatrix} S_1 \\ S_2 \\ S_3 \\ S_4 \\ S_5 \\ S_6 \end{bmatrix}, \quad (2.2)$$

with the index transformations shown in Table 1. Please note that while equation 2.2 provides us with a simpler mathematical form, equation 2.1 provides us with more insight as to the physical deformations that are occurring in the material.

**Table 1. Index transformation for elastic wave equations [47]**

$I$	$ij$
1	11
2	22
3	33
4	23, 32
5	13, 31
6	12, 21

When a body undergoes a time-varying deformation, internal restoring forces develop between neighboring particles. These internal restoring forces are traction forces,  $T$ , and are commonly called stresses. The stresses between neighboring particles act upon a surface, and can be represented as a 3 x 3 matrix,

$$T = \begin{bmatrix} T_{11} & T_{12} & T_{13} \\ T_{21} & T_{22} & T_{23} \\ T_{31} & T_{32} & T_{33} \end{bmatrix}. \quad (2.3)$$

The individual components are best described by examining a cube of arbitrary material (Figure 5). Let's examine the shaded face of the cube in Figure 5, which is one of the two surfaces normal to the  $x_3$  axis. Any internal traction forces acting on this surface can be described as the sum of the traction forces acting in the  $x_1$ ,  $x_2$ , and  $x_3$  directions. The  $x_1$ -

and  $x_2$ -directed components of stress on the shaded  $x_3$  face of the cube are the shear stresses,  $T_{31}$  and  $T_{32}$ , whereas the  $x_3$ -directed component of stress on the shaded face of the cube is the compressional stress,  $T_{33}$ . Thus, for an arbitrary geometry, the stress component  $T_{ij}$  is the  $j$ -directed stress acting on an  $i$  surface, where  $i$  and  $j$  correspond to the Cartesian coordinates  $x_1$ ,  $x_2$ , and  $x_3$ . From this description it can be seen that the units of stress are  $\text{N}/\text{m}^2$ . Due to symmetry  $T_{ij} = T_{ji}$  and a simplified form of the matrix  $T$  can be represented using the transformations given in Table 1 as follows,

$$T = \begin{bmatrix} T_1 \\ T_2 \\ T_3 \\ T_4 \\ T_5 \\ T_6 \end{bmatrix}. \quad (2.4)$$

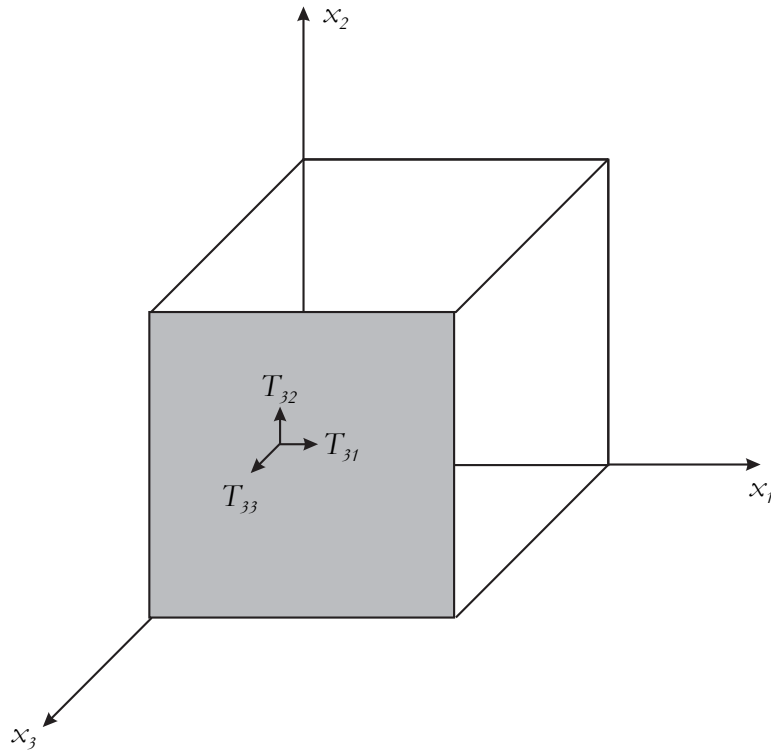


**Figure 5. Stresses on a surface of a cube of arbitrary material**



If we imagine that the particles or atoms that make up the solid are connected by springs, it is easy to see that, as a particle is displaced, the restoring force will work to bring the particle to its initial position. The relation of the restoring force to this displacement is Hooke's Law, [48, 49] described symbolically by the equation

$$[T] = [c][S], \quad (2.5)$$

where  $[c]$  is a matrix of elastic stiffness constants. Since strain is dimensionless, elastic stiffness must have the same units as stress, which are  $\text{N}/\text{m}^2$ . Materials that have small values of  $c$  are easily deformed whereas materials that have larger values of  $c$  are more rigid. This is the same as for a spring, thus elastic stiffness can be imagined as the microscopic spring constant of a material [48]. The elastic stiffness constants form a 6x6 matrix.

$$[c] = \begin{bmatrix} c_{11} & c_{12} & c_{13} & c_{14} & c_{15} & c_{16} \\ c_{21} & c_{22} & c_{23} & c_{24} & c_{25} & c_{26} \\ c_{31} & c_{32} & c_{33} & c_{34} & c_{35} & c_{36} \\ c_{41} & c_{42} & c_{43} & c_{44} & c_{45} & c_{46} \\ c_{51} & c_{52} & c_{53} & c_{54} & c_{55} & c_{56} \\ c_{61} & c_{62} & c_{63} & c_{64} & c_{65} & c_{66} \end{bmatrix}. \quad (2.6)$$

The elastic stiffness constants are a material property and, for anisotropic solids, depend on the orientation of the solid body. If the solid is a crystal and the location of the crystalline axes are known, then  $[c]$  can be easily rotated to the desired crystal orientation using transformation matrices.

Conversely, Hooke's law can also be used to relate the strain to a known stress,

$$[S] = [s][T], \quad (2.7)$$

where  $[s]$  is a matrix of elastic compliance constants. Elastic compliance has units of  $\text{m}^2/\text{N}$  and is the measure of the deformability of the material. Thus, materials with large values of

$[s]$  are easily deformed while materials that have smaller values of  $[s]$  are more rigid. The matrix has the same form as  $[c]$ , therefore

$$[s] = \begin{bmatrix} s_{11} & s_{12} & s_{13} & s_{14} & s_{15} & s_{16} \\ s_{21} & s_{22} & s_{23} & s_{24} & s_{25} & s_{26} \\ s_{31} & s_{32} & s_{33} & s_{34} & s_{35} & s_{36} \\ s_{41} & s_{42} & s_{43} & s_{44} & s_{45} & s_{46} \\ s_{51} & s_{52} & s_{53} & s_{54} & s_{55} & s_{56} \\ s_{61} & s_{62} & s_{63} & s_{64} & s_{65} & s_{66} \end{bmatrix}. \quad (2.8)$$

Hooke's law is an idealized model for relating stress and strain. However, close inspection of equation (2.5) reveals that, under resonant conditions, vibrations in solids would persist indefinitely since there is no term for damping the vibrations. It is similar to investigating a mass attached to a spring—if the mass is dropped the mass will oscillate up and down as the restoring force of the spring acts on the mass. Intuitively, we know that eventually the magnitude of the oscillations will decrease until the mass stops vibrating on the spring. The same is true for elastic waves in solids with the vibrations of the particles being damped over time. Acoustic losses in many materials at room temperature can be adequately described by a viscous damping term [48] and Hooke's law can be modified as follows,

$$[T] = [c][S] + [\eta] \frac{\partial}{\partial t} [S], \quad (2.9)$$

where  $[\eta]$  is the viscosity constant matrix. Viscosity is a linear relation of the rate of strain to stress in the solid and has units of  $\text{N}\cdot\text{s}/\text{m}^2$ . Mathematically, it can be seen that, in the absence of a source of vibrations, the vibrations will initially have an amplitude related to the applied external force, and will decay with a rate depending on the viscosity. Equation (2.9) is the elastic constitutive equation.

In addition to the elastic constitutive equation there are the Newtonian stress equations of motion [50],

$$T_{ij,i} = \rho \ddot{u}_j, \quad (2.10)$$

where  $T_{ij,i}$  is the derivative of  $T_{ij}$  with respect to the  $i$  direction,  $\rho$  is the density of the material, and  $u_j$  is the particle displacement in the  $j$  direction. The two dots above  $u_j$  denote the second derivative of displacement with respect to time. Equation (2.10) is in Cartesian tensor notation where the equation is summed over the subscript  $i$  for the  $x_1$ ,  $x_2$ , and  $x_3$  directions.

The final equation that is needed to describe elastic waves in solids are the strain-mechanical displacement relations

$$S_{ij} = \frac{1}{2}(u_{i,j} + u_{j,i}). \quad (2.11)$$

### 2.1.2. *Electromagnetic Considerations*

When a solid is exposed to electromagnetic fields and waves the behavior is described by the boundary conditions of the solid and Maxwell's equations which are given below in Cartesian tensor notation [50] as follows,

$$H_{i,j} = \dot{D}_i + J_i, \quad (2.12)$$

$$E_{i,j} = -\dot{B}_i, \quad (2.13)$$

$$B_{i,i} = 0, \quad (2.14)$$

and

$$D_{i,i} = \rho_e. \quad (2.15)$$

$H$  is the magnetic field intensity in units of A/m,  $D$ , the electric displacement in units of C/m<sup>2</sup>,  $J$ , the current density in units of A/m<sup>2</sup>,  $E$ , the electric field intensity in units of V/m,  $B$ , the magnetic flux in units of V•s/m<sup>2</sup>, and  $\rho_e$ , the electric charge density in units of C/m<sup>3</sup>. The linear electromagnetic constitutive equations [5] are

$$D_i = \varepsilon_{ij} E_j, \quad (2.16)$$

$$B_i = \mu_{ij} H_j, \quad (2.17)$$

and

$$J_i = \sigma_{ij} E_j, \quad (2.18)$$

where  $\varepsilon$  is the permittivity of the solid in units of F/m,  $\mu$ , the permeability of the solid in units of H/m, and  $\sigma$ , the conductivity of the solid in S/m.

## **2.2. Acoustic Waves in Piezoelectric Crystals**

In chapter 1 piezoelectricity was defined as the generation of bound electrical charges due to a strain in a material and conversely an applied electric field can result in strain in a material [5]. In the previous section the theory of acoustic waves in solids was presented while considering both mechanical and electrical effects on the material.

However, the previous equations described either mechanical effects *or* electrical effects of the material separately. In piezoelectric solids the coupling of the mechanical and electrical equations must be described. The following equations ignore losses due to crystal viscosity.

The magnitude of the piezoelectric effect is described by piezoelectric stress constants,  $e_{ijk}$ , which are measured in units of C/m<sup>2</sup>. The piezoelectric stress constants allow for the coupling of the mechanical and electrical equations through the piezoelectric constitutive equations [50],

$$T_{ij} = c_{ijkl}S_{kl} - e_{kij}E_k \quad (2.19)$$

and

$$D_i = \varepsilon_{ik}E_k + e_{ikl}S_{kl}. \quad (2.20)$$

Careful examination of the first terms in equations (2.19) and (2.20) reveal that they are simply Hooke's law, equation (2.5), and a linear electromagnetic constitutive relation, equation (2.16), without considering the piezoelectric properties of the solid.

As with Hooke's law, stress rather than strain can be the independent variable. The piezoelectric constitutive equations are then given as

$$S_{ij} = s_{ijkl}T_{kl} + d_{ijk}E_k \quad (2.21)$$

and

$$D_i = \varepsilon_{ij}E_j + d_{ijk}T_{jk}, \quad (2.22)$$

where  $d$  are the piezoelectric strain constants in units of C/N.

### 2.2.1. *The Quasistatic Approximation*

In the analysis of acoustic waves in piezoelectric solids, it is convenient to use the quasistatic approximation. This approximation is a result of the fact that the generated electric field,  $\mathbf{E}$ , due to strain in a piezoelectric material does not couple to the magnetic field,  $\mathbf{H}$ . Thus, no electromagnetic energy is carried because of the acoustic wave [51] and the electric field is simply the gradient of scalar potential,  $\phi$ , as follows,

$$E_k = -\phi_{,k}. \quad (2.23)$$

This also means that there is no free charge, (however, there are bound charges due to the acoustic wave), in the solid. This allows for equation (2.15) to be written as

$$D_{i,i} = 0. \quad (2.24)$$

Finally, the quasistatic approximation results in a generated electric field that is longitudinal. This means that the electric potential varies spatially in the direction of the acoustic wave propagation.

### 2.3. Bulk Acoustic Wave Resonators

Bulk acoustic wave (BAW) resonators have been used since the early 20<sup>th</sup> century [4] and are used as frequency control devices, electronic filters, and sensors. There are many designs of BAW resonators, but essentially a BAW resonator consists of a plate of piezoelectric material with two electrodes. The electrodes provide the electrical contact both for delivering the electrical signal to and receiving the electrical response from the resonator. The piezoelectric material undergoes a deformation due to the applied electrical signal and, with proper orientation of the piezoelectric plate, an acoustic wave is propagated through the bulk of the plate. This BAW generates bound charges in the piezoelectric plate resulting in an electrical response of the plate to the input signal.

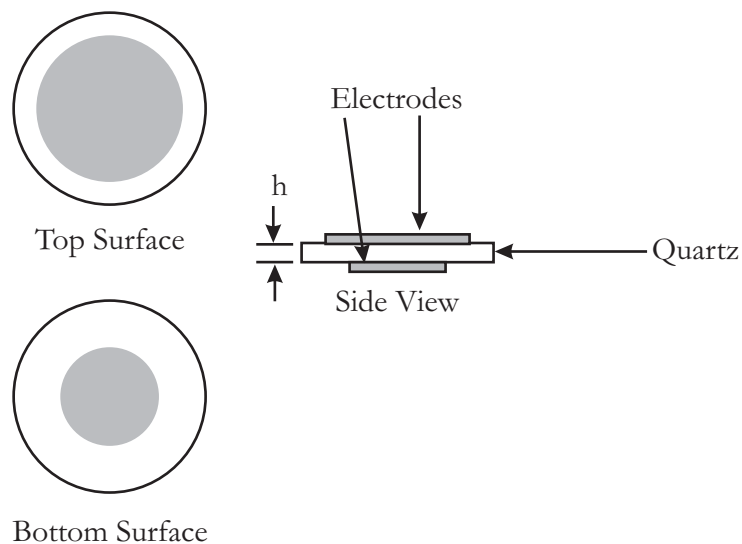


**Figure 6. Geometry of a simple bulk acoustic wave resonator on quartz, not drawn to scale.**

The simplest geometry for a bulk acoustic wave resonator consists of a quartz disc of thickness,  $h$ , with the major surfaces covered by a metallic electrode (Figure 6). Applying a high frequency electrical signal to the electrodes excites the thickness shear mode in the quartz disc.

The thickness shear mode is an elastic standing wave propagated through the thickness,  $h$ , of the crystal. The particle displacement for this mode is perpendicular to the propagation direction (Figure 7). The velocity,  $v_s$ , of the thickness shear mode is expressed as,

$$v_s = f\lambda, \quad (2.25)$$

where  $f$  is the frequency and  $\lambda$ , the wavelength of the acoustic wave. The orientation of the crystal, the crystal density, and its mechanical compliance and piezoelectric properties determines  $v_s$ . The wavelength of the acoustic wave is constrained by the geometry of the plate as follows,

$$h = \frac{n\lambda}{2} \quad (2.26)$$

where  $n = 1, 3, 5, \dots$ . The allowed frequencies of operation can be found by solving equation (2.26) for  $\lambda$  and substituting into equation (2.25) yielding:

$$f^{(n)} = \frac{nv_s}{2h}, \quad (2.27)$$

where  $f^{(n)}$  is the  $n$ th harmonic of the thickness shear mode. Only odd-numbered harmonics, (*i.e.*  $n = 1, 3, 5, \dots$ ), can be excited since the even-numbered harmonics have no particle displacement at the surface of the quartz disc as opposed to odd-numbered harmonics, which have maximum particle displacement at the surfaces of the disc.

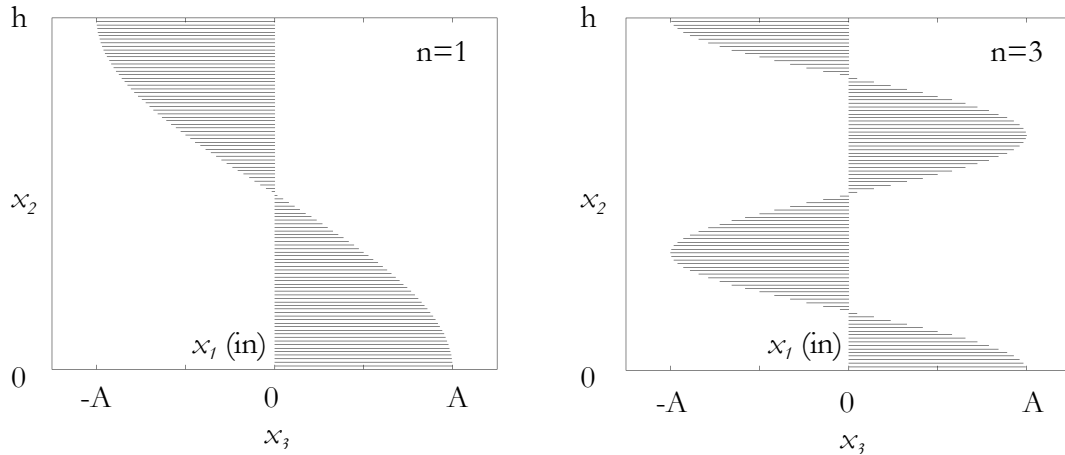


**Figure 7.** The particle displacement profile of the thickness shear mode having arbitrary amplitude,  $A$ , in a quartz disc (side view) for (left) the fundamental ( $n = 1$ ) and (right) the third ( $n = 3$ ) harmonic.

### 2.3.1. Thickness-Field Excited BAW Resonators

The most common way of exciting the thickness shear mode in BAW resonators is by means of thickness-field excitation. Thickness-field excited resonators have electrodes on both major surfaces of the crystal (Figure 6), thus the applied electric field is directed between the electrodes through the thickness of the piezoelectric plate.

The most popular and well-known BAW sensor platform is the quartz crystal microbalance (QCM). The standard electrode geometry of the QCM sensor is shown in Figure 8. The metalized region on the opposite surface (reference side) is outlined with dashed lines. The tab of the electrode on the sensing side wraps around the edge of the crystal to the reference side so that both electrodes can be contacted on the reference side.



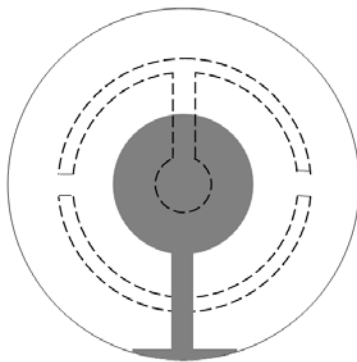


**Figure 8. The top view (sensing surface) of a standard QCM sensor. The shaded and dotted regions are gold. The dotted regions indicate the reference (bottom) side while the shaded regions indicate the sensing (top) side [52].**

QCM rate monitors have a slightly different electrode configuration with the sensing electrode covering almost the entire surface and no electrode wrap-around [14]. In the QCM sensor an electrical signal is delivered to the QCM via two leads that contact the back surface or reference surface of the crystal. The application of a high-frequency electrical signal excites the resonant thickness shear mode in the crystal. The thickness shear mode has mechanical displacements in the  $x_3$  direction that are perpendicular to the propagation in the  $x_2$  direction and parallel to the crystal surfaces (Figure 7). When a mechanical change (mass, viscosity, or elasticity) occurs on the sensor surface, the resonant frequency of the device changes [13, 43, 53]. For the QCM rate monitor, leads are attached to both crystal surfaces, also resulting in thickness field excitation.

Although the QCM rate monitor is the standard for monitoring thin film thicknesses in deposition systems, there are disadvantages associated with the QCM sensor platform. For some chemical or biological sensing applications, such as antibody attachment, the gold electrode on the sensing surface of the QCM necessitates using techniques such as the Langmuir–Blodgett method [54] to attach the selective chemical or biological film to the sensor surface instead of the silicon-based surface chemistries that are often used in chemical

and biological sensing applications. Further, the electric field associated with the thickness shear mode cannot penetrate into the measurand or sensing layer due to the conducting electrode on the sensing surface. Therefore, electrical property changes to the permittivity and/or conductivity of the adjacent liquid or chemi- or bioselective film caused by the target analyte cannot be detected with the standard QCM sensor.

Several researchers have investigated probing the electrical properties of a medium or sensing layer using thickness shear mode resonators by modifying the electrode geometry of the QCM. Josse, *et al.* modified the size and/or shape of the sensing electrode and found that it was effective in detecting conductivity and permittivity changes in liquid environments [21, 22]. In particular, they investigated the effect of decreasing the size of the sensing electrode (Figure 2.(a)) and also used a ring-shaped sensing electrode (Figure 2.(b)) to detect electrical properties in liquid environments. They recognized that resonators with these modified electrodes were capacitance sensors. Measurement of the static capacitance changes due to changes in the liquid environment is made through measurement of the changes in anti-resonant frequency. Thus, these devices combine the advantages of a mass-sensitive QCM with a capacitive sensor.

Zhang and Vetelino also examined the resonators with small sensing electrodes (Figure 2.(a)) and ring-shaped sensing electrodes (Figure 2.(b)) as well as an open-ring electrode (Figure 2.(c)) [23, 24]. They performed extensive experiments characterizing these modified electrode resonators to liquid loads with changing viscosity, conductivity and permittivity. They found that as the overlap between the sensing electrode and the reference electrode was minimized, the sensitivity of the thickness shear mode resonator to liquid electrical property changes was almost 25 times greater than for the standard QCM electrode. Specifically, the results obtained when the devices were exposed to various

concentrations of NaCl in solution showed the decreased size and open-ring sensing electrodes to have much higher frequency shifts than the standard QCM.

Andle, *et al.* examined a novel thickness shear mode sensor referred to as a monolithic piezoelectric sensor [55-57]. This sensor has a circular electrode on the reference side of the piezoelectric disc and two semicircular electrodes separated by a gap on the sensing surface. This structure results in a two-pole coupled resonator in which the electrical response is determined by the mechanical coupling between the input and output electrodes. The two resonant modes of the monolithic piezoelectric sensor were found to be equally sensitive to mass loading by thin solid films, yet exhibited different responses to viscous liquid loading. The advantage of this sensor is that a single-frequency oscillator can be designed to be sensitive only to bound mass at the sensing surface and not to solution effects. The design of the monolithic piezoelectric sensor must be optimized so that there is minimal compressional wave generation.

### ***2.3.2. Lateral-Field Excitation of BAW Resonators***

The thickness shear mode can also be excited in piezoelectric plates by application of an electric field parallel to the crystal surfaces. This excitation is called lateral-field excitation. In an LFE sensor element both electrodes are placed on the surface opposite the sensing medium while still exciting a thickness shear mode (Figure 4). In this case, the sensing surface of the device is bare and one can either expose it directly to a measurand or attach a chemi- or bioselective layer directly on the bare crystal surface. The LFE sensing platform has a simpler electrode structure than the QCM sensor and can be realized in a small portable package. Like the QCM sensor, the measurable output from an LFE sensing platform is a change in its resonant frequency due to mechanical and electrical property changes in the sensing film caused by the measurand.

Recently Hempel, *et al.* have shown that changes in the electrical properties of the analyte can cause a redistribution of the electric field from the lateral direction to the thickness direction [41]. This redistribution results in a piezoelectric stiffening which produces a change in the velocity of the acoustic wave. Thus, the bare quartz sensing surface allows the LFE sensor element to detect both electrical and mechanical property changes in the analyte or sensing film.

#### **2.4. Modeling Bulk Acoustic Waves**

The theory of elastic waves in both non-piezoelectric and piezoelectric solids has been discussed in section 2.2. A full coupled-wave analysis of the thickness shear mode in piezoelectric crystals is mathematically advanced, requiring knowledge in linear algebra, multidimensional calculus, and tensor analysis. The resulting systems of equations often must be solved using numerical methods as the equations can't always be determined analytically and a full 3-dimensional analysis is difficult to solve. Due to the piezoelectric nature of the resonator crystal the particle “displacements and the electrical potential as well as their derivatives with respect to time and location are coupled with each other... [58].” This can result in large errors of the predicted behavior of the thickness shear mode for small errors in the crystal alignment. For certain crystal and electrode orientations a one-dimensional analysis may be used to model the thickness shear mode. In order to use a one-dimensional analysis for a thickness shear mode resonator, the lateral dimensions of the resonator crystal must be much greater than the crystal thickness [59]. The resonator crystal is assumed to be infinite in the lateral directions and further, the physical properties of the crystal are assumed to be constant in the lateral directions [60].

One may simplify this complicated analysis through the use of models. In this section three models for describing the thickness shear mode in BAW resonators will be presented. The models examined are:

1. the Mason circuit model;
2. the Martin circuit model;
3. a transmission line model.

All of the models are derived through use of the equations given in sections 2.1. - 2.3. applied to the specific electrode geometry and crystal orientation for a particular BAW resonator. Since all of the devices examined for this research were fabricated on AT-cut quartz, the following analysis will be applied using this crystal. A summary of the various models and the loads under which an admittance is presented in this section are given in Table 2.

**Table 2. The equivalent circuit models for BAW resonators and the loads under which the admittance is presented**

<b>model</b>	<b>thickness-field excitation</b>	<b>lateral-field excitation</b>
Mason model	air load	air load
Martin model	liquid load reduced to air load	N/A
transmission line model	air and liquid loads	air load

**2.4.1. An Analysis of the Thickness Shear Mode in BAW Resonators**

In order to understand the physical significance of the three models, it is useful to present the equations describing the thickness shear mode in AT-cut quartz for both thickness-field and lateral-field excited BAW resonators. For both methods of excitation the analysis will end with an expression for the admittance of the thickness shear mode in AT-cut quartz. The analysis of thickness-field excited BAW resonators is performed for resonators under liquid loading. The admittance for the thickness-field excited BAW resonator is presented for the special case of a resonator under air loading. The analysis for

the LFE BAW resonators is performed only for the case of an air load. The full analysis of the LFE BAW resonator under liquid loading is given in chapter 3.

#### 2.4.1.1. *Thickness-Field Excited BAW Resonator*

A BAW resonator under liquid load has the geometry shown in Figure 9. The large lateral dimensions of the AT-cut quartz disc (25.4 mm in diameter), with respect to the crystal thickness, ( $h = 0.33$  mm) allows one “to treat the crystal as an infinite plate with finite thickness [59].” Because the quartz plate is assumed to be infinite in the  $x_1$  and  $x_3$  directions (Figure 9), the associated physical properties in these directions are assumed not to change.

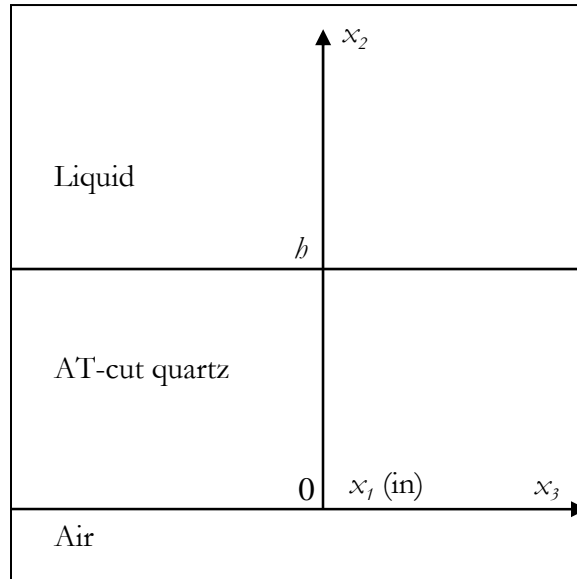


**Figure 9. Cross-sectional view BAW resonator with infinitesimally thin electrodes at  $x_2 = 0$  and  $x_2 = h$ .**

If it is assumed that the thickness shear mode in AT-cut quartz is a pure shear wave when excited by an electric field directed along the  $x_2$  axis, then a one-dimensional model provides a good approximation. The shear stresses for the geometry given in Figure 9 are

the stresses in the  $x_1$  and  $x_3$  direction acting on the surface normal to  $x_2$ , which are defined as  $T_{21}$  and  $T_{23}$  from Figure 5. Recall from section 2.1. that due to the symmetry of the crystal that  $S_{kl} = S_{lk}$  and  $T_{ij} = T_{ji}$ . The pure shear stresses are found from equation (2.19) and can be expressed as

$$T_{21} = T_{12} = c_{66}S_{12} + c_{66}S_{21} - e_{26}E_2 = 2c_{66}S_{12} - e_{26}E_2 \quad (2.28)$$

and

$$T_{23} = T_{32} = c_{44}S_{23} + c_{44}S_{32} - e_{24}E_2 = 2c_{44}S_{23} - e_{24}E_2. \quad (2.29)$$

It must be noted that when applying the index transformation in Table 1 to the piezoelectric stress constants, the transformation is applied to the last two indices, with the first index remaining unchanged. Substituting equations (2.11) and ((2.23)) into equations (2.28) and (2.29) yields

$$T_{12} = c_{66}u_{1,2} + e_{26}\phi_{,2} \quad (2.30)$$

and

$$T_{32} = c_{44}u_{3,2} + e_{24}\phi_{,2}. \quad (2.31)$$

However, if one examines the piezoelectric stress constants for AT-quartz (Table 3), it is found that  $e_{24} = 0$ , meaning that the shear stress,  $T_{32}$ , can not be generated by the electric field,  $E_2$ , and thus, may be ignored. The electrical displacement, found by substituting equations (2.11) and (2.23) into equation (2.20), is

$$D_2 = e_{26}u_{1,2} - \epsilon_{22}\phi_{,2}. \quad (2.32)$$

For a pure shear wave in AT-cut quartz there are only displacements along the  $x_1$  axis that vary only in the  $x_2$  direction (Figure 7), i.e.  $u_1 = f(x_2, t)$ . Therefore, the equation of motion, from equation (2.10) is

$$T_{12,2} = \rho \ddot{u}_1 \quad (2.33)$$

and Maxwell's equation for electrical displacement, from equation (2.24) is

$$D_{2,2} = 0. \quad (2.34)$$

**Table 3. Non zero material constants for AT-cut quartz [47, 61]**

$c_{11} = 86.74 \times 10^9 \text{ N/m}^2$	$c_{12} = -8.25 \times 10^9 \text{ N/m}^2$	$c_{13} = 27.15 \times 10^9 \text{ N/m}^2$
$c_{14} = -3.66 \times 10^9 \text{ N/m}^2$	$c_{22} = 129.77 \times 10^9 \text{ N/m}^2$	$c_{23} = -7.42 \times 10^9 \text{ N/m}^2$
$c_{24} = 5.7 \times 10^9 \text{ N/m}^2$	$c_{33} = 102.83 \times 10^9 \text{ N/m}^2$	$c_{34} = 9.92 \times 10^9 \text{ N/m}^2$
$c_{44} = 38.61 \times 10^9 \text{ N/m}^2$	$c_{55} = 68.81 \times 10^9 \text{ N/m}^2$	$c_{56} = 2.53 \times 10^9 \text{ N/m}^2$
$c_{66} = 29.013 \times 10^9 \text{ N/m}^2$	$e_{11} = -0.171 \text{ C/m}^2$	$e_{12} = -0.152 \text{ C/m}^2$
$e_{13} = -0.0187 \text{ C/m}^2$	$e_{14} = 0.067 \text{ C/m}^2$	$e_{25} = 0.108 \text{ C/m}^2$
$e_{26} = -0.0949 \text{ C/m}^2$	$e_{35} = -0.0761 \text{ C/m}^2$	$e_{36} = 0.06707 \text{ C/m}^2$
$\varepsilon_{11} = 39.21 \times 10^{-12} \text{ C}^2/\text{Nm}^2$	$\varepsilon_{22} = 39.816 \times 10^{-12} \text{ C}^2/\text{Nm}^2$	$\varepsilon_{23} = 0.8678 \times 10^{-12} \text{ C}^2/\text{Nm}^2$
$\varepsilon_{33} = 40.424 \times 10^{-12} \text{ C}^2/\text{Nm}^2$	$\rho = 2649 \text{ kg/m}^3$	

Since the particle displacement and the electric potential have a harmonic time dependence,

$$u(t) = u_i e^{j\omega t} \quad (2.35)$$

and

$$\phi(t) = \phi_i e^{j\omega t}, \quad (2.36)$$

equations (2.30) and ((2.32)) can be rewritten as

$$T_{12} = c_{66} u_{1,2} e^{j\omega t} + e_{26} \phi_{,2} e^{j\omega t} \quad (2.37)$$

and

$$D_2 = e_{26} u_{1,2} e^{j\omega t} - \varepsilon_{22} \phi_{,2} e^{j\omega t}. \quad (2.38)$$

Substituting equation (2.37) into equation (2.33) and rearranging results in:

$$c_{66} u_{1,22} + e_{26} \phi_{,22} + \rho \omega^2 u_1 = 0. \quad (2.39)$$

Similarly, substituting equation (2.38) into equation (2.34) and rearranging yields:



$$\phi_{,22} = \frac{e_{26}}{\varepsilon_{22}} u_{1,22}. \quad (2.40)$$

Next, equation (2.40) is substituted into equation (2.39),

$$\bar{c}_{66} u_{1,22} + \rho \omega^2 u_1 = 0 \quad (2.41)$$

where  $\bar{c}_{66}$  is defined as the piezoelectrically stiffened elastic constant [62] as follows,

$$\bar{c}_{66} = c_{66} + \frac{e_{26}^2}{\varepsilon_{22}}. \quad (2.42)$$

Since the thickness shear mode generates a standing wave in the quartz crystal, the acoustic wave is moving in both the  $+x_2$  and  $-x_2$  directions. The shear particle displacement is then described by

$$u_1 = (A_1 e^{jk_t x_2} + A_2 e^{-jk_t x_2}) e^{j\omega t} \quad (2.43)$$

where  $k_t$  is the wave propagation vector for the thickness-field excited thickness shear mode,

$$k_t = \omega \sqrt{\frac{\rho}{\bar{c}_{66}}}. \quad (2.44)$$

Substituting equation (2.43) into equations (2.39) and (2.40) and integrating both equations twice with respect to  $x_2$  gives

$$T_{12} = [jk_t \bar{c}_{66} (A_1 e^{jk_t x_2} - A_2 e^{-jk_t x_2}) + e_{26} A_3] e^{j\omega t}, \quad (2.45)$$

$$\phi = \left[ \frac{e_{26}}{\varepsilon_{22}} (A_1 e^{jk_t x_2} + A_2 e^{-jk_t x_2}) + A_3 x_2 + A_4 \right] e^{j\omega t}, \quad (2.46)$$

and

$$D_2 = -\varepsilon_{22} A_3 e^{j\omega t}. \quad (2.47)$$

The liquid in contact with the sensing surface is non-piezoelectric and can be treated as infinite in the  $x_2$  direction since the acoustic wave decays in the liquid within several wavelengths. The differential equation in the liquid is

$$c_l u_{1,22} + \omega^2 \rho_l u_1 = 0, \quad (2.48)$$

where  $c_l$  and  $\rho_l$  are the shear modulus and density of the liquid [60]. The shear modulus for a semi-infinite Newtonian liquid is defined [60] as follows,

$$c_l = \omega \eta_l, \quad (2.49)$$

where  $\eta_l$  is the bulk viscosity of the liquid. The solution of equation (2.48) in the liquid then takes the form

$$u_1 = B e^{jk_l x_2}, \quad (2.50)$$

where  $k_l$  is the propagation vector in the liquid.

The boundary conditions for the thickness-field excited BAW resonator are [43, 60]:

1. the particle displacement is continuous at the boundary between the resonator and the contacting liquid,  $(u_1(h^-) = u_1(h^+))$ ,
2. the shear stress is continuous at the boundary between the resonator and the contacting liquid,  $(T_{12}(h^-) = T_{12}(h^+))$ ,
3. the shear stress at the free surface of the resonator disappears,  $(T_{12}(0) = 0)$ ,
4. the electrical potential is the same as the applied potential at the sensing surface,  $(\phi(h) = \pm \phi_0 e^{j\omega t})$  and
5. the electrical potential is the same as the applied potential at the reference surface,  $(\phi(0) = \mp \phi_0 e^{j\omega t})$ .

This analysis of the thickness shear mode in an AT-cut quartz BAW resonator results in five unknowns:  $A_1$ ,  $A_2$ ,  $A_3$ ,  $A_4$ , and  $B$ . The five boundary conditions listed above provide one with the equations necessary to solve for the unknowns. Standard linear algebra methods can be used to solve this system of equations. The impedance for a liquid-loaded thickness-field excited BAW resonator can be shown to be the following [60],

$$Z = \frac{1}{j\omega C_0} \left( 1 - \frac{e_{26}^2 / (\epsilon_{22} \bar{c}_{66})}{k_t h / 2} \frac{\tan\left(\frac{k_t h}{2}\right) - j \frac{Z_L}{\sqrt{\rho \bar{c}_{66}}}}{1 - j \frac{Z_L}{\sqrt{\rho \bar{c}_{66}}} \cot(k_t h)} \right), \quad (2.51)$$

where  $Z_L$  is the impedance of the liquid load, defined [60] as follows,

$$Z_L = (1 + j) \sqrt{\frac{\omega \rho_l \eta_l}{2}}. \quad (2.52)$$

#### 2.4.1.2. *Lateral-Field Excited BAW Resonator*

The analysis of LFE BAW resonators is presented for the case of a resonator under air loading. The treatment for lateral-field excited BAW resonators is similar to that given for thickness-field excited BAW resonators. The primary difference is that the electrodes are positioned such that the electric field is directed along the  $x_3$  axis (Figure 10). The approach used here to find the admittance of LFE resonators was first reported by Yamada and Niizeki [63].

Two assumptions are made to ensure that only laterally-directed electric fields are considered. The first is that the thickness of the plate is small when compared with the other dimensions. The second is that the applied electric field is strictly parallel to the major faces of the plate throughout the crystal plate. Since the applied electric field is assumed to

be only laterally oriented, the fringing fields, which occur due to the small dimensions of the quartz plate, are neglected.

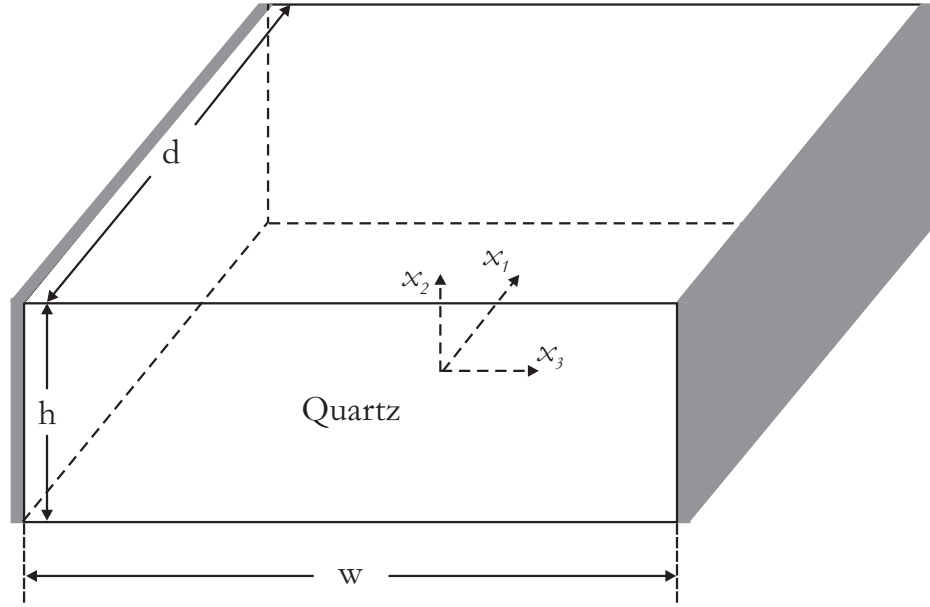


**Figure 10.** A lateral-field excited BAW resonator with the origin of the coordinate system centered on the bottom surface of the plate

The mechanical boundary condition is that the two major faces of the plate are traction free,

$$T_{2j} = 0 \text{ at } x_2 = 0, h. \quad (2.53)$$

The electrical boundary condition is that the electric displacement must be continuous at the major faces of the plate,

$$D_2 = \epsilon_0 (E_{out})_2 \text{ at } x_2 = 0, h, \quad (2.54)$$

where  $(E_{out})_2$  is the external electric field in the  $x_2$  direction. Because of the second assumption where the electric field components are strictly parallel to the major faces of the plate,  $(E_{out})_2 = 0$ . Thus,

$$D_2 = 0 \text{ at } x_2 = 0, h. \quad (2.55)$$

From the two initial assumptions on page 32 all of the basic quantities except  $\phi$  should be independent of  $x_3$  and  $x_1$ . The electric potential,  $\phi$ , depends on  $x_2$  and  $x_3$ . The basic equations, (2.10)-(2.24) for a vibrating plate can now be simplified,

$$T_{2j,2} = \rho \ddot{u}_j, \quad (2.56)$$

$$D_{2,2} = 0, \quad (2.57)$$

$$T_{2j} = c_{2jk} u_{k,2} - e_{22j} E_2 - e_{32j} E_3, \quad (2.58)$$

$$D_2 = e_{22k} u_{k,2} + \varepsilon_{22} E_2 + \varepsilon_{23} E_3, \quad (2.59)$$

and

$$D_3 = e_{32k} u_{k,2} + \varepsilon_{23} E_2 + \varepsilon_{33} E_3. \quad (2.60)$$

From equations (2.55) and (2.57),

$$D_2 = 0 \quad (2.61)$$

for any value of  $x_1$  or  $x_2$ . Substituting equation (2.61) into (2.59),

$$E_2 = -\frac{e_{22k}}{\varepsilon_{22}} u_{k,2} - \frac{\varepsilon_{23}}{\varepsilon_{22}} E_3. \quad (2.62)$$

This new expression for  $E_2$  can then be substituted into equations (2.58) and (2.60), yielding

$$T_{2j} = \bar{c}_{jk} u_{k,2} - \left( e_{32j} - \frac{\varepsilon_{23}}{\varepsilon_{22}} e_{22j} \right) E_3, \quad (2.63)$$

and

$$D_3 = \left( e_{32k} - \frac{e_{22k} \varepsilon_{23}}{\varepsilon_{22}} \right) u_{k,2} + \bar{\varepsilon}_{33} E_3 \quad (2.64)$$

where

$$\bar{c}_{jk} = c_{2jk} + \frac{e_{22j} e_{22k}}{\varepsilon_{22}} \quad (2.65)$$

and

$$\bar{\varepsilon}_{33} = \varepsilon_{33} - \frac{\varepsilon_{23}^2}{\varepsilon_{22}}. \quad (2.66)$$

Since the index, 2, is fixed in equations (2.53)-(2.63), equations (2.56) and (2.63) can be written in matrix notation as follows,

$$\mathbf{T}_{,2} = \rho \ddot{\mathbf{u}}, \quad (2.67)$$

$$\mathbf{T} = [\bar{c}_{jk}] \mathbf{u}_{,2} - \mathbf{e} E_3. \quad (2.68)$$

The components of these vectors are defined [63] as

$$\mathbf{T} = \begin{pmatrix} T_{21} \\ T_{22} \\ T_{23} \end{pmatrix}, \quad \mathbf{u} = \begin{pmatrix} u_1 \\ u_2 \\ u_3 \end{pmatrix}, \quad \mathbf{e} = \begin{pmatrix} e_{321} - e_{221} \varepsilon_{23} / \varepsilon_{22} \\ e_{322} - e_{222} \varepsilon_{23} / \varepsilon_{22} \\ e_{323} - e_{223} \varepsilon_{23} / \varepsilon_{22} \end{pmatrix}. \quad (2.69)$$

The boundary condition given by equation (2.53) may be rewritten using matrix notation and is given:

$$\mathbf{T} = \mathbf{0} \quad \text{at } x_2 = 0, h \quad (2.70)$$

where  $\mathbf{0}$  is the zero vector.

Since  $[\bar{c}_{jk}]$  is a real and symmetric matrix, it can be diagonalized by an orthogonal matrix [64],  $[\beta]$  as follows,

$$[\beta]^T [\bar{c}_{jk}] [\beta] = [c^{(j)} \delta_{jk}] \quad (2.71)$$

where

$$[\beta] = \begin{bmatrix} \beta_1^{(1)} & \beta_1^{(2)} & \beta_1^{(3)} \\ \beta_2^{(1)} & \beta_2^{(2)} & \beta_2^{(3)} \\ \beta_3^{(1)} & \beta_3^{(2)} & \beta_3^{(3)} \end{bmatrix} \quad (2.72)$$

and  $[c^{(j)} \delta_{jk}]$  is a diagonal matrix.  $[\beta]^T$  is the transpose matrix of  $[\beta]$ , which satisfies the relation

$$[\boldsymbol{\beta}]^T [\boldsymbol{\beta}] = [\boldsymbol{\beta}] [\boldsymbol{\beta}]^T = [\boldsymbol{\delta}_{jk}], \quad (2.73)$$

and  $\delta_{jk}$  are the elements of the identity matrix defined as

$$\delta_{jk} = \begin{cases} 1, & j = k \\ 0, & j \neq k \end{cases}. \quad (2.74)$$

Multiplying both sides of equation (2.71) by  $[\boldsymbol{\beta}]$  and substituting (2.73) yields

$$\begin{aligned} [\boldsymbol{\beta}] [\boldsymbol{\beta}]^T [\bar{c}_{jk}] [\boldsymbol{\beta}] &= [\bar{c}_{jk}] [\boldsymbol{\beta}] = [\boldsymbol{\beta}] [c^{(j)} \boldsymbol{\delta}_{jk}] \\ &= \begin{bmatrix} \beta_1^{(1)} & \beta_1^{(2)} & \beta_1^{(3)} \\ \beta_2^{(1)} & \beta_2^{(2)} & \beta_2^{(3)} \\ \beta_3^{(1)} & \beta_3^{(2)} & \beta_3^{(3)} \end{bmatrix} \begin{bmatrix} c^{(1)} & 0 & 0 \\ 0 & c^{(2)} & 0 \\ 0 & 0 & c^{(3)} \end{bmatrix}. \end{aligned} \quad (2.75)$$

Since the matrix  $[c^{(j)} \boldsymbol{\delta}_{jk}]$  contains only nonzero values on the diagonal equation (2.75) can be rewritten as an eigenequation as follows,

$$[\bar{c}_{jk}] \boldsymbol{\beta}^{(i)} = c^{(i)} \boldsymbol{\beta}^{(i)}, \quad (2.76)$$

where

$$\boldsymbol{\beta}^{(i)} = \begin{pmatrix} \beta_1^{(i)} \\ \beta_2^{(i)} \\ \beta_3^{(i)} \end{pmatrix} \quad (2.77)$$

is the eigenvector of  $[\bar{c}_{jk}]$  and  $c^{(i)}$  is the eigenvalue for each of the acoustic modes, where  $i = a, b, c$ . Physically, the eigenvalues,  $c^{(i)}$ , are related to the longitudinal mode, ( $i = a$ ), the fast shear mode, ( $i = b$ ), and the thickness shear mode, ( $i = c$ ) [35]. The longitudinal mode has the eigenvalue,  $c^{(a)}$ , with the largest root and, thus the greatest acoustic wave velocity,  $v_a$ , and the eigenvector,  $\boldsymbol{\beta}^{(a)}$ , has its largest component in the  $x_2$  direction. The fast shear mode has the eigenvalue,  $c^{(b)}$ , with the median root and, thus the median acoustic wave velocity,  $v_a$ , and the eigenvector,  $\boldsymbol{\beta}^{(b)}$ , has its largest component in the  $x_1$  direction. The

thickness shear mode has the eigenvalue,  $c^{(c)}$ , with the smallest root and, thus the smallest acoustic wave velocity,  $v_a$ , and the eigenvector,  $\boldsymbol{\beta}^{(c)}$ , has its largest component in the  $x_3$  direction. These results are summarized in Table 4.

**Table 4. The relationship between the acoustic modes and the eigenvalues for an LFE resonator on AT-cut quartz**

mode	eigenvalue ( $c^{(i)}$ )	eigenvector ( $\boldsymbol{\beta}^{(i)}$ )
longitudinal mode ( $a$ )	the largest root	the largest component is in the $x_2$ direction
fast shear mode ( $b$ )	the median root	the largest component is in the $x_1$ direction
thickness shear mode ( $c$ )	the smallest root	the largest component is in the $x_3$ direction

It is convenient to transform the vectors given in equation (2.69) as follows,

$$\begin{aligned}\mathbf{T} &= [\boldsymbol{\beta}] \boldsymbol{\Gamma}^0, \\ \mathbf{u} &= [\boldsymbol{\beta}] \mathbf{u}^0, \\ \mathbf{e} &= [\boldsymbol{\beta}] \mathbf{e}^0\end{aligned}\tag{2.78}$$

The transformed vectors in equation (2.78) are used along with equations (2.71) and (2.73) to rewrite equations (2.67), (2.68), and (2.70), as

$$\mathbf{T}_{,2}^0 = \rho \ddot{\mathbf{u}}^0,\tag{2.79}$$

$$\mathbf{T}^0 = [\boldsymbol{\beta}]^T [\bar{c}_{jk}] [\boldsymbol{\beta}] \mathbf{u}_{,2}^0 - [\boldsymbol{\beta}]^T [\boldsymbol{\beta}] \mathbf{e}^0 E_3 = [c^{(i)} \delta_{jk}] \mathbf{u}_{,2}^0 - \mathbf{e}^0 E_3,\tag{2.80}$$

and

$$\mathbf{T}^0 = \mathbf{0} \text{ at } x_2 = 0, h.\tag{2.81}$$

Substituting equation (2.80) into equation (2.79) yields

$$[c^{(i)} \delta_{jk}] \mathbf{u}_{,22}^0 - \mathbf{e}^0 E_{3,2} = \rho \ddot{\mathbf{u}}^0 = -\rho \omega^2 \mathbf{u}^0.\tag{2.82}$$

The applied electric field,  $E_3$ , is parallel to the quartz plate and thus, uniform along the  $x_3$  axis, but may vary along the  $x_2$  axis since the mechanical displacement changes along



this axis. The electrodes are on the faces normal to the  $x_3$  axis, therefore the potential difference between the electrodes does not vary along the  $x_2$  axis. If the potential difference between the electrodes is  $\phi_0$  then using equation ((2.23)) and taking the derivative of both sides with respect to  $x_2$  yields

$$E_{3,2} = -\phi_{0,32} = 0. \quad (2.83)$$

Substituting equation (2.83) into equation (2.82) results in

$$[c^{(i)} \delta_{jk}] \mathbf{u}_{,22}^0 = -\rho \omega^2 \mathbf{u}^0. \quad (2.84)$$

Since the  $i$  mode is the only mode that is piezoelectrically coupled to  $E_3$  (Figure 3), equation (2.84) can be simplified as follows,

$$c^{(c)} \mathbf{u}_{,22}^{0(c)} = -\rho \omega^2 \mathbf{u}^{0(c)}. \quad (2.85)$$

The standing wave solution to equation (2.85) is

$$\mathbf{u}^{0(c)} = A_c \sin(k_l^{(c)} x_2) + B_c \cos(k_l^{(c)} x_2), \quad (2.86)$$

where  $A_c$  and  $B_c$  are constants and  $k_l^{(i)}$  is the propagation constant, expressed as

$$k_l^{(c)} = \omega \sqrt{\frac{\rho}{c^{(c)}}}. \quad (2.87)$$

Taking the derivative of equation (2.86) with respect to  $x_2$  yields

$$\mathbf{u}_{,2}^{0(c)} = k_l^{(c)} (A_c \cos(k_l^{(c)} x_2) - B_c \sin(k_l^{(c)} x_2)) \quad (2.88)$$

Substituting equation (2.88) into equation (2.80) yields

$$\mathbf{T}^{0(c)} = c^{(c)} k_l^{(c)} (A_c \cos(k_l^{(c)} x_2) - B_c \sin(k_l^{(c)} x_2)) - \mathbf{e}^{0(c)} E_3. \quad (2.89)$$

Substituting equation (2.89) into the boundary conditions given in equation (2.81) results in

$$\mathbf{T}^{0(c)}(x_2 = 0) = c^{(c)} k_l^{(c)} A_c - \mathbf{e}^{0(c)} E_3 = 0. \quad (2.90)$$

and

$$\mathbf{T}^{0(c)}(x_2 = h) = c^{(c)}k_l^{(c)}\left(A_c \cos(k_l^{(c)}h) - B_c \sin(k_l^{(c)}h)\right) - \mathbf{e}^{0(c)}E_3 = 0. \quad (2.91)$$

Solving equations (2.90) and for  $A_c$  and  $B_c$  results in

$$\begin{aligned} A_c &= \frac{\mathbf{e}^{0(c)}E_3}{c^{(c)}k_l^{(c)}} \\ B_c &= \frac{\mathbf{e}^{0(c)}E_3}{c^{(c)}k_l^{(c)}} \left( \frac{\cos(k_l^{(c)}h) - 1}{\sin(k_l^{(c)}h)} \right) = -\frac{\mathbf{e}^{0(c)}E_3}{c^{(c)}k_l^{(c)}} \tan(k_l^{(c)}h/2). \end{aligned} \quad (2.92)$$

Substituting equation (2.92) into equation (2.88) makes

$$\mathbf{u}_{,2}^{0(c)} = \frac{\mathbf{e}^{0(c)}E_3}{c^{(c)}} \left( \cos(k_l^{(c)}x_2) + \tan(k_l^{(c)}h/2) \sin(k_l^{(c)}x_2) \right) \quad (2.93)$$

The electric displacement,  $D_3$ , between the electrodes can be found by substituting equation (2.69) and then into equation (2.64) results in the following,

$$D_3 = \mathbf{e} \bullet \mathbf{u} + \bar{\epsilon}_{33}E_3. \quad (2.94)$$

Substituting equation (2.78) into equation (2.95) for the  $\iota$  mode yields

$$\begin{aligned} D_3 &= [\beta] \mathbf{e}^{0(c)} \bullet [\beta] \mathbf{u}_{,2}^{0(c)} + \bar{\epsilon}_{33}E_3 = \mathbf{e}^{0(c)} \bullet \mathbf{u}_{,2}^{0(c)} + \bar{\epsilon}_{33}E_3 \\ &= \frac{(\mathbf{e}^{0(c)})^2}{c^{(c)}} E_3 \left( \cos(k_l^{(c)}x_2) + \tan(k_l^{(c)}h/2) \sin(k_l^{(c)}x_2) \right) + \bar{\epsilon}_{33}E_3 \\ &= \bar{\epsilon}_{33}E_3 \left( 1 + (k_m^{(c)})^2 \left( \cos(k_l^{(c)}x_2) + \tan(k_l^{(c)}h/2) \sin(k_l^{(c)}x_2) \right) \right) \end{aligned} \quad (2.96)$$

where  $k_m^{(c)}$  is the lateral coupling factor to the  $\iota$  mode, defined as

$$k_m^{(c)} = \frac{\mathbf{e}^{0(c)}}{\sqrt{c^{(c)}\bar{\epsilon}_{33}}}. \quad (2.97)$$

The total charge on the electrode is given as [65]

$$Q = \int_A D_3|_{x_3=-a} dA, \quad (2.98)$$

where  $dA = dx_1 dx_2$  is the differential area of the electrode. Substituting equation (2.96) into equation (2.98) yields

$$\begin{aligned}
Q &= \int_A \bar{\epsilon}_{33} E_3 \left( 1 + (k_m^{(c)})^2 (\cos(k_l^{(c)} x_2) + \tan(k_l^{(c)} h/2) \sin(k_l^{(c)} x_2)) \right) dx_1 dx_2 \\
&= d \bar{\epsilon}_{33} E_3 \int_0^h \left( 1 + (k_m^{(c)})^2 (\cos(k_l^{(c)} x_2) + \tan(k_l^{(c)} h/2) \sin(k_l^{(c)} x_2)) \right) dx_2 \\
&= d \bar{\epsilon}_{33} E_3 \left( x_2 \Big|_0^h + \frac{(k_m^{(c)})^2}{k_l^{(c)}} \left( \sin(k_l^{(c)} x_2) \Big|_0^h - \tan(k_l^{(c)} h/2) \cos(k_l^{(c)} x_2) \Big|_0^h \right) \right). \quad (2.99) \\
&= dh \bar{\epsilon}_{33} E_3 \left( 1 + \frac{(k_m^{(c)})^2}{k_l^{(c)} h} (\sin(k_l^{(c)} h) - \tan(k_l^{(c)} h/2) (\cos(k_l^{(c)} h) - 1)) \right)
\end{aligned}$$

Recall, from equation (2.26), that the thickness of the crystal,  $h = n\lambda/2$  where  $n$  is an odd integer, thus

$$k_l^{(c)} h = n\pi. \quad (2.100)$$

Substituting equation (2.100) into (2.99) results in the following

$$\begin{aligned}
Q &= dh \bar{\epsilon}_{33} E_3 \left( 1 + \frac{(k_m^{(c)})^2}{k_l^{(c)} h} (\tan(k_l^{(c)} h/2) (1+1)) \right) \\
&= dh \bar{\epsilon}_{33} E_3 \left( 1 + (k_m^{(c)})^2 \frac{\tan(k_l^{(c)} h/2)}{k_l^{(c)} h} \right). \quad (2.101)
\end{aligned}$$

Remembering that the thickness shear mode has a time dependence  $e^{j\omega t}$ , the current between the electrodes is calculated to be

$$I = \frac{\partial Q}{\partial t} = j\omega Q. \quad (2.102)$$

The applied voltage between the electrodes is

$$V = E_3 w. \quad (2.103)$$

The admittance of the LFE resonator can be found by substituting equation (2.101) into equation (2.102) and dividing by equation (2.103) as follows,

$$Y = \frac{I}{V} = \frac{j\omega dh \bar{\epsilon}_{33}}{w} \left( 1 + (k_m^{(c)})^2 \frac{\tan(k_l^{(c)} h/2)}{k_l^{(c)} h/2} \right). \quad (2.104)$$

The static capacitance for the LFE resonator is

$$C_0 = \frac{dh\bar{\epsilon}_{33}}{w}, \quad (2.105)$$

allowing equation (2.104) to be rewritten as

$$Y = j\omega C_0 \left( 1 + (k_m^{(c)})^2 \frac{\tan(k_l^{(c)} h/2)}{k_l^{(c)} h/2} \right). \quad (2.106)$$

Comparison of equation (2.106) to equation (2.51) reveals similarities between the impedance of thickness-field excited BAW resonators and the admittance of lateral-field excited BAW resonators. This duality between the impedance of thickness-field excited resonators and the admittance of LFE resonators is due to the differences of the electrode geometries to excite the thickness shear mode [6].

#### **2.4.2. Mason Circuit Model**

One of the earliest lumped circuit element models is the Mason model, (Figure 11), after Warren Mason, one of the pioneers in crystal acoustics [42]. The term lumped means that the circuit elements have constant impedance, both magnitude and phase, over the length of the element. The lumped elements are derived from the physical characteristics of the piezoelectric crystal.

Some advantages of the Mason model are that it is an accurate wideband representation of a BAW resonator and is capable of modeling layered BAW resonator structures. Disadvantages of the Mason model are that it is “cumbersome to work with [42]” and the impedance of layered structures, including mass and liquid layers, is transcendental. Since the impedance of a liquid-loaded BAW resonator using the Mason model is transcendental, we will examine only the air-loaded case.

### 2.4.2.1. Thickness-Field Excited BAW Resonator

The Mason model for a thickness-field excited BAW resonator is shown in Figure 11. Examination of Figure 11 reveals that there are two acoustic ports and one electrical port, and that the relations between the input force,  $F_1$ , the output force,  $F_2$ , and the voltage across the electrodes,  $V$ , can be obtained by use of this model. One should also note that this model contains the physically unrealizable static capacitance  $-C_0$ . The acoustic impedance,  $Z_c$ , of the crystal for a given propagation direction is defined in terms of stress,  $T$ , and particle velocity,  $v$ , as follows [66],

$$Z_c = -T/v, \quad (2.107)$$

where

$$v = \frac{\partial u}{\partial t}. \quad (2.108)$$

The negative sign in the characteristic impedance of the crystal accounts for the fact that  $T$  and  $v$  are  $180^\circ$  out of phase [66]. When evaluating the acoustic impedance, only the term corresponding to the wave travelling in the  $+x_2$  direction in equation (2.45) needs to be considered. The wave travelling in the  $-x_2$  direction can be ignored as the acoustic impedance is for a given propagation direction. The term containing the electrical components of the thickness shear mode can also be neglected as the acoustic impedance is only a function of the mechanical properties of the crystal. The acoustic impedance for the thickness shear mode in AT-cut quartz is found using by substituting equation ((2.44)) into equation (2.45) and substituting equation (2.43) into equation (2.108),

$$Z_c = -\frac{T_{12}}{v_1} = -\frac{-j\bar{c}_{66}\omega\sqrt{\rho/c_q}A_2e^{-j(k_1x_2-\omega t)}}{j\omega A_2e^{-j(k_1x_2-\omega t)}} = \sqrt{\rho\bar{c}_{66}}. \quad (2.109)$$

However, the Mason model is characterized as a function of the applied force rather than stress. Knowing that the relationship between stress and force is

$$T = FA, \quad (2.110)$$

where  $A$  is the surface area the force is acting on. The characteristic impedance of the medium can then be expressed as a function of force as follows,

$$\bar{Z}_c = A\sqrt{\rho\bar{c}_{66}}. \quad (2.111)$$

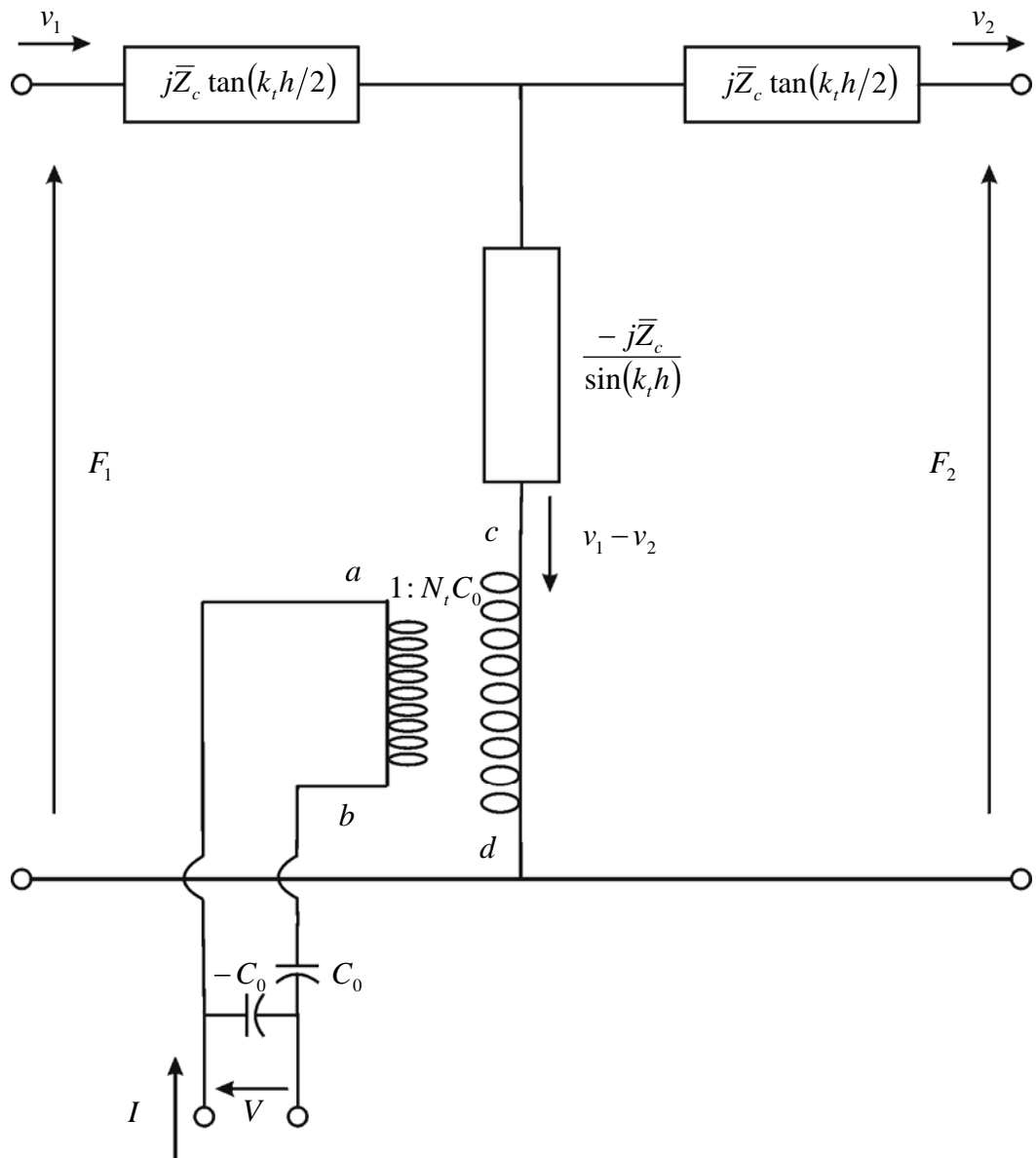


Figure 11. A three-port Mason model for a thickness-field excited BAW resonator

The transformer in the Mason model is the means by which the electrical energy is converted to acoustic energy, or vice versa. The turns ratio in the transformer determines the acoustic current due to the conversion of electrical energy to acoustic energy by the piezoelectric effect. The term  $N_t$ , (Figure 11), is obtained directly from equation (2.40), which describes the scalar potential in terms of the particle displacement, and is defined as [42]

$$N_t = \frac{e_{26}}{\varepsilon_{22}}. \quad (2.112)$$

The acoustic current is  $N_t C_0 (v_1 - v_2)$ , where  $v_1$  and  $v_2$  are the input and output particle velocities, respectively. The static capacitance,  $C_0$ , is due to the geometric configuration of the electrodes on the AT-cut quartz plate (Figure 9) and is given as

$$C_0 = \frac{\varepsilon_{22} A}{h}, \quad (2.113)$$

where  $A$  is the surface area of the electrodes.

Physically, the BAW resonator in Figure 9 is a one-port device. If we assume that the major surfaces of the resonator are stress free then both acoustic ports are shorted. This reduces the Mason model to a one-port model, which can be characterized by the input impedance,  $Z_{in}$  of the resonator. The closed-form expression for  $Z_{in}$  is [42]

$$Z_{in} = \frac{1}{j\omega C_0} \left( 1 - k_m^2 \frac{\tan(k_t h/2)}{k_t h/2} \right), \quad (2.114)$$

where  $k_m^2$  is the electro-mechanical coupling constant

$$k_m^2 = \frac{e_{26}^2}{\varepsilon_{22} \bar{c}_{66}}. \quad (2.115)$$



Substituting equation (2.115) into equation (2.114) reveals that it is similar to equation (2.51). Since this model accounts only for the air loaded case, the sensing surface is stress free and  $Z_L = 0$ , making equation (2.51) identical to equation (2.114). A detailed derivation of the impedance expression for the Mason model is presented in Appendix B.

#### 2.4.2.2. *Lateral-Field Excited BAW Resonator*

The Mason model for an LFE BAW resonator is shown in Figure 12 [6]. The turns ratio,  $N_l$ , for the lateral-field excited BAW resonator is

$$N_l = \frac{e_{36}}{\epsilon_{33}}. \quad (2.116)$$

Unlike the Mason model for thickness-field excited BAW resonators the model for LFE resonators does not contain the term  $-C_0$ . Thickness-field excitation and lateral-field excitation exhibit a duality, thus rather than expressing the LFE resonator in terms of its input impedance it will be expressed in terms of its input admittance,  $Y_{in}$  [6],

$$Y_{in} = j\omega C_0 \left( 1 + K_l^2 \frac{\tan(k_l h / 2)}{k_l h / 2} \right), \quad (2.117)$$

where,

$$C_0 = \frac{dh\epsilon_{33}}{w} \quad (2.118)$$

and

$$K_l^2 = \frac{e_{36}^2}{c_{66}\epsilon_{33}}. \quad (2.119)$$

Comparison of equations (2.117) and (2.106) shows that they are similar in form to each other with differences in defining the propagation constant and the coupling constant.

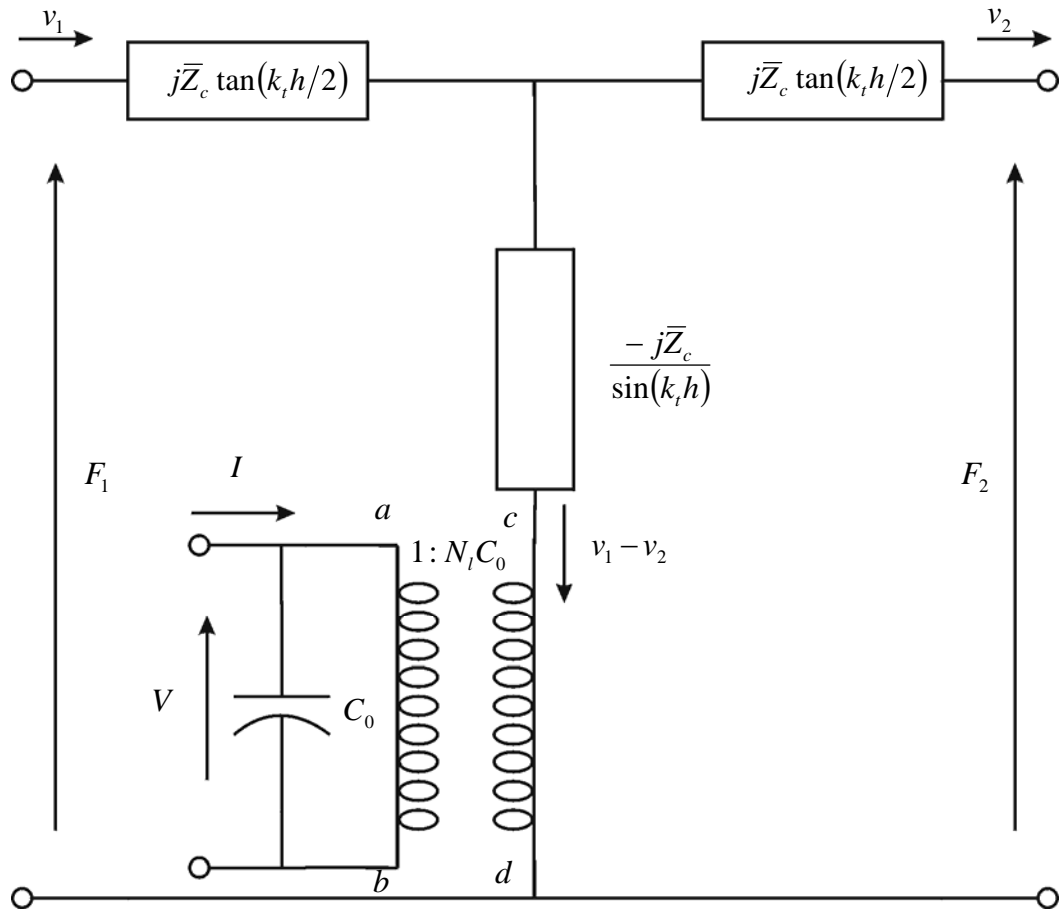


Figure 12. A three-port Mason model for a lateral-field excited BAW resonator

### 2.4.3. Martin Circuit Model

One solution to the disadvantages of the Mason model is to examine the impedance of the BAW resonator at or near resonance. A lumped circuit element model has been described for quartz crystal resonators under mass and viscous loading [43]. The QCM is modeled by using the one-dimensional thickness shear mode equations, (equations(2.30) – (2.50)), and applying the boundary conditions given on page 31. The impedance of the QCM under simultaneous mass and liquid loading is then derived [43] and expressed as

$$Z = \frac{1}{j\omega C_0} \left( \frac{1 + \Lambda \cot(k_t h) - k_m^2 \frac{\tan(k_t h/2) + \Lambda}{k_t h/2}}{1 + \Lambda \cot(k_t h)} \right), \quad (2.120)$$

where  $\Lambda$  is a complex factor containing the influence of liquid and mass loading at the QCM surface and is defined as [43]

$$\Lambda = \frac{\omega \rho_m + \sqrt{\omega \rho_l \eta_l / 2} - j \sqrt{\omega \rho_l \eta_l / 2}}{\sqrt{c_{66}} \rho}. \quad (2.121)$$

and  $\rho_l$  and  $\eta_l$  are the density and viscosity, respectively, of the liquid load and  $\rho_m$  is the density of the mass load.

If the sensing surface of the QCM is exposed to air, then the term  $\Lambda = 0$  and the impedance in equation (2.120) becomes

$$Z_{in} = \frac{1}{j\omega C_0} \left( 1 - k_m^2 \frac{\tan(k_t h/2)}{k_t h/2} \right), \quad (2.122)$$

Comparison of equations (2.114) and (2.122) reveals that the impedances of an unloaded QCM are the same for both models.

The impedance for the QCM derived in [43] is next approximated for operation at or near the resonant frequency. Lumped circuit elements are then derived that are related to the material properties of the mass and viscous loads at the sensing surface and the crystal. The parasitic capacitance,  $C_p$ , is experimentally determined and accounts for the parasitic effects of the electrical interface to the QCM. The static capacitance,  $C_0$ , is a function of the electrode geometry and crystal thickness, and does not influence the resonant conditions of the quartz crystal resonator but is dominant when the conditions are far from resonance. The circuit elements,  $C_1$ ,  $L_1$ , and  $R_1$ , model the unperturbed quartz crystal. The inductor,  $L_2$  and resistor,  $R_2$ , model the behavior of the QCM due to viscous loading. The inductor,  $L_3$ , models the admittance of the QCM due to mass loading in the motional arm of the circuit (Figure 13). This model predicts the same behavior as given by the Kanazawa equation [14] with  $\frac{\Delta f}{f_0} \propto \sqrt{\rho\eta}$  where  $\rho$  is the density and  $\eta$  is the viscosity of the material at the surface of the resonator.

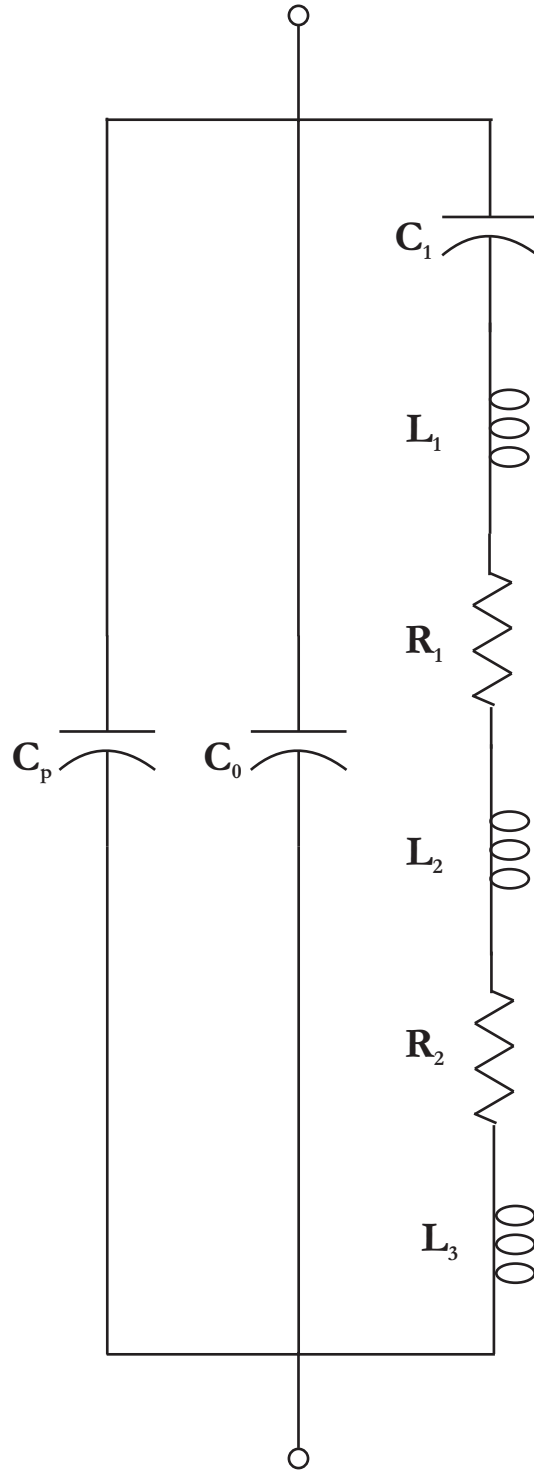


Figure 13. Equivalent circuit under mass and liquid loading including parasitic capacitance  $C_p$ .

The static capacitance is the same as for the Mason model and given by equation

(2.113). The other circuit element values for the Martin model [43] are

$$C_1 = \frac{8k_m^2 C_0}{(n\pi)^2}, \quad (2.123)$$

$$L_1 = \frac{1}{\omega_0^2 C_1}, \quad (2.124)$$

$$R_1 = \frac{\eta}{\bar{c}_{66} C_1} \left( \frac{\omega}{\omega_0} \right)^2, \quad (2.125)$$

$$L_2 = \frac{\omega_0 L_1}{n\pi} \sqrt{\frac{2\rho_l \eta_l}{\omega \bar{c}_{66} \rho}}, \quad (2.126)$$

$$R_2 = \frac{\omega_0 L_1}{n\pi} \sqrt{\frac{2\omega \rho_l \eta_l}{\bar{c}_{66} \rho}}, \quad (2.127)$$

and

$$L_3 = \frac{2\omega_0 L_1 \rho_m}{n\pi \sqrt{\bar{c}_{66} \rho}}. \quad (2.128)$$

If one removed the liquid and mass layer from the sensing surface of the QCM, then both  $\eta_l$  and  $\rho_m$  are zero, as are equations (2.126)-(2.128). This reduces the circuit in Figure 13 to that shown in Figure 14. The equivalent circuit in Figure 14 is known as the Butterworth-Van Dyke circuit.

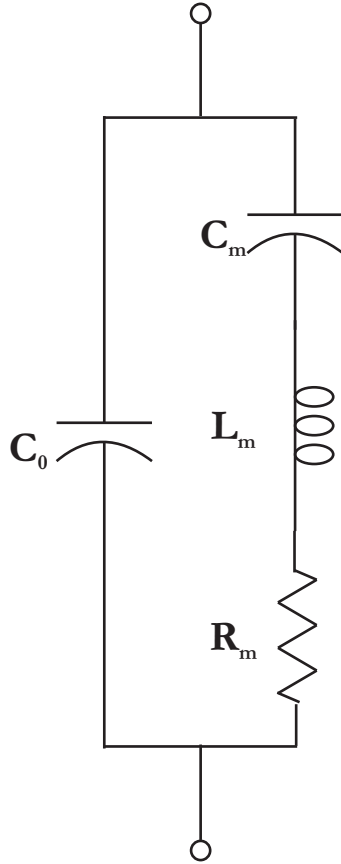


**Figure 14. Butterworth-Van Dyke equivalent circuit for resonator**

When using the LFE resonator as a sensor under liquid loads, the Martin model is insufficient to describe or predict the modifications to the input admittance,  $Y_{in}$ , due to electrical or mechanical changes at the sensor surface. Until now, no model exists for a liquid-loaded LFE BAW resonator similar to the Martin model. The derivation of such a model is the purpose of this work and is presented in chapter 3.

#### **2.4.4. *Transmission Line Model***

The final model that will be examined is the electric transmission line model. The transmission line starts with a three-port model for the piezoelectric crystal itself with two acoustic ports and an electric port. The acoustic input and output ports represent the two major surfaces of the crystal while the electric port represents the exciting electrodes. As

layers are added to the resonator they are modeled as a series of two-port transmission lines, unless the layer is piezoelectric, then it is represented as a three-port transmission line.

The advantages of the transmission line analog are:

- multiple layers on the sensor surface can be easily modeled regardless of the film properties or layer thickness;
- the model is accurate for the entire operating spectrum of the resonator;
- loading effects of the electrodes and standing acoustic waves in the substrate are considered; and
- it can be implemented and integrated in a complete electrical system.

The major limitation of the transmission line model is that it describes the *total* system characteristics. Thus, the transmission line model provides no understanding of what perturbations at the sensing surface of the resonator are due to, i.e. mass accumulation, physical property changes, electrical property changes, etc.

#### **2.4.4.1. Thickness-Field Excited BAW Resonator**

The most common transmission line model for thickness-field excited BAW resonators is referred to as the KLM model after Krimholtz, Leedom, and Matthaei who first described it in [44]. This model is ideal for sensors that have multiple film layers, such as the layers used in thin film bulk acoustic wave resonators. The KLM model for a BAW resonator with an acoustic load on one side of the plate can be represented by the equivalent circuit shown in Figure 15. The elements are [60]

$$N_{tx} = \frac{\sqrt{A}\epsilon_{22}\omega Z_c}{2e_{26} \sin\left(k_t \frac{h}{2}\right)} \quad (2.129)$$

and



$$X_{tx} = \frac{e_{26}^2}{A\varepsilon_{22}^2\omega^2 Z_c} \sin(k_t h), \quad (2.130)$$

with  $C_0$  given by equation (2.113). The admittance for the BAW resonator is then expressed as [60]

$$Z = \frac{1}{j\omega C_0} \left( 1 - \frac{k_m^2}{k_t h/2} \frac{\tan\left(\frac{k_t h}{2}\right) - j \frac{Z_L}{Z_c}}{1 - j \frac{Z_L}{Z_c} \cot(k_t h)} \right), \quad (2.131)$$

where  $Z_L$  is the load impedance and can account for any number of coatings or layers, (see full analysis in Appendix B). For a liquid loaded sensor the load impedance is [60]

$$Z_L = Z_{cl} \tanh\left(j \frac{\omega h'}{\sqrt{c_l/\rho_l}}\right), \quad (2.132)$$

where  $Z_{cl}$  is the acoustic impedance of the liquid load and is expressed as [60]

$$Z_{cl} = \sqrt{c_l \rho_l}. \quad (2.133)$$

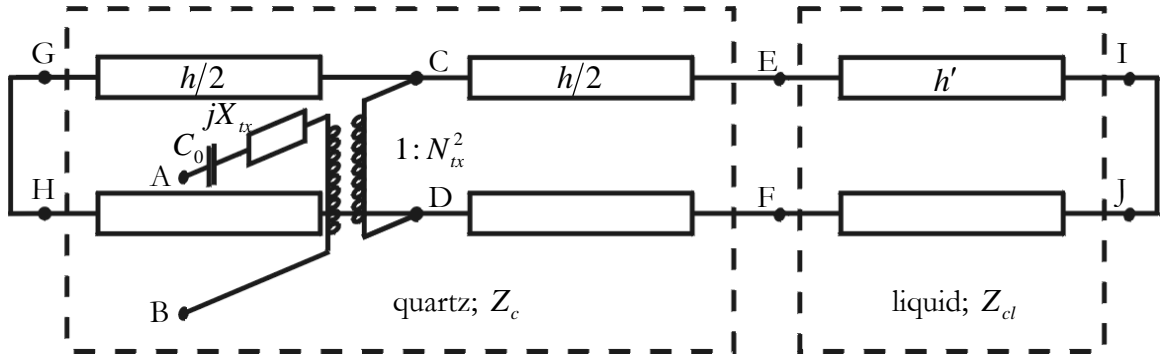


**Figure 15. A transmission line model for a thickness-field excited BAW resonator with an acoustic load on one side**

If we examine the impedance given in equation (2.131) and model the resonator with no load at the sensing surface,  $Z_L = 0$ , the impedance becomes

$$Z = \frac{1}{j\omega C_0} \left( 1 - k_m^2 \frac{\tan(k_t h/2)}{k_t h/2} \right), \quad (2.134)$$

which is precisely the expression for the impedance of a thickness-field excited resonator as given in equation (2.114).

#### 2.4.4.2. Lateral-Field Excited BAW Resonator

A transmission line model for an LFE resonator with two stress free surfaces has been described by Ballato, *et al.* [35] and is shown in Figure 16. The static capacitance,  $C_0$ , for the circuit is given by equation (2.105), the turns ratio of the transformer,  $N_{lx}$ , is expressed as

$$N_{lx} = k_m^{(c)} \sqrt{\frac{C_0 c^{(c)} A}{h}}, \quad (2.135)$$

and the characteristic admittance,  $Y_c^{(c)}$ , is defined as

$$Y_c^{(c)} = \frac{1}{A \sqrt{\rho c^{(c)}}}. \quad (2.136)$$

Analyzing the transmission line, (see Appendix B), one can find the admittance of an LFE BAW resonator, air loaded on both major surfaces, as follows,

$$Y = j\omega C_0 \left( 1 + (k_m^{(c)})^2 \frac{\tan(k_t^{(c)} h/2)}{k_t^{(c)} h/2} \right). \quad (2.137)$$

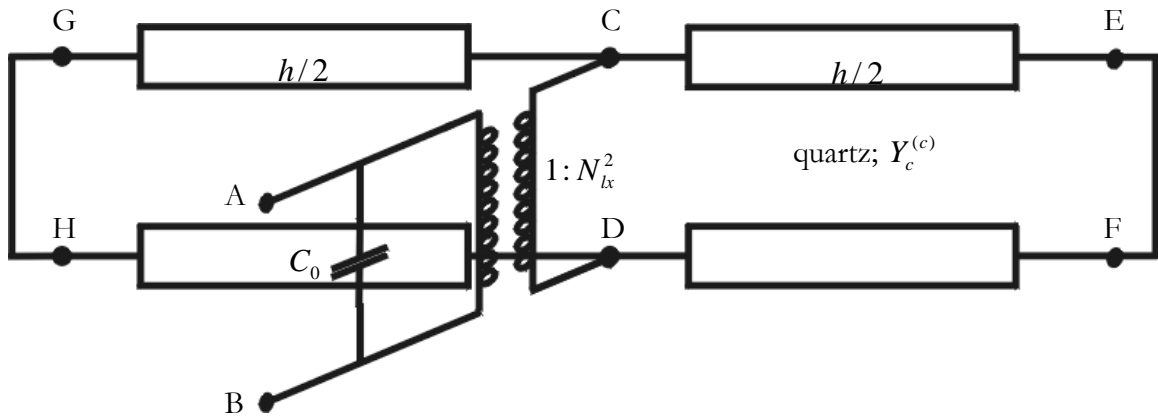


**Figure 16. A transmission line model for an LFE BAW resonator with an acoustic load on one side**

The admittance derived using the transmission line analysis in equation (2.137) is identical to that given in equation (2.106) using the coupled wave equations and similar to the admittance found using the Mason model in equation (2.114). Thus, all three models yield the same results for an LFE BAW resonator exposed to air on both major surfaces.

## Chapter 3

# EQUIVALENT CIRCUIT FOR A LATERAL-FIELD EXCITED SENSOR ELEMENT

In chapter 2, the theory for elastic waves in solids, for both nonpiezoelectric and piezoelectric crystals was presented. This was followed by the theory of operation for bulk acoustic wave (BAW) resonators. The analytic theory for thickness-field excited resonators exposed to liquid on one side and lateral-field excited (LFE) resonators in air was presented. The Mason model for both thickness-field excited and LFE resonators in air was discussed. This was followed by a description of the Martin model for thickness-field excited resonators under simultaneous mass and liquid loading, which was reduced to the air loaded case. The chapter concluded with the theory for the KLM transmission line model for thickness-field excited resonators under liquid loading and LFE resonators under air loading. This chapter focuses on the derivation of the equivalent circuit model used for a liquid-loaded lateral-field excited (LFE) sensor element. Chapter 4 will contain the experimental methods used to obtain the supporting data to verify the accuracy and precision of the equivalent circuit model developed in this chapter.

### **3.1. Setting up the Analysis**

The geometry of the liquid-loaded LFE sensor element is shown in Figure 17. The shaded regions are the metal electrodes, which are on the reference surface, leaving the sensing surface free of metal electrodes. The electrodes are assumed to be perfect conductors and have an infinitesimal thickness. The rotated material constants used in this analysis are for AT-cut quartz (Table 3), although the analysis can be extended to any piezoelectric material and orientation.

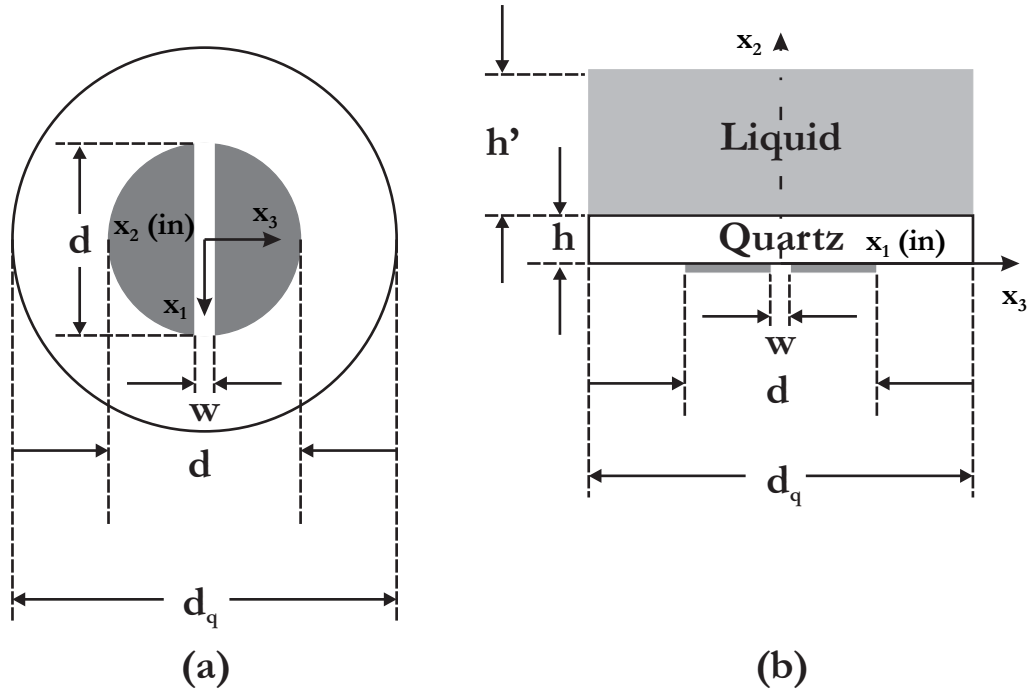


Figure 17. LFE sensor element geometry — the electrodes are shaded and on the reference side only.

### 3.2. Analysis of a Vibrating Lateral-Field Excited AT-Cut Quartz Sensor Element under Liquid Load

#### 3.2.1. *Equations for a Vibrating Quartz Plate*

The following equations for a vibrating AT-cut quartz plate are derived using the same method as Mindlin [67]. While the fundamental equations were presented in chapter 2, they are simplified in this section for the crystal symmetry of AT-cut quartz. Further simplification of the equations is possible if we consider only simple  $x_1$ -thickness-shear modes in the AT-cut quartz plate. Thus, in the quartz plate,  $0 \leq x_2 \leq h$ ,

$$u_1 = u_1(x_2, t) \quad (3.1)$$

and

$$u_2 = u_3 = 0. \quad (3.2)$$

Since only the displacements,  $u_1$ , are nonzero we can rewrite equation (2.11) for shear strain as

$$S_{12} = S_{21} = \frac{1}{2}u_{1,2} \quad (3.3)$$

and

$$S_{13} = S_{31} = \frac{1}{2}u_{1,3}. \quad (3.4)$$

However, from equation (3.1) we see that  $u_1$  is not a function of  $x_3$ , thus only the strain components that must be considered are  $S_{12}$  and  $S_{21}$ .

Rewriting equation (2.19) for simple  $x_1$ -thickness-shear modes in AT-cut quartz (Table 3), and applying the transformations in Table 1, yields

$$\begin{aligned} T_{21} = T_{12} &= c_{66}S_{12} + c_{66}S_{21} - e_{16}E_1 - e_{26}E_2 - e_{36}E_3 \\ &= 2c_{66}S_{12} - e_{16}E_1 - e_{26}E_2 - e_{36}E_3 \end{aligned} \quad (3.5)$$

It must be noted that the piezoelectric stress constant  $e_{16}$  is zero in AT-cut quartz (Table 3).

Thus, the shear stress,  $T_{12}$ , is coupled to the electric field components  $E_2$  and  $E_3$  but not the electric field component  $E_1$ . This allows us to disregard the term containing the electric field component  $E_1$ , thus,

$$E_1 = 0. \quad (3.6)$$

Substituting equations (3.3) and (3.4) into equation (3.5) results in

$$T_{12} = c_{66}u_{1,2} - e_{26}E_2 - e_{36}E_3. \quad (3.7)$$

The acoustic energy in an LFE sensor element was found by Pinkham, *et al.* to have a Gaussian distribution in both the  $x_1$  and  $x_3$  directions under the electrodes (Figure 18)[68].

Thus, the plate can be approximated as infinite in the  $x_1$  and  $x_3$  directions, the electric field

components  $E_2$  and  $E_3$  will vary only in the  $x_2$  direction. The electric field components may now be written

$$E_2 = E_2(x_2, t) \quad (3.8)$$

and

$$E_3 = E_3(x_2, t). \quad (3.9)$$

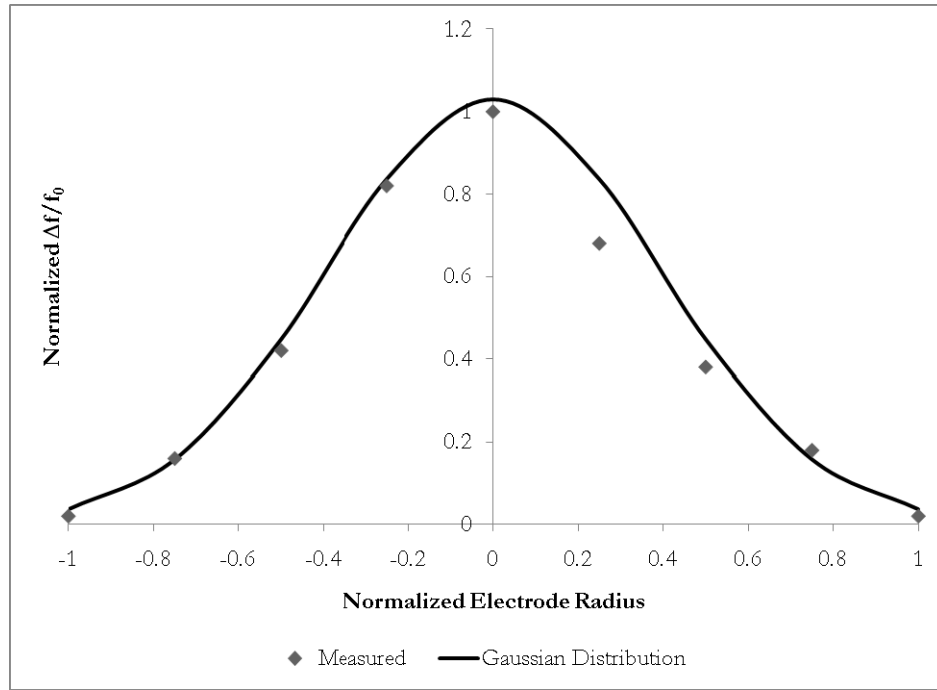


**Figure 18. Acoustic energy of an LFE sensor element under the electrodes in the  $x_1$  and  $x_3$  directions**

Evaluating equation (2.20) for simple  $x_1$ -thickness-shear modes in AT-cut quartz and again applying the transformations in Table 1 and the material constants in Table 3 yields

$$D_1 = 0, \quad (3.10)$$

$$D_2 = e_{26}S_{12} + e_{26}S_{21} + \epsilon_{22}E_2 + \epsilon_{23}E_3 = 2e_{26}S_{12} + \epsilon_{22}E_2 + \epsilon_{23}E_3, \quad (3.11)$$

and

$$D_3 = e_{36}S_{12} + e_{36}S_{21} + \epsilon_{23}E_2 + \epsilon_{33}E_3 = 2e_{36}S_{12} + \epsilon_{23}E_2 + \epsilon_{33}E_3. \quad (3.12)$$

Substituting equation (3.3) into equations (3.10) and (3.12) results in

$$D_2 = e_{26}u_{1,2} + \epsilon_{22}E_2 + \epsilon_{23}E_3, \quad (3.13)$$

and

$$D_3 = e_{36}u_{1,2} + \epsilon_{23}E_2 + \epsilon_{33}E_3. \quad (3.14)$$

It is informative to look more closely at the physics of the propagating wave in the crystal [69]. The assumption is that the electrode configuration shown in Figure 17 results in a driving electric field,  $E_3$ , in the crystal. It will further be assumed that the driving electric field is uniform through the thickness of the crystal. The result is that the LFE sensor element can be treated as an AT-cut quartz plate with the electrodes on the side of the plate (Figure 19).

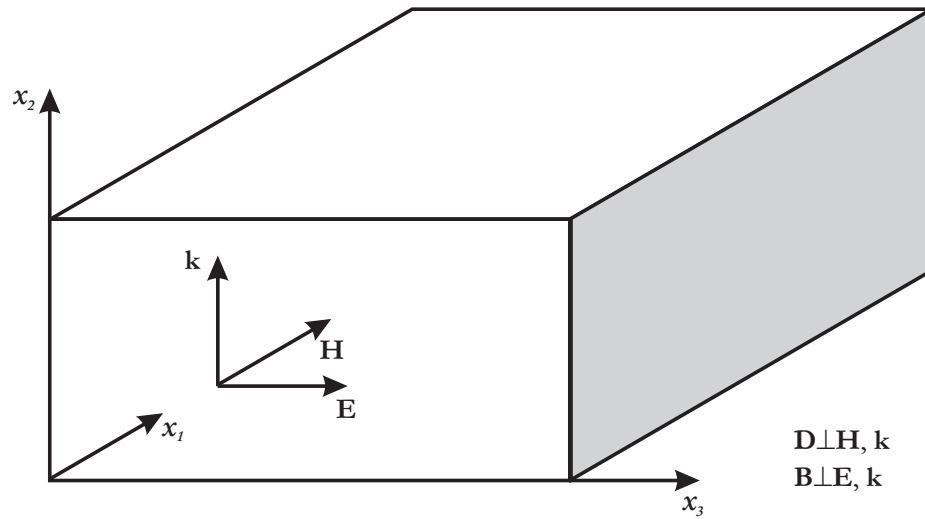


**Figure 19. Propagation of a plane harmonic electromagnetic wave in quartz – the shaded region is the LFE electrode.**

Maxwell's equations in differential form are

$$\nabla \times \mathbf{H} = \dot{\mathbf{D}} \quad (3.15)$$

and



$$\nabla \times \mathbf{E} = -\dot{\mathbf{B}}. \quad (3.16)$$

Expanding the curl in equations (3.15) and (3.16) yields

$$\left( \frac{\partial H_3}{\partial x_2} - \frac{\partial H_2}{\partial x_3} \right) \hat{\mathbf{i}} + \left( \frac{\partial H_1}{\partial x_3} - \frac{\partial H_3}{\partial x_1} \right) \hat{\mathbf{j}} + \left( \frac{\partial H_2}{\partial x_1} - \frac{\partial H_1}{\partial x_2} \right) \hat{\mathbf{k}} = \omega (D_1 \hat{\mathbf{i}} + D_2 \hat{\mathbf{j}} + D_3 \hat{\mathbf{k}}) \quad (3.17)$$

and

$$\left( \frac{\partial E_3}{\partial x_2} - \frac{\partial E_2}{\partial x_3} \right) \hat{\mathbf{i}} + \left( \frac{\partial E_1}{\partial x_3} - \frac{\partial E_3}{\partial x_1} \right) \hat{\mathbf{j}} + \left( \frac{\partial E_2}{\partial x_1} - \frac{\partial E_1}{\partial x_2} \right) \hat{\mathbf{k}} = -\omega (B_1 \hat{\mathbf{i}} + B_2 \hat{\mathbf{j}} + B_3 \hat{\mathbf{k}}). \quad (3.18)$$

Equating the  $\hat{\mathbf{i}}$ ,  $\hat{\mathbf{j}}$ , and  $\hat{\mathbf{k}}$  components for  $\mathbf{D}$  and  $\mathbf{H}$  in equation (3.17) and for  $\mathbf{B}$  and  $\mathbf{E}$  in equation (3.18) reveals that  $\mathbf{D} \perp \mathbf{H}$  and  $\mathbf{B} \perp \mathbf{E}$ , *e.g.* in equation (3.17),

$$\frac{\partial H_k}{\partial x_2} - \frac{\partial H_j}{\partial x_3} = \omega D_i, \quad (3.19)$$

for arbitrary components  $i$ ,  $j$ , and  $k$ . Furthermore, since quartz is nonmagnetic,  $\mathbf{B} = \mu_0 \mathbf{H}$  and therefore,  $\mathbf{H}$  is parallel to  $\mathbf{B}$ .

Considering plane harmonic waves with the form  $e^{j(\omega t - \mathbf{k} \cdot \mathbf{x})}$ , where  $\mathbf{k}$  is the propagation vector, the spatial derivatives in equations (3.17) and (3.18) can be evaluated,

$$(k_3 H_2 - k_2 H_3) \hat{\mathbf{i}} + (k_1 H_3 - k_3 H_1) \hat{\mathbf{j}} + (k_2 H_1 - k_1 H_2) \hat{\mathbf{k}} = \omega (D_1 \hat{\mathbf{i}} + D_2 \hat{\mathbf{j}} + D_3 \hat{\mathbf{k}}) \quad (3.20)$$

and

$$(k_3 E_2 - k_2 E_3) \hat{\mathbf{i}} + (k_1 E_3 - k_3 E_1) \hat{\mathbf{j}} + (k_2 E_1 - k_1 E_2) \hat{\mathbf{k}} = -\omega (B_1 \hat{\mathbf{i}} + B_2 \hat{\mathbf{j}} + B_3 \hat{\mathbf{k}}). \quad (3.21)$$

The left-hand side of equations (3.20) and (3.21) are seen to be the negative curl of  $\mathbf{k}$  and  $\mathbf{H}$  and  $\mathbf{k}$  and  $\mathbf{E}$ , respectively. Equations (3.20) and (3.21) are then rewritten as

$$\mathbf{k} \times \mathbf{H} = -\omega \mathbf{D} \quad (3.22)$$

and

$$\mathbf{k} \times \mathbf{E} = \omega \mathbf{B}. \quad (3.23)$$

Equations (3.22)-(3.23) show that  $\mathbf{D} \perp \mathbf{k}$  and  $\mathbf{B} \perp \mathbf{k}$ . Given that the propagation of the thickness-shear mode,  $\mathbf{k}$ , is in the  $x_2$  direction and the driving electric field is in the  $x_3$  direction, then, from equation (3.23),  $\mathbf{H}$  must be oriented in the  $x_1$  direction. Thus, from equations (3.10), ( $D_1 = 0$ ), and (3.22),  $\mathbf{D}$  has only an  $x_3$  component in the crystal and  $D_2 = 0$ .

Equation (3.13) becomes

$$e_{26}u_{1,2} + \varepsilon_{22}E_2 + \varepsilon_{23}E_3 = 0, \quad (3.24)$$

Solving equation (3.24) for  $E_2$  yields

$$E_2 = -\frac{e_{26}}{\varepsilon_{22}}u_{1,2} - \frac{\varepsilon_{23}}{\varepsilon_{22}}E_3. \quad (3.25)$$

Substituting equation (3.25) into equations (3.7) and (3.14) results in

$$T_{12} = \bar{c}_{66}u_{1,2} - \bar{e}_{36}E_3 \quad (3.26)$$

and

$$D_3 = \bar{e}_{36}u_{1,2} + \bar{\varepsilon}_{33}E_3, \quad (3.27)$$

where

$$\bar{e}_{36} = e_{36} \left( 1 - \frac{\varepsilon_{23}e_{26}}{\varepsilon_{22}e_{36}} \right) \quad (3.28)$$

and

$$\bar{\varepsilon}_{33} = \varepsilon_{33} \left( 1 - \frac{\varepsilon_{23}^2}{\varepsilon_{22}\varepsilon_{33}} \right). \quad (3.29)$$

Rewriting equation (3.16) for the quasistatic approximation results in

$$\nabla \times \mathbf{E} = 0. \quad (3.30)$$

Noting that the acoustic wave is propagating in the  $x_2$  direction and  $E_1 = 0$ , equation (3.30) becomes

$$E_{3,2} = 0. \quad (3.31)$$

Substituting equation (3.26) into equation (2.33), performing the indicated differentiation, and substituting equation (3.31) into the resulting equation yields

$$\bar{c}_{66}u_{1,22} + \rho\omega^2u_1 = 0. \quad (3.32)$$

The standing wave solution for equation (3.32) is

$$u_1 = \left( L_1 e^{j\bar{k}x_2} + L_2 e^{-j\bar{k}x_2} \right) e^{j\omega t}, \quad (3.33)$$

where  $L_1$  and  $L_2$  are amplitude constants found by applying the appropriate boundary conditions and

$$\bar{k} = \omega \sqrt{\frac{\rho}{\bar{c}_{66}}} \quad (3.34)$$

and is defined as the LFE propagation constant.

### 3.2.2. Boundary Conditions

#### 3.2.2.1. Mechanical Boundary Conditions

The first boundary condition from chapter 2.4. is that the particle displacement is continuous at the boundary between the quartz and the contacting liquid,  $(u_1(h^-) = u_1(h^+))$ .

The particle displacement in the quartz crystal is determined from equation (3.33). The particle displacement in an isotropic, Newtonian liquid can be found by substituting equation (2.11) into (2.9), yielding

$$T_{12} = \eta_l \dot{u}_{1,2} = \eta_l v_{1,2}, \quad (3.35)$$

where  $\eta_l$  is the bulk viscosity of the liquid,  $v = \partial u / \partial t$ , and the elastic stiffness,  $c$ , of a Newtonian liquid is zero [60]. The stress equation of motion for the shear stress is, from equation (2.10),

$$T_{12,2} = \rho_l \ddot{u}_1, \quad (3.36)$$

where  $\rho_l$  is the bulk density of the liquid. Taking the derivative of equation (3.35) with respect to  $x_2$  and substituting into (3.36), yields

$$\eta_l v_{1,22} = \rho_l \ddot{u}_1. \quad (3.37)$$

Equation (3.37) is the Navier-Stokes equation for one-dimensional plane-parallel flow [43], rewritten as follows,

$$\eta_l \frac{\partial^2 v_1}{\partial x_2^2} = \rho_l \dot{v}_1 = \rho_l \ddot{u}_1, \quad (3.38)$$

where and, respectively. The solution to equation (3.38) at the sensor/liquid interface is [70]

$$v_1 = L_3 e^{-\gamma(x_2-h)} e^{j\omega t} \quad (3.39)$$

where  $L_3$  is an amplitude constant determined by applying the appropriate boundary conditions and  $\gamma$  is a complex decay constant for the liquid velocity field. We can see only the root containing the positive real part satisfies the condition that  $v_1 \rightarrow 0$  as  $x_2 \rightarrow \infty$  [43].

Substituting equation (3.39) into equation (3.38) results in

$$\gamma = \sqrt{\frac{\omega \rho_l}{2\eta_l}} (1 + j). \quad (3.40)$$

The particle displacement in the liquid at the solid/liquid interface is obtained by integrating equation (3.39) with respect to time and satisfying the condition that  $u_1 \rightarrow 0$  as  $x_2 \rightarrow \infty$

$$u_1 = -j \frac{L_3}{\omega} e^{-\gamma(x_2-h)} e^{j\omega t}. \quad (3.41)$$

Equating equations (3.33) and (3.41) at  $x_2 = h$ , the first boundary condition is

$$L_1 e^{j\bar{k}h} + L_2 e^{-j\bar{k}h} = -j \frac{L_3}{\omega}. \quad (3.42)$$

Rearranging equation (3.42) yields

$$L_1 e^{j\bar{k}h} + L_2 e^{-j\bar{k}h} + j \frac{L_3}{\omega} = 0. \quad (3.43)$$

The second boundary condition is that the shear stress, ( $T_{21} = T_{12}$ ), at the solid/liquid interface is continuous, ( $T_{12}(h^-) = T_{12}(h^+)$ ). The shear stress on the solid side of the interface,  $T_{12}(h^-)$ , is found by substituting equation (3.33) into equation (3.26)

$$T_{12}(h^-) = \left( j\bar{k}\bar{c}_{66} (L_1 e^{j\bar{k}h} - L_2 e^{-j\bar{k}h}) - \bar{e}_{36} E_3 \right) e^{j\omega t}. \quad (3.44)$$

In fluid dynamics, shear stress in fluids,  $T_{12}$ , is defined [71] to be

$$T_{12} = \eta_l \frac{\partial v_1}{\partial x_2}. \quad (3.45)$$

The shear stress,  $T_{12}(h^+)$ , exerted on the sensing surface by the liquid is obtained by substituting equation (3.39) into equation (3.45) and evaluating the derivative at  $x_2 = h$ , resulting in

$$T_{12}(h^+) = -\eta_l \gamma L_3 e^{j\omega t}. \quad (3.46)$$

Equating the shear stresses in the liquid, (equation (3.46)), and solid, (equation (3.44)) at the boundary  $x_2 = h$ , yields

$$j\bar{k}\bar{c}_{66} (L_1 e^{j\bar{k}h} - L_2 e^{-j\bar{k}h}) + \eta_l \gamma L_3 = \bar{e}_{36} E_3. \quad (3.47)$$

The third boundary condition is that the shear stress at the reference surface,  $T_{12}(0)$ , is zero. Substituting equation (3.33) into equation (3.26) and evaluating at  $x_2 = 0$  results in

$$j\bar{k}\bar{c}_{66} (L_1 - L_2) = \bar{e}_{36} E_3. \quad (3.48)$$

The three mechanical boundary conditions, equations (3.43), (3.47), and (3.48) can be arranged in matrix form as follows,

$$\begin{bmatrix} e^{j\bar{k}h} & e^{-j\bar{k}h} & \frac{j}{\omega} \\ j\bar{k}\bar{c}_{66}e^{j\bar{k}h} & -j\bar{k}\bar{c}_{66}e^{-j\bar{k}h} & \eta_1\gamma \\ j\bar{k}\bar{c}_{66} & -j\bar{k}\bar{c}_{66} & 0 \end{bmatrix} \begin{bmatrix} L_1 \\ L_2 \\ L_3 \end{bmatrix} = \begin{bmatrix} 0 \\ \bar{e}_{36}E_3 \\ \bar{e}_{36}E_3 \end{bmatrix}. \quad (3.49)$$

Solving for  $L_1$ ,  $L_2$ , and  $L_3$  yields

$$L_1 = -j \frac{\bar{e}_{36}}{\bar{k}\bar{c}_{66}} \frac{\eta_1\gamma\omega e^{-j\bar{k}h} + \bar{k}\bar{c}_{66}(1 - e^{-j\bar{k}h})}{\eta_1\gamma\omega(e^{j\bar{k}h} + e^{-j\bar{k}h}) + \bar{k}\bar{c}_{66}(e^{j\bar{k}h} - e^{-j\bar{k}h})} E_3, \quad (3.50)$$

$$L_2 = -j \frac{\bar{e}_{36}}{\bar{k}\bar{c}_{66}} \frac{-\eta_1\gamma\omega e^{j\bar{k}h} + \bar{k}\bar{c}_{66}(1 - e^{j\bar{k}h})}{\eta_1\gamma\omega(e^{j\bar{k}h} + e^{-j\bar{k}h}) + \bar{k}\bar{c}_{66}(e^{j\bar{k}h} - e^{-j\bar{k}h})} E_3, \quad (3.51)$$

and

$$L_3 = \omega\bar{e}_{36} \frac{e^{j\bar{k}h} + e^{-j\bar{k}h} - 2}{\eta_1\gamma\omega(e^{j\bar{k}h} + e^{-j\bar{k}h}) + \bar{k}\bar{c}_{66}(e^{j\bar{k}h} - e^{-j\bar{k}h})} E_3. \quad (3.52)$$

### 3.2.2.2. Electrical Boundary Conditions

In evaluating lateral-field excited BAW resonators with both electrodes on the reference surface, (Figure 17), it is assumed that the driving electrical field,  $E_3$ , is parallel to the major surfaces of the AT-cut quartz plate [6, 27-29, 32-35, 61]. Thus, for analyzing the electrical boundary conditions it is assumed that the effective geometry of the LFE sensor element in Figure 17 is two electrodes on the side of the plate, separated by the gap width,  $w$  (Figure 20). It is assumed that the driving electric field,  $E_3$ , is constant in the  $x_2$  direction and that the thickness of the plate is small compared with the other dimensions. The assumptions that the driving electric field is parallel to the major surfaces of the plate and that the thickness of the plate is small are contradictory. This is because fringing electric

fields will arise if the thickness of the crystal is small [63]. However, this provides us with a first-order approximation for the admittance of the LFE sensor element.

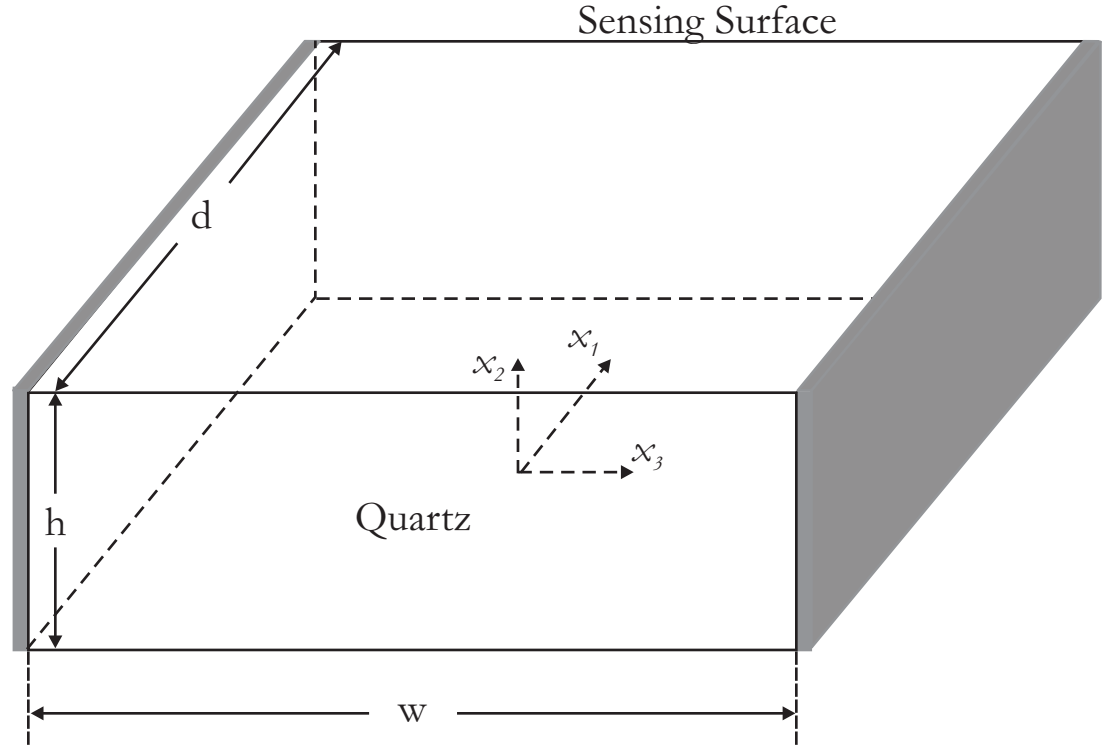


**Figure 20. Configuration of LFE resonator for analysis of equivalent circuit with shaded regions representing a virtual electrode through the thickness of the quartz disc. The origin of the coordinate system is centered on the bottom surface of the quartz plate.**

Close examination of the equations characterizing the LFE thickness-shear mode reveals that in addition to the applied electric field,  $E_3$ , there is also an electric field component in the thickness direction,  $E_2$ , (equation (3.25)). Using the quasistatic approximation and substituting equation ((2.23)) into equation (3.25), yields

$$\phi_{,2} + \frac{\varepsilon_{23}}{\varepsilon_{22}} \phi_{,3} = \frac{e_{26}}{\varepsilon_{22}} u_{1,2}. \quad (3.53)$$

Thus, the scalar potential,  $\phi$ , is clearly a function of both  $x_2$  and  $x_3$ . Additionally, the quasistatic approximation results in an irrotational electric field as given in equation (3.31).

Qualitatively, this means that the applied electric field,  $E_3$ , is constant in the  $x_3$  direction and does not vary along the  $x_2$  axis, validating our earlier assumption regarding the driving electric field being parallel to the major plate surfaces. Thus, we may express  $E_3$  as a function of time only, where

$$E_3 = E_0 e^{j\omega t}. \quad (3.54)$$

In order to solve the partial differential equation (3.53), a solution for the scalar potential is assumed. Since the thickness shear mode is an acoustic standing wave that is piezoelectrically coupled to the applied electric field the solution for the scalar potential must contain a sinusoidal term, proportional to the particle displacement,  $u_1$ . Furthermore, the scalar potential is a function of both  $x_2$  and  $x_3$ , yet must satisfy equation (3.31). Given these constraints the scalar potential is expressed as

$$\phi = \frac{e_{26}}{\epsilon_{22}} u_1 + L_4 x_2 + L_5 x_3, \quad (3.55)$$

where  $L_4$  and  $L_5$  are constants of integration. Substituting equation (3.54) into equation ((2.23)) yields

$$\phi_{,3} = E_0 e^{j\omega t}. \quad (3.56)$$

Taking the derivative of equation (3.55) with respect to  $x_3$  and substituting into equation (3.56), one obtains

$$L_5 = E_0 e^{j\omega t}. \quad (3.57)$$

Next, substituting equation (3.57) into equation (3.55) and then into equation (3.53) yields

$$\frac{e_{26}}{\epsilon_{22}} u_{1,2} + L_4 + \frac{\epsilon_{23}}{\epsilon_{22}} E_0 e^{j\omega t} = \frac{e_{26}}{\epsilon_{22}} u_{1,2}. \quad (3.58)$$

Equation (3.58) is rearranged to solve for  $L_4$  as follows,



$$L_4 = -\frac{\varepsilon_{23}}{\varepsilon_{22}} E_0 e^{j\omega t}. \quad (3.59)$$

Substituting equations (3.57) and (3.59) into equation (3.55) gives the scalar potential as

$$\phi = \frac{e_{26}}{\varepsilon_{22}} u_1 - \frac{\varepsilon_{23}}{\varepsilon_{22}} E_0 e^{j\omega t} x_2 + E_0 e^{j\omega t} x_3. \quad (3.60)$$

The fourth boundary condition is that the scalar potential at the liquid/air interface vanishes. This boundary condition holds as long as the liquid layer thickness,  $h'$ , is greater than the decay length of the potential. Mathematically, this boundary condition is expressed  $\phi(h + h') = 0$ .

In order to evaluate the fourth boundary condition, further information about electric charges in the liquid is necessary. When the sensing surface of the LFE sensor is loaded with an electrolyte solution, the electric field of the thickness shear mode interacts with ions and dipoles in solution [72, 73]. This interaction results in the reorientation of ions and dipoles in solution and determines the electric potential in the liquid.

In general, the electric potential at a point in an electrolyte solution can be found using Poisson's equation,

$$\nabla^2 \phi_l = 4\pi\rho_e / \varepsilon_l, \quad (3.61)$$

where  $\rho_e$  is the net electric charge density and  $\varepsilon_l$  is the permittivity of the solution. Using the approach of Josse, *et al.* [73], Poisson's equation can be modified using the Debye-Hückel theory [74] such that

$$\nabla^2 \phi_l = \kappa^2 \phi_l, \quad (3.62)$$

where  $1/\kappa$  is commonly referred to as the ion atmosphere radius.

The Debye-Hückel theory accounts for the strength and long range of the coulombic interactions between ions in solution [75]. Poisson's equation assumes that the electric

charge is uniformly distributed in the solution. However, due to the attraction between opposite charges, anions are surrounded by a sphere of cations, and cations are surrounded by a sphere of anions. When averaged over time, more oppositely charged ions pass by a given ion than like charged ions. This results in a spherical ionic atmosphere, with a radius  $1/\kappa$ , of oppositely charged ions around the central ion, that is equal in magnitude but opposite in charge [75].

For the geometry shown in Figure 20 the potential in the solution will only vary from a distance normal to the charge at a point on the sensor surface [74]. Thus, the solution to equation (3.62) is

$$\phi_1 = \phi(h)e^{-\kappa x_2}. \quad (3.63)$$

A linear approximation for the exponential decay in equation (3.63) specific to the thickness-shear mode in an AT-cut quartz plate [73] is

$$\phi_1 = \phi_1 x_2 + \phi_2, \quad (3.64)$$

where  $\phi_1$  and  $\phi_2$  will be determined by applying the boundary conditions for the LFE sensor element.

When the ions in solution reorient with the time-varying electric field, an electric double layer occurs in the solution, where there is a layer of charge localized at the surface of the LFE sensor element and a second diffuse layer of charge extending into the bulk of the solution. The thickness of the double layer is  $1/\kappa$ , which is on the order of  $\mu\text{m}$  [74]. In the absence of electric charge, it is assumed that the surface potential decays into the liquid with an attenuation factor of  $e^{-\frac{2\pi}{\lambda}x_2}$ . Thus, the decay length of the surface potential into the liquid is  $\lambda/2\pi$ , which is about 0.1 mm for LFE sensor elements operating at  $\sim 5$  MHz. Since the thickness of the double layer is much less than the decay length of the surface

potential in the absence of electrical charge, the redistribution of charge in the double layer blocks the electric field from penetrating the bulk liquid [72, 73].

However, if the radial frequency,  $\omega$ , of the LFE sensor element exceeds the dielectric relaxation frequency of the solution,  $\omega_r$ , then the electric charge at the interface can not redistribute quickly enough and the electric field penetrates into the bulk of the liquid. The redistribution of ions in solution occurs at  $\omega_r$  and is mathematically defined as [72, 73]

$$\omega_r = \frac{\sigma_l}{\varepsilon_l + \varepsilon_{23}}, \quad (3.65)$$

where  $\sigma_l$  and  $\varepsilon_l$  are the bulk conductivity and bulk permittivity, respectively, of the solution and  $\varepsilon_{23}$  is from the permittivity,  $[\varepsilon]$ , of the AT-quartz (Table 3). Thus, when  $\omega > \omega_r$ , the electric field will interact with the bulk electrical properties of the liquid with a decay length of  $\lambda/2\pi$ .

Evaluating equation (3.64) for the fourth boundary condition, which states that the surface potential vanishes at the air/liquid interface, results in

$$\phi_1(h + h') + \phi_2 = 0. \quad (3.66)$$

Next, solving for  $\phi_2$

$$\phi_2 = -\phi_1(h + h'). \quad (3.67)$$

Substituting equation (3.67) into (3.64) gives us

$$\phi_l = \phi_1(x_2 - h - h'). \quad (3.68)$$

The fifth boundary condition is the continuity of potential at the liquid/quartz interface,  $\phi_l(h) = \phi(h)$ . When operating an LFE resonator in air, the assumption is that the electric field normal to the  $x_1 - x_3$  plane,  $E_2$ , does not extend beyond the boundaries of the

crystal because the electric displacement normal to the surface,  $D_2$ , is zero. Mindlin [67] and Lee [61] have shown that in air there is a small amount of electromagnetic radiation outside of the crystal. However, when the LFE sensor element is exposed to an electrolyte solution, the electric field,  $E_2$ , interacts both with any ions in solution and capacitively couples with the dielectric liquid. This coupling of the thickness-shear mode with the liquid results in a surface charge at the interface and a potential that varies in both the  $x_2$  and  $x_3$  directions [72], since  $E_2$  and  $E_3$  for the thickness shear mode are finite.

Expressions have been derived for both the electric potential in the quartz substrate, (equation (3.60)), and in the liquid, (equation (3.68)). Since the surface potential decays only in the  $x_2$  direction, we are only concerned with the electric displacement normal to the quartz/liquid interface,  $D_2$ , and can ignore the  $x_3$  term in equation (3.60). The fifth boundary condition is written by substituting equation (3.33) into (3.60), substituting the resulting equation into (3.68) and evaluating at  $x_2 = h$ , as follows

$$-\phi_1 h' = \frac{e_{26}}{\epsilon_{22}} \left( L_1 e^{j\bar{k}h} + L_2 e^{-j\bar{k}h} \right) e^{j\omega t} - \frac{\epsilon_{23}}{\epsilon_{22}} E_0 e^{j\omega t} h. \quad (3.69)$$

Solving for  $\phi_1$  results in

$$\phi_1 = \frac{-1}{h'} \left[ \frac{e_{26}}{\epsilon_{22}} \left( L_1 e^{j\bar{k}h} + L_2 e^{-j\bar{k}h} \right) - \frac{\epsilon_{23}}{\epsilon_{22}} E_0 h \right] e^{j\omega t}. \quad (3.70)$$

The sixth boundary condition is  $D_2^{(l)}(h) - D_2(h) = \rho_s$ , where  $\rho_s$  is the surface charge density on the quartz/liquid interface. Already knowing that  $D_2 = 0$  in the quartz crystal, the boundary condition becomes  $D_2^{(l)}(h^+) = \rho_s$ .

In the liquid the electrical displacement,  $D_2^{(l)}$ , is [73]

$$D_2^{(l)} = -\varepsilon_l^* \frac{\partial \phi_l}{\partial x_2}, \quad (3.71)$$

where

$$\varepsilon_l^* = \frac{\sigma_l}{j\omega} + \varepsilon_l. \quad (3.72)$$

Substituting equation (3.70) into equation (3.68) and then substituting equation (3.68) into (3.71) yields

$$D_2^{(l)} = \frac{\varepsilon_l'}{h'} \left[ \frac{e_{26}}{\varepsilon_{22}} (L_1 e^{j\bar{k}h} + L_2 e^{-j\bar{k}h}) - \frac{\varepsilon_{23}}{\varepsilon_{22}} E_0 h \right] e^{j\omega t} = \rho_s. \quad (3.73)$$

### 3.2.2.3. Summary of Boundary Conditions

Six boundary conditions have been applied to solve for the thickness shear mode in an LFE sensor element. Three of the boundary conditions are applied to the mechanical properties of the system and three of the boundary conditions are applied to the electrical properties of the system. The six unknowns that were solved as a result of the boundary conditions are,  $L_1$ ,  $L_2$ ,  $L_3$ ,  $\phi_1$ ,  $\phi_2$ , and  $\rho_s$ .

### 3.2.3. Admittance of the LFE Sensor Element

Admittance,  $Y$ , is simply the ratio of current,  $I$ , to the voltage,  $V$ . Thus, the first step in determining the admittance of the LFE sensor element is to calculate the current between the plates (Figure 20). The surface charge on the electrode of a thickness-field excited resonator is [65]

$$Q_1 = \int_A D_3 \Big|_{x_3=-w/2} dA, \quad (3.74)$$

where  $A$  is the surface area of the electrode in the  $x_1$ - $x_2$  plane (Figure 20). Substituting equations (3.33) and (3.54) into equation (3.27), one obtains

$$D_3 = \left( \bar{\epsilon}_{36} \frac{\partial}{\partial x_2} (L_1 e^{j\bar{k}x_2} + L_2 e^{-j\bar{k}x_2}) + \bar{\epsilon}_{33} E_0 \right) e^{j\omega t}. \quad (3.75)$$

Substituting equation (3.75) into (3.74) yields an expression for  $Q_1$

$$\begin{aligned} Q_1 &= d e^{j\omega t} \int_0^h \left( \bar{\epsilon}_{36} \frac{\partial}{\partial x_2} (L_1 e^{j\bar{k}x_2} + L_2 e^{-j\bar{k}x_2}) + \bar{\epsilon}_{33} E_0 \right) dx_2 \\ &= d e^{j\omega t} \left( \bar{\epsilon}_{36} \left( L_1 e^{j\bar{k}x_2} \Big|_0^h + L_2 e^{-j\bar{k}x_2} \Big|_0^h \right) + \bar{\epsilon}_{33} E_0 x_2 \Big|_0^h \right), \\ &= d \left[ \bar{\epsilon}_{36} (L_1 (e^{j\bar{k}h} - 1) + L_2 (e^{-j\bar{k}h} - 1)) + \bar{\epsilon}_{33} E_0 h \right] e^{j\omega t} \end{aligned} \quad (3.76)$$

where  $d$  is the width of the electrode (Figure 20).

Now an expression for the current in the quartz plate can be found by taking the derivative of equation (3.76) with respect to time,

$$I_1 = \frac{\partial Q_1}{\partial t} = j\omega d \left[ \bar{\epsilon}_{36} (L_1 (e^{j\bar{k}h} - 1) + L_2 (e^{-j\bar{k}h} - 1)) + \bar{\epsilon}_{33} E_0 h \right] e^{j\omega t}. \quad (3.77)$$

The interaction of the LFE thickness-shear mode with the contacting liquid will result in both conduction current due to the drift of ions in the solution and a displacement current due to the dipolar response of the solution. Finding the total charge on the sensing surface from equation (3.73)

$$Q_2 = \rho_3 wd = \frac{wd\epsilon_l^*}{h'} \left[ \frac{\epsilon_{26}}{\epsilon_{22}} (L_1 e^{j\bar{k}h} + L_2 e^{-j\bar{k}h}) - \frac{\epsilon_{23}}{\epsilon_{22}} E_0 h \right] e^{j\omega t}, \quad (3.78)$$

and

$$I_2 = \frac{\partial Q_2}{\partial t} = \frac{j\omega wd\epsilon_l^*}{h'} \left[ \frac{\epsilon_{26}}{\epsilon_{22}} (L_1 e^{j\bar{k}h} + L_2 e^{-j\bar{k}h}) - \frac{\epsilon_{23}}{\epsilon_{22}} E_0 h \right] e^{j\omega t}. \quad (3.79)$$

The two currents are shown in Figure 21. Qualitatively, one can see that the total current between the electrodes is the parallel combination of the current in the quartz plate,  $I_1$ , and the current in the liquid,  $I_2$ . The applied voltage,  $V$ , between the plates is  $E_0 e^{j\omega t} w$ , thus  $Y = (I_1 + I_2)/V$  and

$$Y = \frac{j\omega d}{E_0 w} \times \left[ \bar{e}_{36} (L_1 (e^{j\psi} - 1) + L_2 (e^{-j\psi} - 1)) + \bar{\epsilon}_{33} E_0 h \right], \quad (3.80)$$

$$\times \left[ + \frac{w \epsilon_1^*}{h'} \left( \frac{e_{26}}{\epsilon_{22}} (L_1 e^{j\psi} + L_2 e^{-j\psi}) - \frac{\epsilon_{23}}{\epsilon_{22}} E_0 h \right) \right]$$

where

$$\psi = \bar{k} h. \quad (3.81)$$

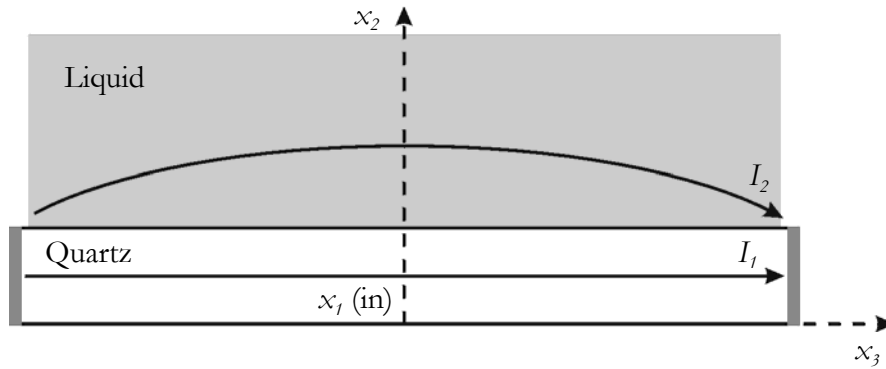


**Figure 21.** The total current between the electrodes is the parallel combination of the current in the quartz plate,  $I_1$ , and the current in the contacting liquid,  $I_2$

### 3.3. Equivalent circuit model

Examination of equation (3.80) reveals that the admittance of the liquid-loaded LFE sensor element contains six terms. The admittance is expressed as the sum of the six terms where

$$Y = \sum_{i=1}^6 Y_i \quad (3.82)$$

Substituting equations (3.50) and (3.51) into equation (3.80) the admittance terms  $Y_1 - Y_6$  can be expressed by

$$Y_1 = \frac{\omega d \bar{e}_{36}^2}{w \bar{k} \bar{c}_{66}} \left[ \frac{\eta_l \gamma \omega (1 - e^{-j\psi}) + \bar{k} \bar{c}_{66} (e^{j\psi} + e^{-j\psi} - 2)}{\eta_l \gamma \omega (e^{j\psi} + e^{-j\psi}) + \bar{k} \bar{c}_{66} (e^{j\psi} - e^{-j\psi})} \right], \quad (3.83)$$

$$Y_2 = \frac{\omega d \bar{e}_{36}^2}{w \bar{k} \bar{c}_{66}} \left[ \frac{-\eta_l \gamma \omega (1 - e^{j\psi}) + \bar{k} \bar{c}_{66} (e^{j\psi} + e^{-j\psi} - 2)}{\eta_l \gamma \omega (e^{j\psi} + e^{-j\psi}) + \bar{k} \bar{c}_{66} (e^{j\psi} - e^{-j\psi})} \right], \quad (3.84)$$

$$Y_3 = j\omega \frac{dh \bar{\varepsilon}_{33}}{w}, \quad (3.85)$$

$$Y_4 = \frac{\omega d \varepsilon_l^* \bar{e}_{36} e_{26}}{h' \varepsilon_{22} \bar{k} \bar{c}_{66}} \left[ \frac{\eta_l \gamma \omega + \bar{k} \bar{c}_{66} (e^{j\psi} - 1)}{\eta_l \gamma \omega (e^{j\psi} + e^{-j\psi}) + \bar{k} \bar{c}_{66} (e^{j\psi} - e^{-j\psi})} \right], \quad (3.86)$$

$$Y_5 = \frac{\omega d \varepsilon_l^* \bar{e}_{36} e_{26}}{h' \varepsilon_{22} \bar{k} \bar{c}_{66}} \left[ \frac{-\eta_l \gamma \omega + \bar{k} \bar{c}_{66} (e^{-j\psi} - 1)}{\eta_l \gamma \omega (e^{j\psi} + e^{-j\psi}) + \bar{k} \bar{c}_{66} (e^{j\psi} - e^{-j\psi})} \right], \quad (3.87)$$

and

$$Y_6 = -j\omega \frac{dh \varepsilon_l^* \varepsilon_{23}}{h' \varepsilon_{22}}. \quad (3.88)$$

Now it is useful to introduce two piezoelectric coupling terms  $K^2$  and  $\bar{K}^2$ , where

$$K^2 = \frac{\bar{e}_{36}^2}{\bar{\varepsilon}_{33} \bar{c}_{66}} \quad (3.89)$$

and

$$\bar{K}^2 = \frac{e_{26} \bar{e}_{36}}{\varepsilon_{23} \bar{c}_{66}}. \quad (3.90)$$

The term  $K^2$  is the coupling factor of the thickness-shear mode to the applied electric field,  $E_3$ , (see appendix A), and the term  $\bar{K}^2$  is defined as the coupling factor of the thickness-shear mode to the induced electric field,  $E_2$ . Energy losses in the quartz caused by the



quartz viscosity,  $\eta$ , are introduced to the LFE sensor element admittance through a complex quartz elasticity term,  $\bar{c}_{66}$  [59], where

$$\bar{c}_{66} = \bar{c}_{66}(1 + j\xi), \quad (3.91)$$

and

$$\xi = \frac{\omega\eta}{\bar{c}_{66}}. \quad (3.92)$$

This energy storage term in the quartz elasticity results in changes to the variables  $\psi$ ,  $K^2$ , and  $\bar{K}^2$ . Thus, new complex variables are introduced

$$\psi'^2 = \frac{\psi^2}{1 + j\xi}, \quad (3.93)$$

$$K'^2 = \frac{K^2}{1 + j\xi}, \quad (3.94)$$

and

$$\bar{K}'^2 = \frac{\bar{K}^2}{1 + j\xi}. \quad (3.95)$$

Close examination of the admittance term  $Y_3$  reveals that it is simply the capacitance between the virtual electrodes along the  $x_3$ -axis. Thus the static capacitance,  $C_0$ , is defined as

$$C_0 = \frac{\bar{\epsilon}_{33}dh}{w}. \quad (3.96)$$

When equations (3.93) and (3.94) are substituted into equations (3.83)-(3.85), and the three terms are combined, the admittance is

$$Y_a = Y_1 + Y_2 + Y_3 = j\omega C_0 \left[ 1 - j \frac{K'^2}{\psi'} \left( \frac{\frac{\eta_l \gamma \omega}{k \bar{c}_{66}} (e^{j\psi'} - e^{-j\psi'}) - 2(2 - e^{j\psi'} - e^{-j\psi'})}{\frac{\eta_l \gamma \omega}{k \bar{c}_{66}} (e^{j\psi'} + e^{-j\psi'}) + (e^{j\psi'} - e^{-j\psi'})} \right) \right]. \quad (3.97)$$

Using Euler's equation, dividing the numerator and denominator of equation (3.97) by  $j\bar{k}\bar{c}_{66}$ , and using trigonometric relations the admittance may be rewritten

$$Y_a = j\omega C_0 \left[ 1 + \frac{K'^2}{\psi'} \left( \frac{\frac{\eta_l \gamma \omega}{j\bar{k}\bar{c}_{66}} + 2 \tan\left(\frac{\psi'}{2}\right)}{\frac{\eta_l \gamma \omega}{j\bar{k}\bar{c}_{66}} \cot \psi' + 1} \right) \right]. \quad (3.98)$$

Note that the properties of the liquid influencing the admittance of the LFE sensor element are contained in a single complex factor. This factor is defined [43] as

$$\Lambda = \sqrt{\frac{\eta_l \omega \rho_l}{2\bar{c}_{66}\rho}} (1 - j). \quad (3.99)$$

Now the admittance  $Y_a$ , in simplified form, is

$$Y_a = j\omega C_0 \left[ 1 + \frac{K'^2}{\psi'} \left( \frac{\Lambda + 2 \tan\left(\frac{\psi'}{2}\right)}{\Lambda \cot \psi' + 1} \right) \right], \quad (3.100)$$

where it can be seen that  $Y_a$  is the static capacitance in parallel with a complex admittance

$Y_\alpha$ , where  $Y_\alpha = 1/Z_\alpha$ . The equivalent circuit for  $Y_a$  is shown in Figure 22.

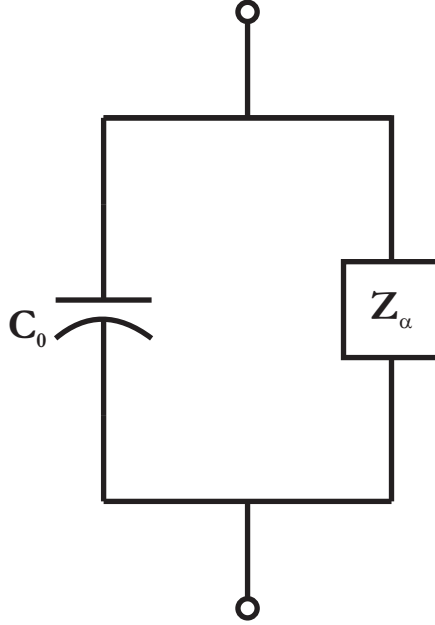


**Figure 22. Equivalent circuit for admittance  $Y_a$**

Examination of equation (3.88) is simplified if we expand the complex permittivity  $\varepsilon'_l$  using equation (3.72). Doing so reveals that the admittance  $Y_6$  is a resistance,  $R_3$ , in parallel with a capacitance,  $C_2$

$$Y_6 = -\left(\frac{1}{R_3} + j\omega C_2\right), \quad (3.101)$$

where

$$R_3 = \frac{\varepsilon_{22}h'}{\varepsilon_{23}dh\sigma_1}, \quad (3.102)$$

and

$$C_2 = \frac{\varepsilon_1\varepsilon_{23}dh}{\varepsilon_{22}h'}. \quad (3.103)$$

Inspection of the circuit parameters  $R_3$  and  $C_2$  reveal that they contain the quartz permittivity ratio,  $\varepsilon_{23}/\varepsilon_{22}$ . This ratio relates the thickness-directed electric field  $E_2$  to the applied electric field  $E_3$  in equation (3.23). Thus, the circuit parameters  $R_3$  and  $C_2$

represent the interaction of the thickness-directed electric field  $E_2$  with the conductivity and permittivity of the contacting liquid at the sensing surface. The negative sign on the admittance  $Y_6$  indicates that the current is flowing in the opposite direction of this branch with reference to the other branches of the equivalent circuit.

Substituting equations (3.93) and (3.95) into equations (3.86)-(3.88) and adding yields

$$Y_b = Y_4 + Y_5 + Y_6 = \left( \frac{1}{R_3} + j\omega C_2 \right) \left[ -j \frac{\bar{K}'^2}{\psi'} \frac{\bar{k}\bar{c}_{66}(e^{j\psi'} + e^{-j\psi'} - 2)}{\eta_1 \gamma \omega (e^{j\psi'} + e^{-j\psi'}) + \bar{k}\bar{c}_{66}(e^{j\psi'} - e^{-j\psi'})} - 1 \right]. \quad (3.104)$$

The admittance is simplified using Euler's equations, some trigonometric identities and substitution of equation (3.99)

$$Y_b = \left( \frac{1}{R_3} + j\omega C_2 \right) \left[ \frac{\bar{K}'^2}{\psi'} \frac{\tan(\psi'/2)}{\Lambda \cot \psi' + 1} - 1 \right]. \quad (3.105)$$

The impedance,  $Z_b$ , can be found by separating the real and imaginary components of equation (3.105), and taking the inverse of the resulting terms as follows,

$$Z_b = Z_\beta + Z_\gamma = \frac{1}{\text{Re}(Y_b)} + \frac{1}{\text{Im}(Y_b)}, \quad (3.106)$$

where

$$Z_\beta = \frac{R_3(\Lambda \cot \psi' + 1)}{(\bar{K}'^2/\psi')\tan(\psi'/2)} \quad (3.107)$$

and

$$Z_\gamma = \frac{-j}{\omega C_2} \frac{(\Lambda \cot \psi' + 1)}{(\bar{K}'^2/\psi')\tan(\psi'/2)}. \quad (3.108)$$

The entire equivalent circuit for the LFE sensor element is shown in Figure 23 with block elements. This configuration is more complex than the standard Butterworth-Van Dyke equivalent circuit in that there are six parallel branches as opposed to two.

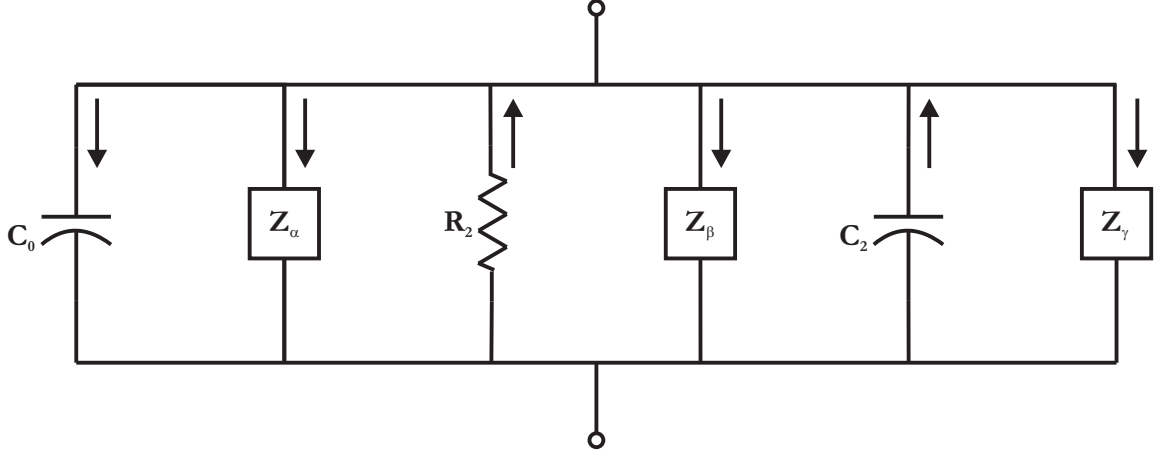


**Figure 23.** Equivalent circuit of LFE sensor element under liquid load. The arrows indicate the direction of electrical current through each branch.

When the LFE sensor element is at resonance, the magnitude of the admittance,  $Y$ , of the LFE sensor element is at its maximum value. The admittance,  $Y$ , is the sum of  $Y_a$ , (equation (3.100)), and  $Y_b$ , (equation (3.105)). Since both  $Y_a$  and  $Y_b$  have the term  $\tan(\psi'/2)$  in the numerator, resonance will occur when  $\psi'$  is about  $n\pi$ , where  $n = 1, 3, 5, \dots$ . The trigonometric functions in equations (3.100) and (3.105) are expanded about the poles as [6, 43]

$$\tan(\psi'/2) \approx \frac{4\psi'}{(n\pi)^2 - \psi'^2} \quad (3.109)$$

and

$$\cot \psi' \approx \frac{-2\psi'}{(n\pi)^2 - \psi'^2}. \quad (3.110)$$

The impedances  $Z_\alpha$ ,  $Z_\beta$ , and  $Z_\gamma$  are approximated by substituting equations (3.109) and (3.110) into equations (3.100), (3.107), and (3.108) and ignoring any terms above the first order of the small quantities  $\Lambda$  and  $(n\pi)^2 - \psi'^2$

$$Z_\alpha = \frac{j}{\omega C_0} \frac{2\psi'\Lambda - (n\pi)^2 + \psi'^2}{8\bar{K}'^2}, \quad (3.111)$$

$$Z_\beta = R_3 \frac{(n\pi)^2 - \psi'^2 - 2\psi'\Lambda}{4\bar{K}'^2}, \quad (3.112)$$

and

$$Z_\gamma = \frac{-j}{\omega C_2} \frac{(n\pi)^2 - \psi'^2 - 2\psi'\Lambda}{4\bar{K}'^2}. \quad (3.113)$$

The maximum electrical admittance occurs at the series resonance of the LFE sensor element, where the phase shift  $\psi$  across the LFE sensor element is  $n\pi$ . Knowing that  $\psi$  is proportional to  $\omega$ , the frequency-dependent form of  $\psi$  is

$$\psi^2(\omega_s) = \left( \frac{\omega}{\omega_s} n\pi \right)^2, \quad (3.114)$$

where  $\omega_s$  is the radial frequency at series resonance of the unperturbed LFE sensor element.

Substituting equation (3.114) into equation (3.93) returns the phase shift  $\psi'$  for a lossy QCM near resonance

$$\psi'^2 = \frac{(n\pi)^2}{1 + j\xi} \left( \frac{\omega}{\omega_s} \right)^2. \quad (3.115)$$

The final step to developing an equivalent circuit for an LFE sensor element under liquid load is to substitute equation (3.115) into equations (3.111)-(3.113). When performing this substitution the expression  $(1 + j\xi)^{1/2}$  is approximately 1 due to the small quantity  $\xi$ . Recall that the factor  $\Lambda$  is complex and is here rewritten  $\Lambda_r - j\Lambda_i$  where  $\Lambda_r = \Lambda_i$  and given in equation (3.99). Equations (3.111)-(3.113) are thus approximated to be

$$Z_\alpha \approx \left( \frac{n\pi\Lambda_i}{4K^2\omega_s C_0} + \frac{(n\pi)^2 \xi}{8K^2\omega C_0} \right) + j\omega \left( \frac{n\pi\Lambda_r}{4K^2\omega_s \omega C_0} + \frac{(n\pi)^2}{8K^2\omega_s^2 C_0} \right) + \frac{1}{j\omega} \frac{(n\pi)^2}{8K^2 C_0}, \quad (3.116)$$

$$Z_\beta \approx \left( \frac{R_3(n\pi)^2}{4\bar{K}^2} - \frac{R_3(n\pi)^2}{4\bar{K}^2} \left( \frac{\omega}{\omega_s} \right)^2 - \frac{R_3 n\pi\Lambda_r \omega}{2\bar{K}^2 \omega_s} \right) + j\omega \left( \frac{R_3(n\pi)^2 \xi}{4\bar{K}^2 \omega} + \frac{R_3 n\pi\Lambda_i}{2\bar{K}^2 \omega_s} \right), \quad (3.117)$$

and

$$Z_\gamma \approx \left( \frac{(n\pi)^2 \xi}{4\bar{K}^2 \omega C_2} + \frac{n\pi\Lambda_i}{2\bar{K}^2 \omega_s C_2} \right) + j\omega \left( \frac{(n\pi)^2}{4\bar{K}^2 \omega_s^2 C_2} + \frac{n\pi\Lambda_r}{2\bar{K}^2 \omega_s \omega C_2} \right) + \frac{1}{j\omega} \frac{(n\pi)^2}{4\bar{K}^2 C_2}. \quad (3.118)$$

Equations (3.116)-(3.118) are rewritten

$$Z_\alpha = (R_1 + R_2) + j\omega(L_1 + L_2) + \frac{1}{j\omega C_1}, \quad (3.119)$$

$$Z_\beta = R_4 + j\omega(L_3 + L_4), \quad (3.120)$$

and

$$Z_\gamma = (R_5 + R_6) + j\omega(L_5 + L_6) + \frac{1}{j\omega C_3}. \quad (3.121)$$

The lumped circuit elements are thus defined for the equivalent circuit in Figure 24,

where

$$C_1 = \frac{8K^2 C_0}{(n\pi)^2}, \quad (3.122)$$

$$L_1 = \frac{1}{\omega_s^2 C_1}, \quad (3.123)$$

$$R_1 = \frac{\eta}{\bar{c}_{66}C_1}, \quad (3.124)$$

$$L_2 = \frac{\omega_s L_1}{n\pi} \sqrt{\frac{2\rho_l \eta_l}{\omega \bar{c}_{66} \rho}}, \quad (3.125)$$

$$R_2 = \frac{\omega_s L_1}{n\pi} \sqrt{\frac{2\omega \rho_l \eta_l}{\bar{c}_{66} \rho}}, \quad (3.126)$$

$$L_3 = \frac{R_3 (n\pi)^2 \eta}{4\bar{K}^2 \bar{c}_{66}}, \quad (3.127)$$

$$L_4 = \frac{R_3 n\pi}{2\bar{K}^2 \omega_s} \sqrt{\frac{\omega \rho_l \eta_l}{2\bar{c}_{66} \rho}}, \quad (3.128)$$

$$R_4 = \frac{R_3 (n\pi)^2}{4\bar{K}^2} \left( 1 - \left( \frac{\omega}{\omega_s} \right)^2 - \frac{\omega}{\omega_s n\pi} \sqrt{\frac{2\omega \rho_l \eta_l}{\bar{c}_{66} \rho}} \right), \quad (3.129)$$

$$C_3 = \frac{4\bar{K}^2 C_2}{(n\pi)^2}, \quad (3.130)$$

$$L_5 = \frac{1}{\omega_s^2 C_3}, \quad (3.131)$$

$$R_5 = \frac{\eta_q}{\bar{c}_{66} C_3}, \quad (3.132)$$

$$L_6 = \frac{\omega_s L_5}{n\pi} \sqrt{\frac{2\rho_l \eta_l}{\omega \bar{c}_{66} \rho_q}}, \quad (3.133)$$

and

$$R_6 = \frac{\omega_s L_5}{n\pi} \sqrt{\frac{2\omega \rho_l \eta_l}{\bar{c}_{66} \rho_q}}. \quad (3.134)$$



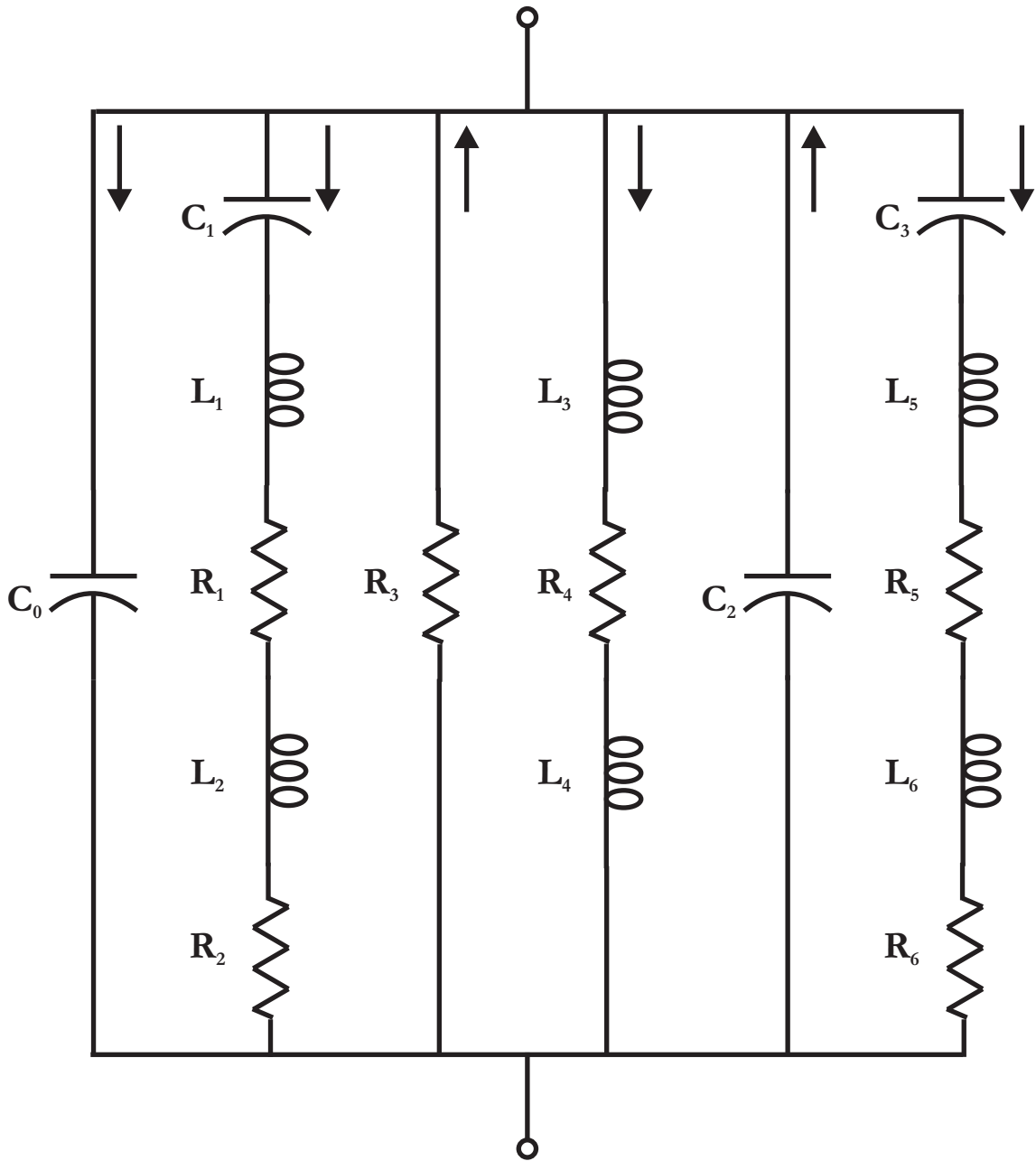


Figure 24. Equivalent circuit with lumped circuit elements for an LFE sensor element under liquid loading. The arrows indicate the direction of electrical current flow through each branch.

A careful examination of the equivalent circuit in Figure 24 and equations (3.122)-(3.134) reveals some similarities with the equivalent circuit for a QCM under liquid and mass loading proposed by Martin, *et al.* [43]. The physical significance of the lumped circuit elements with regard to the mechanical and electrical property changes of the loading liquid is contained in the equivalent circuit.

Examination of the two leftmost branches of the equivalent circuit model for the LFE sensor element (Figure 24) reveals similarity to the model developed by Martin, *et al.* [43]. Indeed, equations (3.96) and (3.122)-(3.126) bear a striking similarity to equations 25 in [43]. The primary differences between the leftmost branches of the circuit model developed here and that in [43] are the LFE coupling constant,  $K^2$ , the static capacitance,  $C_0$ , and the motional resistance,  $R_1$ . Intuitively, it makes sense that the coupling constant and static capacitance are different, in that for the LFE sensor element the thickness shear mode of the resonator is due to an applied electric field,  $E_3$ , directed laterally along the piezoelectric plate, rather than  $E_2$ , directed through the thickness of the piezoelectric plate. The only difference in the motional resistance,  $R_1$ , between the model developed in this work and that in [43] is that their motional resistance includes a factor  $\left(\frac{\omega}{\omega_s}\right)^2$ . However, as was noted

in [43] the error in the admittance magnitude introduced in their model by letting  $\omega = \omega_s$  is less than 0.25% over a 1% bandwidth. Thus, the motional resistances are very nearly the same. The circuit model for the LFE sensor does not contain an inductance for energy storage losses caused by mass loading at the surface, as the LFE sensor element does not have electrodes on the sensing surface, and thus, no mass loading.

The rest of the lumped circuit elements for the equivalent circuit model (Figure 24) are due to the coupling of the thickness shear mode to the induced electric field,  $E_2$ . The physical significance of  $R_3$  and  $C_2$  were discussed earlier in this chapter. The inductances in the fourth branch of the circuit represent energy storage losses due to the viscosity of the quartz,  $L_3$ , and the viscoelastic properties of the contacting liquid,  $L_4$ , caused by the interaction of the induced electric field,  $E_2$ , with conducting ions in the contacting solution. The resistance in the fourth branch of the circuit is complex relating losses due to conductivity in the contacting liquid, changes in the coupling constant,  $\bar{K}^2$ , as the frequency moves from the unperturbed resonance frequency,  $f_s$ , and losses due to viscoelastic properties of the contacting liquid.

Interestingly, the rightmost branch of the model can be thought of as the motional branch caused by the coupling of the induced electric field to the thickness shear mode. Close examination of equations (3.130)-(3.134) to equations (3.122)-(3.126) reveals that they have similar form with the circuit elements in the rightmost branch containing the coupling term  $\bar{K}^2$  and the elements in the second branch from the left containing the coupling term  $K^2$ .

The equivalent circuit in Figure 24 is modeled using the electrode configuration in Figure 20. However, the electrodes are on the reference face of the quartz plate as shown in Figure 17. Thus, the driving electric field, penetrates into the contacting liquid as shown in Figure 25. This interaction of the thickness shear mode with the contacting liquid leads to two additional elements in the equivalent circuit branch,  $Z_2$ . The elements are a capacitance,  $C_l$ , and a resistance,  $R_l$ , expressed as follows,

$$C_l = \frac{\varepsilon_l h_{eff} d}{w}, \quad (3.135)$$

$$R_l = \frac{w}{\sigma_l h_{eff} d}, \quad (3.136)$$

The variable  $h_{eff}$  is the effective penetration depth of the electric field into the bulk liquid.

This effective depth arises because the electrodes are physically on the reference surface (Figure 17) of the LFE sensor element and not on the sides of the quartz plate (Figure 20) as was approximated in the model. The modified equivalent circuit incorporating  $C_l$  and  $R_l$  is given in Figure 26.

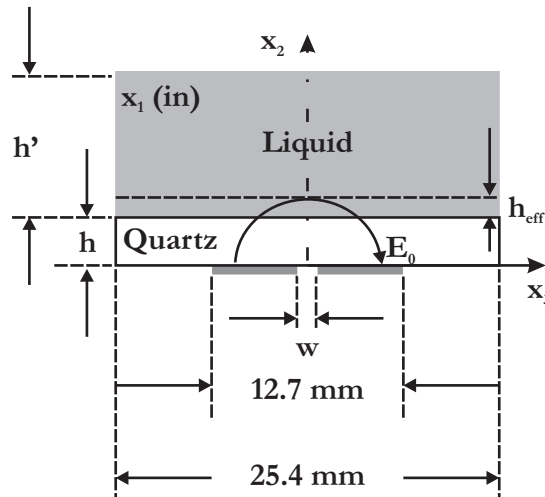


Figure 25. An LFE sensor element showing the interaction of the driving electric field,  $E$ , with contacting liquid

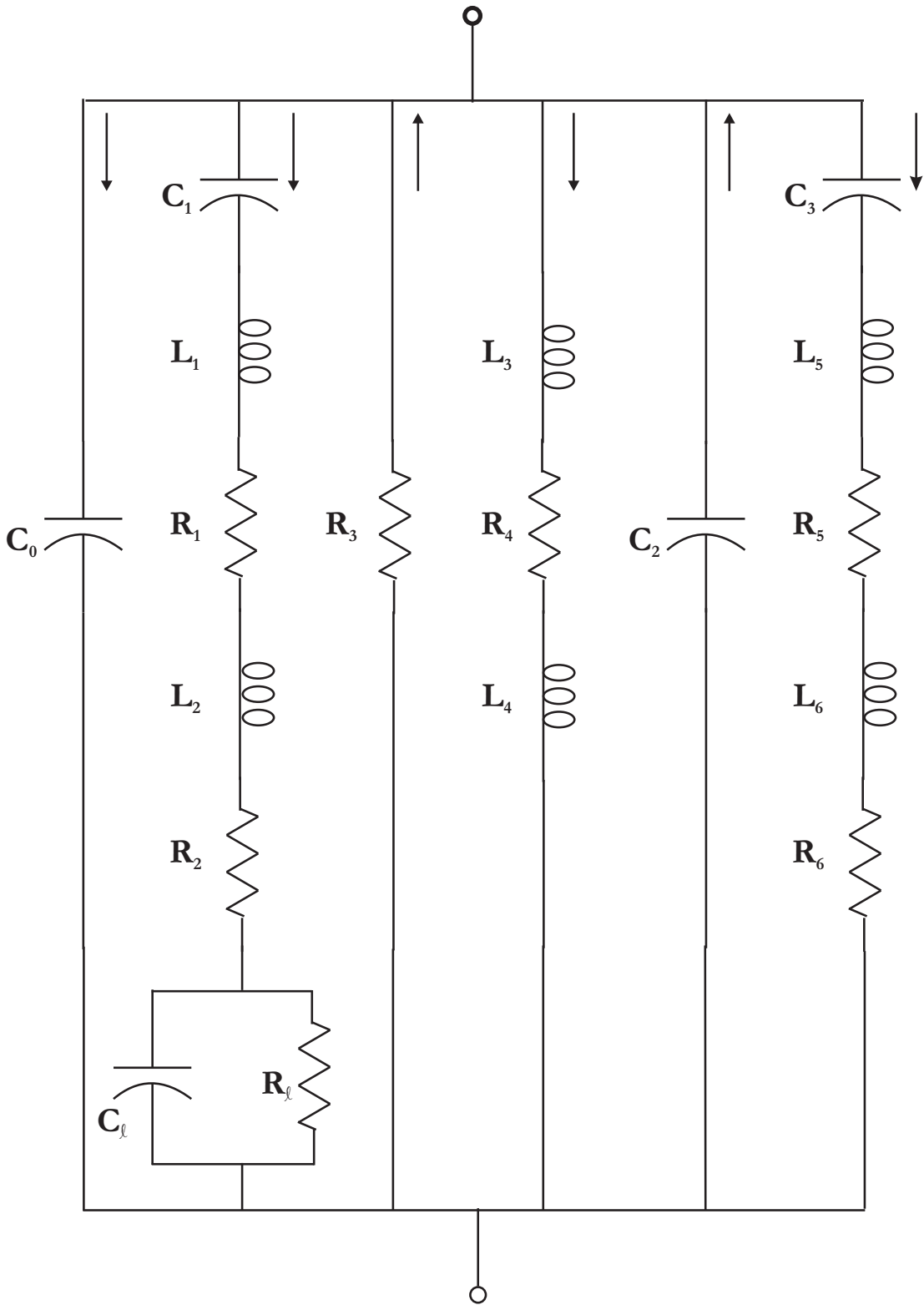


Figure 26. Equivalent circuit including the elements  $C_l$  and  $R_l$ , for an LFE sensor element under liquid loading. The arrows indicate the direction of electrical current flow through each branch.

An expression for the admittance of the LFE sensor element at or near resonance can be obtained from the circuit in Figure 27. This circuit is simply the two leftmost branches of the circuit given in Figure 26. The admittance of this simplified equivalent circuit (Figure 27) very closely approximates the admittance of the of the more complex circuit model (Figure 26), as shown in Figure 28. The admittance of the circuit shown in Figure 27 is the sum of the admittances of the two branches and is expressed as

$$Y = j\omega C_0 + \frac{1}{(R_1 + R_2) + j\omega(L_1 + L_2) + \frac{1}{j\omega C_1} + \frac{1}{\frac{1}{R_1} + j\omega C_1}}. \quad (3.137)$$

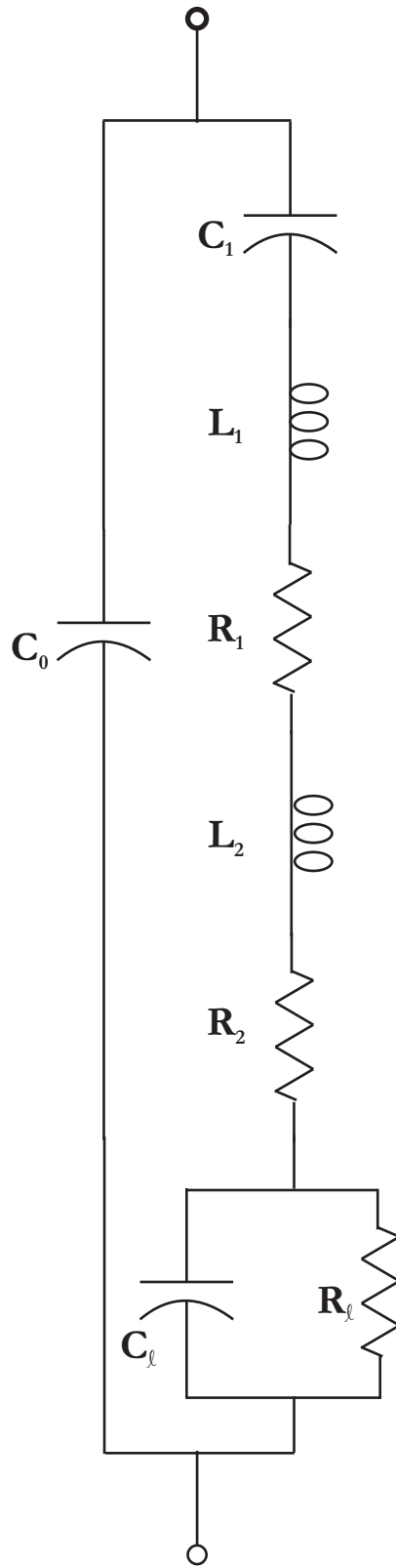


Figure 27. Simplified equivalent circuit model for the LFE sensor element

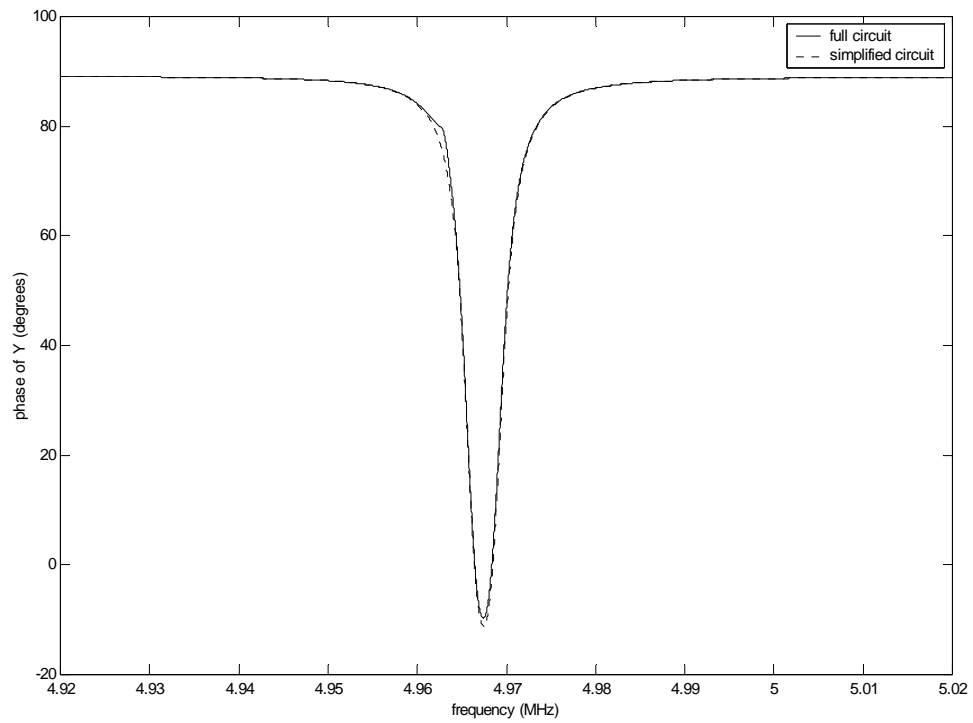
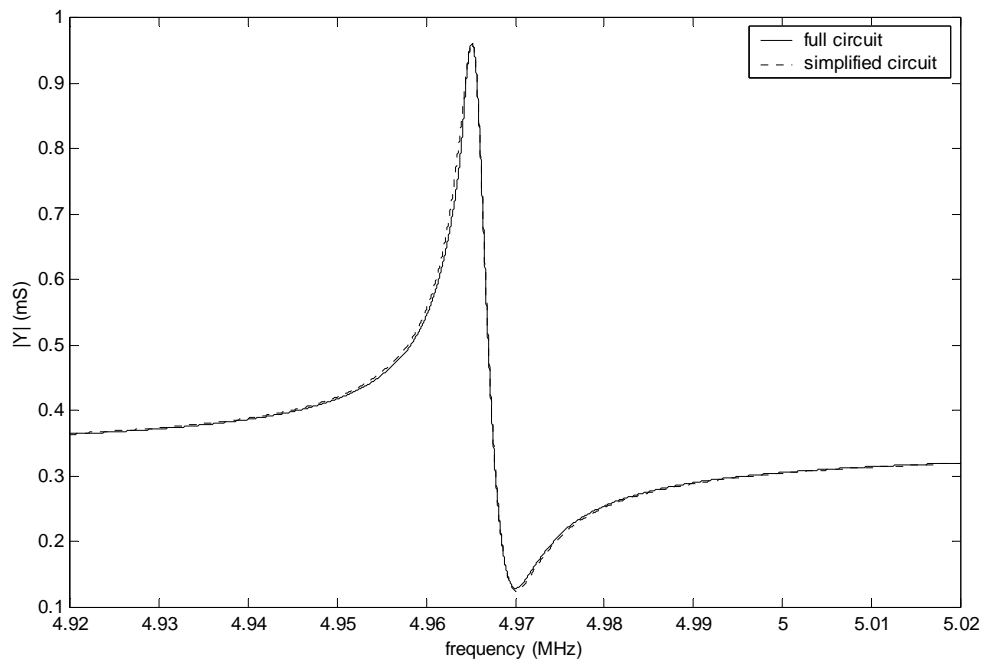


Figure 28. Admittance for the equivalent circuits in Figure 26 (solid line) and Figure 27 (dashed line)



It is clear that the equivalent circuit model for the LFE sensor element presented in this chapter has similarities with the existing model for the QCM under simultaneous mass and liquid loading. Indeed, if one electrically shielded the LFE sensor element from the contacting liquid, the resulting equivalent circuit would be reduced to the circuit in Figure 27 without the parallel combination of  $C_l$  and  $R_l$ .

### 3.3.1. Change in Resonant Frequency

One method of characterizing the response of an LFE sensor element is to measure the change in series resonant frequency,  $f_s$ , due to perturbations of the liquid at the sensing surface. When examining the change in series resonant frequency it is useful to consider changes to the kinematic viscosity (density-viscosity product), permittivity, and conductivity of the liquid separately.

The admittance of the equivalent circuit shown in Figure 27 and given by equation (3.137) is simplified as follows,

$$Y = j\omega C_0 + \frac{1}{Z_m}, \quad (3.138)$$

where  $Z_m$  is the impedance of the equivalent circuit's motional branch and expressed as

$$Z_m = R + j\omega L + \frac{1}{j\omega C_1} + \frac{1}{\frac{1}{R_l} + j\omega C_l}, \quad (3.139)$$

and the resistance and inductance are combined into single terms, defined as

$$R = R_1 + R_2, \quad (3.140)$$

and

$$L = L_1 + L_2. \quad (3.141)$$

### 3.3.1.1. Frequency Changes due to Liquid Kinematic Viscosity

Examination of equations (3.96), (3.122), (3.135) and (3.136), reveal that neither  $C_1$ ,  $C_l$ , nor  $R_l$  are affected by changes in the kinematic viscosity of the liquid. Thus, it is convenient to treat the parallel combination of  $C_l$  and  $R_l$  as a single capacitance,  $C_l'$ , with complex permittivity, defined as

$$C_l^* = C_l + \frac{1}{j\omega R_l}. \quad (3.142)$$

Substitution of equation (3.142) into (3.139) yields

$$Z_m = R + j\omega L + \frac{1}{j\omega C}, \quad (3.143)$$

where

$$C = \frac{C_1 C_l^*}{C_1 + C_l^*}. \quad (3.144)$$

Resonance occurs at the frequency where  $Z_m$  is at its minimum value. The minimum of  $Z_m$  is where the derivative of equation (3.143) with respect to  $\omega$  is equal to zero, as follows

$$\frac{\partial Z_m}{\partial \omega} = \frac{\partial}{\partial \omega} \left( R + j\omega L + \frac{1}{j\omega C} \right) = jL - \frac{1}{j\omega^2 C} = 0. \quad (3.145)$$

Solving equation (3.145) for  $\omega$ , yields

$$\omega_s = \frac{1}{\sqrt{LC}}. \quad (3.146)$$

Equivalently,

$$f_s = \frac{1}{2\pi\sqrt{LC}}. \quad (3.147)$$

The change in resonant frequency is defined to be

$$\Delta f_s = f'_s - f_s^0, \quad (3.148)$$

where the primed quantities are perturbed by changes to the liquid from deionized water and  $f_s^0$  is the series resonant frequency of the LFE sensor element in deionized water. The capacitance,  $C$ , is the series combination of  $C_1$  and  $C_l^*$  and thus, does not vary with changes to the kinematic viscosity of the liquid. Substituting equation (3.147) into (3.148) yields

$$\Delta f_s = \frac{1}{2\pi\sqrt{L'C}} - \frac{1}{2\pi\sqrt{LC}} = \frac{1}{2\pi\sqrt{LC}} \left( \sqrt{\frac{L}{L'}} - 1 \right) = f_s^0 \left( \sqrt{\frac{L}{L'}} - 1 \right). \quad (3.149)$$

An examination of equations (3.96) and (3.122)-(3.136) reveals that only the inductance,  $L_2$ , is affected by the kinematic viscosity of the contacting liquid.

Changes to the inductance,  $L$ , are defined as

$$\Delta L = L' - L. \quad (3.150)$$

Solving equation (3.150) for  $L$  and substituting into equation (3.149) yields

$$\Delta f_s = f_s^0 \left( \sqrt{\frac{L' - \Delta L}{L'}} - 1 \right) = f_s^0 \left( \sqrt{1 - \frac{\Delta L}{L'}} - 1 \right). \quad (3.151)$$

The term under the radical in equation (3.151) can be estimated by taking the first two terms of the binomial series [76] as follows,

$$\Delta f_s = f_s^0 \left( 1 - \frac{1}{2} \frac{\Delta L}{L'} - 1 \right) = -\frac{f_s^0}{2} \frac{\Delta L}{L'}. \quad (3.152)$$

Substituting equations (3.141) and (3.150) into (3.152) returns the expression

$$\Delta f_s = -\frac{f_s^0}{2} \frac{L_1 + L_2' - L_1 - L_2}{L_1 + L_2'} = -\frac{f_s^0}{2} \frac{L_2' - L_2}{L_1 + L_2'}. \quad (3.153)$$

Again, since only small changes to the kinematic viscosity of the contacting liquid are considered,  $L_1 \gg L_2$ , and equation (3.153) can be approximated as follows,

$$\Delta f_s = -\frac{f_s^0}{2} \frac{L_2' - L_2}{L_1}. \quad (3.154)$$

Since relative frequency shifts are considered, and the unperturbed inductance,  $L_2$ , is the reference value, we can arbitrarily let  $L_2 = 0$ . Simplifying equation (3.154) in this way and substituting equation (3.125) results in the expression

$$\Delta f_s = -\frac{(f_s^0)^{3/2}}{n} \sqrt{\frac{\Delta \rho_l \Delta \eta_l}{\bar{c}_{66} \rho}}. \quad (3.155)$$

Equation (3.155) reveals that the LFE sensor element exhibits a similar frequency shift to changes in kinematic viscosity as predicted by Kanazawa and Gordon in [14] and Martin, *et al.* in [43]. Specifically, the frequency shift,  $\Delta f_s$  varies proportionally to both  $\sqrt{\Delta \rho_l \Delta \eta_l}$  and  $(f_s^0)^{3/2}$ .

### 3.3.1.2. Frequency Changes due to Liquid Permittivity

The impedance of the motional branch,  $Z_m$ , can be expressed in its simplest form as follows,

$$Z_m = R_m + jX_m, \quad (3.156)$$

where  $R_m$  and  $X_m$  are the resistance and reactance, respectively, of the motional branch of the equivalent circuit. Resonance is entirely determined by the motional branch and occurs at the frequency for which the magnitude of the impedance is at its minimum or when the reactance disappears [6].

The impedance of the motional branch is given by equation (3.139) and can be rewritten as follows,

$$Z_m = R + j\omega L - \frac{j}{\omega C_1} + \frac{1}{G_l + j\omega C_l}, \quad (3.157)$$

where

$$G_l = \frac{1}{R_l}. \quad (3.158)$$

Equation (3.157) is rewritten by multiplying the last term by its complex conjugate, yielding

$$\begin{aligned} Z_m &= R + j\omega L - \frac{j}{\omega C_1} + \frac{1}{G_l + j\omega C_l} \frac{G_l - j\omega C_l}{G_l - j\omega C_l} \\ &= R + j\omega L - \frac{j}{\omega C_1} + \frac{G_l - j\omega C_l}{G_l^2 + \omega^2 C_l^2} \\ &= R + \frac{G_l}{G_l^2 + \omega^2 C_l^2} + j \left( \omega L - \frac{1}{\omega C_1} - \frac{j\omega C_l}{G_l^2 + \omega^2 C_l^2} \right) \end{aligned} \quad (3.159)$$

The reactance of the motional branch,  $X_m$ , from equations (3.156) and (3.159) is

$$X_m = \omega L - \frac{1}{\omega C_1} - \frac{j\omega C_l}{G_l^2 + \omega^2 C_l^2}. \quad (3.160)$$

At resonance, the reactance of the motional branch,  $X_m$ , is zero. Thus, equation (3.160) is rewritten

$$\omega L - \frac{1}{\omega C_1} - \frac{j\omega C_l}{G_l^2 + \omega^2 C_l^2} = 0. \quad (3.161)$$

Multiplying both sides of equation (3.161) by  $C_1 \omega (G_l^2 + C_l^2 \omega^2)$ , yields

$$C_1 C_l^2 L \omega^4 + (C_1 G_l^2 L - C_l^2 - C_1 C_l) \omega^2 - G_l^2 = 0. \quad (3.162)$$

Equation (3.162) is further modified by dividing both sides by  $C_1 C_l^2 L$ , as follows

$$\omega^4 + \frac{C_1 G_l^2 L - C_l^2 - C_1 C_l}{C_1 C_l^2 L} \omega^2 - \frac{G_l^2}{C_1 C_l^2 L} = \omega^4 + b\omega^2 - c = 0, \quad (3.163)$$

where

$$b = \frac{C_1 G_l^2 L - C_l^2 - C_1 C_l}{C_1 C_l^2 L} \quad (3.164)$$

and

$$c = -\frac{G_l^2}{C_1 C_l^2 L}. \quad (3.165)$$

One can solve for  $\omega^2$  in equation (3.163) using the quadratic equation as follows

$$\omega^2 = \frac{-b \pm \sqrt{b^2 - 4c}}{2}. \quad (3.166)$$

The resonant radial frequency,  $\omega_s$ , is found by taking the square root of equation (3.166),

where

$$\omega_s = \pm \left( \frac{-b \pm \sqrt{b^2 - 4c}}{2} \right)^{1/2}. \quad (3.167)$$

Since the resonant radial frequency must be both real and positive, equation (3.167) is rewritten as follows

$$\omega_s = \left( \frac{-b + \sqrt{b^2 - 4c}}{2} \right)^{1/2}. \quad (3.168)$$

The resonant frequency,  $f_s$ , is then expressed as

$$f_s = \frac{1}{2\pi} \left( \frac{-b + \sqrt{b^2 - 4c}}{2} \right)^{1/2} = \frac{1}{2\sqrt{2}\pi} \left( -b + \sqrt{b^2 - 4c} \right). \quad (3.169)$$

When investigating the resonant frequency change,  $\Delta f_s$ , due to liquid permittivity changes, only the changes in the capacitance,  $C_l$ , are considered as the other circuit elements do not vary with liquid permittivity. In other words, the values for the circuit elements  $L_2$ ,

$R_2$ , and  $R_l$  are fixed for their value in deionized water. Primed quantities indicate the perturbed value due to the liquid, while unprimed values are for deionized water, as in section 3.3.1.1. The change in resonant frequency is expressed as follows

$$\Delta f_s = f_s - f_s^0 = \frac{1}{2\sqrt{2\pi}} \left( \left( -b' + \sqrt{b'^2 - 4c'} \right)^{1/2} - \left( -b + \sqrt{b^2 - 4c} \right)^{1/2} \right), \quad (3.170)$$

where the variables with the subscript  $di$  are the reference values in deionized water. The relative frequency shift can be found using equation (3.170) as follows

$$\begin{aligned} \frac{\Delta f_s}{f_s^0} &= \frac{\left( -b' + \sqrt{b'^2 - 4c'} \right)^{1/2} - \left( -b + \sqrt{b^2 - 4c} \right)^{1/2}}{\left( -b + \sqrt{b^2 - 4c} \right)^{1/2}} \\ &= \left( \frac{-b' + \sqrt{b'^2 - 4c'}}{-b + \sqrt{b^2 - 4c}} \right)^{1/2} - 1 = \left( \frac{-b' - b' \sqrt{1 - 4c'/b'^2}}{-b - b \sqrt{1 - 4c/b^2}} \right)^{1/2} - 1 \end{aligned} \quad (3.171)$$

For the range of liquid permittivity examined, the value  $(4c/b^2)^2 < 1$ , thus the terms under the radical in equation (3.171) can be approximated using the first two terms of a binomial series as follows,

$$\begin{aligned} \frac{\Delta f_s}{f_s^0} &\approx \left( \frac{-b' - b'(1 - 2c'/b'^2)}{-b - b(1 - 2c/b^2)} \right)^{1/2} - 1 = \left( \frac{-2b' - c'/b'^2}{-2b - c/b} \right)^{1/2} - 1 \\ &= \left( \frac{b' - c'/b'}{b - c/b} \right)^{1/2} - 1 \end{aligned} \quad (3.172)$$

Further, the variable  $b$  is approximated as follows,

$$b \approx -\frac{1}{C_1 L} - \frac{1}{C_l L}, \quad (3.173)$$

because  $|G_l^2/C_l'^2| \ll |1/C_1 L + 1/C_l L|$  for the range of permittivities examined.

The resonant frequency can be found by substituting equations (3.165) and (3.173) into (3.172), which yields

$$\frac{\Delta f_s}{f_s^0} = \left( \frac{\frac{1}{C_1 L} - \frac{1}{C'_1 L} - \frac{\frac{G_l^2}{C_1 C_1'^2 L}}{\left(\frac{1}{C_1 L} + \frac{1}{C'_1 L}\right)}}{\frac{1}{C_1 L} - \frac{1}{C'_1 L} - \frac{\frac{G_l^2}{C_1 C_1'^2 L}}{\left(\frac{1}{C_1 L} + \frac{1}{C'_1 L}\right)}} \right)^{\frac{1}{2}} - 1. \quad (3.174)$$

After some algebraic manipulation, equation (3.174) is rearranged and expressed in terms of the equivalent circuit elements as follows,

$$\frac{\Delta f_s}{f_s^0} = \sqrt{\frac{(C'_1 + C_1)^2 + C_1 G_l^2 L}{(C_1 + C'_1)^2 + C_1 G_l^2 L} \frac{C_1^2 + C_1 C'_1}{C_1'^2 + C_1 C'_1}} - 1. \quad (3.175)$$

The frequency shift due to liquid permittivity changes in terms of the quartz constants and liquid properties is obtained by substituting equations (3.122)-(3.136) into equation (3.175) as follows

$$\frac{\Delta f_s}{f_s^0} = \sqrt{\frac{\left(\varepsilon'_l R + \frac{8K^2 C_0}{(n\pi)^2}\right)^2 + \left(\frac{\sigma_l R}{\omega_s}\right)^2 \left(1 + \frac{\omega_s}{n\pi} \sqrt{\frac{2\rho_l \eta_l}{\omega \bar{c}_{66} \rho}}\right) \varepsilon_l'^2 R^2 + \frac{8K^2 C_0 \varepsilon_l' R}{(n\pi)^2}}{\left(\varepsilon_l R + \frac{8K^2 C_0}{(n\pi)^2}\right)^2 + \left(\frac{\sigma_l R}{\omega_s}\right)^2 \left(1 + \frac{\omega_s}{n\pi} \sqrt{\frac{2\rho_l \eta_l}{\omega \bar{c}_{66} \rho}}\right) \varepsilon_l'^2 R^2 + \frac{8K^2 C_0 \varepsilon_l' R}{(n\pi)^2}} - 1, \quad (3.176)$$

where

$$R = h_{\text{eff}} d / w. \quad (3.177)$$

If one were to examine the case of a purely dielectric liquid, then the term containing  $\sigma_l$  in equation (3.176) can be neglected, due to the assumption that  $\sigma_l \rightarrow 0$ . The variable  $A$  is introduced, where it is defined as follows,

$$A = \frac{8K^2 C_0}{(n\pi)^2}. \quad (3.178)$$



An expression for the normalized frequency shift in dielectric liquids is found by substituting equation (3.178) into (3.176) and multiplying the numerator and denominator of the resulting equation by  $w/h_{eff}d$ , as follows

$$\frac{\Delta f_s}{f_s^0} = \frac{\sqrt{(\varepsilon'_l + Aw/h_{eff}d)^2 + \varepsilon_l A}}{\sqrt{(\varepsilon_l + Aw/h_{eff}d)^2 + \varepsilon'_l A}}. \quad (3.179)$$

### 3.3.1.3. Frequency Changes due to Liquid Conductivity

The expression for the change in frequency due to liquid conductivity is, from equation (3.171),

$$\frac{\Delta f_s}{f_s^0} = \left( \frac{-b' + \sqrt{b'^2 - 4c'}}{-b + \sqrt{b^2 - 4c}} \right)^{1/2} - 1. \quad (3.180)$$

The variable  $b$  is approximated as follows,

$$b \approx \frac{G_l'^2}{C_l^2} - \frac{1}{C_l L}, \quad (3.181)$$

because  $|1/C_l L| \ll |G_l'^2/C_l^2 - 1/C_l L|$  for the range of conductivities investigated.

When calculating the change in frequency, only the circuit element,  $R_l$ , varies with liquid conductivity. The notation is that primed quantities are the values that are perturbed due to the contacting liquid, whereas unprimed quantities are unvaried from the deionized water values. Thus, substituting equations (3.165) and (3.181) into (3.180), yields

$$\begin{aligned} \frac{\Delta f_s}{f_s^0} &= \left( \frac{\frac{C_l^2 - C_1 G_l'^2 L + \sqrt{C_1 G_l'^2 L - C_l^2 + 4C_1 C_l^2 G_l'^2 L}}{C_1 C_l^2 L}}{\frac{C_l^2 - C_1 G_l^2 L + \sqrt{C_1 G_l^2 L - C_l^2 + 4C_1 C_l^2 G_l^2 L}}{C_1 C_l^2 L}} \right)^{1/2} - 1 \\ &= \left( \frac{C_l^2 - C_1 G_l'^2 L + \sqrt{C_1 G_l'^2 L - C_l^2 + 4C_1 C_l^2 G_l'^2 L}}{C_l^2 - C_1 G_l^2 L + \sqrt{C_1 G_l^2 L - C_l^2 + 4C_1 C_l^2 G_l^2 L}} \right)^{1/2} - 1 \end{aligned} \quad (3.182)$$

The frequency change due to liquid conductivity changes in terms of the quartz constants and liquid properties is found by substituting equations (3.122)-(3.136) into (3.182), as follows

$$\frac{\Delta f_s}{f_s^0} = \left[ \frac{\varepsilon_l^2 - \frac{\sigma_l'^2}{\omega_s^2} \left( 1 + \frac{\omega_s}{n\pi} \sqrt{\frac{2\rho_l \eta_l}{\omega \bar{c}_{66} \rho}} \right) + \frac{\sqrt{\frac{\sigma_l'^2}{\omega_s^2} \left( 1 + \frac{\omega_s}{n\pi} \sqrt{\frac{2\rho_l \eta_l}{\omega \bar{c}_{66} \rho}} \right) (1 + 4\varepsilon_l R^2) - \varepsilon_l^2}}{R}}{\varepsilon_l^2 - \frac{\sigma_l^2}{\omega_s^2} \left( 1 + \frac{\omega_s}{n\pi} \sqrt{\frac{2\rho_l \eta_l}{\omega \bar{c}_{66} \rho}} \right) + \frac{\sqrt{\frac{\sigma_l^2}{\omega_s^2} \left( 1 + \frac{\omega_s}{n\pi} \sqrt{\frac{2\rho_l \eta_l}{\omega \bar{c}_{66} \rho}} \right) (1 + 4\varepsilon_l R^2) - \varepsilon_l^2}}{R}} \right]^{\frac{1}{2}} - 1 \quad (3.183)$$

Looking at the case of a conductive liquid, it is assumed that  $\sigma/\omega \gg \varepsilon$  [77].

Equation (3.183) can then be written as follows,

$$\frac{\Delta f_s}{f_s^0} = \left( \frac{\left( \frac{\sigma_l' h_{eff} d}{\omega_s w} \right)^2 \left( 1 + \frac{1}{n\pi} \sqrt{\frac{2\omega_s \rho_l \eta_l}{\bar{c}_{66} \rho}} \right) - \sqrt{\left( \frac{\sigma_l' h_{eff} d}{\omega_s w} \right)^2 \left( 1 + \frac{1}{n\pi} \sqrt{\frac{2\omega_s \rho_l \eta_l}{\bar{c}_{66} \rho}} \right)}}{\left( \frac{\sigma_l h_{eff} d}{\omega_s w} \right)^2 \left( 1 + \frac{1}{n\pi} \sqrt{\frac{2\omega_s \rho_l \eta_l}{\bar{c}_{66} \rho}} \right) - \sqrt{\left( \frac{\sigma_l h_{eff} d}{\omega_s w} \right)^2 \left( 1 + \frac{1}{n\pi} \sqrt{\frac{2\omega_s \rho_l \eta_l}{\bar{c}_{66} \rho}} \right)}} \right)^{1/2} - 1 \quad (3.184)$$

Introducing the variable  $B$ , which is defined as follows,

$$B = \left( \frac{h_{eff} d}{\omega_s w} \right)^2 \left( 1 + \frac{1}{n\pi} \sqrt{\frac{2\omega_s \rho_l \eta_l}{\bar{c}_{66} \rho}} \right). \quad (3.185)$$

An expression for the normalized frequency shift of an LFE sensor element in conductive loads is obtained by substituting equation (3.185) into (3.184) as follows,

$$\frac{\Delta f_s}{f_s^0} = - \left( \frac{\sigma_l'^2 B - \sqrt{\sigma_l'^2 B}}{\sigma_l^2 B - \sqrt{\sigma_l^2 B}} \right)^{1/2} - 1. \quad (3.186)$$

### 3.3.1.4. Frequency Changes due to an Arbitrary Liquid

The frequency change due to an arbitrary liquid with varying kinematic viscosity, permittivity, and conductivity is then the sum of equations (3.154), (3.175), and (3.182).

These equations are in terms of the equivalent circuit elements. To obtain the general frequency change in terms of the liquid properties, one would simply need to find the sum of equations (3.155), (3.176), and (3.183) as follows,

$$\begin{aligned} \frac{\Delta f_s}{f_s} = & - \left( \frac{1}{N} \sqrt{\frac{f_s^0 \Delta \rho_l \Delta \eta_l}{\bar{c}_{66} \rho}} \right) \\ & + \frac{\sqrt{\left( \varepsilon_l' R + \frac{8K^2 C_0}{(n\pi)^2} \right)^2 + \left( \frac{\sigma_l R}{\omega_s} \right)^2 \left( 1 + \frac{\omega_s}{n\pi} \sqrt{\frac{2\rho_l \eta_l}{\omega \bar{c}_{66} \rho}} \right) \varepsilon_l'^2 R^2 + \frac{8K^2 C_0 \varepsilon_l' R}{(n\pi)^2}}}{\sqrt{\left( \varepsilon_l R + \frac{8K^2 C_0}{(n\pi)^2} \right)^2 + \left( \frac{\sigma_l R}{\omega_s} \right)^2 \left( 1 + \frac{\omega_s}{n\pi} \sqrt{\frac{2\rho_l \eta_l}{\omega \bar{c}_{66} \rho}} \right) \varepsilon_l'^2 R^2 + \frac{8K^2 C_0 \varepsilon_l' R}{(n\pi)^2}}} \\ & + \left[ \frac{\varepsilon_l'^2 - \frac{\sigma_l'^2}{\omega_s^2} \left( 1 + \frac{\omega_s}{n\pi} \sqrt{\frac{2\rho_l \eta_l}{\omega \bar{c}_{66} \rho}} \right) + \frac{\sqrt{\frac{\sigma_l'^2}{\omega_s^2} \left( 1 + \frac{\omega_s}{n\pi} \sqrt{\frac{2\rho_l \eta_l}{\omega \bar{c}_{66} \rho}} \right) (1 + 4\varepsilon_l' R^2) - \varepsilon_l'^2}}{R}}{\varepsilon_l'^2 - \frac{\sigma_l'^2}{\omega_s^2} \left( 1 + \frac{\omega_s}{n\pi} \sqrt{\frac{2\rho_l \eta_l}{\omega \bar{c}_{66} \rho}} \right) + \frac{\sqrt{\frac{\sigma_l'^2}{\omega_s^2} \left( 1 + \frac{\omega_s}{n\pi} \sqrt{\frac{2\rho_l \eta_l}{\omega \bar{c}_{66} \rho}} \right) (1 + 4\varepsilon_l' R^2) - \varepsilon_l'^2}}{R}} \right]^{\frac{1}{2}} \\ & - 2 \end{aligned} \quad (3.187)$$

An expression for the frequency change can also be obtained for the special case of a purely dielectric liquid by finding the sum of equations (3.155) and (3.179) as follows,

$$\frac{\Delta f_s}{f_s^0} = -\frac{1}{N} \sqrt{\frac{f_s^0 \Delta \rho_l \Delta \eta_l}{\bar{c}_{66} \rho_q}} + \sqrt{\frac{(\varepsilon'_l + Aw/h_{eff}d)^2 + \varepsilon'_l A}{(\varepsilon_l + Aw/h_{eff}d)^2 + \varepsilon'_l A}}. \quad (3.188)$$

The frequency change can also be found for the special case of a conductive liquid by finding the sum of equations (3.155) and (3.186) as follows,

$$\frac{\Delta f_s}{f_s^0} = -\frac{1}{N} \sqrt{\frac{f_s^0 \Delta \rho_l \Delta \eta_l}{\bar{c}_{66} \rho_q}} - \left( \frac{\sigma'_l{}^2 B - \sqrt{\sigma'_l{}^2 B}}{\sigma_l^2 B - \sqrt{\sigma_l^2 B}} \right)^{1/2} - 1. \quad (3.189)$$

In the next chapter, I will present the experimental methods used to test the LFE sensor under liquid loads.

## Chapter 4

### EXPERIMENTAL METHODS

Chapter 3 contains the derivation of the equivalent circuit model for a lateral-field excited (LFE) sensor under liquid load. In this chapter the procedure for fabricating the LFE sensor elements is presented. The procedure is followed by a discussion of the methods for characterizing the LFE sensor elements to changes in the physical properties of liquids. In the next chapter I will present the theoretical and experimental results of LFE sensors under various liquid loads. This is followed by a discussion of the results and a comparison of the theoretical and experimental data.

#### **4.1. Lateral-Field Excited Sensors**

The LFE sensors were fabricated on AT-cut quartz discs with a diameter of 25.4 mm and thickness of 0.33 mm. The discs are plano-plano, (each of the major surfaces are flat), and optically polished. There are two sources for the quartz discs, the first is Sawyer Technical Materials, LLC, Eastlake, OH and the second is Lap-Tech Inc., Bowmanville, ON, Canada.

The electrodes were deposited on AT-cut quartz substrates at the Laboratory for Surface Science and Technology (LASST), at the University of Maine, Orono, ME. A 50-nm adhesion layer of chromium was deposited on one major surface of the quartz disc in a vacuum deposition chamber using radio frequency magnetron sputtering. The chromium layer is required because the lattice spacing between chromium and quartz is closer than that of quartz and gold. A 250-nm layer of gold is sputtered onto the chromium. If gold were to be deposited directly on the quartz substrate, the gold would delaminate from the surface.

The electrodes were patterned on the surface using standard photolithographic techniques (Figure 29). The first step of the photolithographic process is to apply photoresist to the gold-coated surface of the quartz disc. Photoresist is a liquid polymer that is sensitive to ultraviolet light. The photoresist is a physical barrier to the removal of the gold in the region of the electrodes. A photomask, a clear overlay with an opaque electrode pattern, is aligned in the proper position on a Quintal mask aligner. The mask aligner has a vacuum chuck bringing the photomask into physical contact with the quartz wafer. The photoresist is exposed to ultraviolet light where the photomask has no pattern. The photoresist that was exposed to the ultraviolet is removed in developer solution. The gold film in the regions not protected by the photoresist is then removed using a chemical etchant. The final step in the photolithography process is the removal of the photoresist from the electrodes.

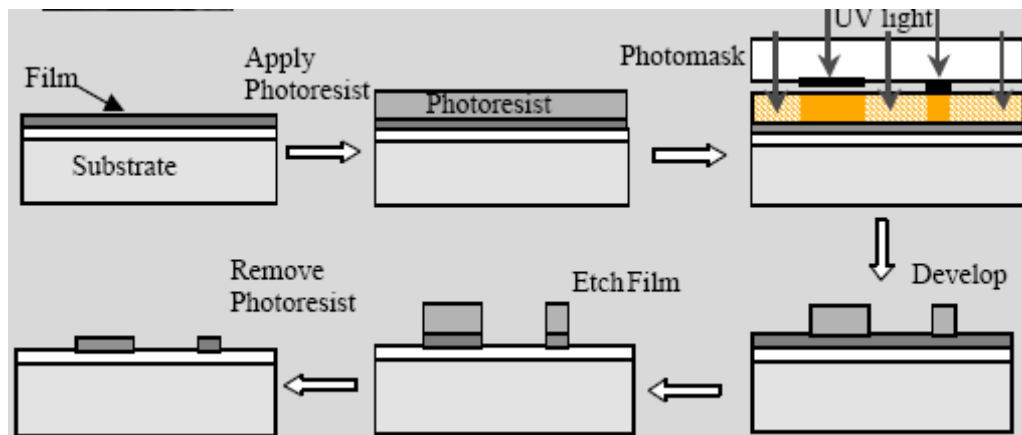


Figure 29. The photolithography process [78]

#### 4.2. Lateral-Field Excited Sensor Element Characterization

The first step in preparing the LFE sensor elements is cleaning. The cleaning process removes any chemical residue that may still be on the sensor elements from the

electrode deposition process. Up to four sensor elements are placed in a Teflon® holder designed for this purpose. The cleaning procedure is as follows:

- Immerse the sensor elements in acetone for about ten minutes.
- Remove the sensor elements from the acetone and immerse in isopropyl alcohol for about ten minutes.
- Remove the sensor elements from the isopropyl alcohol and immerse in deionized water for about ten minutes.
- Remove the sensor elements from the deionized water.
- Remove the LFE sensor elements from the deionized water and the holder.
- Dry the sensor elements individually with pressurized nitrogen. Nitrogen is used rather than compressed air, as compressed air can oxidize the gold electrodes.
- Place the sensor elements, bare side up, in a Boekel UV Clean for 20 minutes. The ultraviolet light removes any organic residue that is on the sensing surface of the LFE sensor elements from the prior cleaning steps.

Each LFE sensor element is placed in a holder prior to testing. The two purposes of the device holder are, first, to make an electrical contact between the LFE sensor element and the measurement instrumentation, and second, to prevent the liquid from contacting the sensor element anywhere but on the sensing surface. If the liquid were to contact the reference surface, the electrical measurements would be compromised as the liquid may have a finite conductivity. Additionally, many solutions, especially the sodium chloride solutions used in these experiments, are highly corrosive and will damage the electrical contacts in the holder. The holder is then connected, by coaxial cable, to a Hewlett-Packard HP4795a network analyzer. A network analyzer is an instrument that measures high frequency

electrical networks, (up to 500 MHz for the HP4795a). The network analyzer was set to record 801 points for every sweep to obtain the best resolution of the device admittance. The network analyzer has the capabilities of converting the measured signal to the equivalent admittance for the LFE sensor element. The admittance of each sensor element was recorded in air before it was exposed to liquid.

The admittance of the LFE sensor element under liquid-loading was measured by lowering the holder containing the sensor element in a 400-ml beaker of the solution to be measured so that the sensor element was completely immersed. The admittance of the sensor element was measured on the network analyzer. Once the measured admittance was stable, with a frequency variation in peak admittance of no more than  $\pm 2$  Hz, the admittance was saved.

Three different solutions were chosen to characterize the LFE sensor elements to physical property changes of liquids. The three physical properties of the solutions that are being varied are viscosity, permittivity, and conductivity. Viscosity is a mechanical property and is defined as the resistance of a liquid to flow. Thus, molasses is an example of a liquid with a high viscosity as it has a high resistance to flow, whereas water at 20°C is an example of a liquid with a low viscosity as it flows easily. Permittivity is an electrical property and is the ability of a material to store a charge. Liquids with a higher permittivity will store an electrical charge with a smaller electric field. Conductivity is also an electrical property and is the ability of a material to conduct electrical current. Liquids with high conductivity will conduct electricity more readily than liquids, such as deionized water, that have very low conductivity.

The solutions were chosen so that varying the concentration of the solution changes one of the physical properties with minimal changes to the other two physical properties.



The solution chosen to measure the LFE sensor elements' responses to changes in liquid viscosity is glycerol. Glycerol solutions have been used in other studies to examine the frequency responses of acoustic wave sensors to changes in liquid viscosity. For the experiments presented here, the glycerol concentration was varied from 0% to 20% glycerol by weight. The solution chosen to measure the LFEs' behavior to changes in liquid permittivity is isopropyl alcohol. The concentration of the isopropyl alcohol solution was varied from 0% to 100% by weight. In order to measure the LFE sensor elements' responses to changes in conductivity a sodium chloride solution was chosen. The concentration of sodium chloride was varied from 0% to 0.15% by weight.

The data was exported to MATLAB, a mathematics software package. The data was plotted and several features of the LFE sensor elements' admittances were characterized as the physical properties of the solutions were varied. The features of the admittance that were characterized are:

- resonant frequency
- antiresonant frequency
- the magnitude of the admittance at the resonant frequency
- the magnitude of the admittance at the antiresonant frequency
- the phase of the admittance at the resonant frequency
- the phase of the admittance at the antiresonant frequency
- the frequency difference between the antiresonant and resonant frequency

The fact that the admittance of the LFE sensor elements is a complex value, containing both a real part and imaginary part, both the magnitude and phase at the resonant and antiresonant frequencies must be evaluated to fully characterize the admittances of the LFE sensor elements.

## Chapter 5

### RESULTS AND DISCUSSION

In chapter 3 a model for the liquid-loaded lateral-field excited (LFE) sensor element was derived. This was followed, in chapter 4, by the experimental methods used in measuring the response of the LFE sensor element to liquid loads with different mechanical and electrical properties. What follows in this chapter is an analysis of the theoretical model for the LFE sensor element. This analysis will examine the response of the model to changes in the kinematic viscosity, electrical conductivity, and permittivity of the contacting liquid. The conclusions of the research and directions for future work are presented in chapter 6.

#### **5.1. Experimentally Determined Parameters for LFE Sensor Elements**

The equivalent circuit model for the LFE sensor element considered the device response due only to changes in the crystal and the contacting liquid. Practically, the LFE sensor element is measured in a holder. The holder is not electrically isolated from the sensor and has a parasitic capacitance,  $C_p$ , and a parasitic resistance,  $R_p$  due to electrical interactions between the holder, the LFE sensor element, and the measurement system. The values for  $C_p$  and  $R_p$  were experimentally determined (Table 5) and depends not only on the holder but on the electrode configuration of the LFE sensor element. The equivalent circuit model modified with the parasitic elements is shown in Figure 30.

**Table 5. Experimentally determined parameters for LFE sensor elements**

<b>electrode gap (mm)</b>	<b><math>f_0</math> (MHz)</b>	<b><math>C_p</math> (pF)</b>	<b><math>R_p</math> (<math>\Omega</math>)</b>	<b><math>C_0</math> (pF)</b>	<b><math>R_1</math> (<math>\Omega</math>)</b>	<b><math>h_{\text{eff}}</math> (mm)</b>
0.5	4.966811	6.7	145	5.0	650	0.86
1.0	4.964884	5.8	145	5.1	650	1.55
2.0	4.964891	4.6	175	5.0	750	3.36

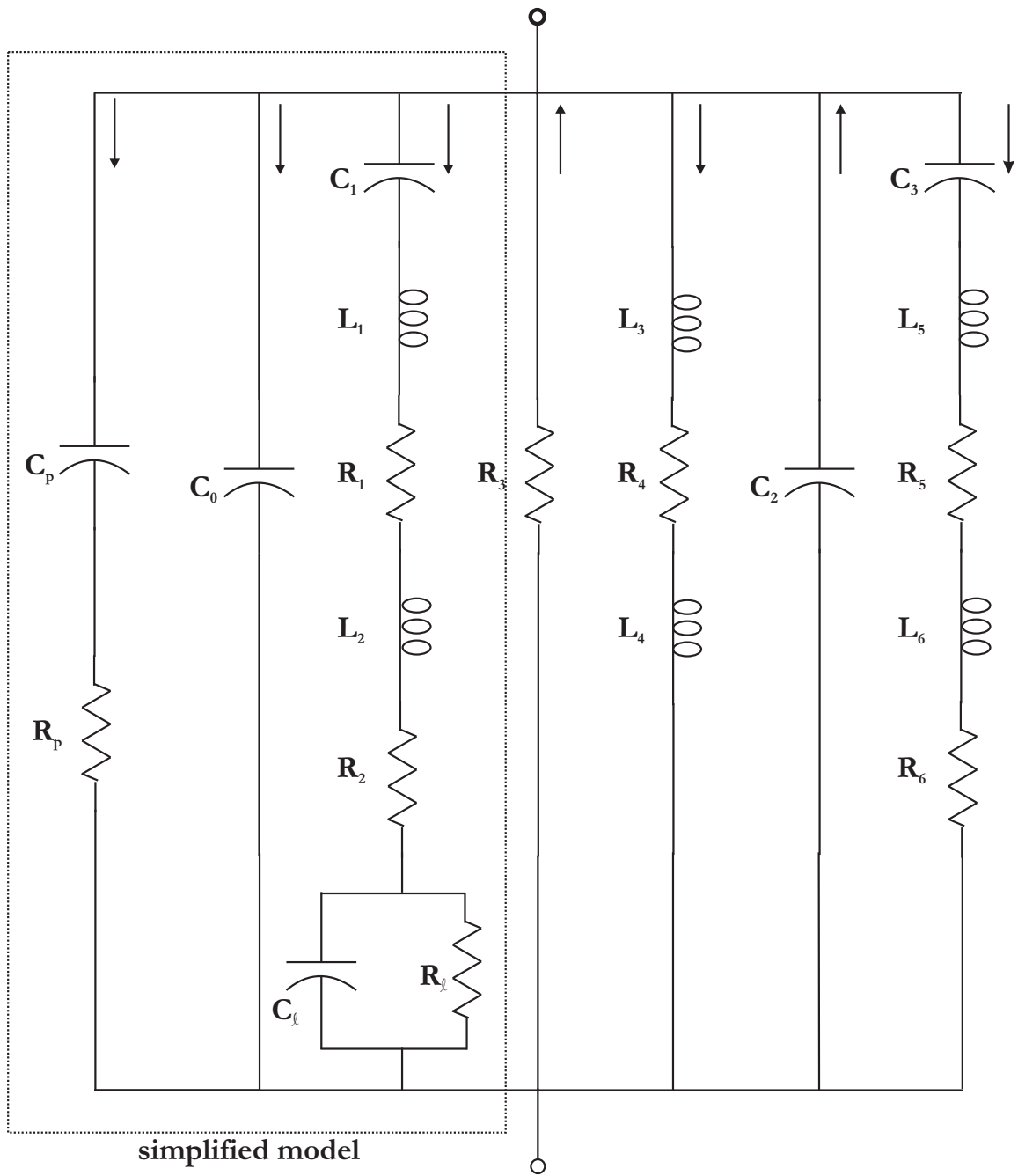


Figure 30. Equivalent circuit for LFE sensor element incorporating the electrical influence of the sensor holder

The circuit in Figure 30 contains all the circuit elements derived from the analysis in chapter 3. However, the equivalent circuit can be estimated using the simplified circuit, which is inside the dashed square of Figure 30. The admittance curves near resonance for both circuits under deionized water loading are shown in Figure 28. The resonant and antiresonant frequencies between the two models differ by no more than 0.02% for the full range of liquid loads tested. The error in the peak magnitude of the admittance between the two models is greater, reaching about 4.4% for the most conductive liquids tested. However, this is, well within the experimental error, which is estimated to be greater than 5%. The simplified circuit model provides ease of analysis without greatly sacrificing accuracy.

Following the approach used by Martin, *et al.* [43] the series resonant frequency,  $f_s$ , and static capacitance,  $C_0$ , were experimentally determined for each device (Table 5). The static capacitance is dependent only on the electrode configuration and the thickness of the quartz plate, thus finding  $C_0$  experimentally does not impact the model with regard to perturbations in the contacting liquid.

The effective penetration depth,  $h_{eff}$ , was also determined experimentally. The effective penetration depth,  $h_{eff}$ , is proportional to the electrode gap width,  $w$ .

## **5.2. Admittance in Deionized Water**

The plots of the theoretical admittance obtained with the lumped element equivalent circuit model were compared to measured data for LFE sensor elements in deionized water (Figure 31 - Figure 33). The plots show very good agreement between the measured and model data, with the model having about a 5% error compared with the experimental data.

The one feature of the measured data that does not occur in the model data is the ripple that occurs out of the resonance band on the high frequency side. This ripple may be due to another acoustic mode or the thickness shear mode reflected at the edge of the plate.

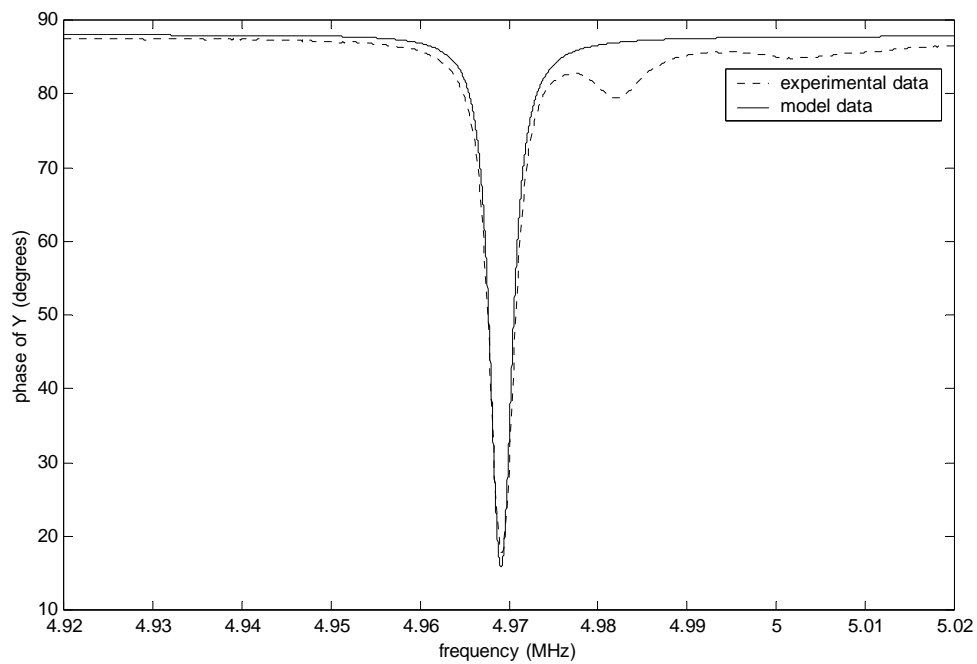
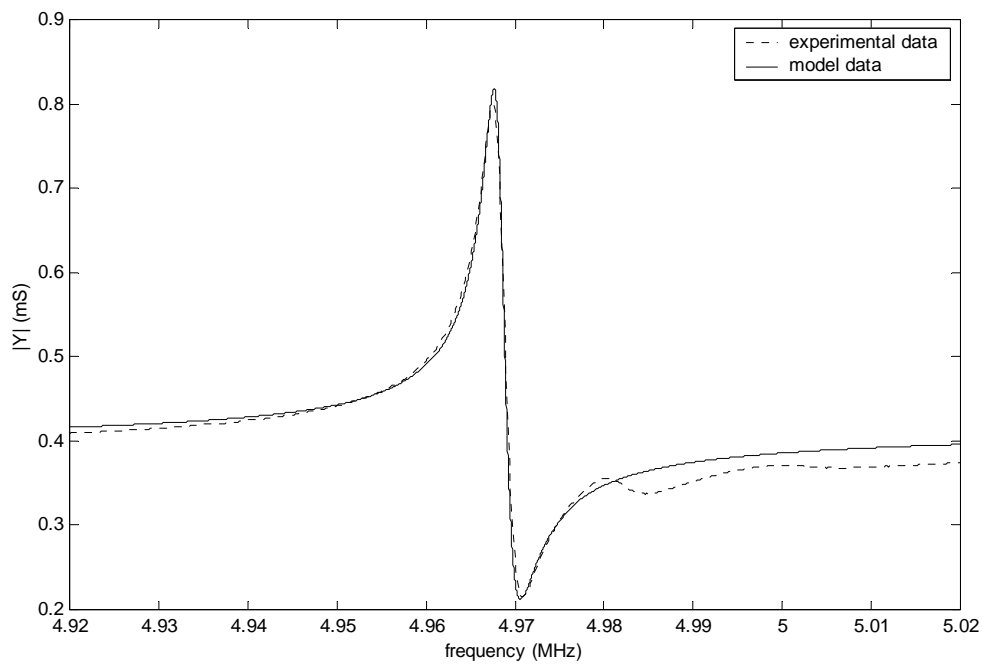


**Figure 31. Theoretical and measured admittance for an LFE sensor element with a 0.5-mm electrode gap under a deionized water load**

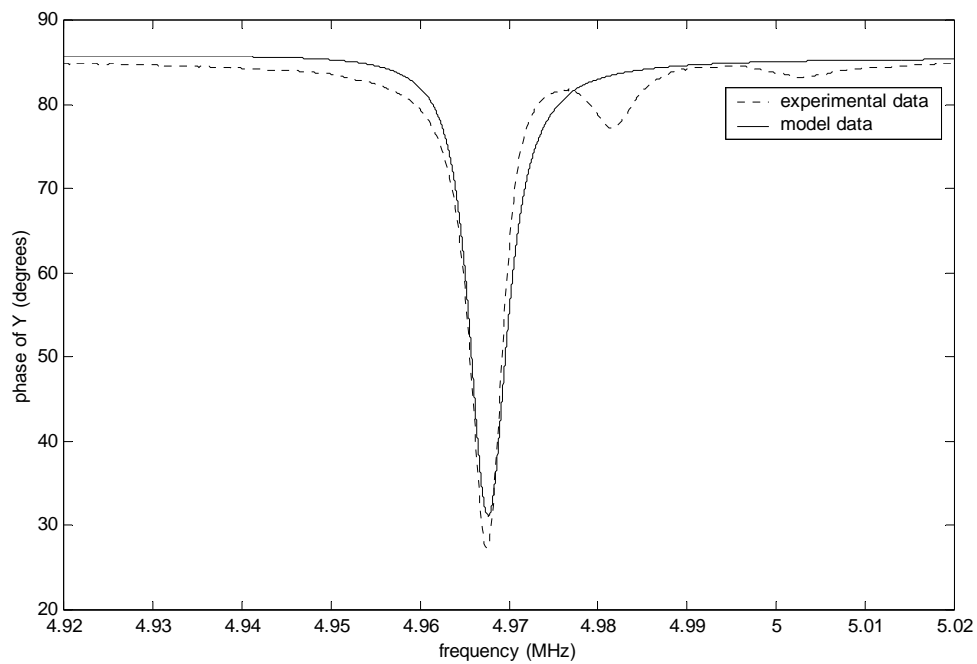
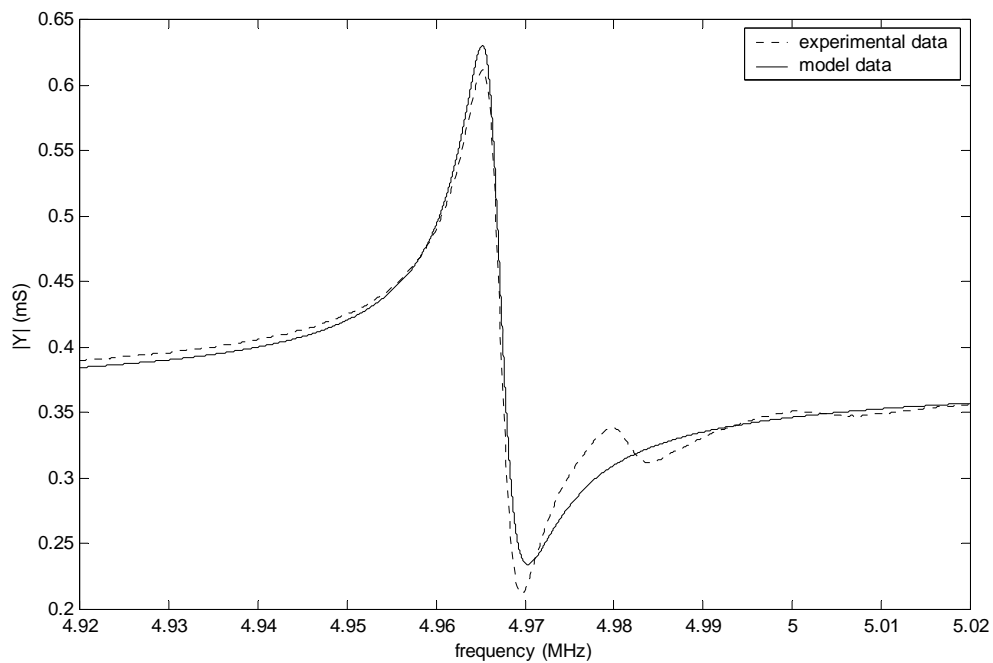


**Figure 32. Theoretical and measured admittance for an LFE sensor element with a 1.0-mm electrode gap under a deionized water load**



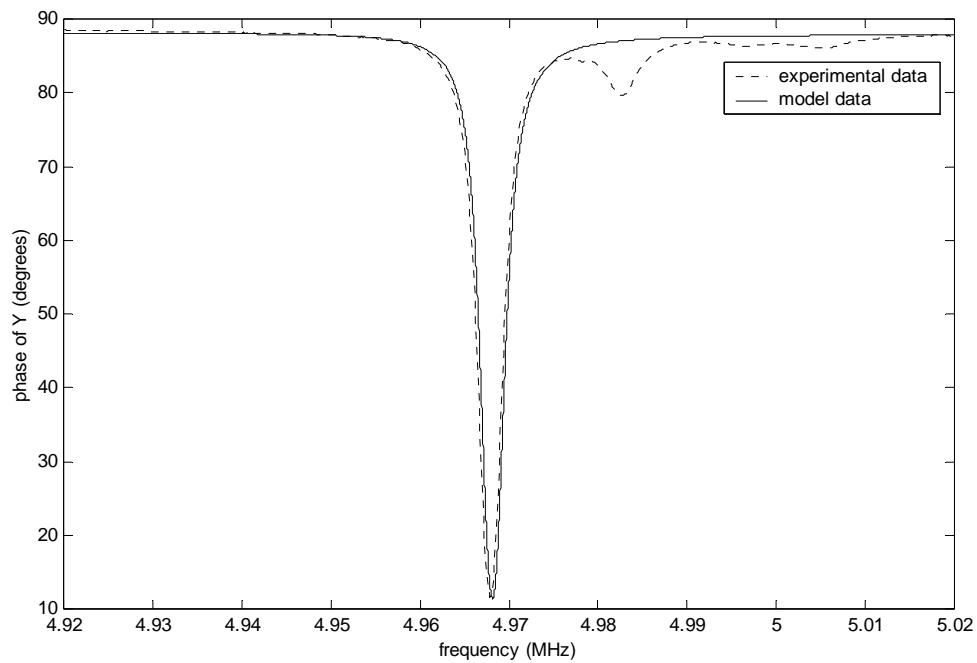
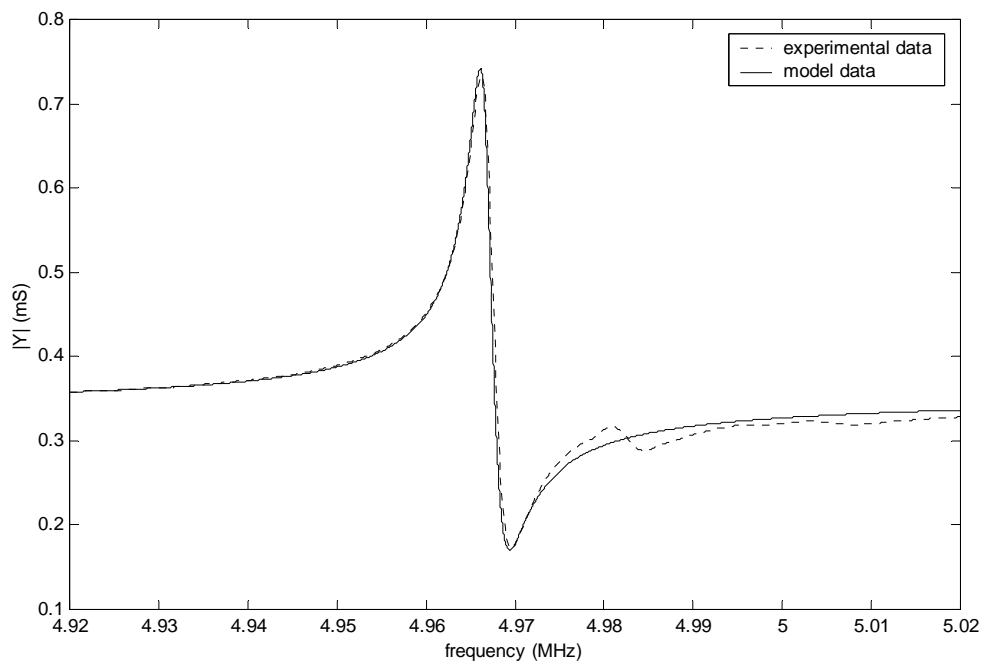


**Figure 33. Theoretical and measured admittance for an LFE sensor element with a 2.0-mm electrode gap under a deionized water load**

### 5.3. LFE Sensor Element Response to Kinematic Viscosity

The data, both measured and from the model, for the LFE sensors exposed to the full range of glycerol solutions are given in Appendix D. The data for the frequency shift, normalized to the series resonant frequency in deionized water as a function of kinematic viscosity are given in Figure 34 - Figure 36. In all cases the magnitude of the frequency shift predicted by the model, (the squares in figures 33 – 35), is less than was measured (the diamonds in figures 33 -35). However, if the frequency shift due to the permittivity is neglected, the model, (the triangles in figures 33 – 35) matches the measured frequency shift within the experimental error. The primary sources of experimental error for these data are the resolution of the network analyzer ( $\pm 25$  ppm), the temperature variations in the laboratory ( $\pm 5$  °C), and errors in the concentration of the solutions ( $\pm 0.5$  %).

The normalized frequency shift was calculated to be  $\pm 5$  ppm using the generalized frequency-temperature curves in [79]. The error also considered possible misalignment of the AT-cut quartz plate to be  $\pm 8$ '.

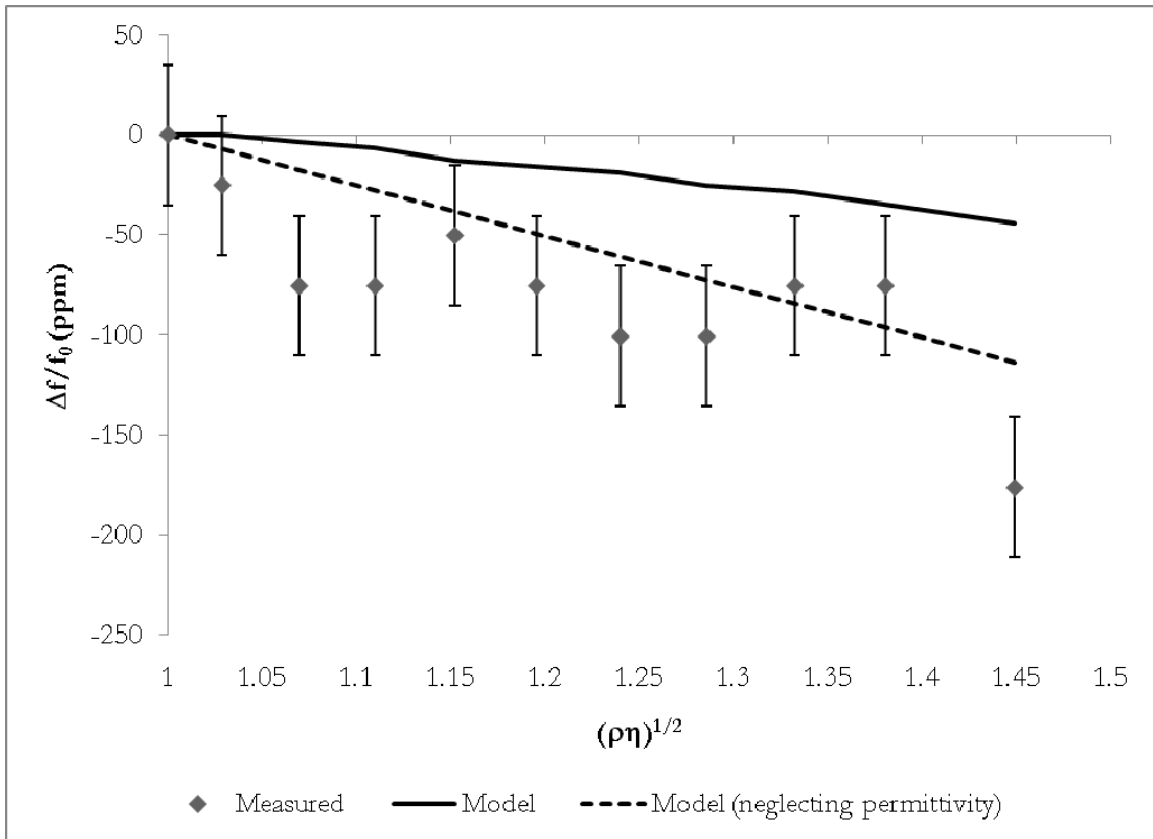


**Figure 34. Normalized frequency shift of an LFE sensor element with a 0.5-mm electrode gap as a function of kinematic viscosity**

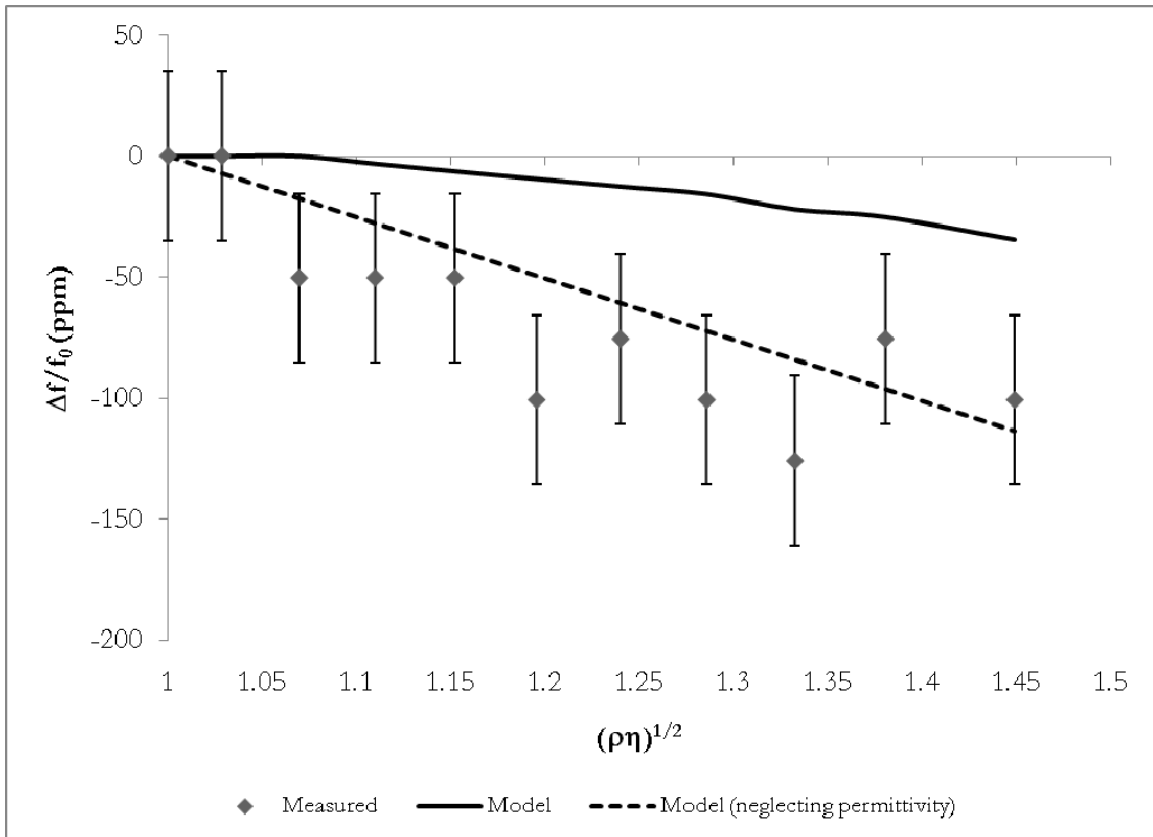
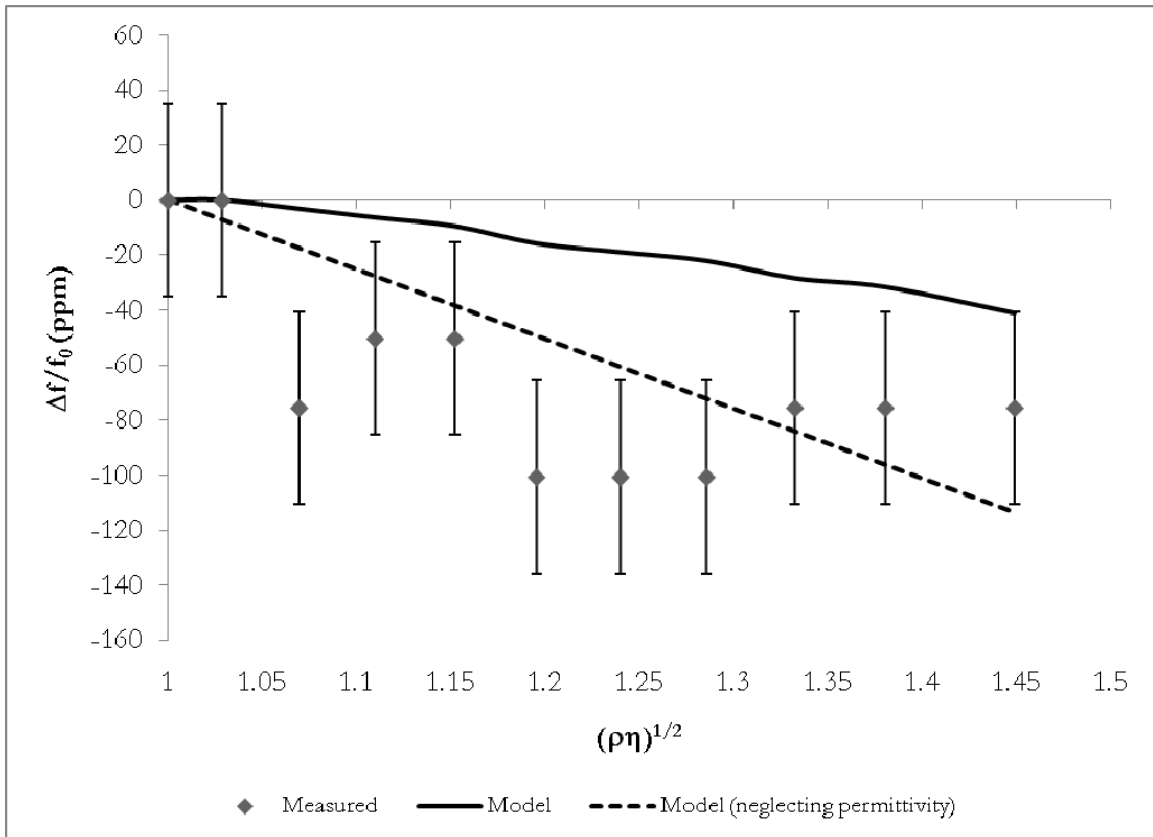


Figure 35. Normalized frequency shift of an LFE sensor element with a 1.0-mm electrode gap as a function of kinematic viscosity



**Figure 36. Normalized frequency shift of an LFE sensor element with a 2.0-mm electrode gap as a function of kinematic viscosity**

The magnitude of the peak admittance for LFE sensor elements with different electrode gaps, normalized to the value in deionized water, is shown in Figure 37 - Figure 39. The decrease in the peak admittance due to kinematic viscosity predicted by the model follows the same trends as the measured data. However, the model consistently predicts a smaller change in peak admittance than was found in the measured data.

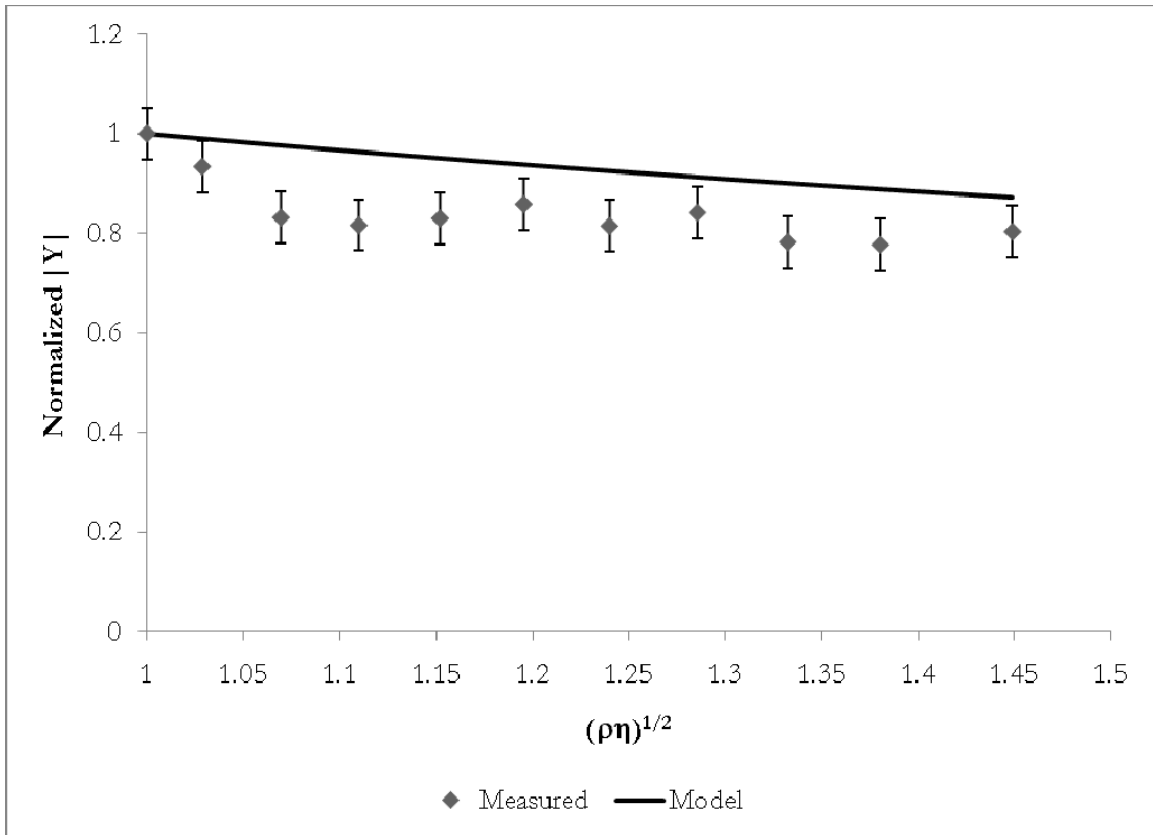


Figure 37. Normalized peak admittance of an LFE sensor element with a 0.5-mm electrode gap as a function of kinematic viscosity

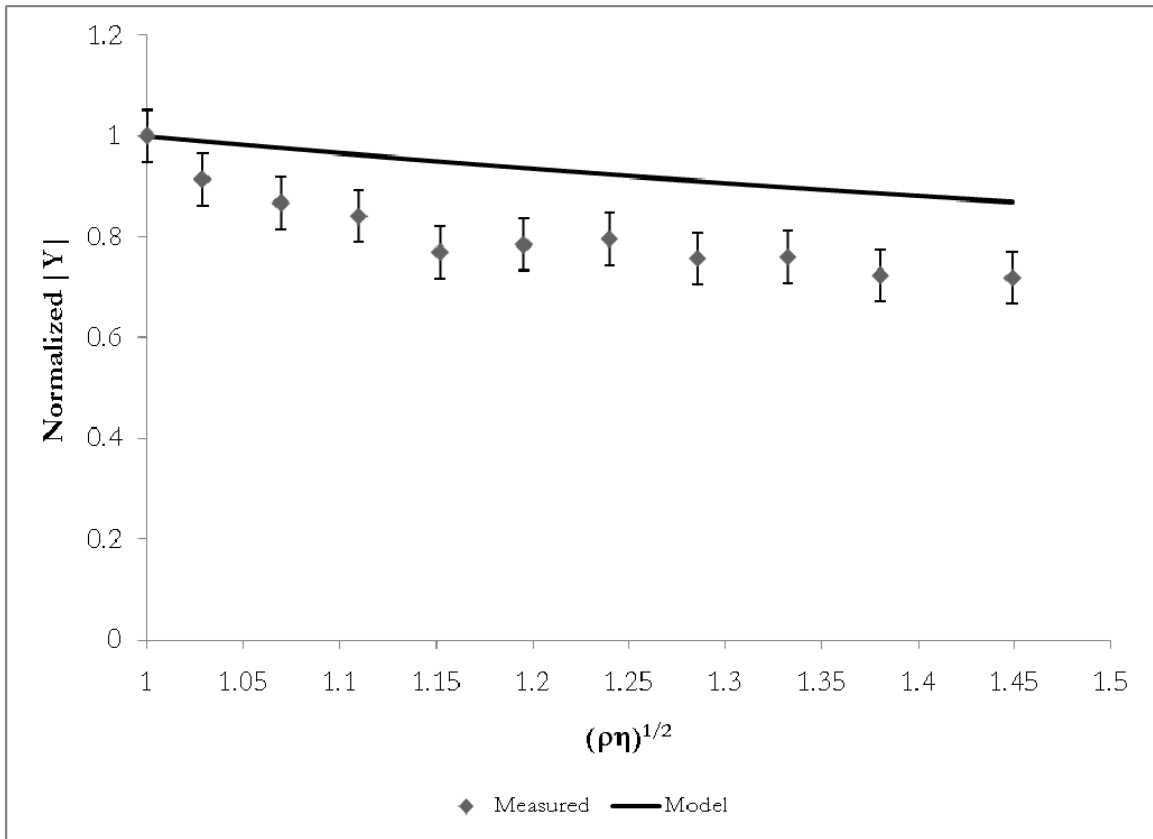
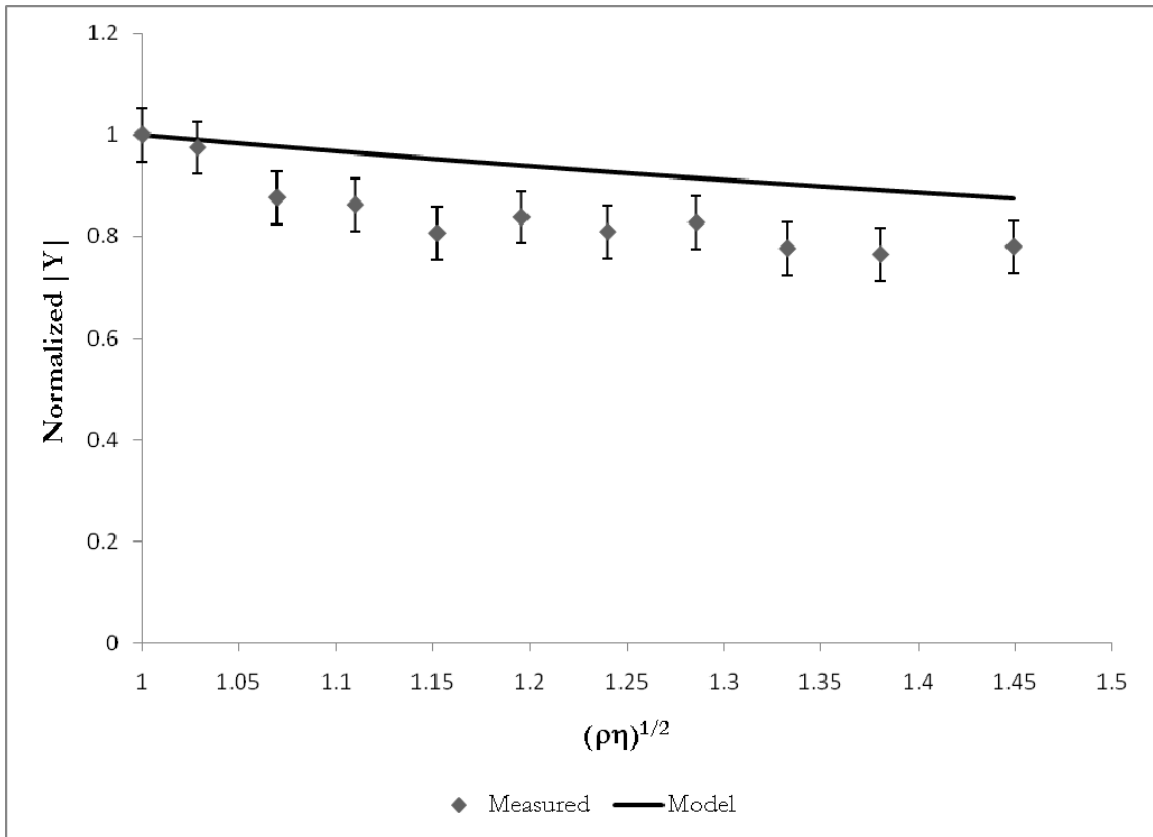


Figure 38. Normalized peak admittance of an LFE sensor element with a 1.0-mm electrode gap as a function of kinematic viscosity



**Figure 39. Normalized peak admittance of an LFE sensor element with a 2.0-mm electrode gap as a function of kinematic viscosity**

The phase of the admittance of the LFE sensor element at its resonant frequency as a function of kinematic viscosity is shown in Figure 40 - Figure 42. The phase predicted by the model is within the experimental error of the measured data.



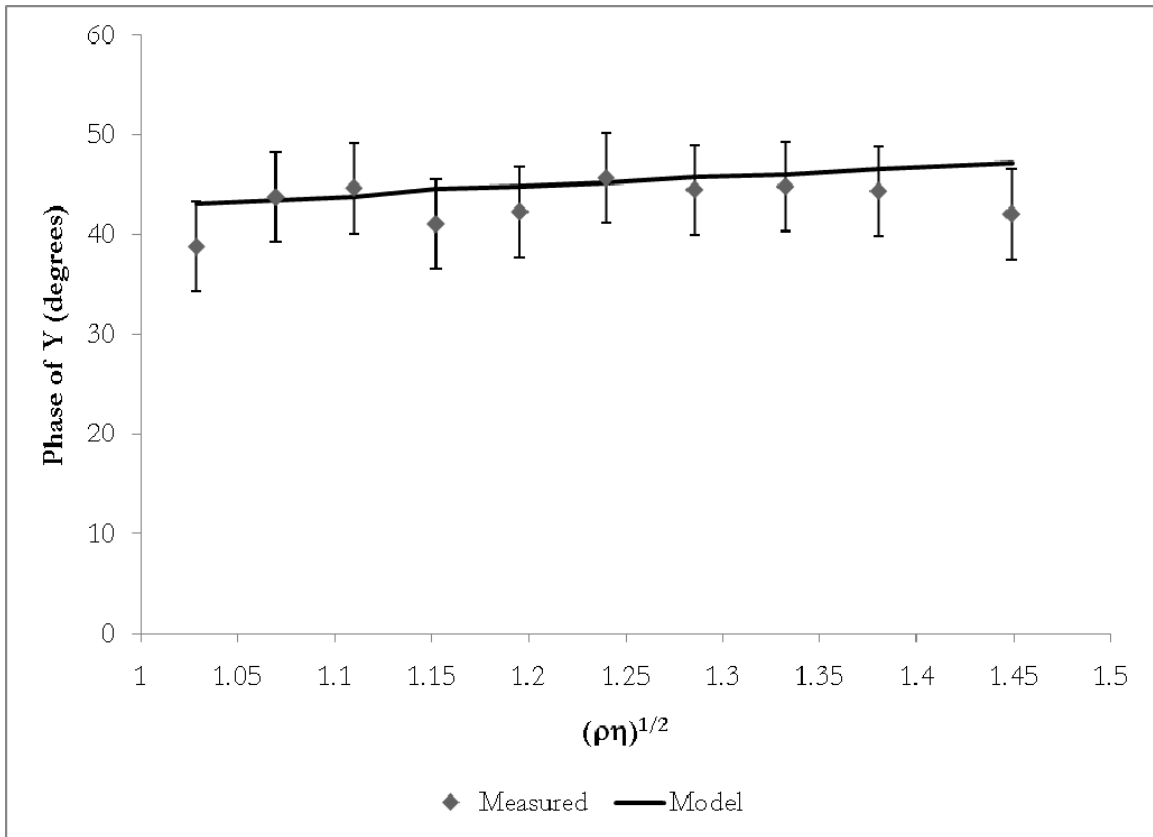


**Figure 40. Phase at resonance of an LFE sensor element with a 0.5-mm electrode gap as a function of kinematic viscosity**

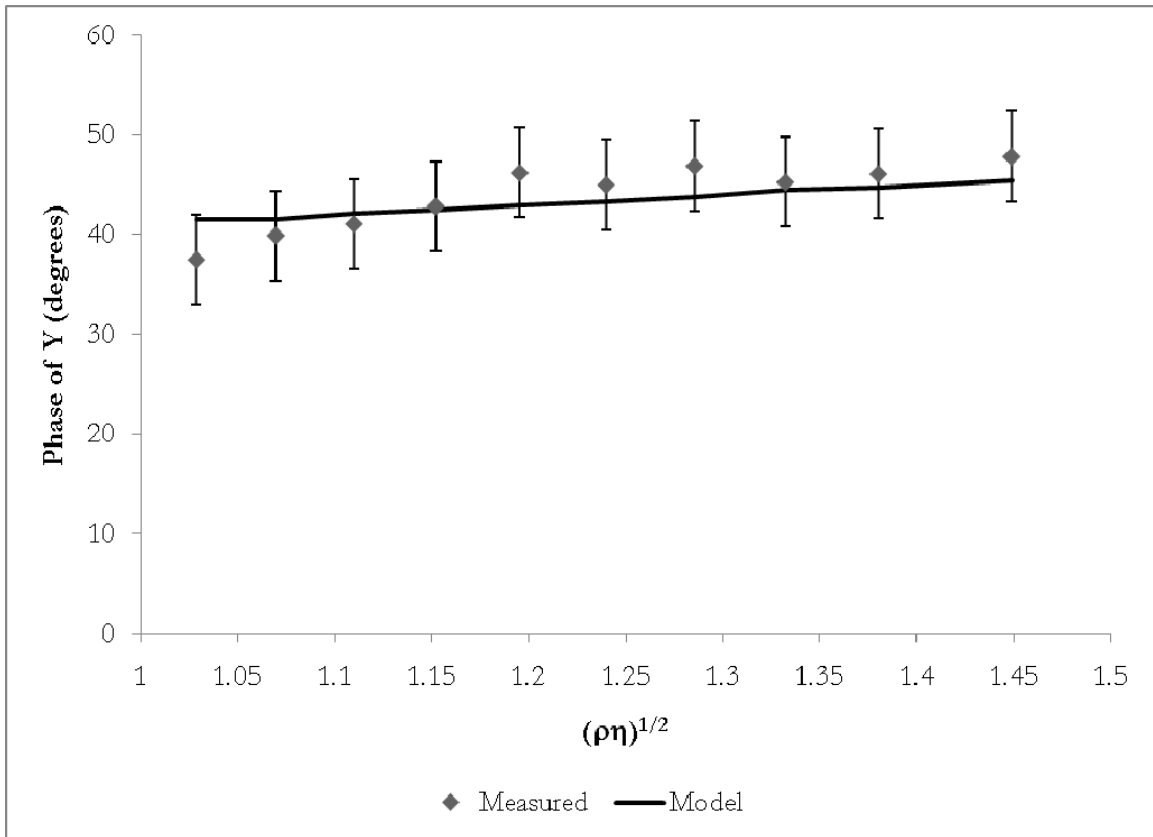
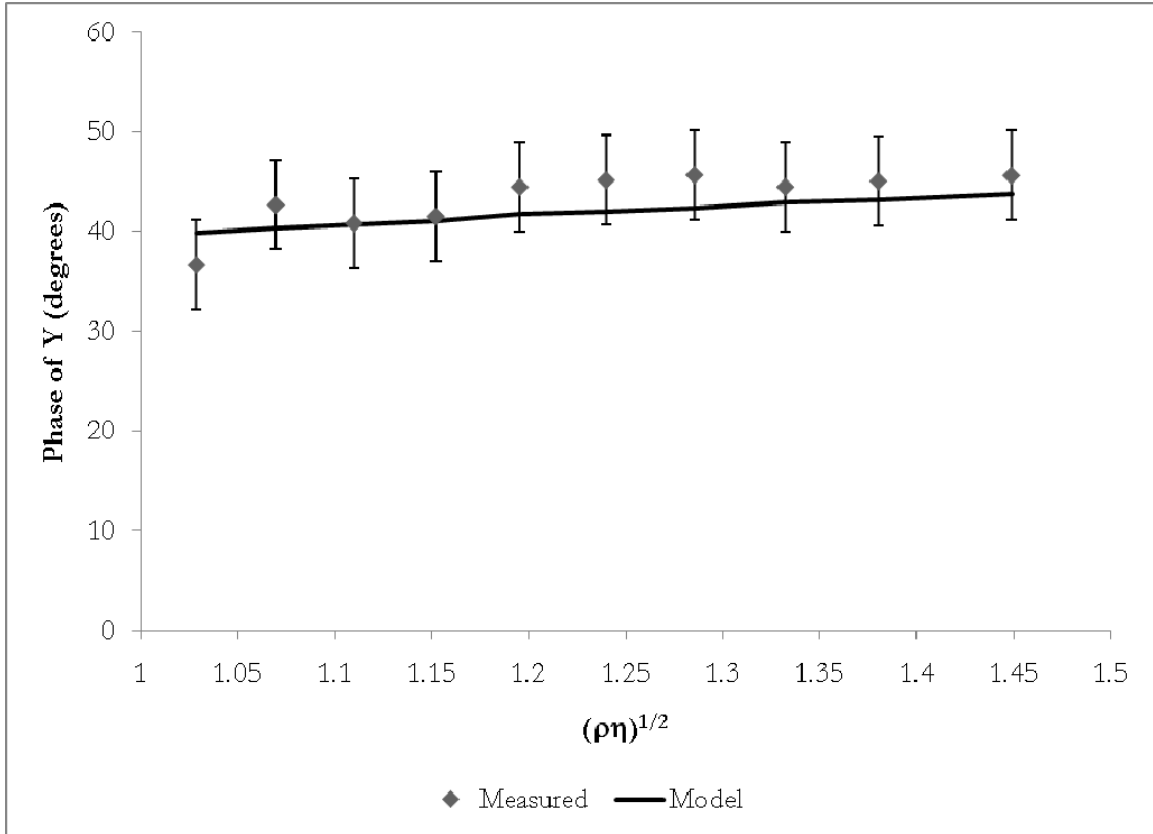


Figure 41. Phase at resonance of an LFE sensor element with a 1.0-mm electrode gap as a function of kinematic viscosity



**Figure 42. Phase at resonance of an LFE sensor element with a 2.0-mm electrode gap as a function of kinematic viscosity**

Overall, the model predicts the admittance trends of the LFE sensor elements due to changes in the kinematic viscosity of the liquid load. The precision of the model is affected by several factors, including the material properties of the quartz and liquid load as well as the influence of temperature on the quartz and liquid load.

#### **5.4. LFE Sensor Element Response to Relative Permittivity**

The data for the frequency shift, normalized to the series resonant frequency in deionized water as a function of relative permittivity are given in Figure 43 - Figure 45. The curves show that the model predicts, within experimental error, the frequency shift due to liquid permittivity changes at the surface of the LFE sensor element. The primary sources of experimental error for these data are the resolution of the network analyzer ( $\pm 25$  ppm),

the temperature variations in the laboratory ( $\pm 5$  °C), and errors in the concentration of the solutions ( $\pm 0.5$  %).

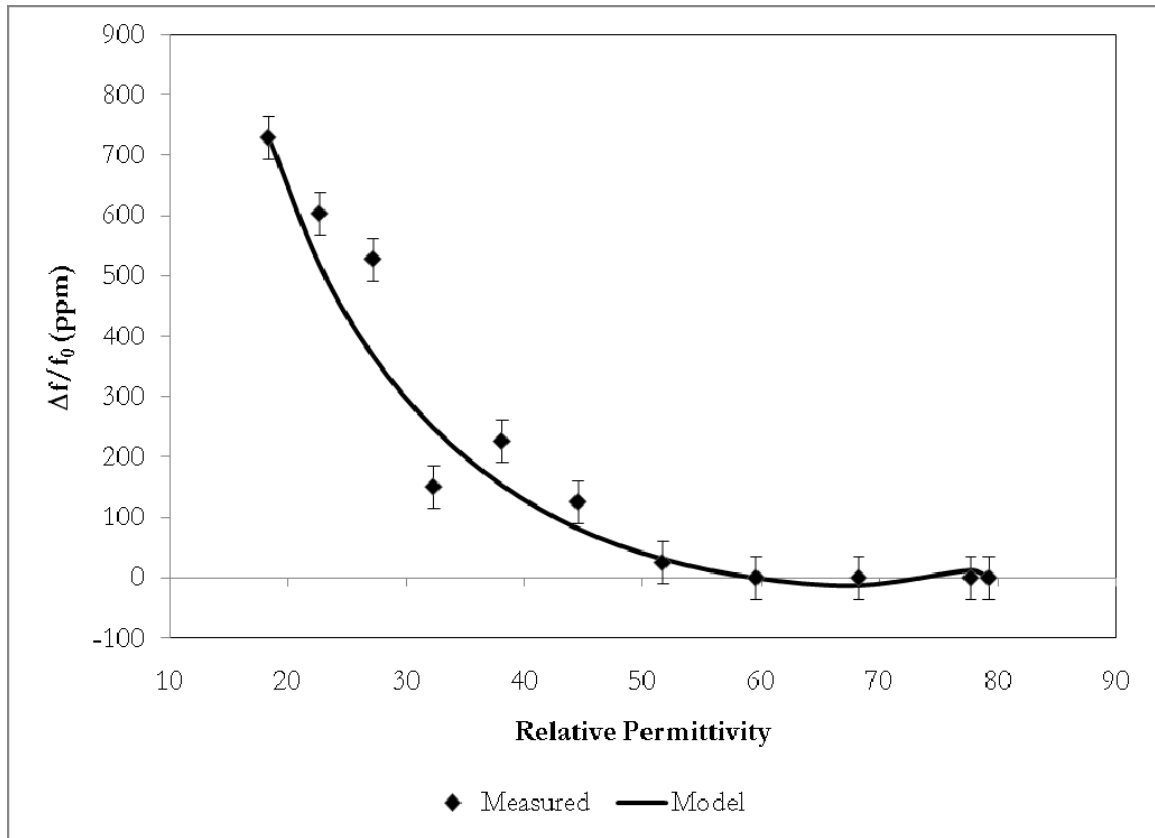


**Figure 43. Normalized frequency shift of an LFE sensor element with a 0.5-mm electrode gap as a function of isopropyl alcohol concentration**

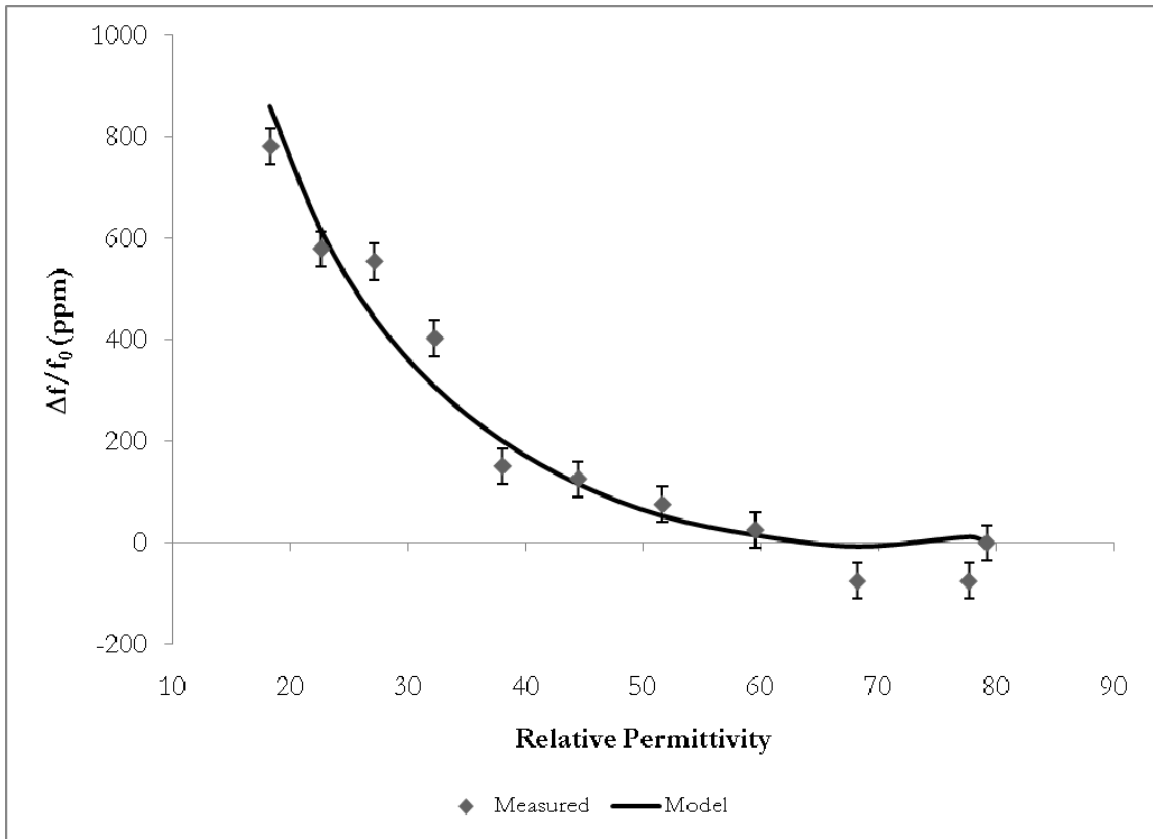


**Figure 44. Normalized frequency shift of an LFE sensor element with a 1.0-mm electrode gap as a function of isopropyl alcohol concentration**

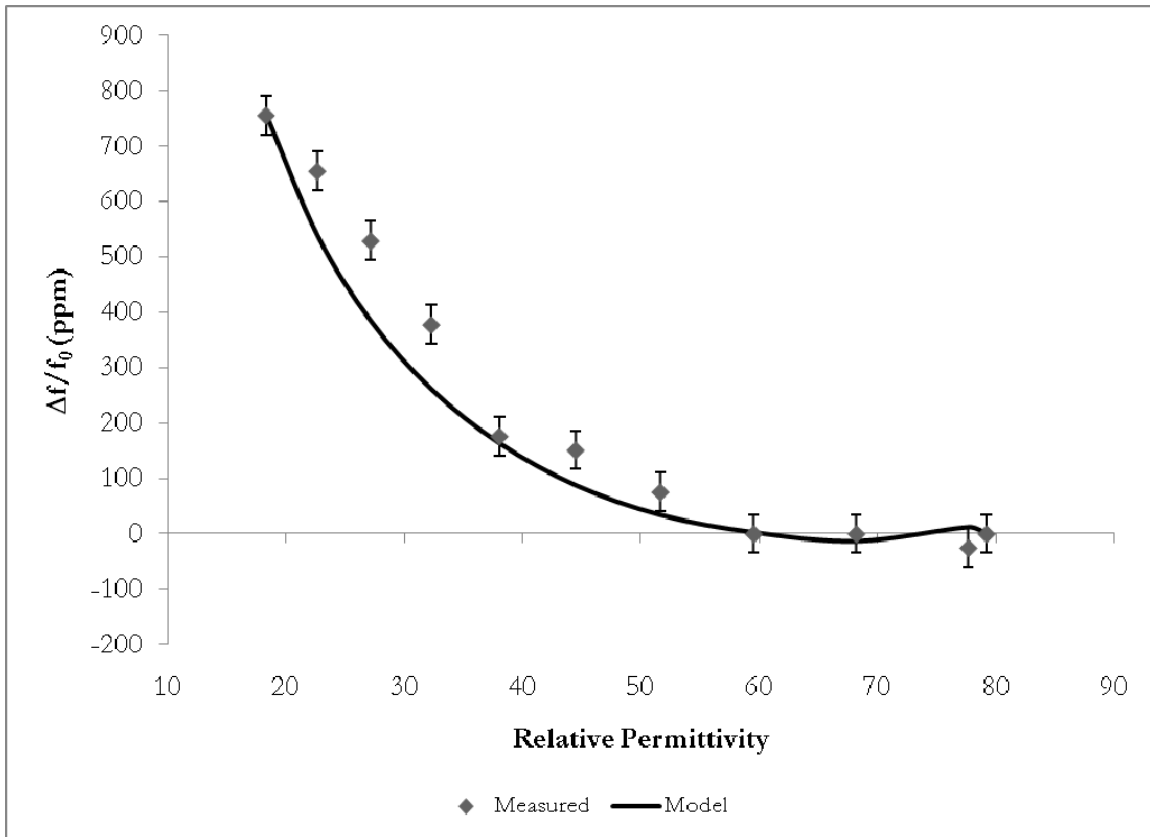


**Figure 45. Normalized frequency shift of an LFE sensor element with a 2.0-mm electrode gap as a function of isopropyl alcohol concentration**

The magnitude of the peak admittance for LFE sensor elements with different electrode gaps, normalized to the value in deionized water, is shown in Figure 46 - Figure 48. The decrease in the peak admittance due to relative permittivity predicted by the model is much less than was found in the measured data.

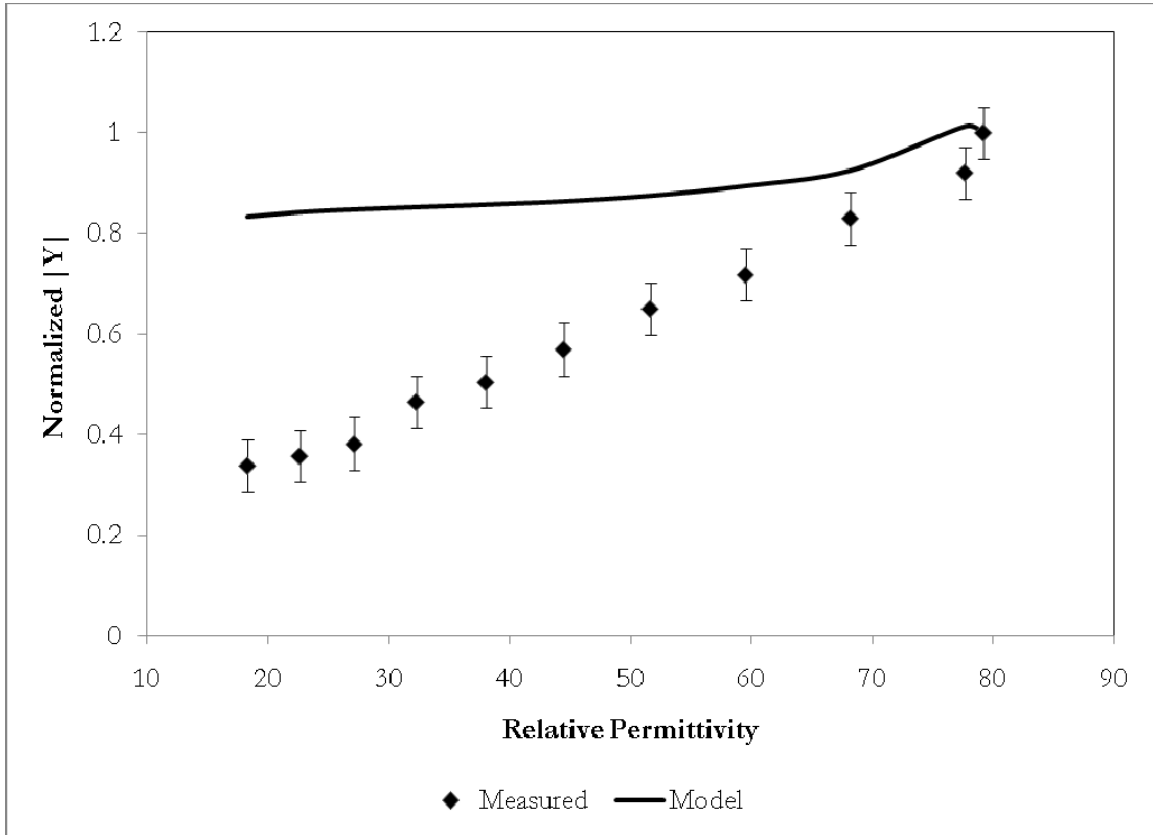


Figure 46. Normalized peak admittance of an LFE sensor element with a 0.5-mm electrode gap as a function of relative permittivity

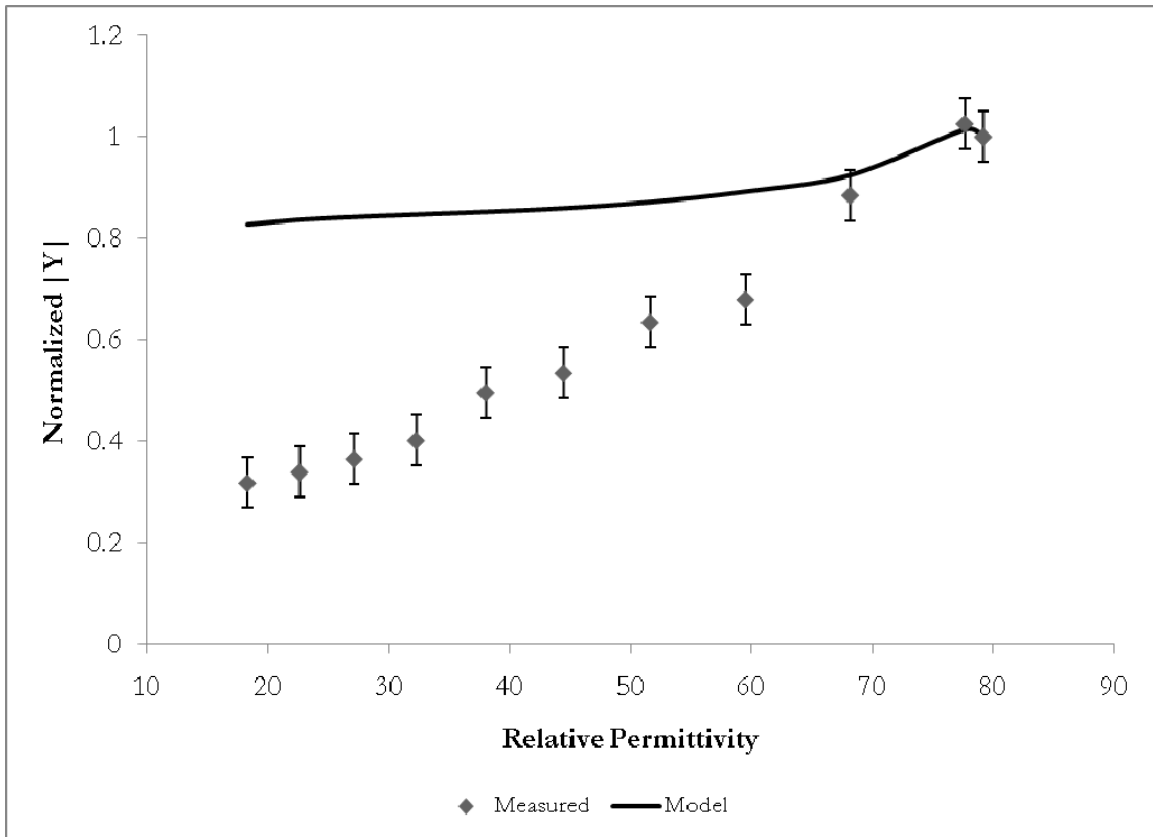
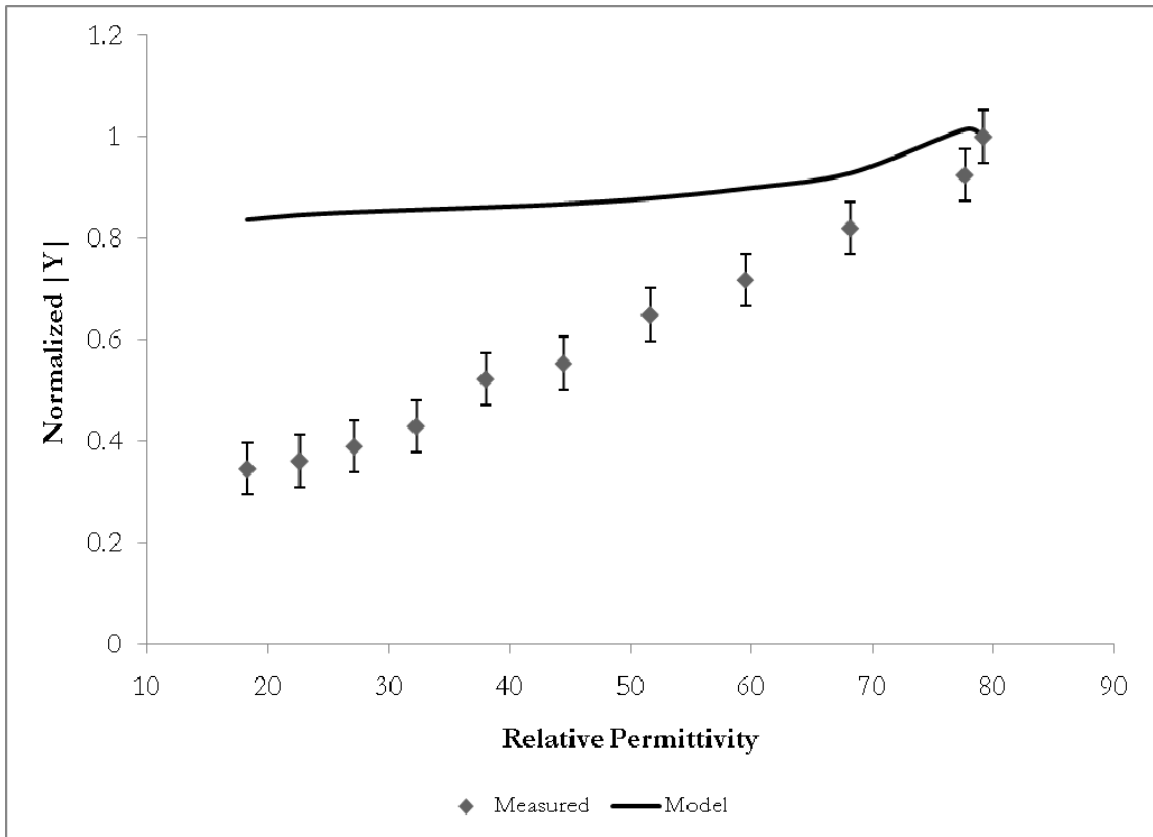


Figure 47. Normalized peak admittance of an LFE sensor element with a 1.0-mm electrode gap as a function of relative permittivity





**Figure 48. Normalized peak admittance of an LFE sensor element with a 2.0-mm electrode gap as a function of relative permittivity**

The phase of the admittance of the LFE sensor element at its resonant frequency as a function of relative permittivity is shown in Figure 49 - Figure 51. The phase at resonance predicted by the model is much less than was determined experimentally.

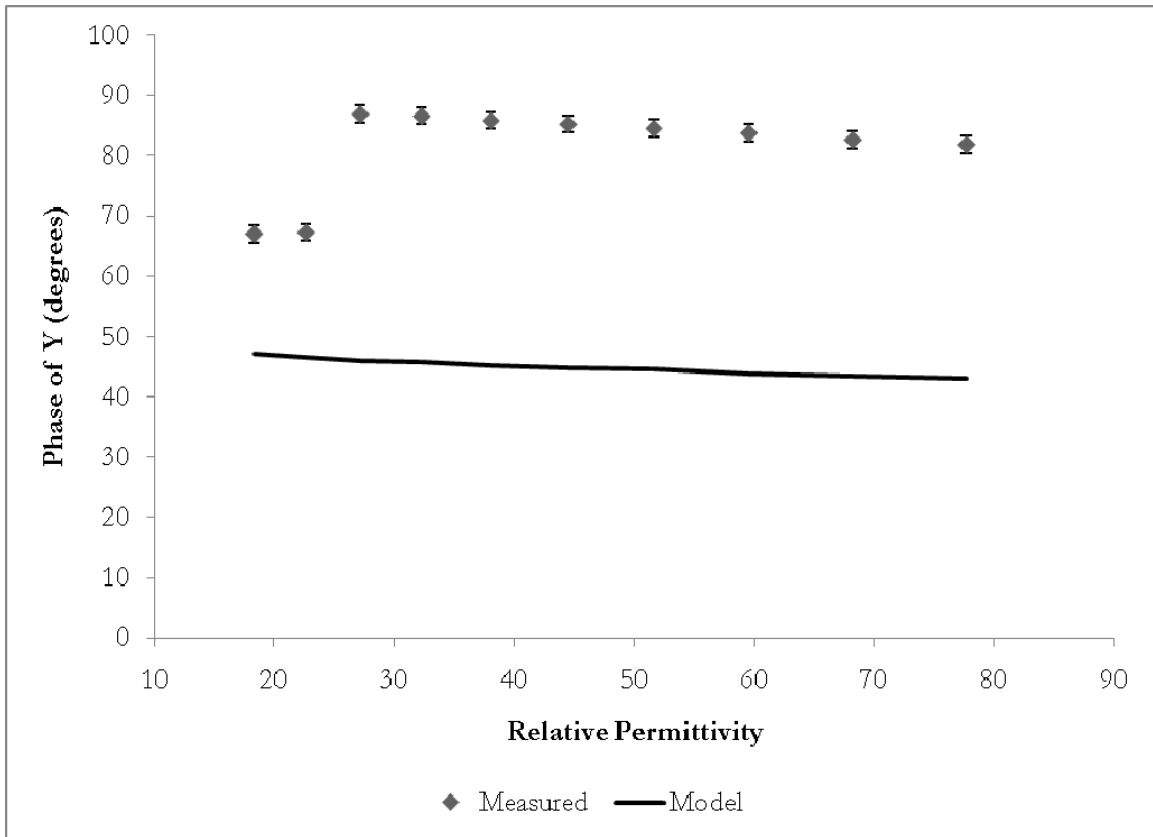
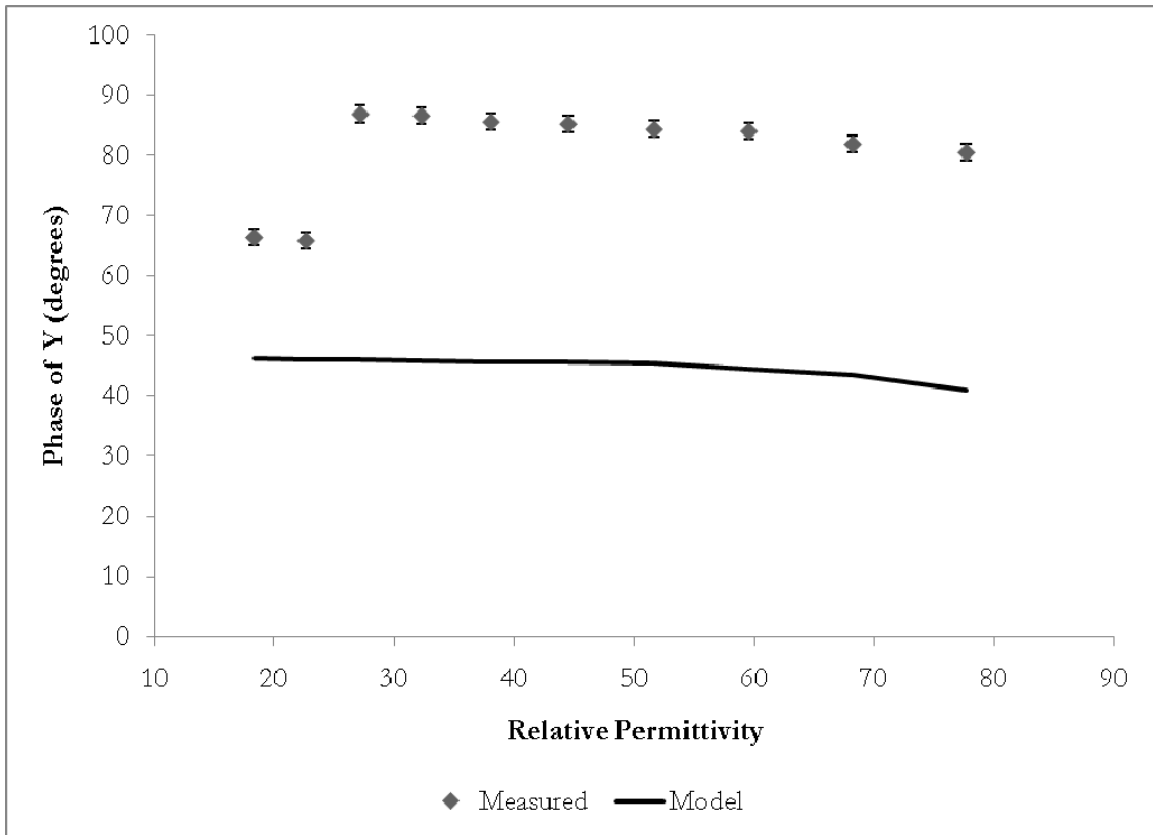
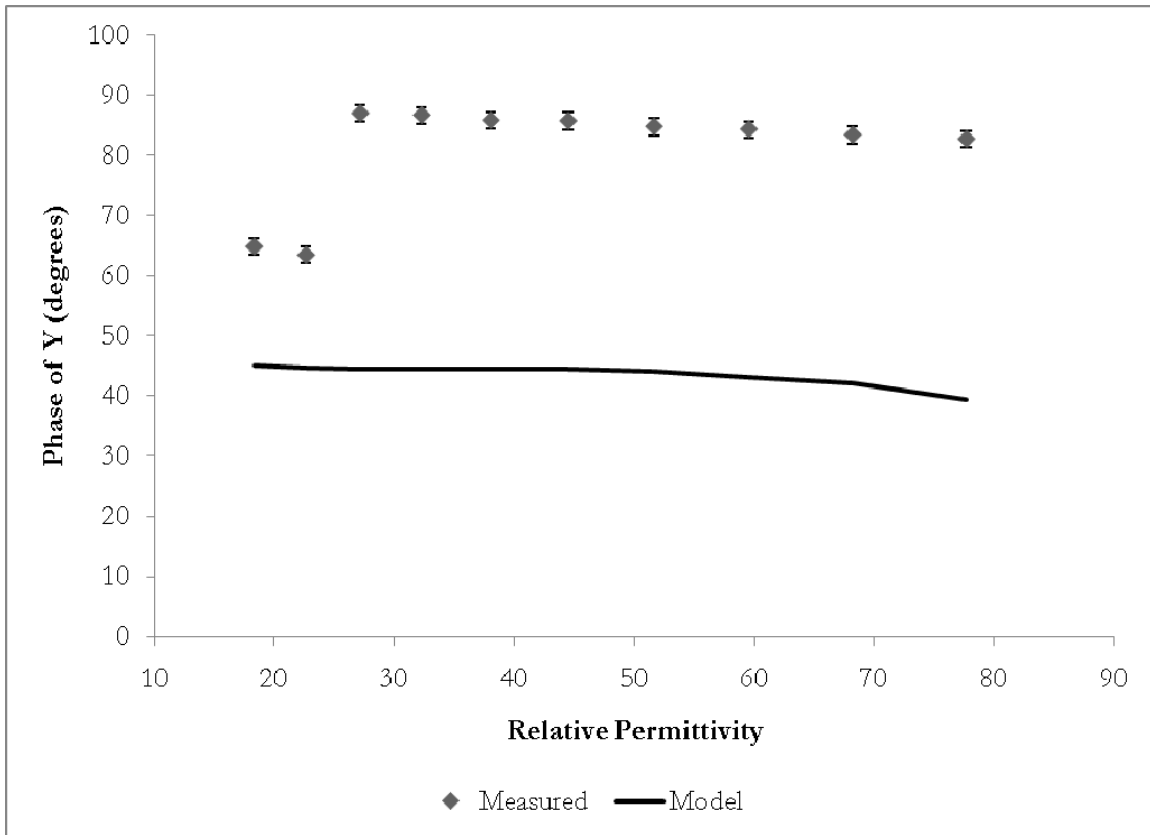


Figure 49. Phase at resonance of an LFE sensor element with a 0.5-mm electrode gap as a function of relative permittivity



**Figure 50. Phase at resonance of an LFE sensor element with a 1.0-mm electrode gap as a function of relative permittivity**



**Figure 51. Phase at resonance of an LFE sensor element with a 2.0-mm electrode gap as a function of relative permittivity**

The model gives a prediction, within experimental error, of the frequency shift due to loading by a dielectric liquid. However, the magnitude and phase of the admittance at the resonant frequency predicted by the model differs substantially from the measured data on the devices. There are two reasons that are believed to be the cause of the error.

The first reason is that the model was developed under the assumption that the driving electric field,  $E_3$ , is uniform between the electrodes, which were modeled on the sides of the quartz plate. However, the LFE sensor element has electrodes mounted on the reference surface of the quartz plate. This will, in practice, lead to a driving electric field that has electric field components,  $E_2$  and  $E_3$ , both in the quartz plate and in the region below the quartz plate. While the static capacitance,  $C_0$ , was experimentally determined, the

assumptions about the quartz plate, while sufficient for determining the admittance of the LFE sensor element in a static environment, such as deionized water, lead to errors in the model when exposed to a dielectric load. One option is to calculate  $C_0$  using elliptic integrals [80].

The second error may be due to changes in the parasitic capacitance of the holder due to the dielectric load. If one examines Figure 49 - Figure 51, it can be noted that even for small permittivity changes from deionized water, the phase of the admittance is almost purely capacitive. This leads to the conclusion that the admittance at resonance is strongly influenced by an interaction between the LFE sensor element holder and the contacting liquid.

### **5.5. LFE Sensor Element Response to Conductivity**

The data for the frequency shift, normalized to the series resonant frequency in deionized water as a function of liquid conductivity are given in Figure 52 - Figure 54. The curves show that the the frequency shift predicted by the model due to liquid conductivity changes at the surface of the LFE sensor element converges to the measured values for the solutions having higher conductivity. The primary sources of experimental error for these data are the resolution of the network analyzer ( $\pm 25$  ppm), the temperature variations in the laboratory ( $\pm 5$  °C), and errors in the concentration of the solutions ( $\pm 5$   $\mu\text{g/ml}$ ).

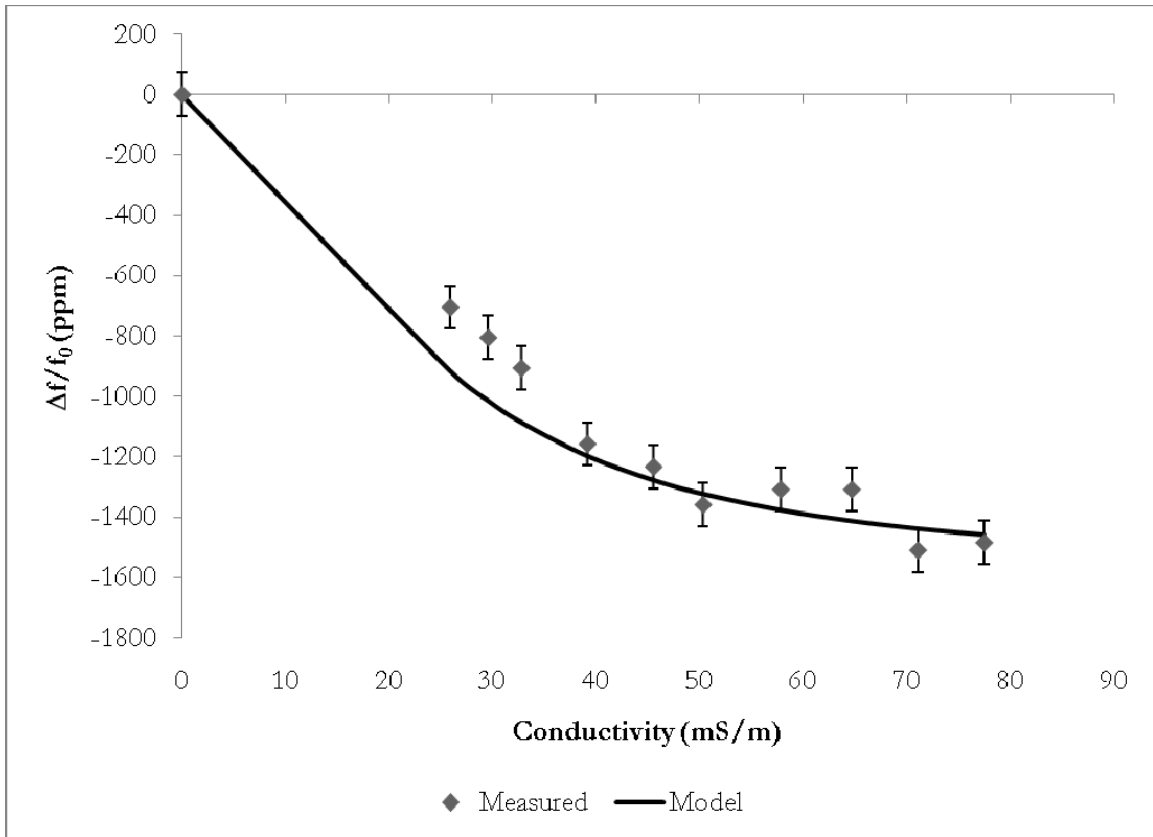


**Figure 52. Normalized frequency shift of an LFE sensor element with a 0.5-mm electrode gap as a function of sodium chloride concentration**

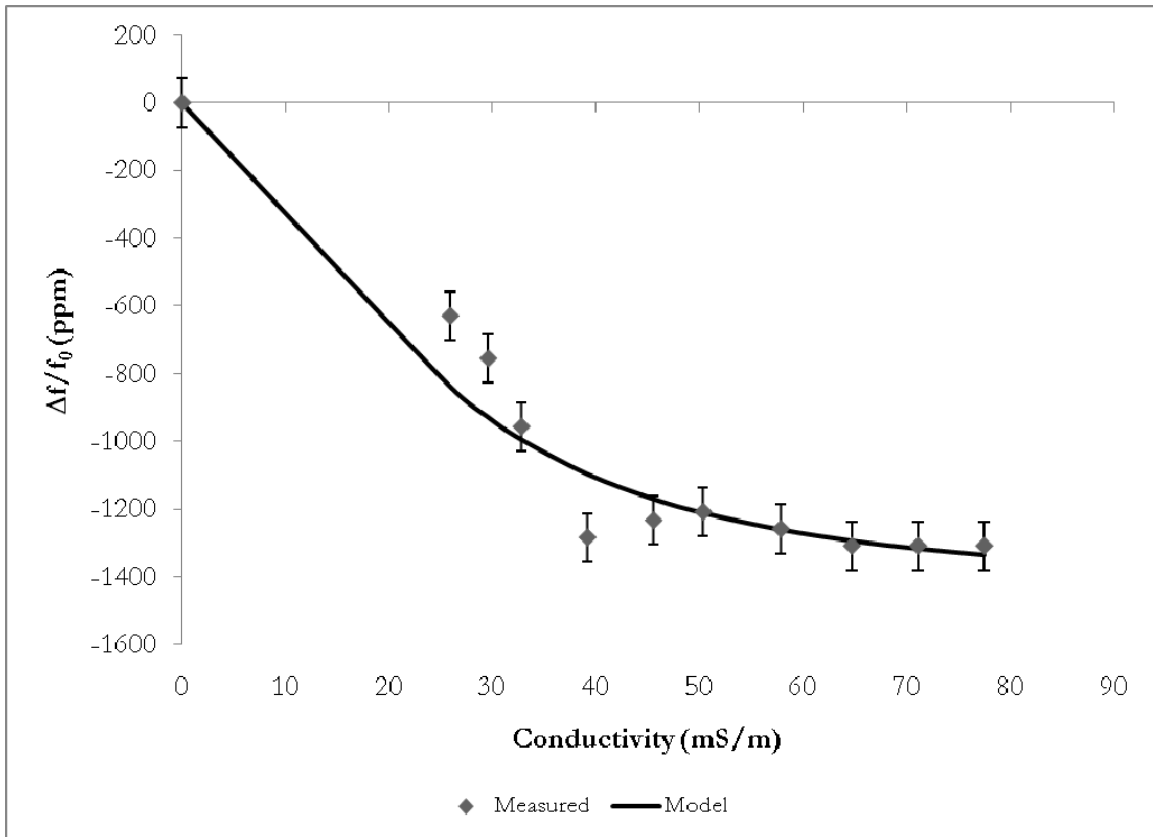


**Figure 53. Normalized frequency shift of an LFE sensor element with a 1.0-mm electrode gap as a function of sodium chloride concentration**

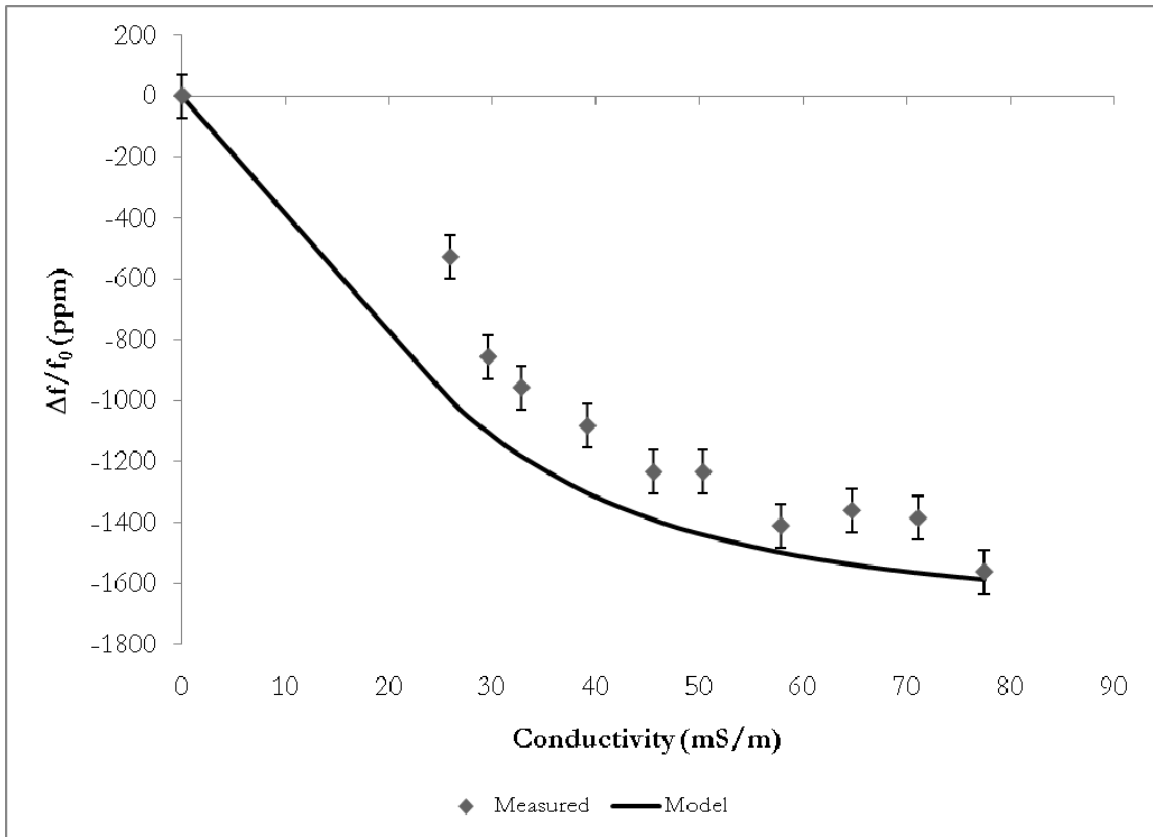


**Figure 54. Normalized frequency shift of an LFE sensor element with a 2.0-mm electrode gap as a function of sodium chloride concentration**

The magnitude of the peak admittance for LFE sensor elements with different electrode gaps, normalized to the value in deionized water, is shown in Figure 55 - Figure 57. The trend of the peak admittance due to liquid conductivity predicted by the model is similar to that of the measured data. However, the peak admittance predicted by the model does not reliably agree with the measured data.



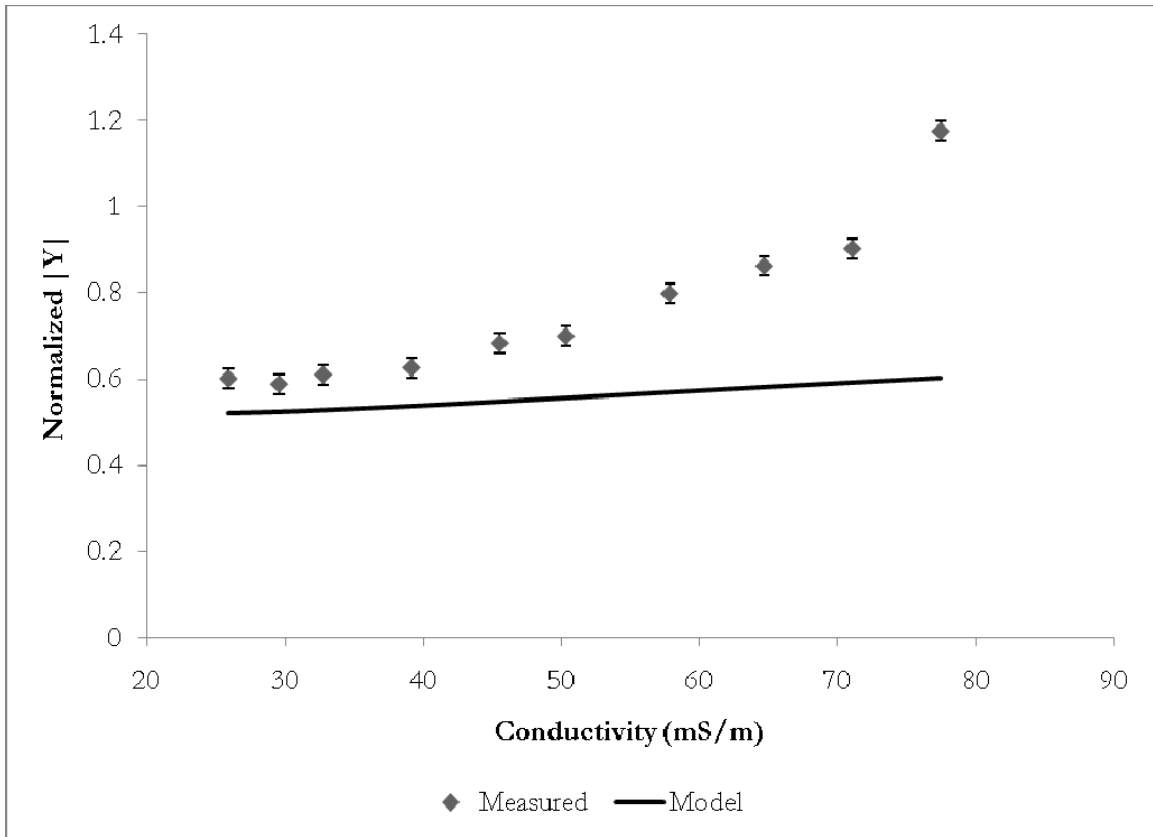


Figure 55. Normalized peak admittance of an LFE sensor element with a 0.5-mm electrode gap as a function of conductivity

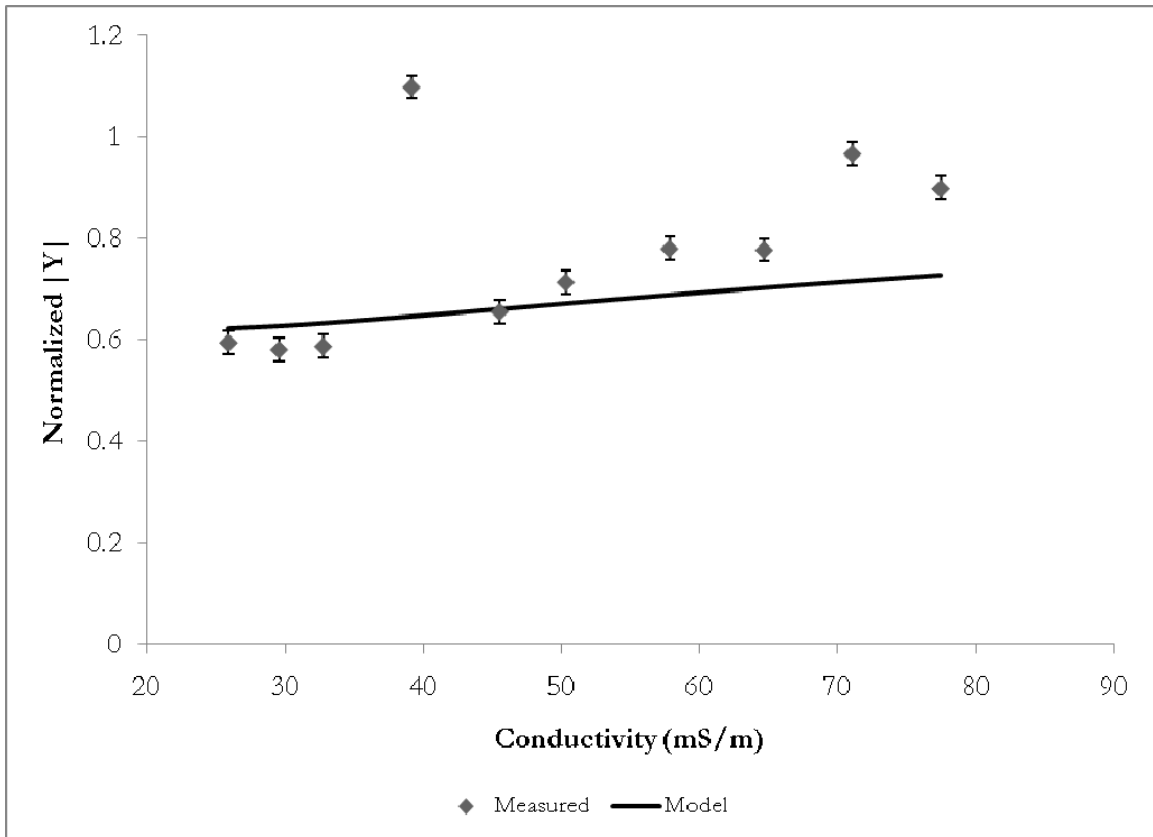
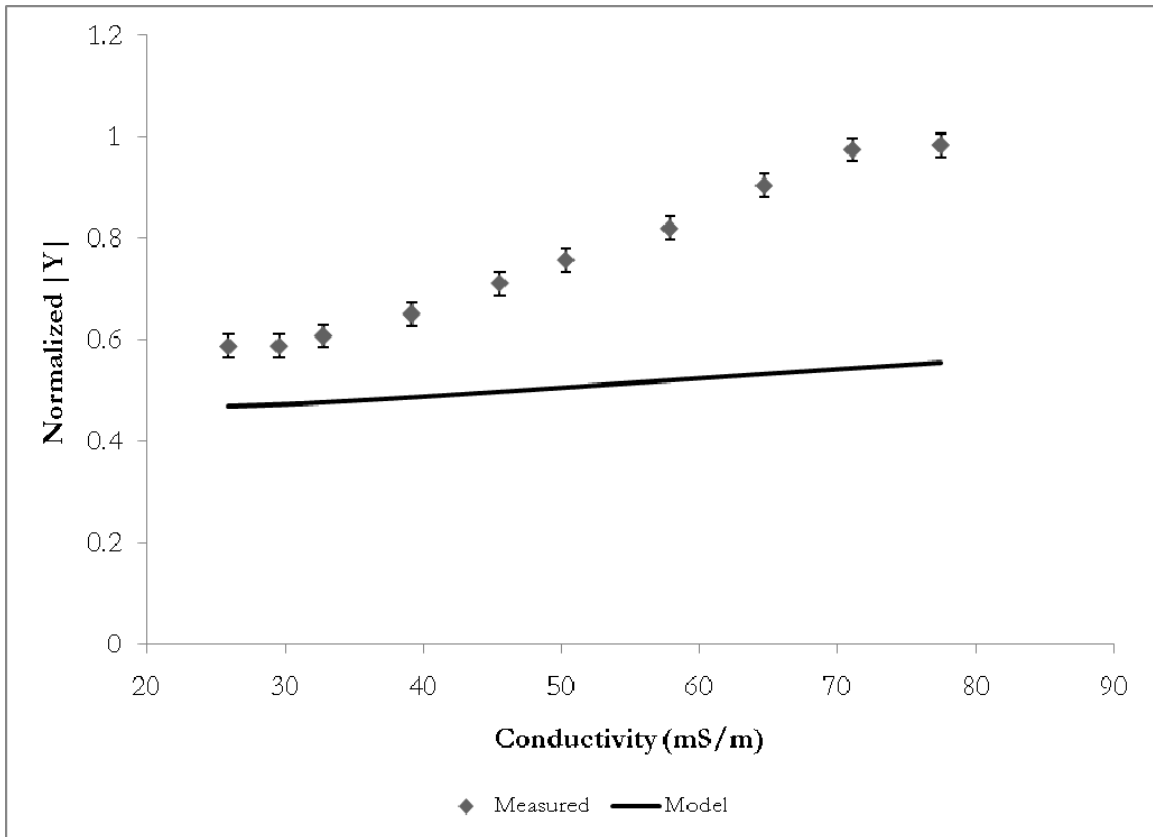


Figure 56. Normalized peak admittance of an LFE sensor element with a 1.0-mm electrode gap as a function of conductivity



**Figure 57. Normalized peak admittance of an LFE sensor element with a 2.0-mm electrode gap as a function of conductivity**

The phase of the admittance of the LFE sensor element at its resonant frequency as a function of liquid conductivity is shown in Figure 58 - Figure 60. The phase of the LFE sensor element at resonance predicted by the model is substantially greater than the measured data.

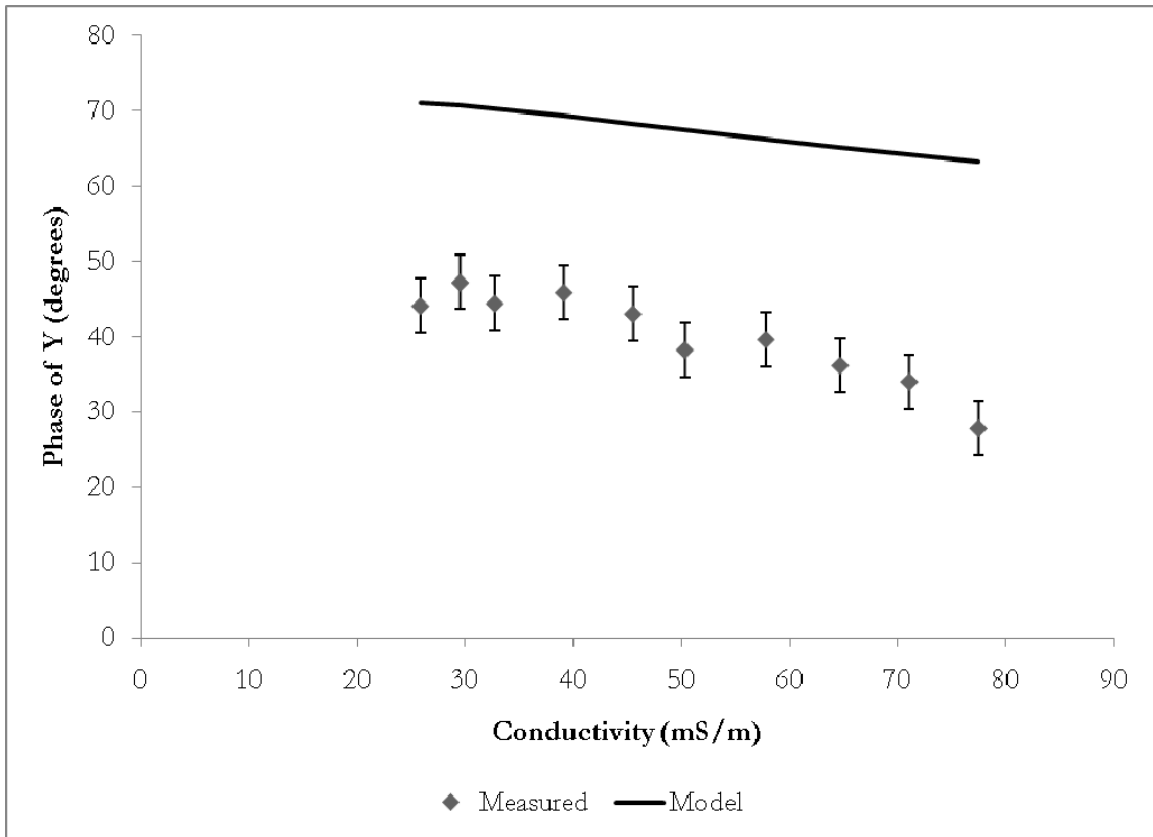
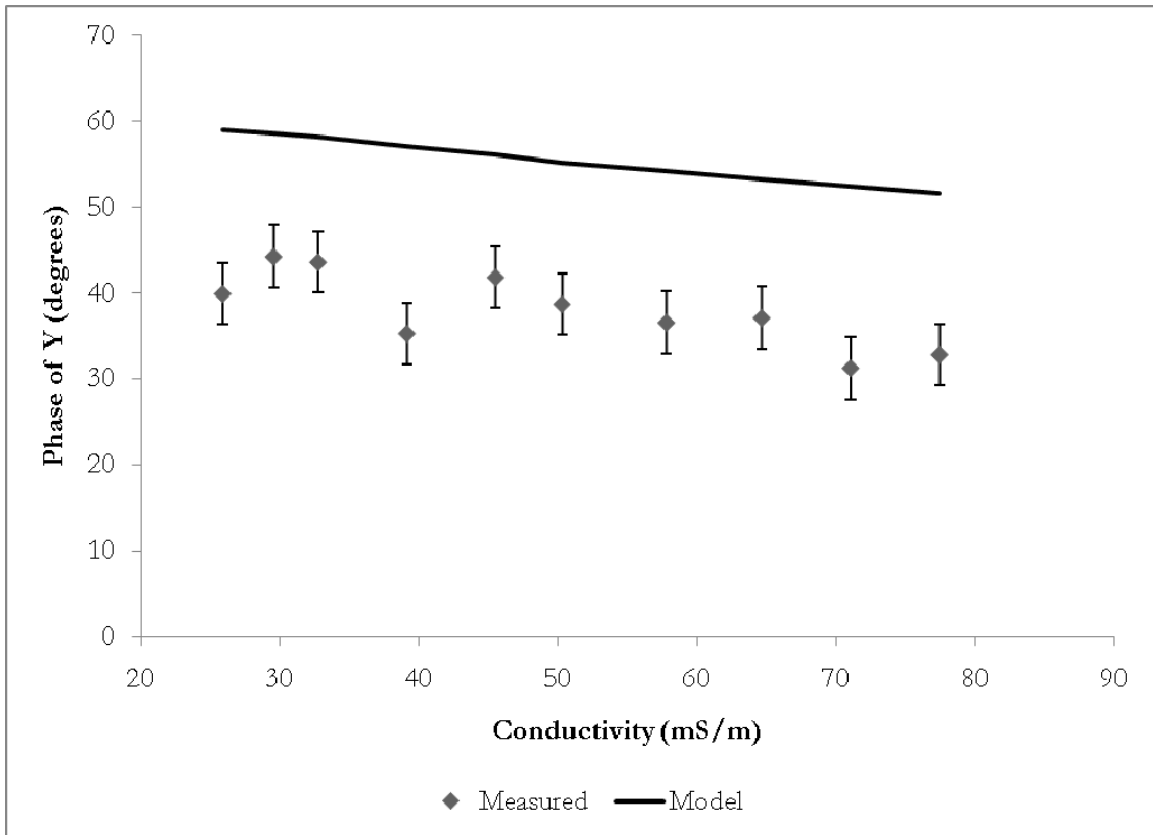
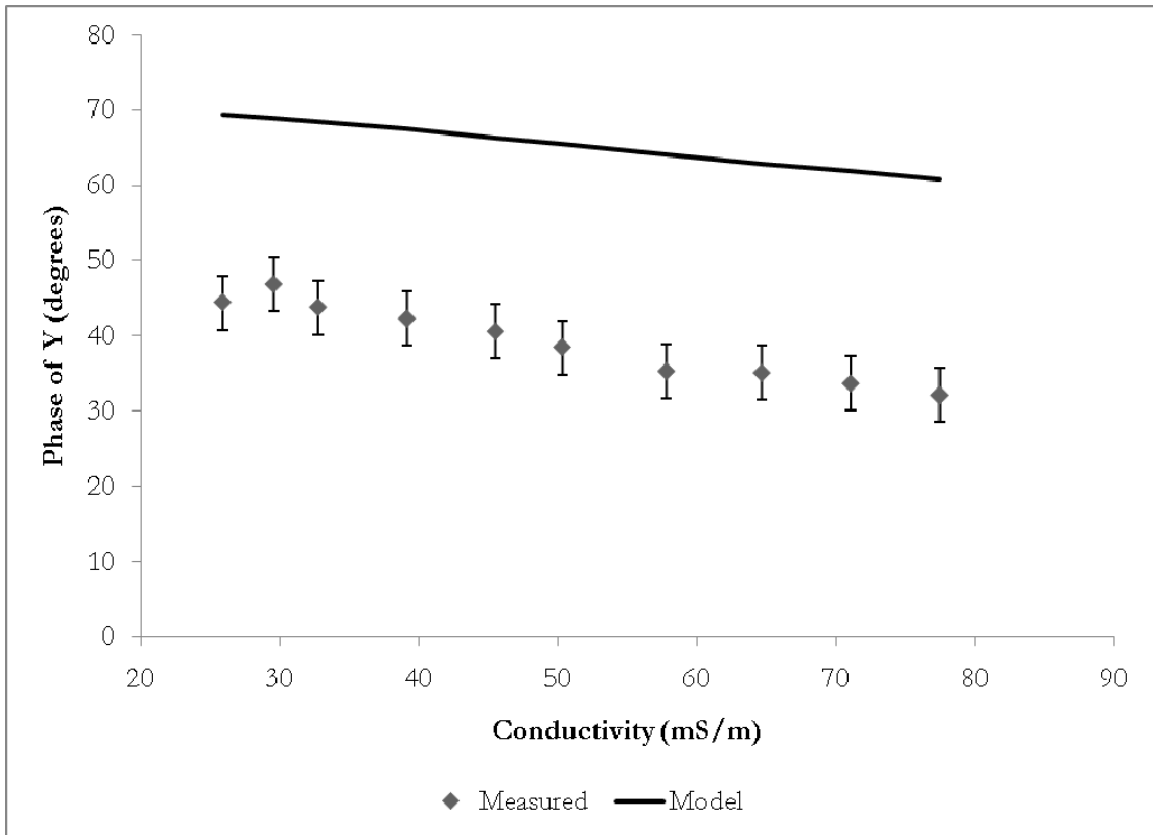


Figure 58. Phase at resonance of an LFE sensor element with a 0.5-mm electrode gap as a function of conductivity



**Figure 59. Phase at resonance of an LFE sensor element with a 1.0-mm electrode gap as a function of conductivity**



**Figure 60. Phase at resonance of an LFE sensor element with a 2.0-mm electrode gap as a function of conductivity**

The model gives a prediction, within experimental error, of the frequency shift due to loading by a conductive liquid. However, the magnitude and phase of the admittance at the resonant frequency predicted by the model differs substantially from the measured data on the devices. The errors are believed to be due to the driving electric field having perpendicular components in addition to the lateral components and to the parasitics of the holder. The frequency change data also leads to the conclusion that the effective penetration,  $h_{eff}$ , into the liquid is a function of conductivity.

## 5.6. Discussion

The model developed here predicts, within experimental error, the frequency shift due to changes in kinematic viscosity, permittivity, and conductivity of the contacting liquid.

However, frequency change is only one parameter of the admittance at or near resonance that changes due to changes in the contacting liquid. Some of the other parameters that can be examined are:

- the magnitude of the admittance at the resonant frequency
- antiresonant frequency
- the magnitude of the admittance at the antiresonant frequency
- the phase of the admittance at the resonant frequency
- the phase of the admittance at the antiresonant frequency
- the frequency difference between the antiresonant and resonant frequency.

The measured and model data for these parameters are given in Appendix D.

It is useful to examine the influence of viscoelastic and dielectric effects on the frequency of the LFE sensor element separately for liquids that exhibit changes in both. The glycerol and isopropanol solutions used in these experiments vary in density, viscosity, and permittivity for the ranges used. The influence of kinematic viscosity and permittivity are separated out for an LFE sensor element with an electrode gap of 0.5 mm and is shown in Figure 61 and Figure 62. The plot in Figure 61 shows that the normalized frequency shift of the LFE sensor is the sum of the normalized frequency shift due to kinematic viscosity and permittivity, within 40 ppm of experimental error. When the LFE sensor element is exposed to a dielectric liquid, (Figure 62), with small changes in kinematic viscosity, the normalized frequency shift of the sensor element is better predicted by treating the liquid as a purely dielectric liquid. Examining the curves in Figure 62 the normalized frequency shift due to permittivity changes in the liquid has an average deviation from experimental error of 70 ppm. The normalized frequency shift due to the sum of permittivity and kinematic viscosity in the liquid has an average deviation from experimental error of 151 ppm. This leads to the

conclusion that the dielectric effects of the liquid on the LFE sensor element dominate the frequency response. The plots for the devices having electrode gaps of 1.0 mm and 2.0 mm exhibited similar behavior.

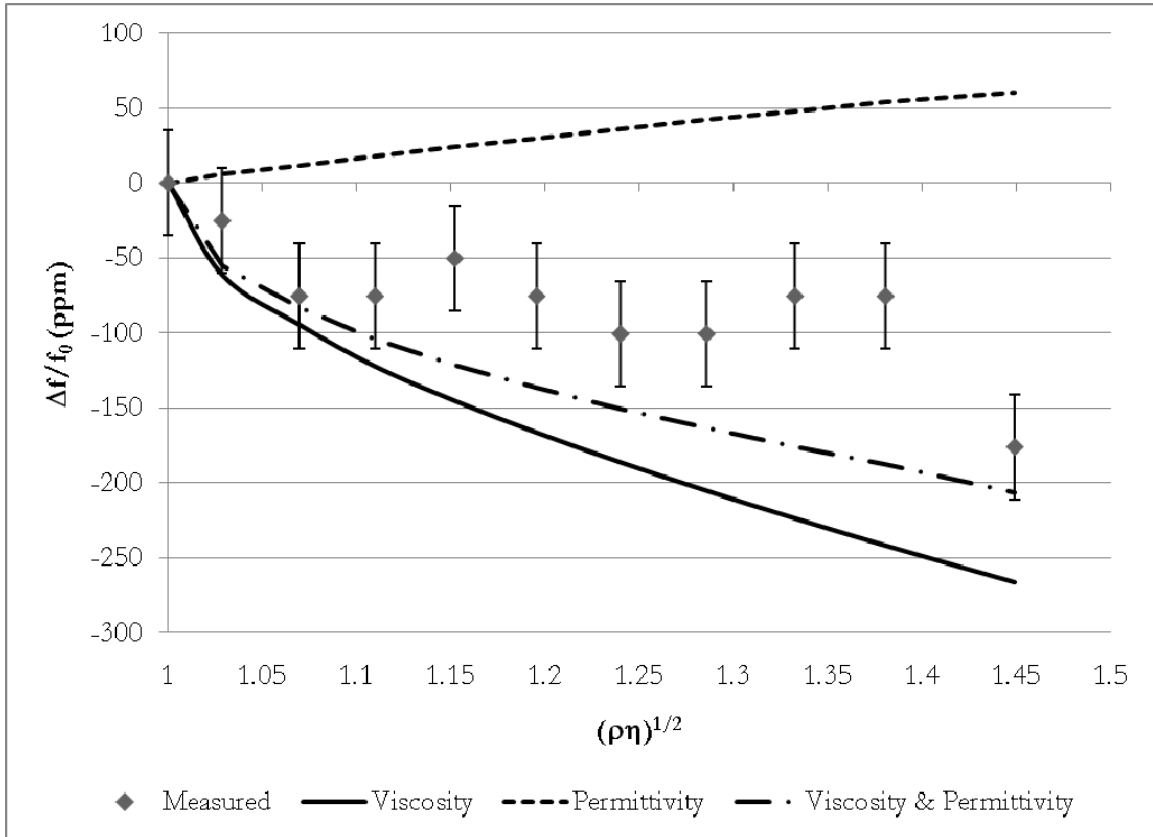


**Figure 61.** Normalized frequency shift of an LFE sensor element with a 0.5-mm electrode gap as a function of kinematic viscosity with the frequency shift due to kinematic viscosity and permittivity separated



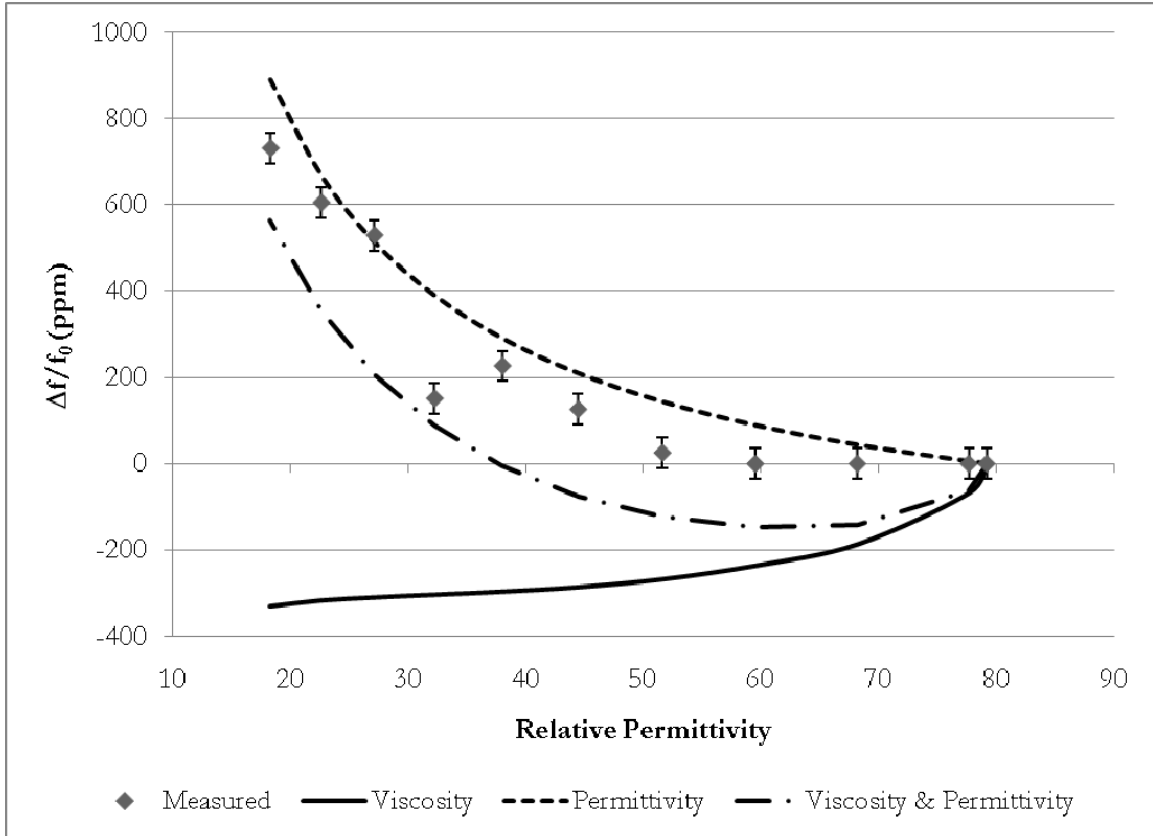


**Figure 62. Normalized frequency shift of an LFE sensor element with a 0.5-mm electrode gap as a function of relative permittivity with the frequency shift due to kinematic viscosity and permittivity separated**

The model is less successful at predicting the peak magnitude of the admittance.

This is most likely due to modeling the electrodes on the side faces of the crystal, rather than where they exist physically, on the reference surface of the quartz disc. The model follows similar trends to the measured data for changes in kinematic viscosity, permittivity, and conductivity. There are considerable discrepancies of the peak magnitude due to electrical property changes. The errors in the model due to electrode geometry will be most evident in the response of the model to liquid permittivity. This is because the static capacitance,  $C_0$ , is more complex for the electrodes on the reference face, than for the geometry assumed in the model. The static capacitance can be more accurately modeled using elliptic integrals for the electrodes on the reference surface of the LFE sensor element [80].

The use of electrodes on the edge of the plate, rather than on the reference surface to calculate the impedance is, most likely, the primary source of error in the equivalent circuit model. The placement of the electrodes on the edge of the plate, allowed for the assumption that the driving electric field,  $E_3$ , does not vary in the  $x_3$  direction. In reality, the driving electric field contains a lateral component,  $E_3$ , and a perpendicular component,  $E_2$  and the electric field will not uniform between the electrodes. In developing the expression for the admittance of the LFE sensor element it was assumed that the driving electric field was contained entirely within the quartz plate. With the electrodes on the reference surface of the quartz plate, there will be an electric field in the air between the two electrodes. The strength of the electric field in the air will decrease as the gap width increases.

It is also interesting to note that the value for the effective penetration of the electric field associated with the thickness shear mode,  $h_{eff}$ , decreases as the liquid conductivity increases. The values for  $h_{eff}$  for the sodium chloride solutions are given in Table 6. The effective penetration depth is roughly proportional to the electrode gap. The change in  $h_{eff}$  is due to the fact that as the conductivity increases, so does the relaxation frequency. As the relaxation frequency approaches the series resonant frequency of the LFE sensor element, electric field probes the bulk liquid less efficiently due to the realignment of the charges in the double layer at the sensor surface.

**Table 6. Effective penetration of the electric field in sodium chloride solutions**

electrode gap (mm)	$h_{eff}$ (mm)
0.5	0.146
1.0	0.340
2.0	0.537

The analysis used to develop the equivalent circuit model is for the thickness shear mode in AT-cut quartz. Quartz is a piezoelectric crystal with symmetry class, trigonal  $32$  [81]. The equivalent circuit will apply to any crystal with symmetry class, trigonal  $32$ ,  $3m$ , and  $\bar{3}m$ , for the thickness shear mode. The circuit itself can be used for crystals of any orientation. However, the expressions for the circuit elements will be different for crystals with different symmetry classes. The same analysis that was used in this work can be applied to crystals with other symmetry classes to derive expressions for the circuit elements.

Overall, the model presents a good first-order approximation of the admittance in deionized water, while also predicting the frequency shift due to changes in liquid kinematic viscosity, permittivity, and conductivity at the surface of the LFE sensor element.

The major weakness of the model presented here is the lack of an analytical determination of the effective penetration depth of the electric field into the liquid. The values for  $h_{eff}$  were determined empirically from the data collected. More work can be done to find an analytic expression for  $h_{eff}$  and how it varies as a function of the liquid conductivity.

## Chapter 6

### SUMMARY, CONCLUSIONS, AND FUTURE WORK

#### 6.1. Summary

An equivalent circuit model for a lateral-field excited (LFE) sensor element under liquid loads has been developed to describe the admittance of the sensor element at or near resonance. Expressions for the admittance at or near resonance and the frequency shift of the LFE sensor element due to changes in kinematic viscosity, permittivity, and conductivity have been developed.

This work has presented the background on bulk acoustic wave (BAW) sensors and LFE resonators and sensors. The theory on elastic waves in non-piezoelectric and piezoelectric solids has been discussed. Qualitative and analytic descriptions of BAW resonators were presented. Three models for BAW resonators were discussed, the Mason model, the Martic model, and the transmission line model for both thickness- and lateral-field excitation. The LFE models were all presented for the air-loaded case. The thickness-field excited resonators were all presented for the air-loaded case and the Martin model and the transmission line model were also discussed under liquid loading.

An analysis of the LFE sensor element under liquid loading was presented. Six boundary conditions, three mechanical and three electrical, were applied to the analysis. From this an expression for the admittance of the LFE sensor element was derived. The analysis was approximated for operation at or near the resonant frequency of the LFE sensor element. An equivalent circuit model was extracted from the admittance. Expressions for the frequency shift of the LFE sensor element due to changes in the kinematic viscosity, permittivity, and conductivity have been derived.

The experimental methods for fabricating, cleaning, and testing the LFE sensor elements was discussed. Finally, the data generated from the equivalent circuit model was compared with measured data under liquid loads with varying kinematic viscosity, permittivity, and conductivity.

## **6.2. Conclusions**

An equivalent circuit model has been developed that reproduces the admittance of an LFE sensor element under deionized water load within  $\pm 5\%$ . An expression for the admittance based on the model at or near resonance has been derived. Additionally, expressions for the frequency shift of an LFE sensor element due to simultaneous viscous, dielectric and conductive loading has been developed.

The equivalent circuit model predicts the frequency shift, within experimental error due to changes in kinematic viscosity, permittivity, and conductivity of a liquid at the sensor surface. Additionally, the model predicts the trend of the peak admittance of the LFE sensor element due to liquid loading.

The advantages of the model are:

- a simple equivalent circuit similar to the Martin and Butterworth-Van Dyke equivalent circuits
- accurate, ( $\pm 5\%$  from measured), prediction of the admittance at or near resonance for the LFE sensor element under deionized water loads
- prediction of the frequency shift due to changes in kinematic viscosity, permittivity, and conductivity within experimental error

The primary limitations of the model are:

- the expressions for the frequency shift due to liquid permittivity and conductivity changes are complex
- the model does not precisely give the peak admittance of the LFE sensor element under liquid loads
- the effective penetration of the electric field associated with the thickness shear mode is not analytically determined

### 6.3. Future Work

While the equivalent circuit model presented in this work is the first analytic approach to modeling the LFE sensor element under liquid loads, there are significant limitations that require additional work.

The first suggested direction for future research is to apply the analysis to electrodes on the reference face of the LFE sensor element. While the model provides a good approximation of the measured data, there are errors that are most likely due to modeling the electrodes on the side faces of the resonator. This is most apparent in the discrepancies between measured and model data for the peak admittance under dielectric loading. The analysis may result in a complex circuit that is cumbersome, but may provide insight to the existing circuit and suggest modifications to the existing circuit elements.

The second suggested direction is to describe, more thoroughly, the electrical interaction between the electric field associated with the thickness shear mode and the double layer at the surface of the LFE sensor element. The purpose of this work is to obtain an expression for the effective penetration depth,  $h_{eff}$ .

The third suggested direction is to apply the analytic equations in section 3.2. to a finite element analysis using commercially available software packages, such as COMSOL, or

a user-developed finite element analysis routine. The complexity of the system, may be more efficiently modeled using the equations presented here in finite element analysis, rather than an equivalent circuit, which has inherent limitations if it is to be easily implemented.

The final suggested direction is to perform the analysis for other crystals with different symmetry classes. The analysis used here can be applied to other crystals and expressions for the circuit elements derived based in this analysis.

## Appendix A

### PIEZOELECTRIC COUPLING FACTOR FOR LATERAL-FIELD EXCITED ACOUSTIC MODES IN AT-CUT QUARTZ

This appendix contains the method for finding the piezoelectric coupling factor,  $k_m^{(i)}$ , of lateral-field excited (LFE) acoustic modes in quartz. The steps follow those detailed by Ballato, *et al.* in [35].

#### ***Step 1. Rotate coordinates $(\phi, \theta, \psi)$***

The material constants for quartz,  $c_{ijkl}$ ,  $e_{kij}$ , and  $\epsilon_{ij}$ , must be transformed from the crystallographic to plate coordinates. When calculating the coupling coefficients in quartz it is unnecessary to consider the viscosity,  $\eta$ , due to it being small. For AT-cut quartz

$$\phi = 0.00^\circ \text{ and } \theta = 35.25^\circ.$$

#### ***Step 2. Stiffen elastic constants***

Once the material constants have been rotated, the piezoelectrically stiffened elastic constant,  $\bar{c}_{2jk2}$ , can be calculated as follows,

$$\bar{c}_{2jk2} = c_{2jk2} + \frac{e_{22j}e_{2k2}}{\epsilon_{22}}. \quad (\text{A.1})$$

#### ***Step 3. Solve eigenvalue problem***

In order to solve the eigenvalue problem, it is necessary to solve the following eigenequation,

$$[\bar{c}_{jk}] \mathbf{\beta}^{(i)} = c^{(i)} \mathbf{\beta}^{(i)}, \quad (\text{A.2})$$



where  $\beta^{(i)}$  is the eigenvector of  $[\bar{c}_{jk}]$ , defined in equation (2.77) and  $c^{(i)}$  is the eigenvalue for each of the acoustic modes, where  $i = a, b, c$ .

**Step 4. Order roots and eigenvectors**

The acoustic modes are the longitudinal,  $a$ , the fast shear,  $b$ , and the slow shear,  $c$ , modes. The roots are ordered as described in Table A.1, where  $X_i$  are the plate coordinates.

**Table A.1. The relationship between the acoustic modes and the eigenvalues for an LFE resonator on quartz**

mode	eigenvalue ( $c^{(i)}$ )	eigenvector ( $\beta^{(i)}$ )
longitudinal mode ( $a$ ) $i = 2$	the largest root	the largest component is along $X_2$
fast shear mode ( $b$ ) $i = 3$	the median root	the largest component is along $X_3$
thickness shear mode ( $c$ ) $i = 1$	the smallest root	the largest component is along $X_1$

**Step 5. Transform  $e_{22j}$  and  $e_{12j}$  to normal coordinates**

The transformation of the piezoelectric stress constants is done using equation (2.78), yielding

$$e_{22p}^0 = \beta_j^{(p)} e_{22j}, \tag{A.3}$$

and

$$e_{12q}^0 = \beta_k^{(q)} e_{12k}. \tag{A.4}$$

**Step 6. Modify the lateral  $e^0$  values**

This step is similar to the transformation using equation (2.69) and is modified as follows,

$$\mathbf{e}_{12q}^0 = e_{12q}^0 - \frac{\varepsilon_{12}}{\varepsilon_{22}} e_{22q}^0. \quad (\text{A.5})$$

**Step 7. Modify the lateral permittivity**

The equation used for this modification is similar to equation (3.29), yielding

$$\bar{\varepsilon}_{11} = \varepsilon_{11} - \frac{\varepsilon_{12}^2}{\varepsilon_{22}}. \quad (\text{A.6})$$

**Step 8. Determine piezoelectric coupling factors**

The lateral-field excited coupling factor is

$$\left(k_m^{(i)}\right)^2 = \frac{\left(e_{12i}^0\right)^2}{c^{(i)} \varepsilon_{11}}. \quad (\text{A.7})$$

Inspection of equation (A.7) reveals that it is similar in form to equation (2.97). Once the piezoelectric coupling factors have been calculated for each of the acoustic modes, they can be plotted as a function of the direction of the applied electric field, (Figure 3).

## Appendix B

### BULK ACOUSTIC WAVE RESONATOR MODELS

#### B.1. Mason Circuit Model

##### B.1.1. *Thickness-Field Excitation*

The Mason model for a thickness-field excited BAW resonator is shown in Figure

11. Expressions for the forces,  $F_1$  and  $F_2$ , can be found by examination of Figure 11 as follows,

$$\begin{aligned} F_1 &= j\bar{Z}_c \tan(k_t h/2)v_1 - j\frac{\bar{Z}_c}{\sin(k_t h)}(v_1 - v_2) + V_{cd} \\ &= j\bar{Z}_c \left( \tan(k_t h/2) - \frac{1}{\sin(k_t h)} \right) v_1 + j\frac{\bar{Z}_c}{\sin(k_t h)} v_2 + V_{cd} \end{aligned} \quad (\text{B.1})$$

and

$$\begin{aligned} F_2 &= -j\bar{Z}_c \tan(k_t h/2)v_2 - j\frac{\bar{Z}_c}{\sin(k_t h)}(v_1 - v_2) + V_{cd} \\ &= -j\frac{\bar{Z}_c}{\sin(k_t h)} - j\bar{Z}_c \left( \tan(k_t h/2) - \frac{1}{\sin(k_t h)} \right) v_2 + V_{cd} \end{aligned} \quad (\text{B.2})$$

The voltage,  $V_{cd}$ , is expressed as

$$V_{cd} = V_{ab} N_t C_0. \quad (\text{B.3})$$

The voltage,  $V_{ab}$ , is from inspection of Figure 11

$$V_{ab} = V + \frac{I_1}{j\omega C_0}, \quad (\text{B.4})$$

where  $I_1$  is the current through the transformer, which can be expressed as follows,

$$I_1 = I - j\omega C_0 V. \quad (\text{B.5})$$

Substituting equation (B.5) into (B.4) yields

$$V_{ab} = V + \frac{I - j\omega C_0 V}{j\omega C_0} = V + \frac{I}{j\omega C_0} - V = \frac{I}{j\omega C_0}. \quad (\text{B.6})$$

An expression for  $V_{cd}$  is obtained by substituting equation (B.6) into (B.3) as follows,

$$V_{cd} = \frac{N_t}{j\omega} I. \quad (\text{B.7})$$

Using the following trigonometric identity

$$\frac{1}{\tan(k_t h)} = \frac{1}{\sin(k_t h)} - \tan(k_t h/2) \quad (\text{B.8})$$

and substituting equation (B.7) into (B.1) and (B.2) yields expressions for  $F_1$  and  $F_2$ ,

$$F_1 = \bar{Z}_c \left( \frac{v_1}{j \tan(k_t h)} - \frac{v_2}{j \sin(k_t h)} \right) + \frac{N_t}{j\omega} I \quad (\text{B.9})$$

and

$$F_2 = \bar{Z}_c \left( \frac{v_1}{j \sin(k_t h)} - \frac{v_2}{j \tan(k_t h)} \right) + \frac{N_t}{j\omega} I. \quad (\text{B.10})$$

Since both surfaces are stress free,

$$F_1 = F_2 = 0. \quad (\text{B.11})$$

Thus, both mechanical ports of the model are “short-circuited”.

The final equation that is necessary to calculate the impedance of the Mason model is an expression for the voltage. First, an expression for the electric field,  $E_2$ , is found by substituting equation (2.23) into (2.32) and rearranging as follows,

$$E_2 = \frac{D_2}{\epsilon_{22}} - \frac{e_{26}}{\epsilon_{22}} u_{1,2}. \quad (\text{B.12})$$

Next, the voltage is found by integrating  $E_2$  through the thickness of the quartz, yielding

$$V = \int_0^h E_2 dx_2 = \frac{D_2 h}{\epsilon_{22}} - \frac{e_{26}}{\epsilon_{22}} (u_1(h) - u_1(0)). \quad (\text{B.13})$$

From Maxwell's equations the current density,  $J_2$ , through the crystal is given by the expression

$$J_2 = \frac{\partial D_2}{\partial t} = j\omega D_2, \quad (\text{B.14})$$

and thus,

$$I = J_2 A = j\omega D_2 A, \quad (\text{B.15})$$

where  $A$  is the cross-sectional area of the quartz resonator. Finally, solving for  $D_2$  in equation (B.15) and substituting into (B.13) while substituting equations (2.112), (2.109), and the relation  $v = \partial u / \partial t$  into (B.13) yields

$$V = \frac{I}{j\omega C_0} + \frac{N_t}{j\omega} (v_2 - v_1). \quad (\text{B.16})$$

Using the same approach as Rosenbaum [42], equations (B.9) and (B.10) are simplified as follows,

$$\frac{\bar{Z}_c}{j \tan(k_i h)} x - \frac{\bar{Z}_c}{j \sin(k_i h)} y + c = 0 \quad (\text{B.17})$$

and

$$\frac{\bar{Z}_c}{j \sin(k_i h)} x - \frac{\bar{Z}_c}{j \tan(k_i h)} y + c = 0, \quad (\text{B.18})$$

where

$$x = \frac{v_1}{I}, \quad (\text{B.19})$$

$$y = \frac{v_2}{I}, \quad (\text{B.20})$$

and

$$c = \frac{N_t}{j\omega}. \quad (\text{B.21})$$

Subtracting equation (B.18) from (B.17) yields

$$\left( \frac{\bar{Z}_c}{j \tan(k_i h)} - \frac{\bar{Z}_c}{j \sin(k_i h)} \right) x + \left( \frac{\bar{Z}_c}{j \tan(k_i h)} - \frac{\bar{Z}_c}{j \sin(k_i h)} \right) y = 0, \quad (\text{B.22})$$

where it is clear that

$$x = -y. \quad (\text{B.23})$$

Substituting equation (B.23) into (B.17) yields

$$\frac{\bar{Z}_c}{j \tan(k_i h)} x + \frac{\bar{Z}_c}{j \sin(k_i h)} x + c = \left( \frac{\bar{Z}_c}{j \tan(k_i h)} + \frac{\bar{Z}_c}{j \sin(k_i h)} \right) x + c = 0. \quad (\text{B.24})$$

Using the trigonometric identity

$$\frac{1}{\tan(k_i h/2)} = \frac{1}{\tan(k_i h)} + \frac{1}{\sin(k_i h)} \quad (\text{B.25})$$

and solving for  $x$  in equation (B.24) results in the following expression,

$$x = \frac{-c}{jZ_c} \tan(k_i h/2). \quad (\text{B.26})$$

The impedance of the resonator can be expressed by dividing equation (B.16) by  $I$  and substituting equations (B.19), (B.20), and (B.23) as follows,

$$Z = \frac{V}{I} = \frac{1}{j\omega C_0} + \frac{N_t}{j\omega} (x - y) = \frac{1}{j\omega C_0} + \frac{2N_t}{j\omega} x. \quad (\text{B.27})$$

Substituting equations (B.21) and (B.26) into (B.27) yields

$$Z = \frac{1}{j\omega C_0} - \frac{2N_t c}{\omega \bar{Z}_c} \tan(k_i h/2) = \frac{1}{j\omega C_0} - \frac{2N_t^2}{j\omega^2 \bar{Z}_c} \tan(k_i h/2). \quad (\text{B.28})$$

The final expression for the impedance is found by substituting equations (2.44), (2.111), (2.113), and (2.115) into (B.28) as follows,

$$Z = \frac{1}{j\omega C_0} \left( 1 - k_m^2 \frac{\tan(k_l h/2)}{k_l h/2} \right). \quad (\text{B.29})$$

### B.1.2. Lateral-Field Excitation

The Mason model for a lateral-field excited BAW resonator is shown in Figure 12. Similar to the process that was used for the case of thickness-field excited resonators, expressions for the forces,  $F_1$  and  $F_2$ , can be found by inspection of Figure 12 as follows,

$$\begin{aligned} F_1 &= j\bar{Z}_c \tan(k_l h/2) v_1 + \frac{\bar{Z}_c}{j \sin(k_l h)} (v_1 - v_2) + V_{cd} \\ &= j\bar{Z}_c \left( \tan(k_l h/2) - \frac{1}{\sin(k_l h)} \right) v_1 + j \frac{\bar{Z}_c}{\sin(k_l h)} v_2 + V_{cd} \end{aligned} \quad (\text{B.30})$$

and

$$\begin{aligned} F_2 &= -j\bar{Z}_c \tan(k_l h/2) v_2 - \frac{\bar{Z}_c}{j \sin(k_l h)} (v_1 - v_2) + V_{cd} \\ &= -j \frac{\bar{Z}_c}{\sin(k_l h)} v_1 - j\bar{Z}_c \left( \tan(k_l h/2) - \frac{1}{\sin(k_l h)} \right) v_2 + V_{cd}. \end{aligned} \quad (\text{B.31})$$

The voltage,  $V_{cd}$ , is expressed as

$$V_{cd} = V_{ab} N_l C_0. \quad (\text{B.32})$$

The voltage,  $V_{ab}$ , is, from inspection of Figure 12

$$V_{ab} = V. \quad (\text{B.33})$$

An expression for  $V_{cd}$  is obtained by substituting equations (2.116), (2.118), and (B.33) into (B.32), as follows

$$V_{cd} = \frac{dhe_{36}}{w} V. \quad (\text{B.34})$$

Using the trigonometric identity in equation (B.8) and substituting equation (B.34) into (B.30) and (B.31) yields

$$F_1 = \bar{Z}_c \left( \frac{v_1}{j \tan(k_i h)} - \frac{v_2}{j \sin(k_i h)} \right) + \frac{dhe_{36}}{w} V \quad (\text{B.35})$$

and

$$F_2 = \bar{Z}_c \left( \frac{v_1}{j \sin(k_i h)} - \frac{v_2}{j \tan(k_i h)} \right) + \frac{dhe_{36}}{w} V. \quad (\text{B.36})$$

An expression for the current,  $I$ , is necessary to calculate the admittance for the Mason model. If the current is assumed to vary harmonically in time,  $e^{j\omega t}$ , then

$$I = \frac{\partial Q}{\partial t} = j\omega Q, \quad (\text{B.37})$$

where  $Q$  is the charge between the electrodes. Assuming the current,  $I$ , is uniform along the  $x_1$  direction (Figure 10), the current is expressed by substituting equation (3.74) into (B.37) as follows

$$I = j\omega d \int_0^h D_3 dx_2. \quad (\text{B.38})$$

Substituting equation (2.20) into (B.38) yields

$$I = j\omega d \int_0^h \left( \varepsilon_{33} E_3 + e_{36} \frac{\partial u_1}{\partial x_2} \right) dx_2. \quad (\text{B.39})$$

The applied electric field is assumed to be uniform, thus

$$E_3 = \frac{V}{w}. \quad (\text{B.40})$$

Substituting equation (B.40) into (B.39) yields

$$I = \frac{j\omega d \varepsilon_{33} V}{w} \int_0^h dx_2 + j\omega d e_{36} \int_0^h \frac{\partial u_1}{\partial x_2} dx_2 = \frac{j\omega d \varepsilon_{33} V h}{w} + j\omega d e_{36} (u_1(h) - u_1(0)). \quad (\text{B.41})$$



The final expression for the current,  $I$ , is obtained by substituting equation (2.118) into

(B.41) and recognizing the  $j\omega u = v$  as follows,

$$I = j\omega C_0 V + de_{36}(v_2 - v_1). \quad (\text{B.42})$$

The admittance for the Mason model is calculated by dividing equation (B.42) by  $V$  as follows,

$$Y = \frac{I}{V} = j\omega C_0 + de_{36} \left( \frac{v_2}{V} - \frac{v_1}{V} \right). \quad (\text{B.43})$$

Next, substituting equation (B.11) into (B.35) and (B.36) are divided by  $V$ , yields,

$$\frac{\bar{Z}_c}{j \tan(k_i h)} x - \frac{\bar{Z}_c}{j \sin(k_i h)} y = -c \quad (\text{B.44})$$

and

$$\frac{\bar{Z}_c}{j \sin(k_i h)} x - \frac{\bar{Z}_c}{j \tan(k_i h)} y = -c, \quad (\text{B.45})$$

where

$$x = \frac{v_1}{V}, \quad (\text{B.46})$$

$$y = \frac{v_2}{V}, \quad (\text{B.47})$$

and

$$c = \frac{dhe_{36}}{w}. \quad (\text{B.48})$$

Subtracting equation (B.45) from (B.44) yields

$$\left( \frac{\bar{Z}_c}{j \tan(k_i h)} - \frac{\bar{Z}_c}{j \sin(k_i h)} \right) x + \left( \frac{\bar{Z}_c}{j \tan(k_i h)} - \frac{\bar{Z}_c}{j \sin(k_i h)} \right) y = 0. \quad (\text{B.49})$$

Inspection of equation (B.49) reveals that

$$x = -y. \quad (\text{B.50})$$

Substituting equation (B.50) into (B.44) results in

$$\left( \frac{\bar{Z}_c}{j \tan(k_t h)} + \frac{\bar{Z}_c}{j \sin(k_t h)} \right) x = -c. \quad (\text{B.51})$$

Solving equation (B.51) for  $x$  and substituting equation (B.25) yields

$$x = \frac{-c}{j\bar{Z}_c} \tan\left(\frac{k_t h}{2}\right). \quad (\text{B.52})$$

The final form of  $x$  is obtained by substituting equation (B.48) into (B.52) as follows

$$x = \frac{dhe_{36}}{jw\bar{Z}_c} \tan\left(\frac{k_t h}{2}\right). \quad (\text{B.53})$$

Finally, the admittance can be found by substituting equations (B.50) and (B.53) into (B.43)

as follows

$$Y = j\omega C_0 - \frac{2d^2 e_{36}^2 h}{jw\bar{Z}_c} \tan\left(\frac{k_t h}{2}\right) = j\omega C_0 \left( 1 + \frac{2d^2 e_{36}^2 h}{\omega C_0 w \bar{Z}_c} \tan\left(\frac{k_t h}{2}\right) \right). \quad (\text{B.54})$$

Substituting equations (2.111) and (2.118) into (B.54) yields

$$Y = j\omega C_0 \left( 1 + \frac{2e_{36}^2}{\omega \varepsilon_{33} h \sqrt{\rho \bar{c}_{66}}} \tan\left(\frac{k_t h}{2}\right) \right). \quad (\text{B.55})$$

The final form of the admittance for the Mason model applied to a lateral-field excited BAW

is found by substituting equations (2.44) and (2.119) into (B.55) as follows

$$Y = j\omega C_0 \left( 1 + K_l^2 \frac{\tan(k_t h/2)}{k_t h/2} \right). \quad (\text{B.56})$$

## B.2. Transmission Line Model

### B.2.1. *Thickness-Field Excitation*

The impedance at AB,  $Z_{AB}$ , is found, by examining Figure 15, to be

$$Z_{AB} = \frac{1}{j\omega C_0} + jX_{tx} + \frac{1}{N_{tx}^2} Z_{CD}. \quad (\text{B.57})$$

The reactance,  $X_{tx}$ , and the turns ratio,  $N_{tx}$ , are defined by equations (2.129) and (2.130), respectively.

The reactance term can be rearranged by substituting equations (2.109), (2.113), and (2.115) into (2.130) as follows,

$$X_{tx} = \frac{1}{\omega C_0} \frac{k_m^2}{\omega \sqrt{\rho/\bar{c}_{66}} h} \sin(k_t h). \quad (\text{B.58})$$

Substituting equation (2.44) into (B.58), yields

$$X_{tx} = \frac{1}{\omega C_0} \frac{k_m^2}{k_t h} \sin(k_t h). \quad (\text{B.59})$$

Thus,

$$jX_{tx} = \frac{j}{\omega C_0} \frac{k_m^2}{k_t h} \sin(k_t h) = \frac{1}{j\omega C_0} \frac{j^2 k_m^2}{k_t h} \sin(k_t h) = \frac{1}{j\omega C_0} \frac{-k_m^2}{k_t h} \sin(k_t h). \quad (\text{B.60})$$

The turns ratio,  $N_{tx}$ , can be expressed by substituting equations (2.44), (2.109), (2.113), and (2.115) into (2.129) and rearranged for the form given in equation (B.1), such that

$$\frac{1}{N_{tx}^2} Z_{CD} = \frac{1}{\omega C_0} \frac{4k_m^2}{k_t h Z_c} \sin^2(k_t h/2) Z_{CD}. \quad (\text{B.61})$$

The impedance at CD is the parallel combination of the impedance looking to the left of the transmission line,  $Z_l$ , and the impedance looking to the right of the transmission line,  $Z_r$ , where

$$Z_{CD} = \frac{Z_l Z_r}{Z_l + Z_r}. \quad (\text{B.62})$$

The impedance,  $Z_l$ , is

$$Z_l = Z_c \tanh\left(\frac{jk_t h}{2}\right) = jZ_c \tan\left(\frac{k_t h}{2}\right). \quad (\text{B.63})$$

Expressing the liquid load with a single impedance term,  $Z_L$ , the impedance,  $Z_r$ , is

$$Z_r = Z_c \frac{Z_L + Z_c \tanh(jk_t h/2)}{Z_c + Z_L \tanh(jk_t h/2)} = Z_c \frac{Z_L + jZ_c \tan(k_t h/2)}{Z_c + jZ_L \tan(k_t h/2)}. \quad (\text{B.64})$$

Substituting equations (B.63) and (B.64) into equation (B.62) yields

$$Z_{CD} = \frac{Z_c (jZ_L \tan(k_t h/2) - Z_c \tan^2(k_t h/2))}{Z_L (1 - \tan^2(k_t h/2)) + j2Z_c \tan(k_t h/2)}. \quad (\text{B.65})$$

An expression for the impedance,  $Z_{AB}$ , is obtained by substituting equation (B.65) into (B.61) and substituting the resulting equation and (B.60) into equation (B.1), yielding

$$Z_{AB} = \frac{1 + \frac{k_m^2}{k_t h} \left( -\sin(k_t h) + \frac{4 \sin^2(k_t h/2) (jZ_L \tan(k_t h/2) - Z_c \tan^2(k_t h/2))}{2Z_c \tan(k_t h/2) - jZ_L (1 - \tan^2(k_t h/2))} \right)}{j\omega C_0}. \quad (\text{B.66})$$

The term in parenthesis of equation (B.66) is rewritten as follows,

$$\frac{\sin(k_t h) (2Z_c \tan(k_t h/2) - jZ_L (1 - \tan^2(k_t h/2)))}{jZ_L (1 - \tan^2(k_t h/2)) - 2Z_c \tan(k_t h/2)} - \frac{4 \sin^2(k_t h/2) (jZ_L \tan(k_t h/2) - Z_c \tan^2(k_t h/2))}{jZ_L (1 - \tan^2(k_t h/2)) - 2Z_c \tan(k_t h/2)}. \quad (\text{B.67})$$

The numerator of equation (B.67) is next separated into its real and imaginary components.

First the real part of the numerator is, after much algebraic manipulation,

$$\begin{aligned} & \sin(k_i h)(2Z_c \tan(k_i h/2)) + 4 \sin^2(k_i h/2) Z_c \tan^2(k_i h/2) \\ &= 2Z_c \tan(k_i h/2) (\sin(k_i h) + 2 \sin^2(k_i h/2) \tan(k_i h/2)) = 4Z_c \tan^2(k_i h/2). \end{aligned} \quad (\text{B.68})$$

The imaginary part of the numerator is

$$\begin{aligned} & \sin(k_i h)(-Z_L)(1 - \tan^2(k_i h/2)) - 4 \sin^2(k_i h/2)(Z_L) \tan(k_i h/2) \\ &= -4Z_L \tan(k_i h/2). \end{aligned} \quad (\text{B.69})$$

The impedance for the transmission line model is further modified by substituting equations (B.68) and (B.69) into (B.67), which is then inserted into (B.66), yielding

$$Z_{AB} = \frac{1}{j\omega C_0} \left( 1 + \frac{k_m^2}{k_i h} \frac{4Z_c \tan^2(k_i h/2) - j4Z_L \tan(k_i h/2)}{jZ_L(1 - \tan^2(k_i h/2)) - 2Z_c \tan(k_i h/2)} \right). \quad (\text{B.70})$$

Dividing the numerator and denominator of equation (B.70) by  $2Z_c \tan(k_i h/2)$

results in the final form of the admittance,  $Z_{AB}$ , as follows

$$Z = \frac{1}{j\omega C_0} \left( 1 - \frac{k_m^2}{k_i h/2} \frac{\tan\left(\frac{k_i h}{2}\right) - j \frac{Z_L}{Z_c}}{1 - j \frac{Z_L}{Z_c} \cot(k_i h)} \right). \quad (\text{B.71})$$

### B.2.2. Lateral-Field Excitation

The admittance of the LFE resonator in air is found by inspection of the circuit in Figure 16 and is expressed as

$$Y_{AB} = j\omega C_0 + N_{lx}^2 Y_{CD}, \quad (\text{B.72})$$

where  $C_0$  is the static capacitance, defined in equation (2.105), and  $N_{lx}$  is the transformer turns ratio, defined in equation (2.135), for the LFE resonator. Substituting equation (2.135) into (B.72) yields

$$Y_{AB} = j\omega C_0 + (k_m^{(c)})^2 \frac{C_0 c^{(c)} A}{h} Y_{CD} = j\omega C_0 \left( 1 + (k_m^{(c)})^2 \frac{c^{(c)} A}{j\omega h} Y_{CD} \right), \quad (\text{B.73})$$

where  $c^{(c)}$  is the eigenvalue of the thickness shear mode and  $k_m^{(c)}$  is the lateral coupling factor, defined in equation (2.97) for the LFE resonator.

The admittance at  $CD$  can be found by first recognizing that the model is considered to be air loaded at both surfaces,

$$Y_l = Y_r. \quad (\text{B.74})$$

Thus, the admittance,  $Y_{CD}$ , is expressed as follows

$$Y_{CD} = Y_l + Y_r = 2Y_l. \quad (\text{B.75})$$

The admittance,  $Y_l$ , is [26]

$$Y_l = jY_c \tan\left(\frac{k_l^{(c)} h}{2}\right). \quad (\text{B.76})$$

Substituting equation (2.136) into (B.76) and the resulting expression into (B.75), yields

$$Y_{CD} = j \frac{2}{A\sqrt{\rho c^{(c)}}} \tan\left(\frac{k_l^{(c)} h}{2}\right). \quad (\text{B.77})$$

The admittance can be found by substituting equation (B.77) into (B.73) as follows

$$Y_{AB} = j\omega C_0 \left( 1 + (k_m^{(c)})^2 \frac{c^{(c)}}{\omega h} \frac{2}{\sqrt{\rho c^{(c)}}} \tan\left(\frac{k_l^{(c)} h}{2}\right) \right). \quad (\text{B.78})$$

The final expression for the admittance is obtained by substituting equation (2.87) into equation (B.78) as follows

$$Y_{AB} = j\omega C_0 \left( 1 + (k_m^{(c)})^2 \frac{\tan(k_l^{(c)} h/2)}{k_l^{(c)} h/2} \right). \quad (\text{B.79})$$

## Appendix C

### MATERIAL PROPERTIES OF LIQUIDS

**Table C.1. Material properties of glycerol solutions [82, 83]**

% glycerol by volume	$\rho$ (kg/m <sup>3</sup> )	$\eta$ (kg/s*m)	$\epsilon_r$	$\sigma$ (S/m)
0	998.2	0.001002	79.2	5.56E-06
2	1000.3	0.001057	77.5	5.58E-06
4	1009.7	0.001133	75.9	5.60E-06
6	1010.7	0.001214	74.3	5.62E-06
8	1015.9	0.001300	72.8	5.64E-06
10	1021.1	0.001391	71.3	5.66E-06
12	1026.3	0.001488	69.9	5.68E-06
14	1031.5	0.001590	68.5	5.70E-06
16	1036.7	0.001698	67.2	5.72E-06
18	1041.9	0.001812	65.9	5.74E-06
20	1056.1	0.001988	64.7	5.76E-06

**Table C.2. Material properties of isopropyl alcohol solutions [82, 84, 85]**

% isopropyl alcohol by volume	$\rho$ (kg/m <sup>3</sup> )	$\eta$ (kg/s*m)	$\epsilon_r$	$\sigma$ (S/m)
0	998.2	0.001002	79.2	5.56E-06
10	985.9	0.000943	77.7	5.56E-06
20	968.3	0.001587	68.2	5.56E-06
30	949.9	0.001959	59.5	5.56E-06
40	930.6	0.002262	51.6	5.56E-06
50	910.4	0.002483	44.5	5.56E-06
60	889.2	0.002648	38.0	5.56E-06
70	866.9	0.002792	32.3	5.56E-06
80	843.5	0.002940	27.1	5.56E-06
90	818.8	0.003113	22.6	5.56E-06
100	784.8	0.003417	18.3	5.56E-06

**Table C.3. Material properties of sodium chloride solutions [82, 86]**

% sodium chloride by mass	$\rho$ (kg/m <sup>3</sup> )	$\eta$ (kg/(m*s))	$\epsilon_r$	$\sigma$ (S/m)
0.0077	998.4	0.001000	79.9	0.02589
0.01	998.4	0.001000	79.9	0.02956
0.012	998.4	0.001000	79.9	0.03276
0.016	998.4	0.001000	79.9	0.03914
0.02	998.4	0.001001	79.9	0.04553
0.023	998.5	0.001001	79.9	0.05032
0.0277	998.5	0.001001	79.9	0.05782
0.032	998.5	0.001001	79.9	0.06468
0.036	998.6	0.001001	79.9	0.07107
0.04	998.6	0.001001	79.9	0.07746



## Appendix D

### MEASURED AND THEORETICAL DATA FOR LIQUID-LOADED LATERAL FIELD EXCITED SENSOR ELEMENTS

**Table D.1. Measured data for LFE sensor elements with a 0.5-mm electrode gap under glycerol solution loads**

% Glycerol	$f_{\max}$ (Hz)	$\Delta f/f_0$ (ppm)	$ Y_{\max} $ (S)	Phase( $Y_{\max}$ ) (degrees)	$f_{\min}$ (Hz)	$ Y_{\min} $ (S)	Phase( $Y_{\min}$ ) (degrees)	$f_{\min}-f_{\max}$ (Hz)
0	4966875	0	0.0009993	81.00848	4970875	0.0001800	87.01247	4000
2	4966750	-25	0.0009333	38.79191	4970875	0.0001658	36.16166	4125
4	4966500	-76	0.0008316	43.71858	4970750	0.0001870	43.60579	4250
6	4966500	-76	0.0008161	44.65299	4970750	0.0001885	43.57077	4250
8	4966625	-50	0.0008300	41.04924	4970875	0.0001814	39.82089	4250
10	4966500	-76	0.0008584	42.28613	4970875	0.0001857	40.52129	4375
12	4966375	-101	0.0008147	45.62357	4970875	0.0001988	43.51174	4500
14	4966375	-101	0.0008415	44.48505	4970875	0.0001991	42.33946	4500
16	4966500	-76	0.0007825	44.79383	4971000	0.0001700	41.73351	4500
18	4966500	-76	0.0007773	44.33924	4971125	0.0001747	43.92573	4625
20	4966000	-176	0.0008033	42.05938	4970500	0.0001552	38.58411	4500

**Table D.2. Model data for LFE sensor elements with a 0.5-mm electrode gap under glycerol solution loads**

% Glycerol	$f_{\max}$ (Hz)	$\Delta f/f_0$ (ppm)	$ Y_{\max} $ (S)	Phase( $Y_{\max}$ ) (degrees)	$f_{\min}$ (Hz)	$ Y_{\min} $ (S)	Phase( $Y_{\min}$ ) (degrees)	$f_{\min}-f_{\max}$ (Hz)
0	4966875	0	0.0009694	42.8942	4971484	0.0001472	42.0054	4609
2	4966875	0	0.0009599	43.0549	4971516	0.0001484	42.5162	4641
4	4966859	-3	0.0009468	43.4310	4971531	0.0001502	42.8315	4672
6	4966844	-6	0.0009344	43.8136	4971563	0.0001520	43.5107	4719
8	4966813	-13	0.0009218	44.5725	4971578	0.0001538	43.8339	4766
10	4966797	-16	0.0009094	44.8823	4971594	0.0001556	44.1673	4797
12	4966781	-19	0.0008972	45.1684	4971625	0.0001575	44.8651	4844
14	4966750	-25	0.0008852	45.8234	4971641	0.0001594	45.2131	4891
16	4966734	-28	0.0008734	46.0607	4971672	0.0001613	45.9090	4938
18	4966703	-35	0.0008618	46.6468	4971688	0.0001632	46.2737	4984
20	4966656	-44	0.0008458	47.2285	4971703	0.0001659	46.9347	5047

**Table D.3. Measured data for LFE sensor elements with a 0.5-mm electrode gap under isopropyl alcohol solution loads**

% Isopropyl Alcohol	$f_{\max}$ (Hz)	$\Delta f/f_0$ (ppm)	$ Y_{\max} $ (S)	Phase( $Y_{\max}$ ) (degrees)	$f_{\min}$ (Hz)	$ Y_{\min} $ (S)	Phase( $Y_{\min}$ ) (degrees)	$f_{\min}-f_{\max}$ (Hz)
0	4966875	0	0.0009993	81.0085	4970875	0.0001800	87.0125	4000
10	4966875	0	0.0009199	81.8370	4971125	0.0001991	86.9651	4250
20	4966875	0	0.0008293	82.6338	4971125	0.0002119	86.8609	4250
30	4966875	0	0.0007172	83.7700	4971375	0.0002063	87.0666	4500
40	4967000	25	0.0006496	84.5269	4971500	0.0002141	87.0616	4500
50	4967500	126	0.0005693	85.2401	4971875	0.0002201	87.0771	4375
60	4968000	227	0.0005043	85.8242	4972750	0.0002167	87.3389	4750
70	4967625	151	0.0004650	86.5770	4971875	0.0002475	87.4344	4250
80	4969500	529	0.0003814	86.8968	4973625	0.0002054	87.6371	4125
90	4969875	604	0.0003575	67.2273	4973875	0.0002145	65.5116	4000
100	4970500	730	0.0003386	66.9946	4974250	0.0002125	67.2310	3750

**Table D.4. Model data for LFE sensor elements with a 0.5-mm electrode gap under isopropyl alcohol solution loads**

% Isopropyl Alcohol	$f_{\max}$ (Hz)	$\Delta f/f_0$ (ppm)	$ Y_{\max} $ (S)	Phase( $Y_{\max}$ ) (degrees)	$f_{\min}$ (Hz)	$ Y_{\min} $ (S)	Phase( $Y_{\min}$ ) (degrees)	$f_{\min}-f_{\max}$ (Hz)
0	4966875	0	0.0009694	42.8942	4971484	0.0001472	42.0054	4609
10	4966938	13	0.0009830	42.4763	4971516	0.0001454	41.4129	4578
20	4966813	-13	0.0008979	45.2337	4971656	0.0001574	44.6755	4844
30	4966875	0	0.0008679	46.5998	4971875	0.0001621	46.1611	5000
40	4967031	31	0.0008491	47.4208	4972125	0.0001652	46.7470	5094
50	4967281	82	0.0008382	47.9870	4972453	0.0001670	47.2642	5172
60	4967641	154	0.0008317	48.1476	4972859	0.0001678	47.6043	5219
70	4968109	249	0.0008269	48.1960	4973359	0.0001684	47.8240	5250
80	4968703	368	0.0008224	48.2387	4973969	0.0001689	47.8272	5266
90	4969453	519	0.0008173	48.3464	4974750	0.0001697	48.1187	5297
100	4970516	733	0.0008084	48.4302	4975844	0.0001712	48.4675	5328

**Table D.5. Measured data for LFE sensor elements with a 0.5-mm electrode gap under sodium chloride solution loads**

% NaCl	$f_{\max}$ (Hz)	$\Delta f/f_0$ (ppm)	$ Y_{\max} $ (S)	Phase( $Y_{\max}$ ) (degrees)	$f_{\min}$ (Hz)	$ Y_{\min} $ (S)	Phase( $Y_{\min}$ ) (degrees)	$f_{\min}-f_{\max}$ (Hz)
0	4966875	0	0.0009993	81.0085	4970875	0.0001800	87.0125	4000
0.0077	4963375	-705	0.0006006	44.0706	4970500	0.0001497	41.1015	7125
0.01	4962875	-805	0.0005878	47.1937	4970625	0.0001793	44.0853	7750
0.012	4962375	-906	0.0006100	44.3998	4970500	0.0001803	44.3076	8125
0.016	4961125	-1158	0.0006262	45.8611	4970125	0.0001871	43.2895	9000
0.02	4960750	-1233	0.0006822	43.0024	4969750	0.0001860	39.6747	9000
0.023	4960125	-1359	0.0006989	38.2450	4969750	0.0001610	38.0868	9625
0.0277	4960375	-1309	0.0007976	39.6342	4969375	0.0002213	37.7291	9000
0.032	4960375	-1309	0.0008617	36.1800	4969125	0.0002434	34.3738	8750
0.036	4959375	-1510	0.0009022	34.0013	4969000	0.0001697	33.3248	9625
0.04	4959500	-1485	0.0011743	27.8304	4969125	0.0004301	24.1188	9625

**Table D.6. Model data for LFE sensor elements with a 0.5-mm electrode gap under sodium chloride solution loads**

% NaCl	$f_{\max}$ (Hz)	$\Delta f/f_0$ (ppm)	$ Y_{\max} $ (S)	Phase( $Y_{\max}$ ) (degrees)	$f_{\min}$ (Hz)	$ Y_{\min} $ (S)	Phase( $Y_{\min}$ ) (degrees)	$f_{\min}-f_{\max}$ (Hz)
0	4966875	0	0.0009694	42.8942	4971484	0.0001472	42.0054	4609
0.0077	4959094	-1567	0.0005036	71.0565	4970375	0.0002674	71.0603	11281
0.01	4958719	-1642	0.0005069	70.6728	4969781	0.0002657	70.7070	11063
0.012	4958469	-1692	0.0005108	70.3015	4969313	0.0002637	70.3117	10844
0.016	4958172	-1752	0.0005202	69.3353	4968500	0.0002591	69.3357	10328
0.02	4958031	-1781	0.0005308	68.2512	4967844	0.0002540	68.2603	9813
0.023	4957984	-1790	0.0005392	67.4215	4967438	0.0002502	67.4356	9453
0.0277	4957953	-1796	0.0005523	66.2184	4966922	0.0002445	66.1825	8969
0.032	4957969	-1793	0.0005643	65.1141	4966547	0.0002395	65.0845	8578
0.036	4958000	-1787	0.0005751	64.1242	4966266	0.0002351	64.1465	8266
0.04	4958031	-1781	0.0005856	63.2357	4966016	0.0002311	63.1593	7984

**Table D.7. Measured data for LFE sensor elements with a 1.0-mm electrode gap under glycerol solution loads**

% Glycerol	$f_{\max}$ (Hz)	$\Delta f/f_0$ (ppm)	$ Y_{\max} $ (S)	Phase( $Y_{\max}$ ) (degrees)	$f_{\min}$ (Hz)	$ Y_{\min} $ (S)	Phase( $Y_{\min}$ ) (degrees)	$f_{\min}-f_{\max}$ (Hz)
0	4965125	0	0.0009955	80.8271	4969250	0.0001584	87.0690	4125
2	4965125	0	0.0009098	37.4766	4969375	0.0001472	34.9902	4250
4	4964875	-50	0.0008632	39.9100	4969125	0.0001541	38.6048	4250
6	4964875	-50	0.0008364	41.0778	4969250	0.0001570	41.3294	4375
8	4964875	-50	0.0007661	42.8415	4969375	0.0001518	41.5340	4500
10	4964625	-101	0.0007807	46.2011	4969500	0.0001756	43.2747	4875
12	4964750	-76	0.0007920	44.9995	4969500	0.0001831	43.6688	4750
14	4964625	-101	0.0007535	46.8990	4969500	0.0001833	45.3275	4875
16	4964500	-126	0.0007565	45.2656	4969375	0.0001622	43.2308	4875
18	4964750	-76	0.0007202	46.1023	4969500	0.0001630	42.6790	4750
20	4964625	-101	0.0007152	47.8430	4969500	0.0001551	43.6297	4875

**Table D.8. Model data for LFE sensor elements with a 1.0-mm electrode gap under glycerol solution loads**

% Glycerol	$f_{\max}$ (Hz)	$\Delta f/f_0$ (ppm)	$ Y_{\max} $ (S)	Phase( $Y_{\max}$ ) (degrees)	$f_{\min}$ (Hz)	$ Y_{\min} $ (S)	Phase( $Y_{\min}$ ) (degrees)	$f_{\min}-f_{\max}$ (Hz)
0	4965125	0	0.000961	41.2385	4970016	0.000129	39.7521	4891
2	4965125	0	0.000952	41.5173	4970047	0.00013	40.1772	4922
4	4965125	0	0.000938	41.5603	4970078	0.000131	40.8046	4953
6	4965109	-3	0.000926	42.0624	4970094	0.000133	41.0125	4984
8	4965094	-6	0.000913	42.5158	4970125	0.000134	41.6379	5031
10	4965078	-9	0.0009	42.9443	4970156	0.000136	42.2586	5078
12	4965063	-13	0.000888	43.3430	4970172	0.000138	42.5183	5109
14	4965047	-16	0.000876	43.7207	4970203	0.00014	43.1441	5156
16	4965016	-22	0.000864	44.4472	4970234	0.000141	43.7744	5219
18	4965000	-25	0.000852	44.7655	4970250	0.000143	44.0643	5250
20	4964953	-35	0.000835	45.4515	4970281	0.000146	44.9908	5328

**Table D.9. Measured data for LFE sensor elements with a 1.0-mm electrode gap under isopropyl alcohol solution loads**

% Isopropanol	$f_{\max}$ (Hz)	$\Delta f/f_0$ (ppm)	$ Y_{\max} $ (S)	Phase( $Y_{\max}$ ) (degrees)	$f_{\min}$ (Hz)	$ Y_{\min} $ (S)	Phase( $Y_{\min}$ ) (degrees)	$f_{\min}-f_{\max}$ (Hz)
0	4965125	0	0.0009955	80.8271	4969250	0.0001584	87.0690	4125
10	4964750	-76	0.0010210	80.5176	4969250	0.0001410	87.2979	4500
20	4964750	-76	0.0008808	81.8740	4969250	0.0001520	87.2265	4500
30	4965250	25	0.0006767	84.0549	4969875	0.0001923	87.1455	4625
40	4965500	76	0.0006318	84.3717	4969875	0.0001901	87.1405	4375
50	4965750	126	0.0005325	85.2402	4970250	0.0001783	87.3686	4500
60	4965875	151	0.0004942	85.5891	4969875	0.0001696	87.3526	4000
70	4967125	403	0.0004006	86.6241	4971125	0.0001825	87.5299	4000
80	4967875	554	0.0003646	86.8957	4971875	0.0001889	87.6254	4000
90	4968000	579	0.0003384	65.8117	4972125	0.0001857	63.3576	4125
100	4969000	780	0.0003172	66.3608	4972625	0.0001951	65.3684	3625

**Table D.10. Model data for LFE sensor elements with a 1.0-mm electrode gap under isopropyl alcohol solution loads**

% Isopropanol	$f_{\max}$ (Hz)	$\Delta f/f_0$ (ppm)	$ Y_{\max} $ (S)	Phase( $Y_{\max}$ ) (degrees)	$f_{\min}$ (Hz)	$ Y_{\min} $ (S)	Phase( $Y_{\min}$ ) (degrees)	$f_{\min}-f_{\max}$ (Hz)
0	4965125	0	0.0009614	41.2385	4970016	0.0001285	39.7521	4891
10	4965188	13	0.0009747	40.9303	4970063	0.0001269	39.4692	4875
20	4965094	-6	0.0008883	43.5378	4970219	0.0001378	42.5685	5125
30	4965203	16	0.0008571	44.5320	4970453	0.0001421	43.7873	5250
40	4965391	53	0.0008372	45.5058	4970750	0.0001450	44.6249	5359
50	4965703	116	0.0008256	45.7107	4971125	0.0001466	45.2243	5422
60	4966125	201	0.0008187	45.7191	4971578	0.0001474	45.4502	5453
70	4966656	308	0.0008137	45.8664	4972141	0.0001479	45.6179	5484
80	4967328	444	0.0008090	46.0031	4972828	0.0001484	45.5562	5500
90	4968188	617	0.0008038	45.9941	4973719	0.0001491	45.9948	5531
100	4969391	859	0.0007947	46.1853	4974953	0.0001505	46.2743	5563

**Table D.11. Measured data for LFE sensor elements with a 1.0-mm electrode gap under sodium chloride solution loads**

% NaCl	$f_{\max}$ (Hz)	$\Delta f/f_0$ (ppm)	$ Y_{\max} $ (S)	Phase( $Y_{\max}$ ) (degrees)	$f_{\min}$ (Hz)	$ Y_{\min} $ (S)	Phase( $Y_{\min}$ ) (degrees)	$f_{\min}-f_{\max}$ (Hz)
0	4965125	0	0.0009955	80.8271	4969250	0.0001584	87.0690	4125
0.0077	4962000	-629	0.0005919	39.9086	4968875	0.0001334	38.5077	6875
0.01	4961375	-755	0.0005781	44.2441	4969000	0.0001603	42.0684	7625
0.012	4960375	-957	0.0005845	43.6082	4968875	0.0001620	41.7330	8500
0.016	4958750	-1284	0.0010928	35.2511	4968375	0.0006786	34.5150	9625
0.02	4959000	-1234	0.0006528	41.8224	4968250	0.0001724	36.7957	9250
0.023	4959125	-1208	0.0007104	38.6981	4968000	0.0001830	37.8555	8875
0.0277	4958875	-1259	0.0007761	36.5337	4967750	0.0002088	34.3707	8875
0.032	4958625	-1309	0.0007736	37.0943	4967750	0.0001737	34.1644	9125
0.036	4958625	-1309	0.0009621	31.2304	4967375	0.0002799	28.2289	8750
0.04	4958625	-1309	0.0008940	32.8051	4967500	0.0001619	29.1705	8875

**Table D.12. Model data for LFE sensor elements with a 1.0-mm electrode gap under sodium chloride solution loads**

% NaCl	$f_{\max}$ (Hz)	$\Delta f/f_0$ (ppm)	$ Y_{\max} $ (S)	Phase( $Y_{\max}$ ) (degrees)	$f_{\min}$ (Hz)	$ Y_{\min} $ (S)	Phase( $Y_{\min}$ ) (degrees)	$f_{\min}-f_{\max}$ (Hz)
0	4965125	0	0.0009614	41.2385	4970016	0.0001285	39.7521	4891
0.0077	4958375	-1359	0.0004977	68.0421	4968922	0.0002347	68.0655	10547
0.01	4958031	-1429	0.0005013	67.6761	4968391	0.0002330	67.6272	10359
0.012	4957828	-1470	0.0005056	67.1882	4967984	0.0002311	67.2068	10156
0.016	4957563	-1523	0.0005160	66.1365	4967281	0.0002265	66.1656	9719
0.02	4957422	-1551	0.0005277	65.0333	4966703	0.0002216	64.9624	9281
0.023	4957375	-1561	0.0005368	64.1616	4966359	0.0002180	64.1264	8984
0.0277	4957359	-1564	0.0005510	62.7785	4965906	0.0002125	62.7526	8547
0.032	4957359	-1564	0.0005639	61.6825	4965594	0.0002078	61.6766	8234
0.036	4957391	-1558	0.0005755	60.5923	4965344	0.0002038	60.6451	7953
0.04	4957406	-1555	0.0005866	59.7439	4965141	0.0002000	59.7221	7734

**Table D.13. Measured data for LFE sensor elements with a 2.0-mm electrode gap under glycerol solution loads**

% Glycerol	$f_{\max}$ (Hz)	$\Delta f/f_0$ (ppm)	$ Y_{\max} $ (S)	Phase( $Y_{\max}$ ) (degrees)	$f_{\min}$ (Hz)	$ Y_{\min} $ (S)	Phase( $Y_{\min}$ ) (degrees)	$f_{\min}-f_{\max}$ (Hz)
0	4965000	0	0.0008850	81.6481	4969875	0.0001450	87.2723	4875
2	4965000	0	0.0008628	36.6934	4969625	0.0001430	37.4982	4625
4	4964625	-76	0.0007758	42.6707	4969375	0.0001550	43.5740	4750
6	4964750	-50	0.0007632	40.8405	4969375	0.0001516	42.8886	4625
8	4964750	-50	0.0007136	41.5198	4969500	0.0001355	44.7729	4750
10	4964500	-101	0.0007414	44.4646	4969375	0.0001635	42.7620	4875
12	4964500	-101	0.0007161	45.1472	4969500	0.0001661	44.0768	5000
14	4964500	-101	0.0007324	45.6634	4969500	0.0001687	44.7923	5000
16	4964625	-76	0.0006873	44.4678	4969500	0.0001421	43.1280	4875
18	4964625	-76	0.0006770	45.0432	4969625	0.0001484	45.6623	5000
20	4964625	-76	0.0006903	45.6110	4969750	0.0001482	45.2232	5125

**Table D.14. Model data for LFE sensor elements with a 2.0-mm electrode gap under glycerol solution loads**

% Glycerol	$f_{\max}$ (Hz)	$\Delta f/f_0$ (ppm)	$ Y_{\max} $ (S)	Phase( $Y_{\max}$ ) (degrees)	$f_{\min}$ (Hz)	$ Y_{\min} $ (S)	Phase( $Y_{\min}$ ) (degrees)	$f_{\min}-f_{\max}$ (Hz)
0	4965000	0	0.0008684	39.7466	4970328	0.00011	39.0945	5328
2	4965000	0	0.0008602	39.9165	4970344	0.000111	39.1725	5344
4	4964984	-3	0.0008488	40.2973	4970375	0.000112	39.8393	5391
6	4964969	-6	0.0008380	40.6844	4970391	0.000113	40.1043	5422
8	4964953	-9	0.0008270	41.0298	4970406	0.000115	40.4002	5453
10	4964922	-16	0.0008161	41.7573	4970438	0.0001160	41.0648	5516
12	4964906	-19	0.0008053	42.0491	4970453	0.000117	41.3806	5547
14	4964891	-22	0.0007947	42.3255	4970484	0.000119	42.0460	5594
16	4964859	-28	0.0007842	42.9484	4970500	0.00012	42.3824	5641
18	4964844	-31	0.0007739	43.1770	4970516	0.000122	42.7276	5672
20	4964797	-41	0.0007596	43.7724	4970547	0.000124	43.6867	5750

**Table D.15. Measured data for LFE sensor elements with a 2.0-mm electrode gap under isopropyl alcohol solution loads**

% Isopropanol	$f_{\max}$ (Hz)	$\Delta f/f_0$ (ppm)	$ Y_{\max} $ (S)	Phase( $Y_{\max}$ ) (degrees)	$f_{\min}$ (Hz)	$ Y_{\min} $ (S)	Phase( $Y_{\min}$ ) (degrees)	$f_{\min}-f_{\max}$ (Hz)
0	4965000	0	0.0008850	81.6481	4969875	0.0001450	87.2723	4875
10	4964875	-25	0.0008181	82.6564	4969625	0.0001741	87.1293	4750
20	4965000	0	0.0007256	83.3536	4969625	0.0001777	87.1449	4625
30	4965000	0	0.0006354	84.3007	4969625	0.0001772	87.1912	4625
40	4965375	76	0.0005745	84.7497	4969875	0.0001795	87.2336	4500
50	4965750	151	0.0004898	85.6744	4970875	0.0001886	87.4405	5125
60	4965875	176	0.0004626	85.7693	4970250	0.0001695	87.4145	4375
70	4966875	378	0.0003803	86.6380	4971125	0.0001689	87.6212	4250
80	4967625	529	0.0003452	86.9215	4971750	0.0001661	87.7172	4125
90	4968250	655	0.0003195	63.4445	4972125	0.0001735	63.6127	3875
100	4968750	755	0.0003059	64.8671	4972375	0.0001712	63.3388	3625

**Table D.16. Model data for LFE sensor elements with a 2.0-mm electrode gap under isopropyl alcohol solution loads**

% Isopropanol	$f_{\max}$ (Hz)	$\Delta f/f_0$ (ppm)	$ Y_{\max} $ (S)	Phase( $Y_{\max}$ ) (degrees)	$f_{\min}$ (Hz)	$ Y_{\min} $ (S)	Phase( $Y_{\min}$ ) (degrees)	$f_{\min}-f_{\max}$ (Hz)
0	4965000	0	0.0008684	39.7466	4970328	0.00011	39.0945	5328
10	4965063	13	0.0008804	39.3468	4970359	0.000109	38.4898	5297
20	4964938	-13	0.0008060	42.1288	4970500	0.000117	41.5086	5563
30	4965016	3	0.0007796	43.2054	4970703	0.000121	42.4860	5688
40	4965172	35	0.0007629	44.1457	4970969	0.000123	43.2174	5797
50	4965438	88	0.0007533	44.5324	4971313	0.000124	43.8467	5875
60	4965813	164	0.0007475	44.5643	4971719	0.000125	43.9620	5906
70	4966297	261	0.0007432	44.5378	4972234	0.000125	44.2181	5938
80	4966906	384	0.0007392	44.5692	4972859	0.000126	44.2000	5953
90	4967672	538	0.0007346	44.7458	4973656	0.000126	44.4055	5984
100	4968750	755	0.0007265	45.0513	4974781	0.000128	44.8143	6031



**Table D.17. Measured data for LFE sensor elements with a 2.0-mm electrode gap under sodium chloride solution loads**

% NaCl	$f_{\max}$ (Hz)	$\Delta f/f_0$ (ppm)	$ Y_{\max} $ (S)	Phase( $Y_{\max}$ ) (degrees)	$f_{\min}$ (Hz)	$ Y_{\min} $ (S)	Phase( $Y_{\min}$ ) (degrees)	$f_{\min}-f_{\max}$ (Hz)
0	4965000	0	0.0008850	81.6481	4969875	0.0001450	87.2723	4875
0.0077	4962375	-529	0.0005193	44.4124	4969500	0.0001364	43.9771	7125
0.01	4960750	-856	0.0005198	46.8252	4969250	0.0001470	45.6266	8500
0.012	4960250	-957	0.0005374	43.7442	4969000	0.0001487	43.0920	8750
0.016	4959625	-1083	0.0005760	42.2497	4968500	0.0001588	38.7471	8875
0.02	4958875	-1234	0.0006293	40.5545	4968625	0.0001577	39.5771	9750
0.023	4958875	-1234	0.0006698	38.4550	4968375	0.0001716	38.4559	9500
0.0277	4958000	-1410	0.0007251	35.2612	4967750	0.0001590	33.2511	9750
0.032	4958250	-1360	0.0008000	35.0509	4967500	0.0002213	35.4381	9250
0.036	4958125	-1385	0.0008625	33.6453	4967250	0.0002027	30.2812	9125
0.04	4957250	-1561	0.0008704	32.0718	4967250	0.0001741	32.0777	10000

**Table D.18. Model data for LFE sensor elements with a 2.0-mm electrode gap under sodium chloride solution loads**

% NaCl	$f_{\max}$ (Hz)	$\Delta f/f_0$ (ppm)	$ Y_{\max} $ (S)	Phase( $Y_{\max}$ ) (degrees)	$f_{\min}$ (Hz)	$ Y_{\min} $ (S)	Phase( $Y_{\min}$ ) (degrees)	$f_{\min}-f_{\max}$ (Hz)
0	4965000	0	0.0009107	41.5271	4967250	0.0001264	39.3114	2250
0.0077	4956578	-1696	0.0004279	69.3531	4968984	0.0002112	69.3632	12406
0.01	4956156	-1781	0.0004310	68.9719	4968344	0.0002097	68.9942	12188
0.012	4955891	-1835	0.0004346	68.5357	4967828	0.0002080	68.5392	11938
0.016	4955563	-1901	0.0004435	67.4846	4966953	0.0002039	67.4953	11391
0.02	4955406	-1932	0.0004536	66.3016	4966234	0.0001995	66.2858	10828
0.023	4955344	-1945	0.0004614	65.4433	4965797	0.0001962	65.3930	10453
0.0277	4955328	-1948	0.0004738	64.0230	4965250	0.0001911	64.0805	9922
0.032	4955328	-1948	0.0004851	62.9058	4964844	0.0001868	62.8803	9516
0.036	4955359	-1942	0.0004953	61.8391	4964531	0.0001831	61.8046	9172
0.04	4955406	-1932	0.0005052	60.7755	4964281	0.0001796	60.8636	8875

## REFERENCES

- [1] J. Vetelino and A. Reghu, *Introduction to Sensors*. Boca Raton, FL: CRC Press, 2011.
- [2] M. Baraton, *Sensors for Environment, Health and Security*. M. Baraton, Ed. Dordrecht, The Netherlands: Springer, 2009, pp. vii-ix.
- [3] J.F. Vetelino, "Lateral field excited acoustic wave sensor," U.S. Patent 7 075 216, Jul. 11 2006.
- [4] C. Steinem and A. Janshoff, Eds., *Piezoelectric Sensors*. Berlin: Springer, 2006.
- [5] B.A. Auld, *Acoustic Fields and Waves in Solids*. 2<sup>nd</sup> ed., vol. 1, Malabar, FL: Krieger, 1990, pp. 101-131.
- [6] J.F. Rosenbaum, *Bulk Acoustic Wave Theory and Devices*. Boston, MA: Artech House, 1988, pp. 376-397.
- [7] A. Ballato, "Piezoelectric Resonators," in *Design of Crystal and Other Harmonic Oscillators*, B. Parzen. New York: Wiley-Interscience, 1983, pp. 66-122.
- [8] D. Salt, *Handbook of Quartz Crystal Devices*. Wokingham, England: Von Nostrand Reinhold, 1987, pp. 18-22.
- [9] D. Salt, *Handbook of Quartz Crystal Devices*. Wokingham, England: Von Nostrand Reinhold, 1987, pp. 23-44.
- [10] W.A. Marrison, "The Evolution of the quartz crystal clock," *The Bell System Technical Journal*, vol. 27, pp. 510-588, Jul. 1948.
- [11] R. Aigner, "SAW and BAW technologies for RF filter applications: a review of the relative strengths and weaknesses," in *Proc. IEEE Ultrason. Symp.*, 2008, pp. 582-589.
- [12] D.S. Ballantine, R.M. White, S.J. Martin, A.J. Ricco, E.T. Zellers, G.C. Frye, H. Wohltjen, *Acoustic Wave Sensors*. San Diego, CA: Academic Press, 1997, pp. 36-70.
- [13] G. Sauerbrey, "Use of quartz vibrator for weighing thin films on a microbalance," *Z. Phys.*, vol. 155, pp. 206-222, Apr. 1959
- [14] C. Lu and O. Lewis, "Investigation of film-thickness determination by quartz resonators with large mass load," *J. Appl. Phys.*, vol. 43, pp. 4385-4390, Nov. 1972.
- [15] J.W. Grate, "Acoustic wave microsensor arrays for vapor sensing," *Chem. Rev.*, vol. 100, pp. 2627-2648, Jul. 2000.

- [16] K.A. Marx, "The quartz crystal microbalance and the electrochemical QCM: applications to studies of thin polymer films, electron transfer systems, biological macromolecules, biosensors, and cells," in *Piezoelectric Sensors*, C. Steinem and A. Janshoff, Eds. Berlin: Springer, 2006, pp. 371-424.
- [17] M. Rodahl, F. Höök, A. Krozer, P. Brzezinski, and B. Kasemo, "Quartz crystal microbalance setup for frequency and Q-factor measurements in gaseous and liquid environments," *Rev. Sci. Instrum.*, vol. 66, pp. 3924-3930, Jul. 1995.
- [18] M. Rodahl and B. Kasemo, "A simple setup to simultaneously measure the resonant frequency and the absolute dissipation factor of a quartz crystal microbalance," *Rev. Sci. Instrum.*, vol. 67, pp. 3238-3241, Sep. 1996.
- [19] F. Höök, M. Rodahl, C. Keller, K. Glasmästar, C. Fredriksson, P. Dahlgvist, and B. Kasemo, "The dissipative QCM-D Technique: interfacial phenomena and sensor applications for proteins, biomembranes, living cells and polymers," in *Proc. IEEE Freq. Contr. Symp.*, 1999, pp. 966-972.
- [20] F. Höök and B. Kasemo, "The QCM-D technique for probing biomacromolecular recognition reactions," in *Piezoelectric Sensors*, C. Steinem and A. Janshoff, Eds. Berlin: Springer, 2006, pp. 425-447.
- [21] F. Josse, "Acoustic wave liquid-phase-based microsensors," *Sens. Act. A*, vol. 44, pp. 199-208, Sep. 1994.
- [22] Y. Lee, D. Everhart, and F. Josse, "The quartz crystal resonator as detector of electrical loading: an analysis of sensing mechanisms," in *Proc. IEEE Freq. Contr. Symp.*, 1996, pp. 577-585.
- [23] C. Zhang and J. Vetelino, "Bulk acoustic wave sensors for sensing measurand-induced electrical property changes in solutions," *IEEE Trans. Ultrason., Ferroelectr., Freq. Contr.*, vol. 48, pp. 773-778, May 2001.
- [24] C. Zhang and J. Vetelino, "A bulk acoustic wave resonator for sensing liquid electrical property changes," in *Proc. IEEE Freq. Contr. Symp.*, 2001, pp. 535-541.
- [25] Y. Hu, L.A. French Jr., K. Radecsky, M.P. da Cunha, P. Millard, and J.F. Vetelino, "A lateral field excited liquid acoustic wave sensor," *IEEE Trans. Ultrason., Ferroelectr., Freq. Contr.*, vol. 51, pp. 1373-1380, Nov. 2004.
- [26] J.V. Atanasoff and P.J. Hart, "Dynamical determination of the elastic constants and their temperature coefficients for quartz," *Phys. Rev.*, vol. 59, pp. 85-96, Jan. 1941.
- [27] R. Bechmann, "Improved high-precision quartz oscillators using parallel field excitation," *Proc. IRE*, vol. 48, pp. 367-368, Mar. 1960.
- [28] R. Bechmann, "Excitation of piezoelectric plates by use of a parallel field with particular reference to thickness modes of quartz," *Proc. IRE*, vol. 48, pp. 1278-1280, Jul. 1960.

- [29] R. Bechmann, "Parallel field excitation of thickness modes of quartz plates," in *Proc. Freq. Cont. Symp.*, 1960, pp. 68-88.
- [30] W. Ianouchevsky, "High Q crystal units," in *Proc. Freq. Cont. Symp.*, 1963, pp. 233-247.
- [31] A. W. Warner, "Use of parallel-field excitation in the design of quartz crystal units," in *Proc. Freq. Cont. Symp.*, 1963, pp. 248-266.
- [32] E.R. Hatch and A. Ballato, "Lateral-field excitation of quartz plates," in *Proc. IEEE Ultrason. Symp.*, 1983, pp. 512-515.
- [33] A. Ballato, E.R. Hatch, M. Mizan, B.H.T. Chai, R.S. Tilton, and T.J. Lukaszek, "Lateral-field excitation of Berlinite," *Proc. IEEE Freq. Cont. Symp.*, 1984, pp. 206-224.
- [34] A. Ballato, E.R. Hatch, M. Mizan, T. Lukaszek, and R. Tilton. "Simple thickness modes driven by lateral fields," in *Proc. IEEE Freq. Cont. Symp.*, 1985, pp. 462-472.
- [35] A. Ballato, E. R. Hatch, M. Mizan, and T. J. Lukaszek. "Lateral field equivalent networks and piezocoupling factors of quartz plates driven in simple thickness modes," *IEEE Trans. Ultrason., Ferroelectr., Freq. Cont.*, vol. UFFC-33, pp. 385-393, Jul. 1986.
- [36] I.V. Abramson, A.N. Dikidzhi, A.I. Kutalev, and S.V. Plachotin, "Application of TC-cut quartz resonators excited by lateral electrical field," in *Proc. IEEE Freq. Cont. Symp.*, 1993, pp. 535-540.
- [37] W.W. Lau, Y. Song, and E.S. Kim, "Lateral-field excitation acoustic resonators for monolithic oscillators and filters." *Proc. IEEE Freq. Cont. Symp.*, 1996 pp. 558-562.
- [38] J.R. Vig and A. Ballato, "Techniques for sensing the properties of fluids with a resonator assembly," U.S. Patent 6 260 408, Jul. 17 2001.
- [39] J.R. Vig, "Chemical and biological sensor based on microresonators," U.S. Patent 5 744 902, Apr. 28 1998.
- [40] Y. Hu, L.A. French, K. Radecsky, M. Pereira da Cunha, P. Millard, and J.F. Vetelino, "A lateral field excited liquid acoustic wave sensor." in *Proc. IEEE Ultrason. Symp.*, 2003, pp. 46-51.
- [41] U. Hempel, R. Lucklum, J.F. Vetelino, and P.R. Hauptmann, "Advanced application of the impedance spectrum of a lateral field excited sensor," *Sens. Act. A*, vol. 142, pp. 97-103, Mar. 2008.
- [42] J.F. Rosenbaum, *Bulk Acoustic Wave Theory and Devices*, Boston, MA: Artech House, 1988, pp. 167-198.
- [43] S.J. Martin, V.E. Granstaff, and G.C. Frye, "Characterization of a quartz crystal microbalance with simultaneous mass and liquid loading," *Anal. Chem.*, vol. 63, pp. 2272-2281, Oct. 1991.

- [44] R. Krimholtz, D. Leedom, and G. Matthaiei, "New equivalent circuits for elementary piezoelectric transducers," *Electron. Lett.*, vol. 6, pp. 398-399, Jun. 1970.
- [45] B.A. Auld, *Acoustic Fields and Waves in Solids*. 2<sup>nd</sup> ed., vol. 1, Malabar, FL: Krieger, 1990, pp. 1-12.
- [46] J. Lubliner. (2006). *Plasticity Theory*. (Revised Ed.) [Online]. Available: <http://www.ce.berkeley.edu/~coby/plas/pdf/book.pdf>
- [47] H.F. Tiersten, *Linear Piezoelectric Plate Vibrations*. New York: Plenum Press, 1969, pp. 51-61.
- [48] B.A. Auld, *Acoustic Fields and Waves in Solids*. 2<sup>nd</sup> ed., vol. 1, Malabar, FL: Krieger, 1990, pp. 57-97.
- [49] J.F. Rosenbaum, *Bulk Acoustic Wave Theory and Devices*. Boston, MA: Artech House, 1988, pp. 45-86.
- [50] H.F. Tiersten, *Linear Piezoelectric Plate Vibrations*. New York: Plenum Press, 1969, pp. 33-39.
- [51] J.F. Rosenbaum, *Bulk Acoustic Wave Theory and Devices*. Boston, MA: Artech House, 1988, pp. 136-143.
- [52] D.F. McCann, L.A. French Jr., M.S. Wark, and J.F. Vetelino, "Recent advances in lateral field excited and monolithic spiral coil acoustic transduction bulk acoustic wave sensor platforms," *Meas. Sci. Technol.*, vol. 20, pp. 124001-124012, Dec. 2009.
- [53] K. Kanazawa and J. Gordon, "Frequency of a quartz microbalance in contact with liquid," *Anal. Chem.*, vol. 57, pp. 1770-1771, Jul. 1985.
- [54] S.C. Ng, X.C. Zhou, Z.K. Chen, P. Miao, H.S.O. Chan, S.F.Y. Li, and P. Fu, "Quartz crystal microbalance sensor deposited with Langmuir-Blodgett films of functionalized polythiopenes and application to heavy metal ions analysis," *Langmuir*, vol. 14, pp. 1748-1752, Mar. 1998.
- [55] M.G. Schweyer, J.A. Hilton, J.E. Munson, and J.C. Andle, "A novel monolithic piezoelectric sensor," in *Proc. IEEE Freq. Cont. Symp.*, 1997 pp. 32-40.
- [56] M.G. Schweyer, J.A. Hilton, J.E. Munson, and J.C. Andle, "A novel monolithic piezoelectric sensor," in *Proc. IEEE Ultrason. Symp.*, 1997 pp. 371-374.
- [57] J.C. Andle and R.M. Lec, "Monolithic piezoelectric sensor (MPS) for sensing chemical, biochemical, and physical measurands," U.S. Patent 6 033 852, Mar. 7 2000.
- [58] R. Lucklum and P. Hauptmann, "Transduction mechanism of acoustic-wave based chemical and biochemical sensors," *Meas. Sci. Technol.*, vol. 14, pp. 1854-1864, Nov. 2003.

- [59] C.E. Reed, K.K. Kanazawa, and J.H. Kaufman, "Physical description of a viscoelastically loaded AT-cut quartz resonator," *J. Appl. Phys.*, vol. 68, pp. 1993-2001, Sep. 1990.
- [60] R. Lucklum, D. Soares, and K. Kanazawa, "Models for resonant sensors," in *Piezoelectric Transducers and Applications*, 2<sup>nd</sup> ed., A.A. Vives, Ed. Berlin: Springer, 2008, pp. 63-96.
- [61] P.C.Y. Lee, "Electromagnetic radiation from an AT-cut quartz plate under lateral-field excitation," in *Proc. IEEE Ultrason. Symp.*, 1988, pp. 407-411.
- [62] B.A. Auld, *Acoustic Fields and Waves in Solids*. 2<sup>nd</sup> ed., vol. 1, Malabar, FL: Krieger, 1990, pp. 281-307.
- [63] T. Yamada and N. Niizeki, "Formulation of admittance for parallel field excitation of piezoelectric plates," *J. Appl. Phys.*, vol. 41, pp. 3604-3609, Aug. 1970.
- [64] R.O. Hill, Jr., *Elementary Linear Algebra with Applications*. 2<sup>nd</sup> ed., San Diego, CA: Harcourt Brace Jovanovich, 1991, pp. 347-353.
- [65] H.F. Tiersten, *Linear Piezoelectric Plate Vibrations*. New York, NY: Plenum Press, 1969, pp. 157-158.
- [66] J.F. Rosenbaum, *Bulk Acoustic Wave Theory and Devices*, Boston, MA: Artech House, 1988, pp. 1-43.
- [67] R.D. Mindlin, "Electromagnetic radiation from a vibrating quartz plate," *Int. J. Solids Structures*, vol. 9, pp. 697-702, 1973.
- [68] W. Pinkham, M. Wark, S. Winters, L. French, D.J. Frankel, and J.F. Vetelino, "A Lateral Field Excited Wave Pesticide Sensor," in *Proc. IEEE Ultrason. Symp.*, 2005, pp. 2279-2283.
- [69] A. Ballato, "Mindlin's elastoelectrodynamics problem," in *Proc. IEEE Freq. Cont. Symp.*, 1988, pp. 6-13.
- [70] A.P.M. Glassford, "Response of quartz crystal microbalance to liquid deposit," *J. Vac. Sci. Technol.*, vol. 15, pp. 1836-1843, 1978.
- [71] R.B. Bird, W.E. Stewart, and E.N. Lightfoot, *Transport Phenomena*. 2<sup>nd</sup> ed., New York: Wiley, 2001.
- [72] T.M. Niemczyk, S.J. Martin, G.C. Frye, and A.J. Ricco, "Acoustoelectric interaction of plate modes with solutions," *J. Appl. Phys.*, vol. 64, pp. 5002-5008, Nov. 1988.
- [73] F. Josse, Z.A. Shana, D.E. Radtke, and D.T. Haworth, "Analysis of piezoelectric bulk-acoustic wave resonators as detectors in viscous conductive liquids," *IEEE Trans. on Ultrason. Ferroelec. and Freq. Cont.*, vol. 37, pp. 359-368, Sep. 1990.
- [74] A.W. Adamson, *Physical Chemistry of Surfaces*, 4<sup>th</sup> ed., New York, NY: Wiley, Ch. 5.

- [75] P.W. Atkins, *Physical Chemistry*, 4<sup>th</sup> ed., New York, NY: W.H. Freeman and Company, 1990, pp. 250-252.
- [76] W.H. Beyer, ed., *CRC Standard Mathematical Tables*, 27<sup>th</sup> ed., Boca Raton, FL: CRC Press, 1984, pp. 295-298.
- [77] J.D. Krauss and D.A. Fleisch, *Electromagnetics*, 5<sup>th</sup> ed., Boston, MA: WCB/McGraw-Hill, 1999, pp. 178-181.
- [78] R. Smith, Lecture notes from ECE 598: Advanced Topics in Electrical and Computer Engineering – Microsensor Fabrication and Design, University of Maine, Orono, ME, Fall 2006.
- [79] R.E. Bennett, ed., *Quartz Resonator Handbook*, Niles, IL: Comptometer Corp., 1960, p. 90.
- [80] P.N. Wolfe, "Capacitance calculations for several simple two-dimensional geometries," *Proc. IRE*, vol. 50, pp. 2131-2132, Oct. 1962.
- [81] B.A. Auld, *Acoustic Fields and Waves in Solids*. 2<sup>nd</sup> ed., vol. 1, Malabar, FL: Krieger, 1990, pp. 365-390.
- [82] R.C. Weast, ed., *CRC Handbook of Chemistry and Physics*, 54<sup>th</sup> ed., Cleveland, OH: CRC Press, 1974, pp. D-192 – D-2.
- [83] J.R. Huck, G.A. Noyel, and L.J. Norat, "Dielectric Properties of Supercooled Glycerol-Water Solutions," *IEEE Trans. On Elec. Insul.*, vol. 23, pp. 627-638, Aug. 1988.
- [84] F. Pang, C. Seng, T. Teng, and M.H. Ibrahim, "Densities and viscosities of aqueous solutions of 1-propanol and 2-propanol at temperatures from 293.15 K to 333.15 K," *J. Mol. Liquids*, vol. 136, pp. 71-78, Nov. 2007.
- [85] G. Åkerlöf, "Dielectric Constants of Some Organic Solvent-Water Mixtures at Various Temperatures," *J. Am. Chem. Soc.*, vol. 54, pp. 4125-4139, Nov. 1932.
- [86] A. Peyman, C. Gabriel, and E.H. Grant, "Complex Permittivity of Sodium Chloride Solutions at Microwave Frequencies," *Bioelectromagnetics*, vol. 28, pp. 264-274, May 2007.

## BIOGRAPHY OF THE AUTHOR

Lester A. French was born in Manchester, NH on 22 July 1966. He was raised and attended school in Pembroke, NH and graduated from Pembroke Academy in 1985. Lester attended the University of New Hampshire, Durham, NH and graduated with a Bachelor's Degree in Electrical Engineering with a minor in Optical and Illumination Engineering in 1993. From 1993 to 1996 he worked as Commercial Engineer for the lighting manufacturer, Duro-Test Corporation, Fairfield, NJ. He attended the University of Maine, Orono, ME and graduated with a Master's Degree in Electrical Engineering in 2002. While pursuing his Master's Degree he worked as Research Engineer for BIODÉ Corporation on acoustic wave sensors for detecting chemicals in liquid. Lester taught ECE 453: Microwave Engineering at the University of Maine from 1999-2000 as a Teaching Assistant and in 2001 he received the Edward T. Bryand Graduate Teaching Assistant Award. In 2002 he was awarded a National Science Foundation GK-12:*Sensors*/Fellowship, teaching science, technology, engineering, and math topics to middle and high school students in Bangor, Carmel, Hermon, and Levant, ME, while pursuing an interdisciplinary Ph.D. in Sensors at the University of Maine. He has been with Mainely Sensors, LLC as Senior Research Engineer since its founding in 2002 and Director of Business Development since 2008. He is currently an Adjunct Instructor of Chemistry and Math at Husson University where he has taught since 2009. His research focus has been on acoustic wave sensors for chemical and biological analytes in liquid. He has been principal investigator on three Small Business Innovation Research grants. He has been co-author of 18 technical papers in peer reviewed journals and conference proceedings and has given oral presentations at five international conferences. Lester is a candidate for the Doctor of Philosophy in Sensors at The University of Maine in August 2011.